Buoyancy-Assisted Microfluidics

Chaurasia, Ankur Shubhlal

Awarding institution:
King's College London

KING'S College LONDON

University of London

DOCTORAL THESIS

Buoyancy-Assisted Microfluidics

by

Ankur Shubhlal Chaurasia

A thesis submitted in fulfilment of the requirements for the degree of

Doctor of Philosophy in Physics

to

Department of Physics

School of Natural and Mathematical Sciences

KING'S COLLEGE LONDON

May 2016

Declaration of Authorship

I, Ankur Shubhlal Chaurasia, declare that this thesis, titled "Buoyancy-Assisted Microfluidics", and the work presented in it are my own, and that the word limit prescribed in the College regulations is not exceeded. I further confirm that where I have consulted or quoted from the published work of others, this is always clearly attributed and referenced accordingly.

Sign: _____

Date: _____

Dedicated to my parents, Shri. Shubhlal Chaurasia and Smt. Sharda Chaurasia, and my brother Rajan Chaurasia

Acknowledgements

Words cannot express my gratitude and appreciation towards my family, including my parents, brother and sister-in-law, for providing continuous support of all kinds, and sharing the highs and lows of this exhilarating, and sometimes enduring, research experience.

I would also like to extend my sincere gratefulness to my supervisor Dr. Shahriar Sajjadi for the research opportunity and his incessant support throughout the course, which was monumental in making it an enjoyable and memorable experience. I would particularly like to thank him for being ever so accessible and welcoming, for uncountable, intense and long brainstorming sessions, and for the valuable writing advices over the last four years. I would also like to thank my second supervisor Dr. Gregory Wurtz for constant encouragement and for advice towards realising the broader scope of the research.

During this research period, I was fortunate to have been surrounded by a bunch of amazingly warm and affectionate friends: Ali, Andreas, Angela, Boz, Dimitris, Hina, Hugo, Joao, Mohammad and Radhwan.

My special thanks goes out to Dimitris for his incredible support in the lab and for regular scientific discussions, but more importantly for sharing the long hours of ping-pong play in daylight as well as under the floodlights to bust the stress of research life. I would also like to thank Angela and Joao for the much-needed support and companionship, particularly in the last year of the research. I am also indebted to Mohammad for giving me a delightful company, for regular updates about the political current affairs in the Middle East where Saudi Arabia is always right, and for enriching my understanding of running a potato-chips business. Last but not the least, I feel fortunate to have found an

amazing friend in Hina, who always helped with a balanced outsider’s perspective, being the closest friend from outside the research bubble.

The extensive lab works carried out during this research would not have been possible without the highest level of technical support by Mr. Julian Greenberg, who I also thank sincerely for his extraordinarily swift action to resolve all kind of crises. I would also like to extend my appreciation to Dr. Fatemeh Jahanzad for enriching our lab with several precious instruments, especially the high speed camera and the pumps. I further thank Mr. William Luckhurst for helping out with SEM imaging at several occasions.

Finally, I would like to thank the Engineering and Physical Sciences Research Council (EPSRC) for providing a range of high-speed recording cameras at multiple times during the course time, and the King's Graduate School for providing the King's Alumni Bursary as financial support during this research.

Abstract

A buoyancy-assisted microfluidic approach is introduced for facile production and collection of uniform drops within a wide range of sizes, particularly on a millimetre scale, which is not easily achievable via conventional microfluidic approach. The proposed methodology, characterised by vertical orientation and non-confined quiescent outer phase of the device used, was also applied to droplet-in-droplet and droplet-in-fibre encapsulation using a co-axial glass microcapillary arrangement, to obtain millimetric capsules and multi-compartmental fibres.

The shell thickness of double emulsions was tuned, via altering flow rates and formulations, to produce millimetric ultrathin shelled capsules. Alginate fibres with different oil-encapsulate geometries were fabricated, via simultaneous oil-droplet formation and encapsulation, and characterised and analysed for their encapsulation volume, surface roughness, spillage ratio and mechanical strength. Furthermore, the size and locations of oil encapsulates were manipulated to obtain asymmetric fibres with parallel oil streams. An asymmetric encapsulation approach was designed and used to fabricate dehydration-responsive fibres, which demonstrated a benign and facile dehydration-triggered core-release mechanism. This core-release response was also demonstrated for fibres with parallel oil-encapsulates with multiple cargos. The fibre morphology was also tuned to provide an enhanced response to its mechanical failure, marked by a simultaneous release of potentially reactive components at the point of fracture. Such fibres, can behave as fibres with self-repairing properties.

The buoyancy-assisted microfluidics was also used to produce microfibres containing gas encapsulates with tuneable morphology. The buoyancy force, driven by the trapped microbubbles, was utilised for stretching the gelling alginate fibres to fabricate ultrathin alginate microfibres, a feature not possible via conventional horizontally-oriented microfluidic techniques. The collected bubble-filled fibres were also morphed to produce new varieties of fibres, such as beaded fibres and fibres with segmented aqueous cores.

Table of Contents

List of Figures

List of Tables

Nomenclature

Symbol	Meaning
CMC	Critical Micellar Concentration
Surfactant	Surface active agent
SDS	Sodium Dodecyl Sulfate
We	Weber number
Bo	Bond number
Ca	Capillary number
SEM	Scanning Electron Microscopy
CLSM	Confocal Laser Scanning Microscopy
PDMS	Poly(dimethylsiloxane)
t_c	Capillary time
t_f	Drop formation time
Q	Volumetric flow rate
t_p	Pinch-off time
t_g	Growth time of the jet
ρ	Density
u	Velocity
$\Delta\rho$	Density difference
V_{drop}	Drop volume

r_w	Wetting radius
σ	Interfacial tension
θ	Contact angle
F_k	Kinetic force
F_b	Buoyancy force force
F_d	Drag force
η	Viscosity
C_v	Coefficient of variation
σ'	Standard deviation
μ'	Mean
Re	Reynolds number
f	Formation frequency
t_{av}	Surface-average age of a drop
t_c	Characteristic time
l_g	Gelled alginate thickness
l_{alg}	Alginate shell thickness
UTS	Ultimate tensile stress
E	Young's modulus
CSA	Cross section area
F_{max}	Failure load
ϕ	Volumetric phase ratio

S_{sat}	Saturation swelling ratio of fibres (),
w_{wet}	Weight of a fully hydrated alginate fibre
w_{dry}	Weight of a fully dried alginate fibre
S_{rup}	Swelling ratio at which the shell rupture occured
P	air pressure

Chapter 1 Introduction

1.1. MICROFLUIDIC TECHNOLOGY: ADVANTAGES AND CHALLENGES

Microfluidics has rapidly emerged as a powerful tool for advanced fluid manipulation at micro- and nano-scale in the last two decades, particularly for fabrication of uniform drops and structures. Microfluidic technology offers unprecedented advantages over other competitive technologies such as membrane emulsification on the uniformity and precision by which sophisticated structures can be made, and their reproducibility and reliability, but suffers from lack of scalability. The droplet formation within the small confinements of a typical microfluidic device is primarily dominated by drag force exerted by the high fluid velocities. This allows the formation of highly monodisperse droplets on a micrometre scale, ranging from simple liquid-liquid dispersions to intricately complex high-order emulsions, which usually find their applications in different research areas, such as biomedical and pharmaceutical fields, where highly ordered materials are required.

While there have been numerous intensive and extensive researches conducted on drag-dominated microfluidic drop formation, there appears to be very limited amount of study performed on drop formation in a microfluidic device under the buoyancy effect. This is quite intriguing as droplet formation by buoyancy-assisted micro capillaries precedes the microfluidic era as most fundamental studies of drop formation including terminal drop velocity and surface tension measurements (pendant drop) have been traditionally conducted on the behaviour of single drops under the influence of buoyancy. It comes as no surprise that the compound multi-phase microfluidic emulsification under the gravity effect has remained largely unexplored.

Conventional microfluidic devices suffer from some operational challenges, such as its inability to produce a desirably wide range of drop sizes, particularly on a millimetre scale. A wide drop size range is necessary to address a variety of applications, such as cell encapsulation and manipulation [1].

In order to achieve millimetre-sized drops in existing microfluidic devices, the velocity of the continuous phase should be minimised to reduce the dominant shear force, which otherwise severely limits the drop size to well below a millimetre scale. However, the use of low continuous phase velocities in conventional devices is not feasible, as the transportation of resulting large droplets becomes problematic due to their accumulation in dead zones inside the device because of their tendency to rise. Furthermore, the transportation of emulsion via a continuous flow of the outer phase requires additional work, and also makes it difficult to scale up the device for higher throughput.

We introduce a modified microfluidic approach for emulsification, which has been termed as “Non-Confined Microfluidics”. This hybrid approach provides a novel and advantageous emulsification system, which benefits from the highly controlled fluid manipulation associated with microfluidic techniques, and also enjoys the advantages of buoyancy-assisted features namely a convenient transportation mechanism and a scalable design due to the quiescent continuous phase. In this research, the non-confined microfluidic technique was extensively investigated and its features, characteristics and limitations were analysed. This technique was applied to a wide variety of systems including buoyancy-assisted drop formation and encapsulated (compound) drop formation to fabricate millimetre-sized ultrathin shell capsules. The technique was also extended to encapsulate low density phases, such as oil droplets and bubbles, in a jetting middle phase, to obtain compound fibres, which were formed and collected under the

buoyancy effect. Additionally, the encapsulate morphology and location were tuned to fabricate microfibres with configurable internal architecture.

1.2. RESEARCH OBJECTIVES

In this thesis, we introduce a modified microfluidic technique (termed as non-confined microfluidics) which takes advantage of the buoyancy to produce a wide range of drop sizes with a convenience of buoyancy-assisted transportation and improved scalability. This technique is also extended to undertake the droplet-in-droplet and droplet/bubble-in-fibre encapsulation. Various fundamental physical models are derived for predicting the size of droplets under the buoyancy effect. The main objectives of this research are as follows.

a) To re-visit droplet formation under the buoyancy effect, both experimentally and theoretically, where the drag force is eliminated due to a quiescent outer phase, and refine the underlying theory describing the process.

b) To extend the study to the formation of core-shell drops having a wide drop-size range under the buoyancy effect, using a one-step encapsulation approach, with the focus being on making core-shell capsules with ultrathin shells on a millimetre scale.

c) To explore droplet-in-fibre encapsulation under the buoyancy effect, investigate how buoyancy effect can contribute to the morphology of encapsulates as well as the fibres under various conditions, and analyse how encapsulate geometry, location and orientation can be tuned to fabricate fibres with flexible internal architecture.

d) To take advantage of buoyancy-assisted approach to conduct bubble-in-fibre encapsulation, which facilitates the transportation of the resulting fibres, to explore the

possibility of using the buoyancy force to produce thin microfibres, and to fabricate fibres with different sizes/structures.

1.3. THESIS STRUCTURE

A literature review is presented in Chapter 2, which includes a brief summary of the drop formation studies. It begins with a review of drop formation studies in quiescent liquid-liquid systems, followed by a summary account of the microfluidic emulsification techniques in the contemporary research. The literature review ends with a brief section on the conclusions drawn from the literature review.

Chapter 3 describes the common experimental details, and different measurement and characterisation techniques used throughout the research presented in this thesis.

Chapter 4 presents the study on simple drop formation under the buoyancy effect, which also involves a theoretical model for drop size predictions that takes into account the effect of dynamic interfacial tension.

Chapter 5 discusses the details of investigation in the formation of millimetric core-shell drops under the buoyancy effect, which is studied and compared in the absence and presence of surfactants in the middle and outer phases, to analyse the role of interfacial tension in reducing the shell thickness. This chapter also includes a fundamental physical model for drop size predictions. Following the understandings obtained from Chapter 5, a wider range of surfactant concentrations is explored in Chapter 6 to find the optimum condition for achieving ultrathin shelled drops for a wide drop size range.

Chapter 7 deals with the symmetric encapsulation of oil droplets in biocompatible alginate microfibres in the non-confined device, where the low-density encapsulates transport the fibres under the buoyancy effect. The encapsulate geometry is tuned across

a wide range of shapes, from segmented sphere to continuous tubular. The impact of different encapsulate geometries on the fibre properties is also studied, such as encapsulation volume, spillage ratio, degree of waviness of fibres and mechanical strength when exposed to uniaxial tensile testing. A physical model is also introduced for drop size predictions in a non-gelling system, where the buoyancy force dominates the drop formation. The model is used to study the viscosity variations in the gelling alginate phase with the flow conditions and formulations.

Chapter 8 introduces a flexible approach to fabricate fibres with asymmetric oil-encapsulates. The effect of flow conditions on the encapsulation asymmetry is also explored. Different strategies for hybrid assembly of asymmetric fibres is presented, which could be useful for custom-designing of oil-loaded fibre pads. The advantages of asymmetric encapsulation in fibres is demonstrated with two specific examples. We demonstrated these asymmetric microfibres can be made to release the core content upon their dehydration, which could meet triggered-release requirements for biomedical applications. These fibres were also modified to show the capability of simultaneous release of multiple materials in the event of their mechanical fracture, which could form the basis to design self-repairing fibres.

Chapter 9 investigates the encapsulation of gas phase in alginate fibres, which also assists in stretching the fibre in the vertically oriented device to reduce its thickness below the device geometry. The impact of encapsulated bubble geometry and the shell formulation on the rate of release of gas cores via its dissolution is also studied.

In the end, Chapter 10 presents some general conclusions derived from the research and lays out some recommended extensions of this work in future.

Chapter 2 Background and Literature Review

2.1. BACKGROUND

This section introduces the details of the *emulsification* process, which is a generic term for manipulating two or more immiscible fluids for creating liquid-in-liquid dispersions. The governing parameters in this technique, such as the role of surfactants, the stability of emulsions and the dynamics of interfacial tension, are also explained.

2.1.1. Emulsification

Emulsions [2], which are dispersion of one immiscible liquid into another, play a vital role in our daily lives. Examples of commonly used emulsions include milk, paints and creams. The simplest type of emulsion is a single emulsion, where one fluid is dispersed into another liquid phase (Figure 2.1e). When this single emulsion is introduced as a dispersed phase into a third phase called as *outer phase*, it leads to the formation of a *double emulsion* (Figure 2.1f). Double emulsions can have one or more core drops encapsulated in the middle phase, which is dispersed into the outer phase. A *core-shell* drop is a type of double emulsion which contains only a single core drop within. Even higher order emulsions (W/O/W/O, W/O/W/O/W etc.) can be obtained by extending the process with further repetitive steps. A high degree of droplet uniformity is of paramount importance for achieving a colloidal model system with a highly predictable behaviour. Such model systems can give a desired response with impeccable accuracy to external variables, as each droplet in a highly monodisperse system would respond identically.

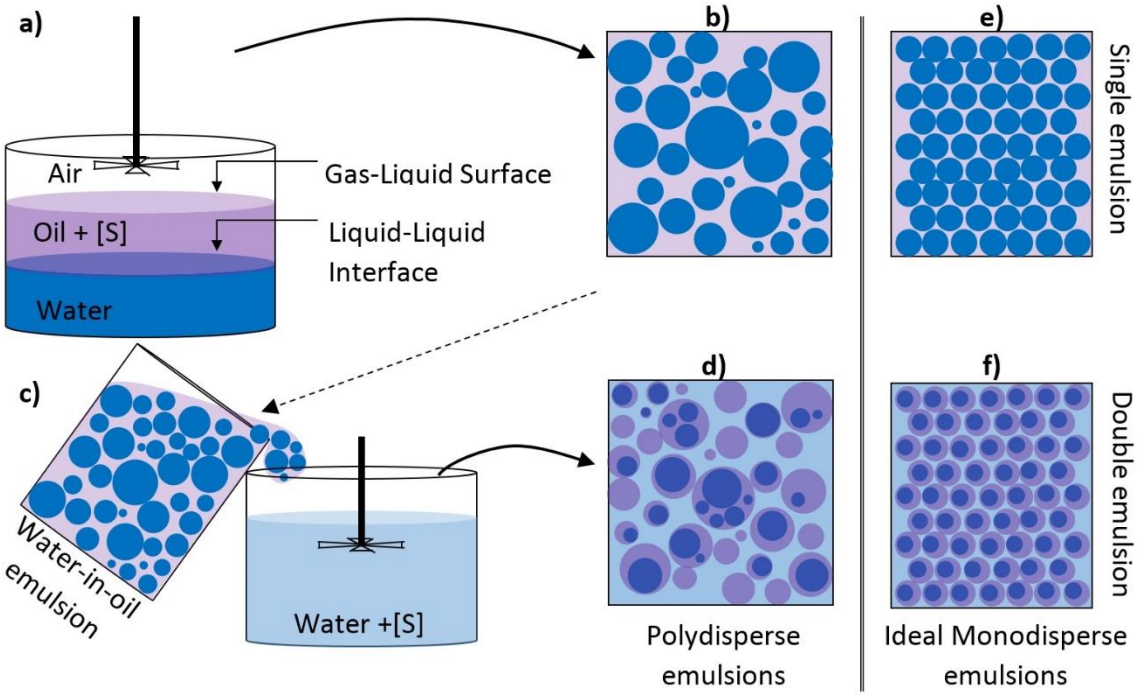

Figure 2.1 (a) The schematic shows the formed gas-liquid and liquid-liquid interfaces when a layer of oil is added on top a water phase. When this oil-water system is agitated, it results in the formation of a polydisperse single (water-in-oil) emulsion (b). (c) The single emulsion can be dispersed into a third aqueous phase to obtain a non-uniform double emulsion. (e) and (f) depict the ideally monodisperse single and double emulsions respectively.

Conventional emulsification techniques usually involve pouring a bulk of dispersed phase directly into the continuous phase, which is then agitated using a vigorous mixer or a rotor-stator system to break down the dispersed phase bulk into small droplets (Figure 2.1a). This process can be repeated to produce high-order compound emulsions (Figure 2.1c). While conventional emulsification techniques are scalable due to their high-yield capacity, their main drawback is that they suffer from a very poor drop size uniformity (Figure 2.1b) due to the uncontrolled mixing, which usually gets worse with increasing the order of emulsions (Figure 2.1d). Several techniques have been developed to improve the droplet uniformity, such as membrane [3] and microfluidic [4] emulsification techniques. Membrane emulsification approaches provide a significant improvement in droplet uniformity at the cost of throughput, in comparison with conventional methods.

Microfluidic techniques suffer from a much lower throughput, as they carefully produce one drop at a time, with a typical volumetric production rate of ~1-10 millilitres per hour. However, the attractive combination of requiring only small fluid volumes with exquisite control over fluid manipulation makes microfluidic techniques an ideal candidate for undertaking a wide range of analyses and research studies.

The liquid-liquid interface (Figure 2.1a), created around the dispersed phase in an emulsion, is characterised by the build-up of an intermolecular attraction force, which is usually referred to as *interfacial tension*. The interfacial tension drives the droplets to take spherical shape to minimize their surface energy. This is similar to the surface tension which exists at the gas-liquid surface. Various techniques have been developed to measure interfacial tension between two fluids. Direct measurement method using microbalance techniques (Wilhelmy plate method, Du Nouy ring method) involve measuring interfacial tension by measuring the force exerted on the plate/ring and translating it into interfacial tension. A second class of technique involves an indirect estimation of the interfacial tension, which is based on the deformation of drop shape under the influence of gravity, such as Pendant drop and Sessile drop techniques.

2.1.2. Emulsion stability and role of surfactants

The quality of the emulsion-based products depends on the stability of the emulsion, where the stability is usually measured as a resistance against any change in the emulsion's properties with time. Unstable emulsions are often characterised by one or a combination of these phenomena: *coalescence*, *creaming*/*sedimentation*, *flocculation* and *Ostwald Ripening*. Coalescence occurs when two small-sized dispersed droplets merge to become a single large droplet, which adversely affects the uniformity, and usually leads to an eventual phase separation [5]. In the case of creaming/sedimentation, the dispersed

droplets migrate towards the top or the bottom of the emulsion bulk due to the buoyancy effect (density difference), which reduces the homogeneous dispersion of the droplets in the continuous phase [6]. Flocculation is characterised by the formation of a cluster of droplets due to high inter-droplet attractive forces, which then usually undergoes creaming/sedimentation [7]. Ostwald Ripening is another destabilising phenomenon where, in case of a non-uniform dispersion, the larger droplets tend to grow by consuming the smaller droplets [8]. A class of surface active agents, known as *surfactants*, are usually added to the continuous phase to suppress the destabilisation of emulsions and improve its stability[9]. The surfactant molecules usually contain two parts, hydrophilic (head) and hydrophobic (tail), one which is attracted to the dispersed phase and the other part to the continuous phase [10]. Because of this amphiphilic property, the surfactant molecules settle at the liquid-liquid interface and reduce the interfacial tension. There are different types of surfactants such as, anionic, cationic and non-ionic. Sodium Dodecyl Sulfate (SDS) is an example of anionic surfactant which is soluble in water. When two droplets with anionic surfactant molecules at their interfaces approach each other, the exterior-heads of the surfactant molecules at both droplet interfaces create a repulsion force due to same charges, which prevents the coalescence. Nonionic surfactants stabilise droplets via "steric effects". Surfactants are also used for cleaning purposes, altering wetting properties, emulsification and anti-foaming. An increase in the surfactant concentration decreases the interfacial tension to a certain extent, beyond which the interfacial tension does not change once the available interface is fully saturated by the surfactant molecules. This limit in the surfactant concentration is known as *Critical Micellar Concentration* (CMC) [11]. A further increase in surfactant concentration adds superfluous surfactant molecules in the bulk phase, where they may arranged themselves in different geometries

as aggregates of molecules known as *Micelles* [12]. Micelles do not alter the interfacial tension, but it may affect other properties of the bulk phase, such as its viscosity.

From the previous discussion, it can be understood that the interfacial tension is a function of surfactant concentration. However, the interfacial tension may also vary with time, as the diffusion of surfactant molecules from the bulk location to the liquid-liquid interface is a time-dependent phenomenon [13], where the rate of diffusion also depends on the size of molecules. This makes the measurement of interfacial tension with time a dynamic process, and this measurement is known as *dynamic interfacial tension*. The dynamic interfacial tension also plays an important role in the physics of drop formation.

2.1.3. Dimensionless numbers for drop formation analysis

In the physics of drop formation, four main forces determine the final drop size, namely interfacial tension force, kinetic force, buoyancy force and drag force. The interfacial tension force, which arises from the interfacial tension present at the liquid-liquid interface, is cohesive in nature. The kinetic and buoyancy forces are detaching in nature. The kinetic force pushes the drop away from its position due to the momentum gained by the moving dispersed phase, while the buoyancy force usually promotes drop detachment due to the density difference between the dispersed and continuous phase. The nature of drag force is circumstantial. It may act as a disruptive force if the velocity of the continuous phase is higher than that of the forming drop, or become cohesive in the opposite condition. In case of non-confined microfluidics, where the continuous phase remains quiescent, the drag force remains cohesive, however, its magnitude is extremely small compared to other forces.

To quantify the relative significance and dominance of different forces involved in the drop detachment process, several dimensionless numbers, namely *Weber number*, *Bond*

number and *Capillary number*, are usually used. The Weber number (*We*) is defined as the ratio of kinetic force to the interfacial tension force, which signifies the extent of contribution of the kinetic force to the drop detachment, in comparison with other detaching forces. Similarly, the Bond number (*Bo*) and Capillary number (*Ca*) are computed as the ratio of buoyancy and drag forces to the interfacial tension force, respectively.

2.2. LITERATURE REVIEW

The literature review on droplet formation studies is divided into four sections. The first part presents a brief summary of the buoyancy-driven drop formation studies in the pre-modern era. The next section accounts for the remarkable transition in the drop formation techniques with the arrival of microfluidic technology, which facilitated the formation of uniform sub-millimetric droplets for the first time. In the third section, several successful reports demonstrating unprecedented dexterity of the microfluidic technology are covered, which also include the formation of uniform double- and higher order emulsions, which has enabled the fabrication of new class of active and smart materials. The last section reviews a relatively new and upcoming usage of the microfluidics technology as a tool for fabricating simple and compound microfibres with high precision and accuracy. The increasing number of reports on microfluidic fabrication of hybrid microfibres, particularly in the recent few years, indicates that this technique holds significant potential for future investigations.

2.2.1. Buoyancy-driven drop formation studies

The study of drop formation has been a subject of research interest for a long time, dating back as far as 1850s. Below is a brief chronological account of some of the defining drop

formation studies reported in the 19th and the 20th century, most of which based their studies on the role of buoyancy in the drop formation.

The drop formation studies, which began in 1840s by Savart [14], has been followed in both liquid/gas and liquid/liquid configurations with constantly evolving understandings. A review on the drop formation studies done in pre-modern times was presented by Egger [15], which stated Savart's argument that 'the break-up of liquid jets is governed by laws independent of the circumstances under which a jet is produced'. Interestingly, without any recording facility to document the drop formation event, which typically takes a fraction of a second, Savart presented schematics of the drop break up mechanism with his naked eye. Later in 1849, Joseph Plateau [16] developed his own technique to study break-up of a liquid column into droplets by dispersing one liquid into another (immiscible system) after matching the density of the two liquids, which removed the effect of buoyancy on the drop break up. Shortly after in 1879, Rayleigh [17] introduced the flow dynamics into the break-up process by relating the inertial and surface tension forces. He proposed that the time scale of break-up of a liquid column is directly proportional to column radius and density, and inversely proportional to the surface tension, for a specific case of low viscosity liquid.

In 1919, Harkins and Brown [18] developed a model to predict the size of drops formed in a buoyancy-driven system at an extremely small volumetric flow rate, by equating interfacial tension force with the buoyancy force. They also added a correction factor to include the liquid volume which remained attached to the needle after drop detachment. The Harkins and Brown equation was later improved by Hayworth and Treybal in 1950 [19], with the inclusion of the velocity and drag effects on the drop formation. In 1996, Rao et al. [20] developed a two-stage model for drop size prediction, in which the first

stage used the Harkins and Brown equation, while the second stage took into consideration the additional fluid volume that enters the drop during the pinch-off process after the force-balance is reached and the drop detachment begins. They also developed a model for the pinch-off time for two separate systems, one with low viscosity (low viscosity dispersed and continuous phase) and another with a high viscosity continuous phase. In 2004, this two-stage model was applied to a two-aqueous phase system to estimate the final drop volume by Barhate et al. [21]. The buoyancy-driven drop generation mechanism was also used as a means to measure surface tension and interfacial tension for liquid/gas and liquid/liquid systems respectively [22].

A numerical study of the drop formation in liquid-liquid systems was also reported by Richards et al. [23] in 1995. They studied the drop formation before and after jetting of a liquid phase injected vertically into another immiscible liquid phase. This was the first numerical model reported that was able to quantitatively predict the size of drops formed in liquid-liquid systems under conditions where all relevant forces, inertia, viscosity, surface tension and gravity were important.

The historical narrative presented above clearly illustrates that the origin and the initial development of the drop formation theories centred around the gravitational force acting on the drops due to the simplicity of the system.

2.2.2. Microfluidic droplet formation studies

In this section, we review different features of microfluidic devices, their applications, geometrical classifications, and also elaborate on some important investigations undertaken using these devices.

2.2.2.1.Features and applications of microfluidic emulsification techniques

In spite of the ease and simplicity, the usage of buoyancy-driven drop formation mechanism was limited due to the lack of considerable fluid manipulation. A revolutionary approach for fluid manipulation was formally introduced in 1993 by Gravesen et al. [24], which was termed as '*microfluidics'*, as it enabled the manipulation of fluids at micrometre scale. Microfluidics broadly include systems with at least one parameter, of the parameters involved in the drop formation, in the device, or in the drop sizes or other fluid flow parameters constrained to sub-millimetre scale.

The device primarily consisted of a small block of PDMS material with narrows channels etched within, into which the fluids can be injected at a desired rate, which could be manipulated appropriately and collected at the other end. Furthermore, a microfluidic device consumes only a small volume of liquids, typically a few millilitres, for performing a wide range of complex investigations, which could be extremely beneficial in certain situations where the availability of some precious liquids is scarce or highly expensive. This reduces the necessity and wastage of precious samples, increases the data quality and provides multiple reliable parameters to vary the droplet sizes, which are not possible by using the conventional emulsification techniques. However, the main disadvantage of the microfluidic approach is the low throughput.

As an emulsification tool, the microfluidic technique involves producing one drop at a time which allows for producing simple as well as complex emulsions without compromising on the high degree of monodispersity. Such tailored liquid-liquid dispersions have been used as templates to fabricate different structured materials, such as microparticles [4], microcapsules [25] and microfibres [26] of configurable size, shape and composition, some examples of which are schematically shown in Figure 2.2. These

structured materials have found several applications. For example, solid microparticles can be used as the carriers of drugs, which are usually embedded in the particle's polymer matrix [27], and then gradually released via diffusion or matrix dissolution processes. In such cases, the particle's shape may strongly affect the release behaviour. In contrast, hollow particles have a continuous solid polymer shell covering a hollow interior, which can be filled with non-solid phases such liquids and gases [28]. The hollow particles may have one or multiple cores of different shapes and sizes.

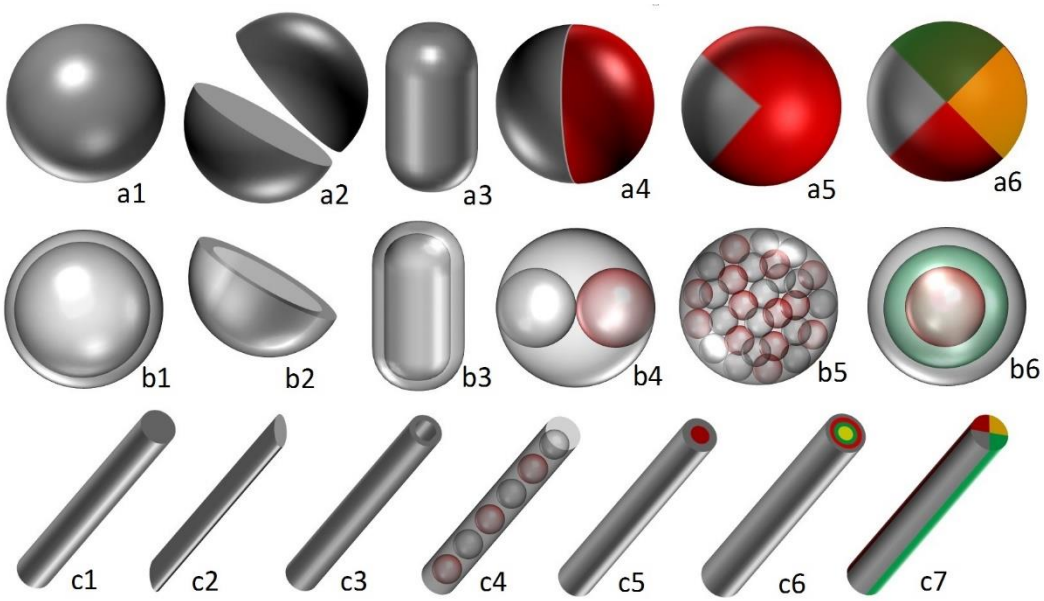

Figure 2.2 Schematics of different formats of (a) solid particles, (b) hollow particles and (c) fibres

Capsules, which have a single core, are generally useful for encapsulating different types of aqueous and non-aqueous liquids and even gaseous phases for their safe storage, as well as their efficient transport and delivery to a desired location. The release from capsules usually occurs via diffusion through the porous shell, where the rate of release could be tuned by altering the shell thickness and porosity [29]. Alternatively, recent investigations into the core-release from capsules with ultrathin shells show the release could happen in a burst mode if the thin shell is ruptured [30]. However, a more controlled and gradual release may also be achieved by creating a small hole in the shell via local

plasticization, through which the core-content can be released over an extended period of time [30]. Microfluidic techniques have also been employed for the formation of structured microfibres, which are typically used for fabricating complex 3D fibrous structures like scaffolds used in tissue engineering applications [31]. A more complex fibre structure, such as ribbon-like fibres [32], could be useful for improving the fibres' performance due to the increase in fibre's surface area, such as enhancement of cell adhesion, cell spreading and cell proliferation [32]. Microfibres with hollow tubular interiors have also been fabricated [33]. These hollow fibres act as basic models to study liquid transportation in micro-tubular structures [33], which can mimic a variety of naturally-occurring tubular structures, such as blood vessels in human body and xylem and phloem tubes in plant's leaves. In terms of fibre composition, several hybrid fibre geometries have been reported, such as multi-layered and multi-compartmental fibres [34,35]. Furthermore, different encapsulate geometries have also been achieved, including uni-core or tubular encapsulation, and multi-core or discrete encapsulation [33,36], which enhances their multi-functional properties.

2.2.2.2. Classification of microfluidic devices

The variety of available microfluidic devices can be broadly classified into two types: *two-dimensional* and *three-dimensional*. The two-dimensional devices are also known as *planar* microfluidic devices [4], which have channels etched on a substrate through which the fluids flow (Figure 2.3a). The continuous phase usually flows only around the sides of the drop and not around its top or bottom; hence it is also known as two-dimensional device. In such devices, the surface properties of the microchannels strongly affect the drop formation mechanism, and even decide the type of emulsion (W/O or O/W) that will be formed [37]. The advantage of planar microfluidic devices is that it allows exceptional flexibility in design and is highly reproducible, since it is fabricated using the standard

soft-lithography technique [38]. Here, the drop formation is dominated by a high shear force exerted on the dispersed phase by the continuous phase. The droplet shape can also be manipulated by altering the geometry of the microfluidic channels (Figure 2.3b-c).

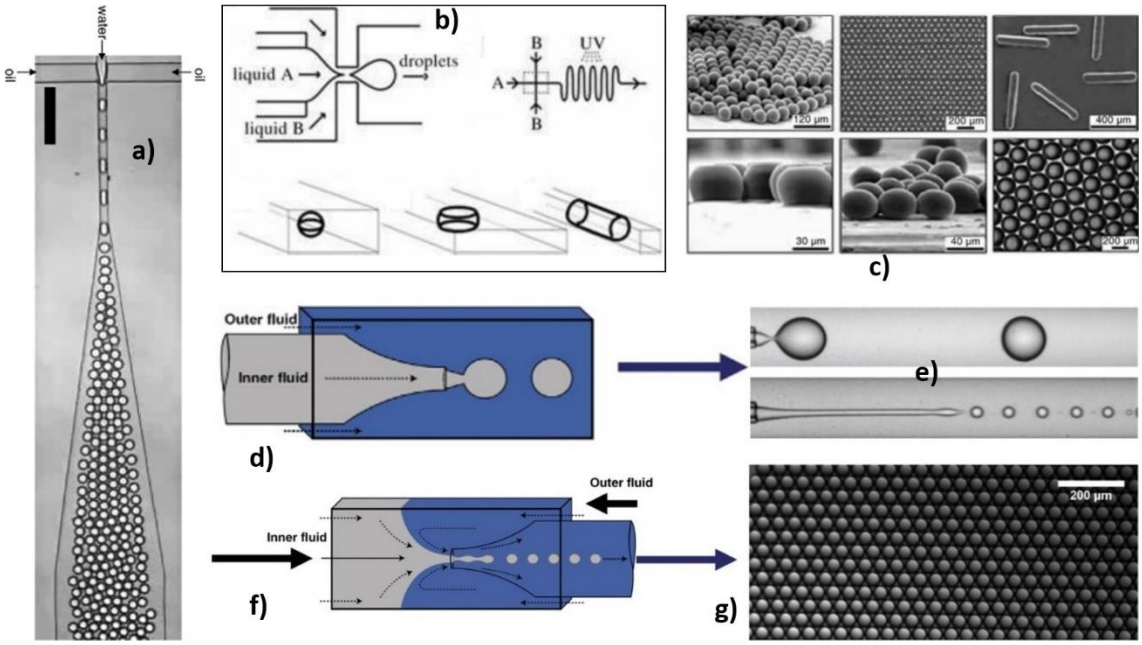

Figure 2.3 a) Micrograph showing uniform microdroplets formed in a planar PDMS microfluidic device. b) A schematic of a planar microfluidic device to create uniform liquid-liquid dispersion, where droplet shapes can be altered with the device geometry. c) SEM images of the resulting shaped microparticles produced via the UV polymerisation of the microdroplets. d) A schematic of a glass-capillary based microfluidic device in a co-flow arrangement. e) The micrographs show droplet formation via two different mechanisms, dripping and jetting of the dispersed phase, in a co-flow approach. f) A schematic of glass-capillary based flow-focus droplet formation. g) A microscopic image of the highly monodispersed droplets, which are produced via the flow-focused approach. Figures (b-c) are taken from [4]. Figures (a) and (d-g) are taken from [39].

On the other hand, a three-dimensional (3D) microfluidic device may use a variety of three-dimensional microstructures for fluid flow, such as a metallic microneedle or microtube and a glass microcapillary in different configurations. Typical 3D microfluidic devices use glass capillaries due to its inert properties, economic viability and availability.

Droplet formation in glass-capillary device holds several advantages against other contemporary approaches, mainly because the device is made of glass, which is known to be highly inert. Another advantage is that the glass surface properties do not generally play a significant role in the drop formation mechanism, as the dispersed phase does not come in contact with the collecting glass capillary surfaces during drop formation. In a typical glass-capillary based microfluidic device, a circular glass-micro-capillary tube (also called inner capillary) carries the dispersed phase, which is inserted into a square glass tube through which the continuous phase flows (Figure 2.3d). The drop is formed at the tip of the inner capillary (Figure 2.3e), where the dispersed phase leaves the inner capillary and is dispersed into the continuous phase as highly uniform droplets (Figure 2.3g). Here, the continuous phase flows around the sides as well as the top and bottom of the growing droplets.

Depending on the direction in which the continuous phase flows around the droplet, a microfluidic device can be called as *co-flowing* or *flow-focusing* type. The dispersed and continuous phases flow in the same direction in the co-flow configuration (Figure 2.3d), whereas in the flow-focus design, the continuous phase reverses its direction of flow at the capillary tip (Figure 2.3f). In both configurations, the drop detaches from the tip when drag force on the drop due to outer phase flow overcomes the interfacial tension force.

The applications of microfluidic devices were initially seen in the field of biotechnology [40], in which the turbulent and inertial effects were non-existent, and mixing was primarily driven by diffusion. These features opened the possibility for using this device for biological processing, such as DNA analysis on a small scale [41]. However, it was still not being seen as a highly efficient emulsification tool. This changed in 1998 when Duffy et al. [38,42] introduced for the first time, the fabrication of microfluidic systems

in an elastomeric material: *poly(dimethylsiloxane) (PDMS)*. The advantages of a 2D PDMS microfluidic device allowed its use for several wide-ranging applications, including emulsification. Several theoretical and experimental studies on the droplet formation in microfluidic devices soon followed, which helped the scientists to better understand the features and capabilities of the device. A condensed summary of some of the important experimental, analytical and numerical investigations into various physical analysis of droplet formation mechanisms using the microfluidic technology are presented below.

2.2.2.3.Modes and analyses of droplet formation

Similar to the two modes of drop formation in the buoyancy-driven mechanism, the dripping and jetting modes also exist in microfluidic devices (Figure 2.3e), as reported by Utada et al. [43,44]. The dripping mode in microfluidic emulsification has the same characteristics as that in buoyancy-assisted mechanisms. However, unlike buoyancy-driven systems which only allows one jetting mode to form, the jetting in microfluidic devices can be of two types, *widening* and *narrowing* jets. A widening jet is formed at a high dispersed phase velocity, which prevents the pinching-off of the dispersed phase close to the tip due to the high kinetic force [44]. This moves the pinch-off location further away from the tip where the dispersed phase velocity reduces. The diameter of a widening jet increases as it moves away from the tip, which is similar to the jetting observed in buoyancy-assisted systems. In case of a narrowing jet, the dispersed phase undergoes jetting due to a high continuous phase velocity (Figure 2.3e bottom). A high continuous phase velocity increases the shear stress, which suppresses the interfacial instabilities close to the tip. Thus the influx of dispersed phase gets carried forward and form a jet, whose diameter usually decreases away from the tip. Thus, the nature of the two jets and droplet size they form are very different, as the narrowing jet leads to the formation of

smaller droplets than the widening jet. However, both types of jetting are usually associated with an increase in polydispersity.

Thorsen et al. [45] and Ganan-Calvo et al. [46] reported some of the first experimental studies on the formation of microdroplets and microbubbles in a PDMS microfluidic device, which is dominated by the drag force. A high shear force in microfluidic devices allowed the formation of extremely small droplets around 10μm [45,46], a scale at which the gravitational force becomes virtually non-existent. In 2009, Marin et al. [47] showed how micron sized drops and bubbles could be formed by increasing the viscosity of continuous phase which increases the drag force.

The significance of shear force in droplet formation in microfluidic devices can be analysed by performing dimensionless analysis. In one such investigation, Serra et al. [48] found that the normalised drop diameter (normalised against the capillary tip diameter) is a function of the ratio of Capillary Numbers of continuous and dispersed phases. In a similar dimensionless analysis performed by Utada et al. [44], the transition from dripping to jetting was observed when the sum of outer Capillary Number (Ca_o) and inner Weber Number (We_i) was of the order of 1. Ca_o represents the shear force due to a high continuous phase velocity, while We_i signifies the inertial force exerted by the dispersed phase.

Several alternative drag-dominated microfluidic emulsification techniques have also been invented to improve the throughput and scalability. In one such example, an approach for producing monodisperse single drops at high frequency was introduced by Umbanhowar et al. [49], where the dispersed phase was introduced into a rotating body of continuous phase containing a surfactant via a tapered capillary. This device was able to produce droplets in dripping mode with drop size ranging between 2-200μm, and was argued to

be scalable for industrial production by introducing multiple capillaries together in a rotating chamber. The rotating continuous phase created a stream-wise force on the dispersed phase emerging out of the capillary tip. The drop size was found to be a function of the capillary tip size, the velocity and viscosity of continuous and dispersed phases and interfacial tension.

A physical model for size prediction of droplets in microfluidic flow-focus geometry in dripping mode was proposed by Erb et al. [50]. The analytical expressions for drop sizes were based on the Capillary Number (*Ca*). It was assumed that the droplet rupture occurred when *Ca* reached a critical value 'on the order of 1'. A universal *Ca* value was was found to satisfy the condition for droplet rupture for a wide range of viscosity ratio (0.0005-5). This analysis was simplified by assuming the dispersed phase flow rate to be negligible.

In contrast to drag-dominated drop formation, studies related to buoyancy-driven droplet formation in microfluidic systems have been scarce. In one such investigation, Wang et al. [51] studied the formation of organic drops from a microcapillary in a static water phase at low flow rates, in which the drop detaches when the buoyancy force overcomes the adhesion of drop to the tip due to interfacial tension. They also presented a force balance model for calculating the forces acting on the drops. The dynamics of drop evolution was explained in four different stages, which were based on the variations in the contact angle.

2.2.2.4.Numerical analysis and modelling of droplet formation

Several numerical investigations have also been undertaken to highlight and understand the dynamics of different aspects of droplet formation such as pinch-off mechanism and dripping-jetting transition during droplet formation in different microfluidic devices.

Zhou et al. [52] reported a numerical simulation model to study the droplet formation in a 2D flow-focusing microfluidic device, using a standard computational fluid dynamics technique known as adaptive mesh technique. They reported that the pinch-off mechanism occurs due to a combined effect of propagation of capillary waves and the stretching of neck due to the drag force. They viewed the pinch-off phenomenon as a continuous and fast process, during which the inner fluid supplies a flow into the jet which resists its thinning, while the outer flow exerts drag which stretches the neck to minimize its thickness. This combined action of simultaneous forces decreased the neck radius to smaller minima in successive cycles of wave oscillations. Each time the neck reached a local minima, the liquid in the jet is prevented from entering the drop and is later pushed into the drop only when the neck expands. This causes a vortex rings to be formed near the neck, due to a high capillary pressure driving the fluid into reverse motion. The dripping and jetting modes are described as a race between two time scales, *capillary time* t_c, for growth of interfacial disturbance, and the *flow time* t_f, for the convection of the fluid. If $t_c < t_f$, the pinch off occurs near the orifice, resulting in dripping. In other case, the disturbance is carried downstream before getting amplified, thus leading to jetting.

Another numerical investigation, by Hong and Wang [53] on the single drop formation in a co-flow microfluidic device, explored the effect of flow rates on the drop sizes produced using microcapillary devices in a co-flow environment. They found that, across a wide range of flow conditions, the drop size can become nearly independent of the ratio of dispersed-to-continuous phase flow rate (Q_d/Q_c), or be strongly dependent on the flow rate ratio. The drop size was found to be a function of the flow rate ratio for $Q_d/Q_c < 0.1$, where the drop size reduced with Q_d/Q_c due to high viscous drag. For $Q_d/Q_c > 0.1$, the droplet size was found to be weakly dependent on the flow rate ratio, where the reduction in shear force was compensated by the increase in the inertial force, which left the droplet

size unaffected. They also observed that, if the outer fluid velocity at the tip was larger than that of the dispersed fluid, flow-focusing phenomena would happen even without using a narrower orifice. Based on this, they concluded that the co-flow setup is similar to flow-focused setup and generate theoretically identical drops if the outer velocities in both cases are kept the same.

2.2.2.5.Dynamic interfacial tension in microfluidic devices

The effects of surfactants within microfluidic devices have also been studied due to high frequency drop formations and interface generation in microfluidics. For example, Xu et al. [54] presented the dynamic effects of surfactants on droplet formation in coaxial microfluidic devices. They divide the adsorption of surfactant on the fresh interface into multiple steps depending on whether the concentration is above CMC or not. The first step is the transportation of free surfactant molecules and micelles if above CMC from the bulk to the 'subsurface' which refers to the boundary layer close to the interface where only adsorption occurs. The second step involves breaking up of micelles at the boundary layer leading to reduced free surfactant molecules thus causing micelles-molecules imbalance. In the third step, the free surfactant molecules adsorb from 'subsurface' to the interface, while the adsorbed molecules rearrange into an equilibrium state as the last step. This indicated that dynamic interfacial tension becomes more important within microfluidic devices as the drop formation time reduces significantly.

2.2.3. Microfluidic formation of double-emulsions and higher-order emulsions

The droplet formation approach in 2D and 3D microfluidic devices can also be extended to produce uniform double emulsions. In case of a 2D planar device, the uniform single emulsion obtained earlier can be manipulated to be dispersed in a third immiscible phase to form uniform double emulsion with controllable internal droplets (Figure 2.4a-b) [55].

Double-emulsion formation in a glass-capillary based microfluidic device requires an extra circular microcapillary to be added from the other side of the square capillary, which introduces the inner phase in the middle phase before its dispersion in the continuous phase (Figure 2.4c) [25]. In both the devices, the number of core droplets is controlled by adjusting the phase flow rates.

In 2005, Utada et al. [25] introduced a novel microfluidic technique to produce highly monodispersed double emulsions using glass micro-capillaries. The study stated that the effective interfacial tension for a coaxial fluid thread is modified by the presence of two interfaces. It was also suggested that the Rayleigh-Plateau Instability (the wave-like instability at the interface) cannot occur until the length of jet has grown comparable to its radius. Two different regimes of drop formation were also introduced for the formation of compound dripping and jetting. To differentiate between the dripping and jetting regime with respect to the middle phase flow, the *pinch-off time* (t_p) of droplet and *growth time* of the jet (t_g) were compared. It was found that for $t_p < t_g$, droplets form quickly as jet remains small to sustain instability, but the jet quickly becomes unstable and as a result forms droplets close to the tip, thus leading to dripping regime. In case of $t_p > t_g$, the jet grows faster than the droplet can form, thus leading to the jetting regime, where the droplets are formed downstream. Based on this discussion, the Capillary number was defined as the ratio of pinch off time and growth time, which was used to state that the transition between dripping and jetting occurred at $Ca \sim 1$, where the system drips when $Ca < 1.0$. A physical model was also presented for prediction of the droplet size formed in this device. The drop size predictions in dripping regime involved a simplifying assumption, that the velocity profiles of all three phases, inner, middle and outer, in the proximity of the tip of collecting tube is linear and flat. The mass conservation of fluids was applied to relate the drop size to the width of its liquid threads.

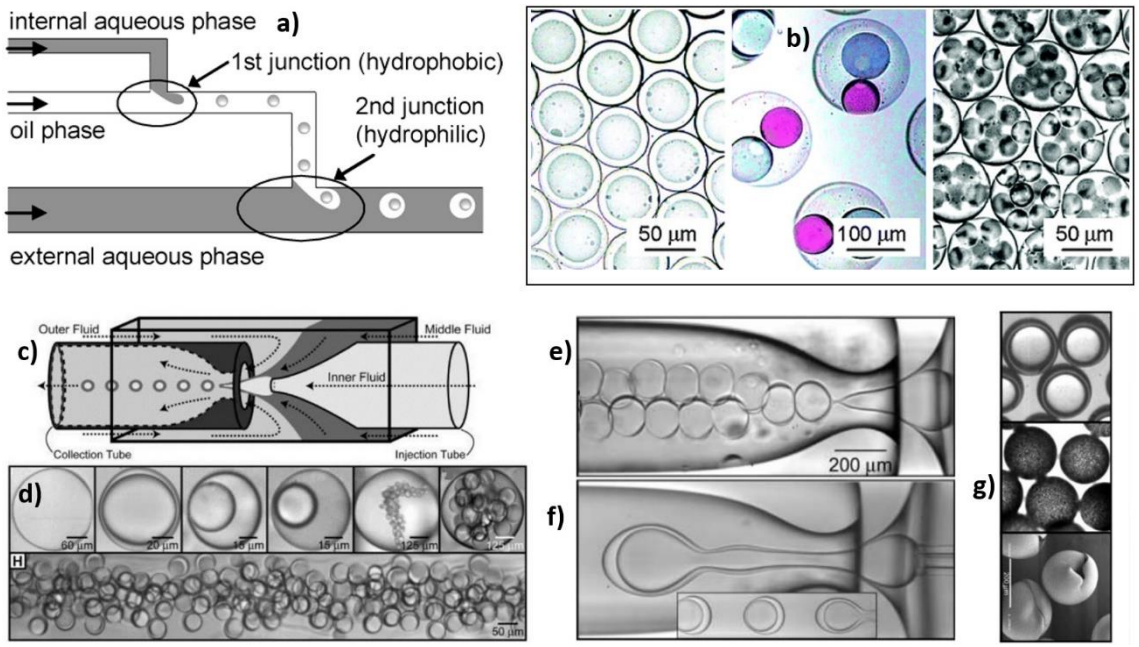

Figure 2.4 a) A schematic of a planar microfluidic device to create uniform double emulsion, where the number of droplets can be controlled with the flow conditions. b) Micrographs of double emulsions with different number of core droplets. c) A schematic of a glass-capillary based microfluidic device for the formation of double emulsion in a flow-focus arrangement. d) Double emulsions with different sizes and numbers of core droplets, formed in a glass-capillary microfluidic device. The micrographs in (e) and (f) show the double emulsion formation via two different mechanisms, dripping and jetting of the dispersed phase, respectively. g) The images show the microcapsules fabricated via shell-polymerisation of the core-shell droplets. Figures (a-b) are taken from [55]. Figures (c-g) are taken from [25].

Other studies also reported drop-size prediction models for double emulsion droplets. The empirical law for the single drop size prediction in a co-flow microfluidic device [56] was extended to predict the double emulsion drop sizes. The model proposed by Erb et al. [50], for predicting simple droplet sizes in a glass capillary based flow-focused device, was also extended to predict the size of dripping double emulsion droplets, in particular core-shell droplets. Additionally, a condition was also proposed for different possible cases of droplet formation; it stated that if the middle fluid breaks off due to shear induced by the outer fluid flow, the inner drop is forced to break off before its critical *Ca* is reached. In this case, the diameter of overall droplet would be determined through

satisfying the critical Capillary number equation for the droplet of middle fluid, while the diameter of the core would be calculated by the mass balance as the time of formation will be the same for inner drop and the overall drop. Alternatively, if inner phase ruptures first, then multiple inner drippings might occur in every overall drop. In the model presented, however, only the former case was considered.

Zhou et al. [52] also investigated the formation of double emulsions experimentally and proposed that the number of internal drops was dependent on the flow rates and viscosity ratios of outer and middle phases. It was asserted that to gain control over compound drop formation, say for core-shell double emulsion (drop with a single core), the inner and outer capillary waves at the interfaces must be selectively controlled within a certain narrow range of input parameters which would lead to capillary wave matching and preventing formation of satellite drops or more than one major internal drop. This theoretical understanding could be a strong step towards getting rid of polydispersity, especially in jetting phase, though, the range of values of various parameters available to control capillary wave matching would get narrower with increasing outer velocity.

Chen et al. [57] reported a numerical study on droplet formation in co-flowing liquid streams. They numerically reproduced the dripping and jetting (narrowing and widening) regimes and the numerical results indicated that operating in dripping regime, rather than the jetting regime, is a better way of producing monodisperse emulsions. More importantly, they found that in dripping and widening jet regime (both of these have low continuous phase flow rate in common) the drop breakup is induced by higher pressure in the neck of the liquid that connects the drop to the tip. This high pressure in the neck squeezes liquid into low pressure region in the primary and secondary drops. However, in the narrowing jet regime where the continuous phase flow rate is very high, the jet

breaks up into droplets due to slow velocity at the lagging end of the necking region as compared to its leading end.

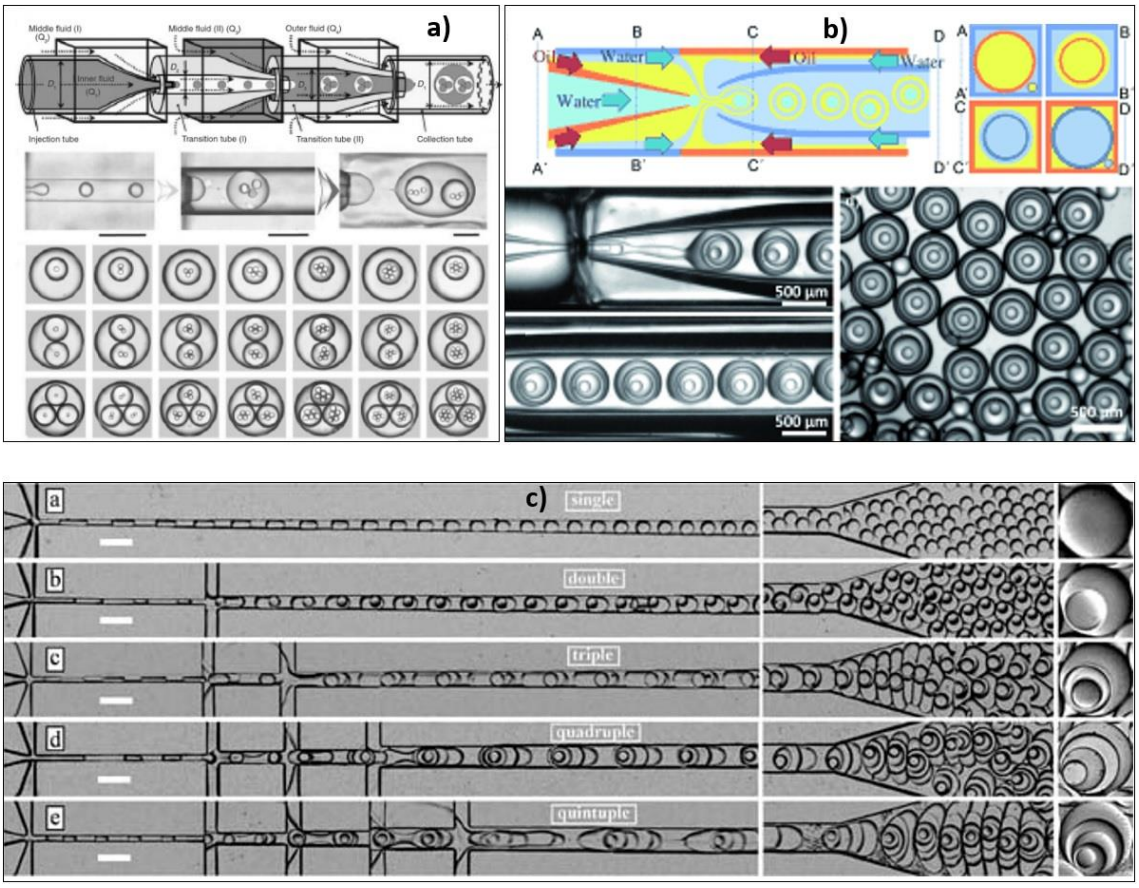

Figure 2.5 a) The schematic and microscopic images show the formation of uni-core and multi-core triple emulsions with controllable internal droplets in a multi-stage glass-capillary based microfluidic device. b) One-step formation of highly uniform quintuple emulsions by utilizing the suitable modified surface affinity of the glass-capillary device. c) Multi-stage formation of emulsions with increasing order of complexity in a PDMS device. Figures (a), (b) and (c) are taken from [39], [58] and [59] respectively.

More advanced double emulsions were also produced using variable surface modifications of the device. For example, Kim et al. [60] altered the surface properties of the channels and created a bi-phasic flow within the glass microcapillary channels to produce core-shell drops having very thin shells. It was argued that such structures have very high stability as the structure enters a ‘lubrication regime’ when it has a very thin

shell layer. Later, Abbaspourrad et al. [30] demonstrated that such ultrathin shelled capsules can be programmed to actively release the content within the core.

Microfluidics also allows the formation of higher order emulsions with an unprecedented level of droplet complexity, whilst maintaining a high degree of uniformity at all levels. Shah et al. [39] demonstrated the formation of highly monodispersed triple emulsions with multi-cores (Figure 2.5a). The production of triple emulsion was facilitated by appending a third droplet formation stage at the end of a two-stage glass-capillary set up. The droplet frequencies were carefully matched to obtain the desired number of core droplets at each level, which was achieved by altering the individual flow conditions. Even more complex emulsions have also been reported. Figure 2.5c shows the formation of up to quintuple emulsion (five-layered droplets) in a PDMS device with the help of a sequential multi-stage technique [59], which is similar to the methodology used for triple emulsion formation in a glass-capillary based device (Figure 2.5a) [39]. However the quintuple emulsion was formed in a glass-capillary based device in just a single step [58], as shown in Figure 2.5b. This was achieved by forming a stabilised multi-layered compound jet inside the outer glass capillary, which emulsified together at the tip of the inner glass capillary. The surface affinity of the glass capillaries was desirably modified to form a stable compound jet.

2.2.4. Microfluidic fabrication of simple and compound microfibres

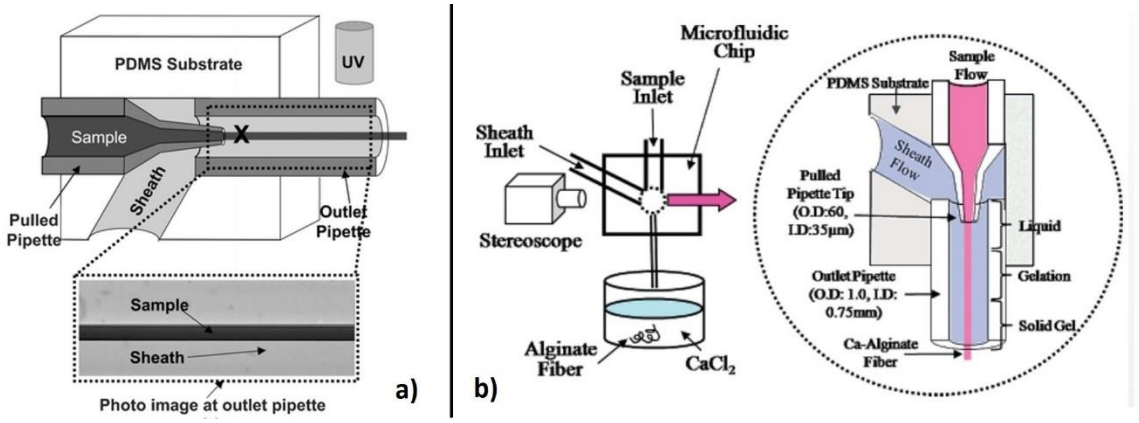

Figure 2.6 Schematics of fibre formation techniques in a microfluidic device for obtaining (a) synthetic microfibres via UV polymerisation of a monomer jet, and (b) a hydrogel microfibre via chemical reaction between the aqueous sodium alginate jet and the calcium chloride solution. Figure (a) and (b) are taken from [26] and [61], respectively.

Similar to the uniform droplet formation, the microfluidic devices have also been employed to fabricate highly uniform microfibres. Microfibres can be made out of different kinds of materials by different processes, depending on the application. Jeong et al. [26] fabricated synthetic microfibres made of polyacrylate via in-situ photo-polymerisation of the pre-polymer phase, inside a PDMS microfluidic device embedded with glass-capillary (Figure 2.6a). These microfibres were used to immobilise biocatalysts into themselves to create biosensors in fibrous geometry. Shin et al. [61] employed the same device for a continuous generation of biocompatible calcium-alginate microfibres, which were used as a reliable cell carriers for tissue-engineering applications. The microfibres were formed via coaxial flow of the sample and sheath aqueous solutions containing sodium alginate and calcium chloride ($CaCl_2$), respectively (Figure 2.6b). The sodium alginate jet was solidified by its chemical reaction with the diffusing Ca^{2+} ions from the continuous calcium chloride solution, to produce calcium alginate microfibre.

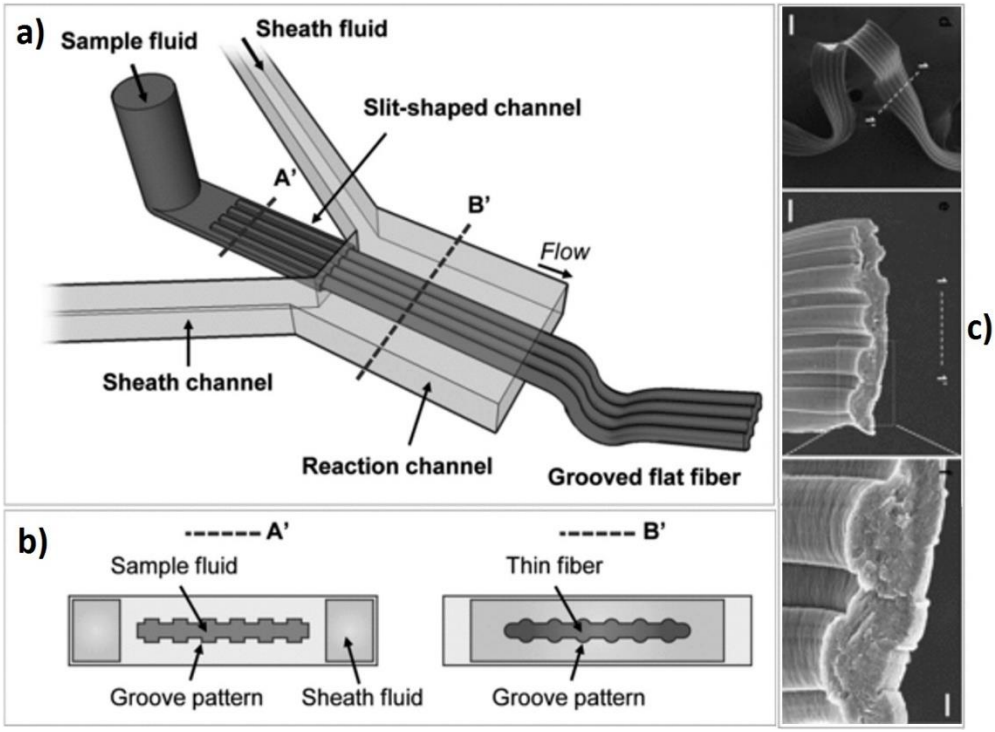

Figure 2.7 a) Schematic of the microfluidic device, with a grooved orifice geometry shown in (b), for fabrication of flat and grooved alginate microfibres. c) The SEM images show the well-defined flat-grooved alginate microfibres. All figures are taken from [32].

The flexible microfluidic technology also allows for controlled tuning of the shape and surface morphology of the resulting microfibres, which could improve their performance in certain applications. This was demonstrated by Kang et al. [32] who fabricated flat-grooved alginate microfibres, which were found to enhance the adhesion, spreading and proliferation of cells on the fibre's surface. To fabricate such fibres, a tailored microfluidic device was used which had a flat and grooved orifice geometry (Figure 2.7a), where the aspect ratio of fibres and the definition of the grooves were strongly governed by the sample and sheath flow conditions, and the alginate and calcium chloride concentrations. They observed that slower sample (alginate) flow rates or faster sheath (calcium chloride) flow rates produced thinner flat-fibres, however, increasing the sheath flow rate was found to be more effective in reducing the fibre thickness. The grooves on the flat fibres were well-defined at high alginate and $CaCl_2$ concentrations.

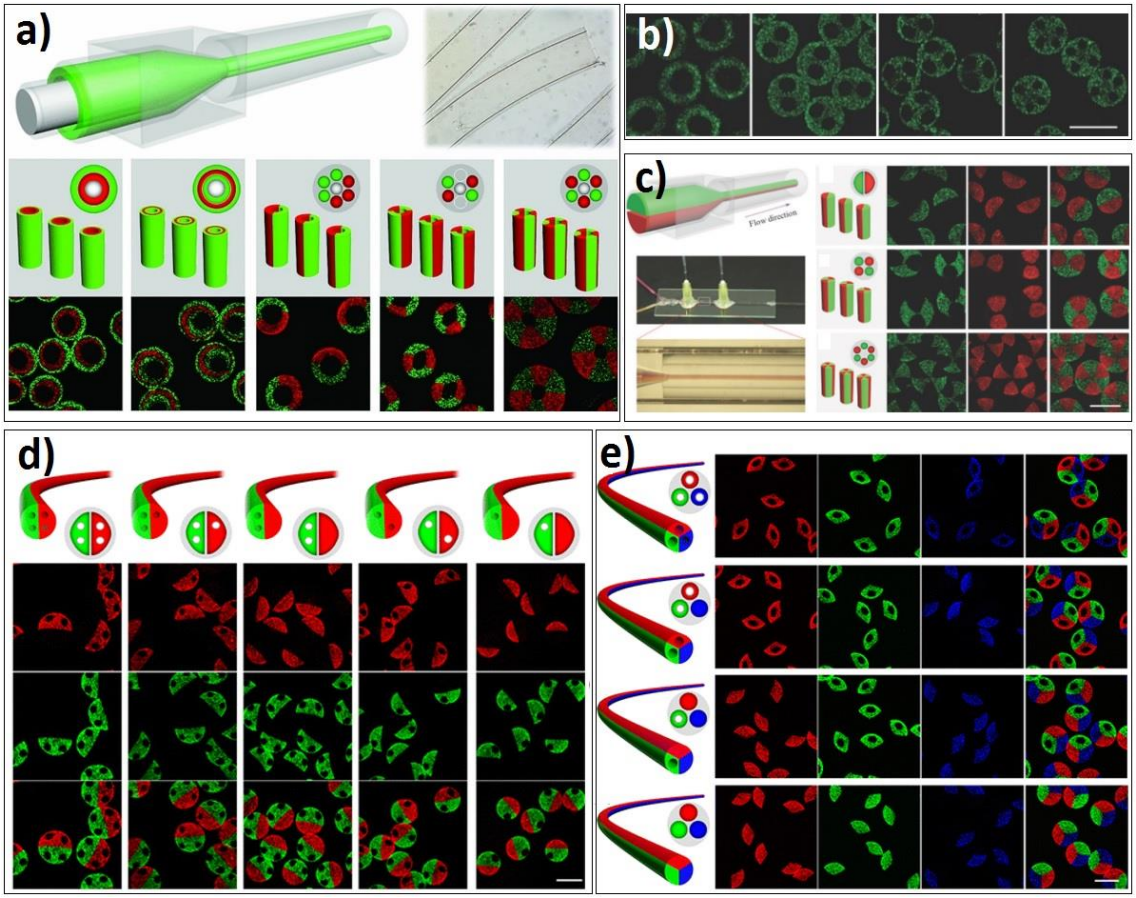

Figure 2.8 a) Schematic for fabrication and CLSM (confocal laser scanning microscopy) images of tubular alginate microfibres with complex radial shell composition. b) CLSM Images of multi-tubular alginate microfibres produced using multi-barrel glass capillaries. c) Schematics and CLSM images of solid microfibres with configurable multi-sectional radial composition. d) Schematics and CLSM images of two-compartment Janus-hollow microfibres and e) three-compartment hollow alginate microfibres. Figures (a-c) and (d-e) are taken from [34] and [35] respectively.

In recent few years, yet wider variety of fibres have been formed via microfluidic techniques, which demonstrate a flexible tuning of fibre geometry and composition with a high degree of precision and accuracy. For example, multi-layered fibres (Figure 2.8a) can be formed using a multi-barrel glass capillary for parallel flows. Furthermore, the solid and hollow cylindrical fibres can also be made with multi-segmented radial compositions (Figure 2.8b-e). Apart from tuning of the fibre's geometry and composition, different types of liquids can also be encapsulated within the fibres. The encapsulation of

aqueous and non-aqueous phases in microfibres, particularly in alginate fibres, have been achieved for a variety of applications. The encapsulation of aqueous phase, which leads to its tubular encapsulation due to low interfacial tension, has been commonly used to encapsulate various biological suspensions, like cells and proteins, for tissue engineering applications such as making templates for reconstruction of fibre-shaped functional tissues [62].

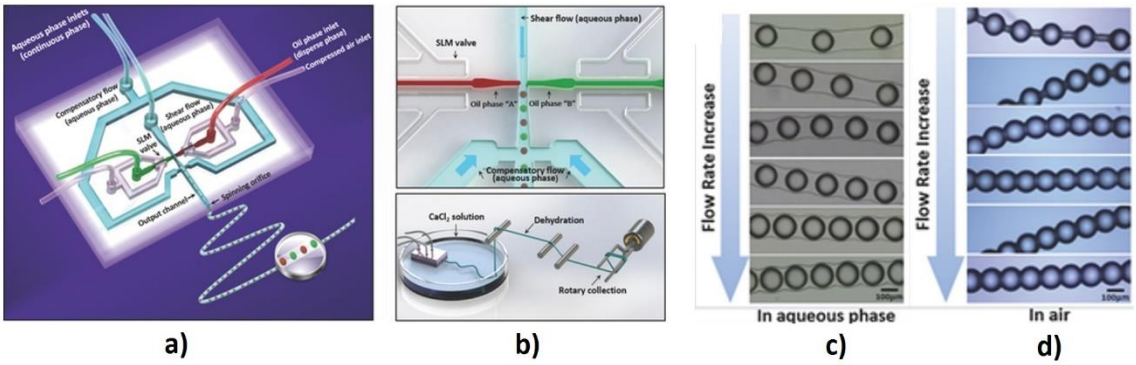

Figure 2.9 (a) Schematic of the device designed for encapsulation of a stream oil droplets in alginate hydrogel microfibres, which can also be extended to encapsulating multiple oil streams (b). (c) and (d) show the oil-loaded microfibres in hydrated and dehydrated states respectively. All figures are taken from [36].

Recently, encapsulation of non-aqueous phases in alginate fibres has also been pursued, to increase their multi-functional properties. For example, Yu et al. [36] investigated the encapsulation of oil droplets in alginate microfibres (Figure 2.9), to produce fibres loaded with polymeric microspheres as well as multicellular spheroids. The oil-loaded microfibres have also been employed to generate fibres with regularly spaced spindle-knots [63]. These fibres were magnetically manipulated to create a web-like fibre assembly, which demonstrated enhanced water collection properties due the adhesion of large volumes of water around the spindle knots. A more complex encapsulation approach was also undertaken to produce fibres with regularly spaced double-emulsion alginate-in-oil droplets, to make fibres with a greater level of hierarchical structuring [64]. They

propose that such fibres could be useful for multi-level storage and delivery purposes, where the each level could be selectively dissolved for stage-wise release of encapsulates.

2.3. CONCLUSIONS FROM LITERATURE REVIEW

The literature review presented above reveals that not only the literature available on buoyancy-driven drop formation is scarce, but also aspects such as the combined effects of buoyancy and kinetic forces at low flow rates on drop formation, the dynamic interfacial tension effect at low velocities, and the relationship between polydispersity and drop size in buoyancy-driven jetting regime need further studies. More importantly, while the microfluidics has revolutionised the drop formation process due to the high degree of uniformity and precision it offers, its use under the conditions that buoyancy effects become significant has so far been neglected and largely unexplored as yet, particular for compound multi-phase flow studies.

Furthermore, the conventional microfluidic encapsulation technique, where the core droplets are usually formed first and then encapsulated downstream, may limit the flexibility in droplet-in-droplet and droplet-in-fibre encapsulation. In case of droplet-in-droplet encapsulation, this *two-step* sequential approach usually breaks the inner phase into multiple droplets to form multi-core droplets. The flow conditions have to be appropriately tuned to form uni-core droplets, which are superior to multi-core droplets for applications such as controlled core-release, and to achieve high encapsulation volume. Similarly, in case of encapsulation in fibres, the *two-step* approach prevents the asymmetric encapsulation of droplets with respect to the fibre's central axis, which could show versatile responses to various external stimuli that fibres usually encounter, such as dehydration and mechanical fracture. Therefore, an encapsulation mechanism is sought to avoid the formation of multi-core double emulsion, and allow a flexible tuning of encapsulates' location within the fibres. A *one-step* encapsulation technique can address these issues, where the core is encapsulated during its formation.

In this thesis, the buoyancy-driven drop formation system is revisited to refine the underlying fundamental theory of drop formation and its associated aspects. A hybrid drop formation strategy is devised to unite the convenience of the buoyancy effect for drop formation and transportation, and the robustness of the microfluidic technique for high-precision fluid manipulation, to produce compound drops on a millimetre scale with tuneable shell thickness using the *one-step* encapsulation technique, with the aim of fabricating highly monodispersed millimetric ultrathin shelled capsules. The proposed encapsulation strategy is also extended to investigate droplet/bubble-in-fibre encapsulation, to explore the advantages of fibre formation under the buoyancy effect, and to study the impact of tuning the encapsulate size shape and location.

Chapter 3 Experimental Methods

This chapter describes the different materials used, along with the details of surface modification procedure followed. The assembly and fabrication of device, its operation and some common operational challenges are also discussed. At the end, the techniques used to measure different properties of fluids are also mentioned.

3.1. MATERIALS

For single drop study, n-Octane (C_8H_{18}), n-Dodecane ($C_{12}H_{26}$) and n-Hexadecane ($C_{16}H_{34}$) were used as the dispersed phase, which was dispersed in the quiescent continuous water phase containing varying degrees of SDS (sodium dodecyl sulphate) concentration. To produce core-shell drops, two different surfactants were employed, one ionic (SDS) and the other non-ionic (Span-85: Sorbitan trioleate) surfactant. 0.1wt% SDS was dissolved in the outer water phase to stabilize the overall drops, while 0.1wt% Span85 was dissolved in the middle oil phase to stabilize the inner water drops. For achieving core-shell drops with ultra-thin shells, the surfactant concentrations of both SDS and Span85 was increased above 0.1wt%. The CMC value for SDS and Span85 was found to be 0.25wt% and 0.8wt% respectively.

For fabricating alginate microfibres, an aqueous solution of sodium alginate (~0.5-8wt%) was used as the middle phase, while n-Octane was used as the model oil encapsulates. For bubble encapsulation in alginate fibres, the compressed and filtered air was introduced as the inner phase at a wide range of air pressures (0.1- 2.0 psi). The outer aqueous phase contained a varying range of dissolved calcium chloride (~0.1-10wt%).

3.2. SURFACE MODIFICATION

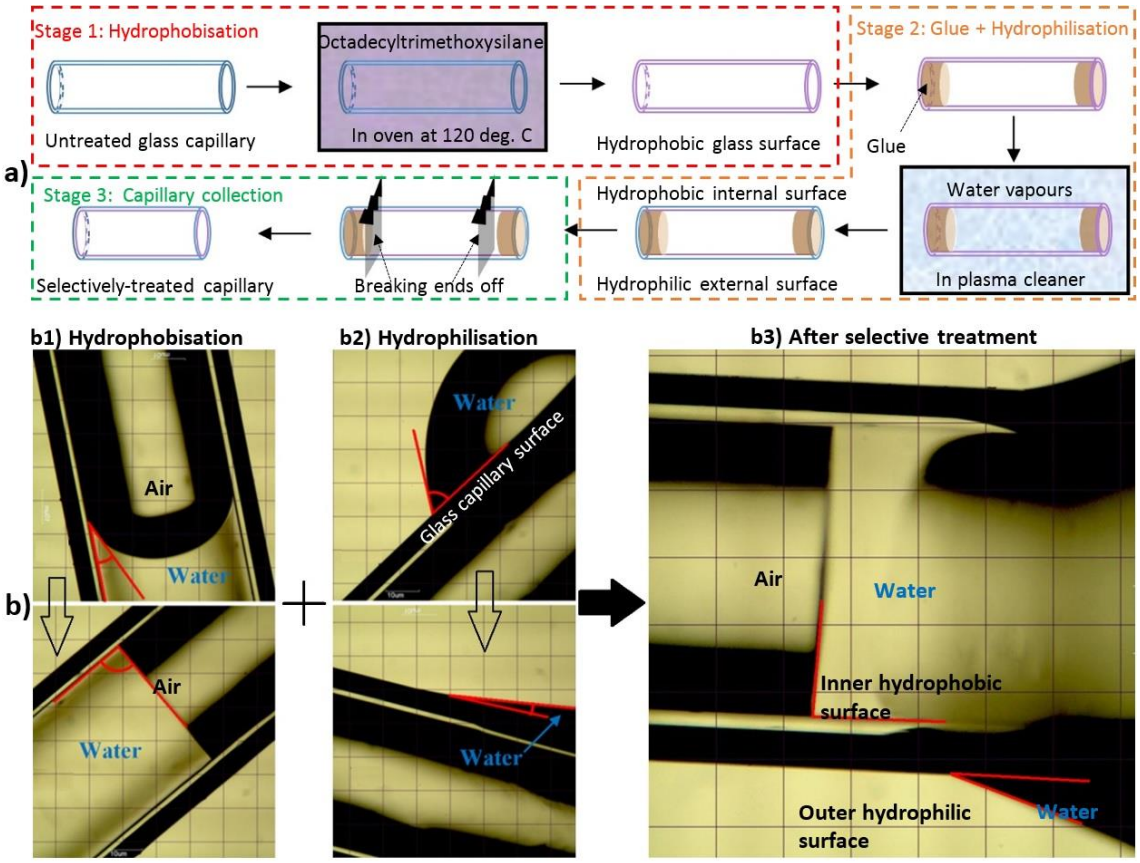

Figure 3.1 a) The schematic shows three-stage procedure for selective treatment of glass capillary surface. b) The microscopic images show capillaries after hydrophobisation (b1) and hydrophilisation (b2) of the inner and outer glass capillary surface respectively. The capillary shown in (b3) has selectively-treated inner and outer surface, which was obtained after following the process shown in (a).

The inner and outer surface properties of the inner and outer capillaries were modified according to the inner, middle and outer phases. For example, for producing water-in-oil-in-water drops, the oil phase was introduced through the outer channel, while water was introduced through inner channel, and also as the outer phase which was contained in a cuvette. Therefore, for such a requirement, the inner channel's surface should be treated to be hydrophobic to avoid it being wetted by inner water phase. This was done by treating the surface with n-Octadecyltrimethoxysilane. To avoid the wetting problem by the

middle oil phase, the outer surface of the outer channel should be hydrophilic, while its inner surface should be hydrophobic to make the middle oil phase completely wet the inner surface and thus axisymmetrically engulf the inner water phase. The initial condition of the inner and outer surface of an untreated borosilicate glass microcapillary is shown in Figure 3.1b1-b2 (top), where the images show the contact angles (in red) that the water makes with the inner and outer surface respectively, where smaller contact angle indicate more hydrophilic surface.

The selective treatment was done in three steps. Firstly, both the inner and the outer surface were treated to become hydrophobic (Figure 3.1a, stage 1). This increased the contact angle of the glass surface with water, as shown for the inner glass surface in Figure 3.1b1. In the second stage, both the ends of the capillary were glued to secure the treated inner surface from further changes in its properties, and the outer glass surface was subjected to the plasma cleaning to make it hydrophilic (Figure 3.1a, stage 2). This resulted in a decrease in the contact angle, as shown Figure 3.1b2. In the last stage, the glued ends of the capillary were broken-off to retrieve the open-ended glass capillary with the inner hydrophobic surface and outer hydrophilic surface, which is presented in Figure 3.1b3.

3.3. DEVICE ASSEMBLY AND FABRICATION

For single drop study, a J-shaped needle made of stainless steel was used as the channel for the dispersed phase. This needle was lowered into a plastic cuvette which contained the continuous phase (Figure 3.2a). It was important to ensure that there was no air trapped in the channels which would affect the flow rate of the dispersed phase as air is compressible. Also, different needle tips were observed to have different surface properties. In the case of surfactants at and above CMC, the drop wetted the minimum tip

surface for some needles such that the wetting diameter was closer to the inner tip diameter, while it wetted the whole of tip surface for other needles. The experiment was conducted with only those needles that wetted the tip completely for all surfactant concentration cases, thus fixing the wetting diameter to be equal to the outer tip diameter.

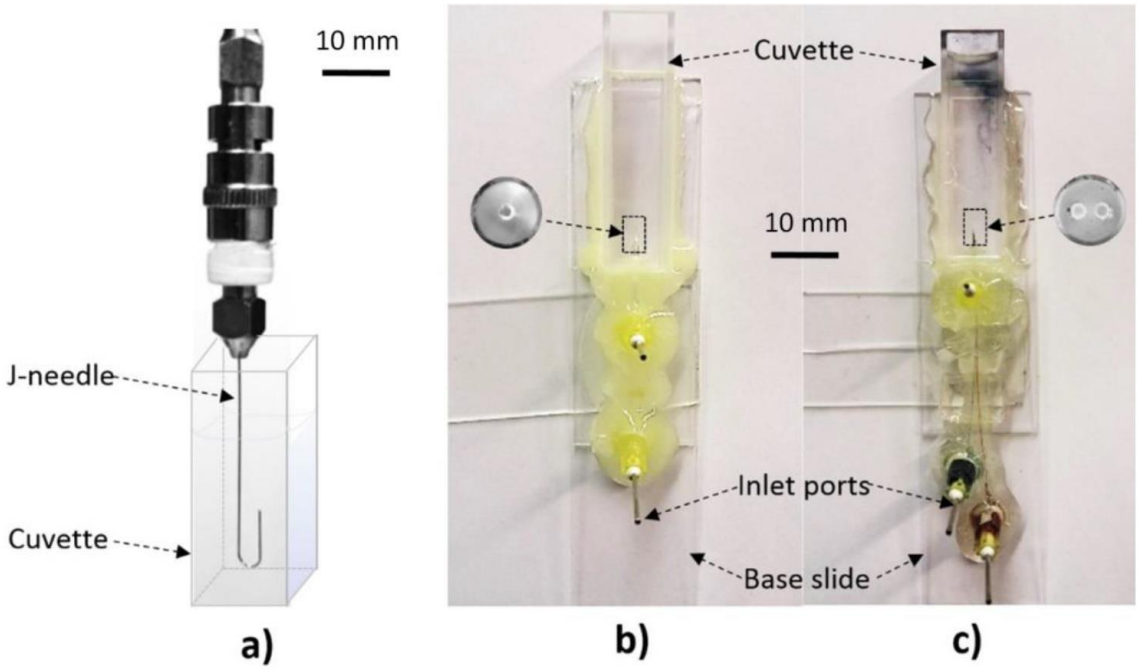

Figure 3.2 a) The device assembly for buoyancy-driven drop formation study is presented, which shows an image of the J-type needle used for introducing organic oil phase into a cuvette containing water phase. b) The image shows a non-confined microfluidic device, which was used to study double-emulsion formation under the buoyancy effect. It was also used to produce alginate fibres with symmetrically encapsulated microdroplets and microbubbles. c) A non-confined device with two inner capillaries is shown, which was used to produce fibres with two types of oil encapsulates.

To produce core-shell drops under buoyancy effect, the device used was vertically oriented. The device consisted of introducing one tapered capillary channel inside another tapered channel with axisymmetric alignment at the same level. The coupled capillary assembly was introduced in a wide cuvette, which housed the outer quiescent phase for buoyancy-assisted drop formation and transportation.

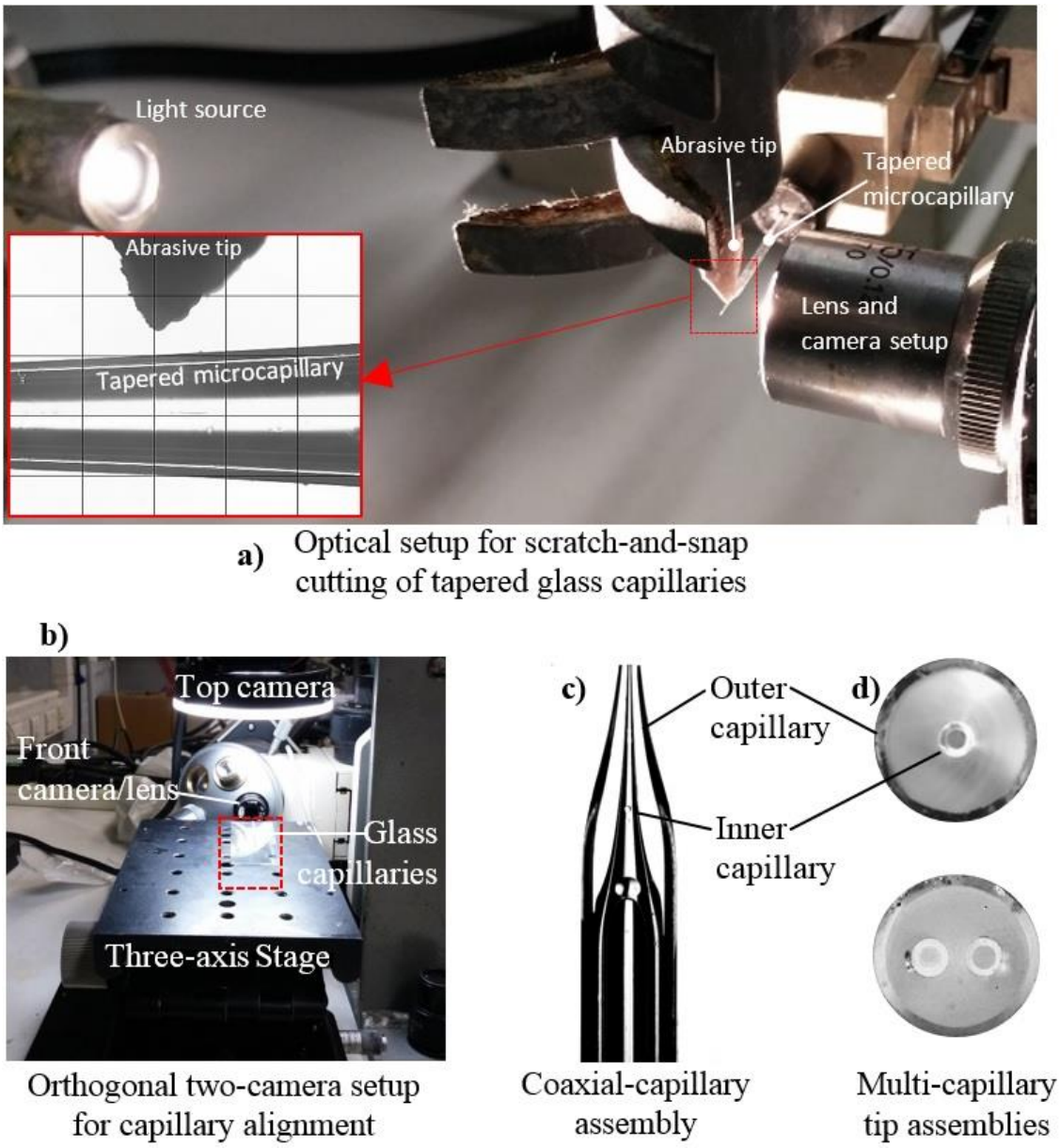

Figure 3.3 a) Optical setup for controlled cutting of tapered glass microcapillaries. b) An orthogonal two-camera setup for precise tip alignment of coaxially assembled capillaries. c) An optical micrograph of a typical coaxially assembled and symmetrically aligned setup. d) A front view of the tip assembly for devices with two and three capillary tips.

In order to obtain a coaxially-aligned glass microcapillary assembly, a number of steps were followed. The first step was to taper a cylindrical glass microcapillary via pulling it using a pipette puller (P-1000, Sutter Instrument, Novato, USA). In order to cut the

tapered end of the capillary for a desired orifice dimensions, a pointed, abrasive tip was used to scratch the glass surface at the required position, as shown in Figure 3.3a. The scratch was wetted by soapy water to weaken the scratched surface. Lastly, the tapered section beyond the scratched point was exposed to a gentle and rapid stroke against the rigid abrasive tip, which snapped the tapered end from the main capillary at the scratched location.

Once the circular and square tapered capillaries were cut to desired orifice dimensions, the circular capillary was inserted in the square capillary for tip alignment. A two-camera optical setup, for a top and front view of the capillary tips, was assembled as shown in Figure 3.3b. Figure 3.3c shows a typical coaxially assembled and symmetrically aligned glass capillaries. The front view of the tip, shown in Figure 3.3d, also reveals that the tip of the square capillary turned circular during its pulling.

3.4. COMMON OPERATIONAL CHALLENGES AND TROUBLESHOOTING

The most common operational challenge in a microfluidic device is the clogging of the capillary due to debris. To avoid this, water and oil filters (2µm sieve) were used. However, despite using filters as a precautionary measure, a poor handling of the fluids and the device may still lead to the clogging to occur. In such cases, some debris could be taken out of the system by flushing the outer fluid into the clogged capillary from its tip, which could carry the debris out of the inlet ports and into the withdrawing syringe. However, for debris which remain awkwardly secured inside the capillary even after flushing the device, the use of surfactant in the outer phase is suggested, which can also be coupled with exposing the device to a high frequency vibrations, which may displace the debris to allow it removal by fluid flow. As a warning, too strong vibrations could break the glass microcapillary tips, which should be taken care of.

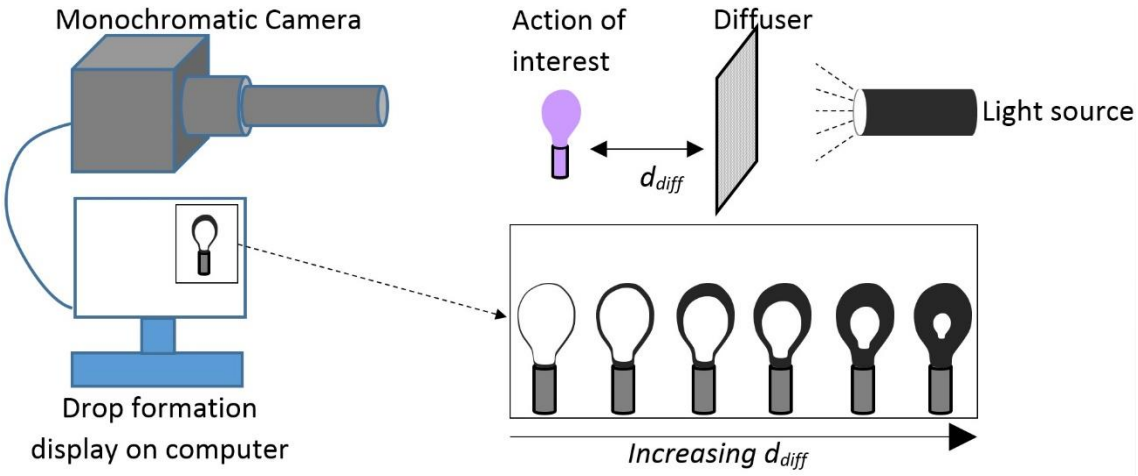

Figure 3.4 Schematic of an optical setup for drop formation imaging. The thickness of drop interface increases with the distance between the diffuser and the object of interest, which is depicted in the schematic of the imaged drops.

Microfluidics-related research also require an appropriate optical set-up involving several units, as shown in Figure 3.4, to obtain clear images of drop formation for its accurate representation. An important aspect of droplet imaging is to identify its interface between the two immiscible phases involved. However, a coarsely assembled optical set-up usually shows a thick interface. A reasonably thin and distinctly clear interface can be achieved by a fine adjustment of the distance between the drop formation (action of interest) and the diffuser, as repreented in Figure 3.4.

3.5. SAMPLE IMAGING AND CHARACTERISATION

Ultrathin shelled capsules and compound alginate microfibres were also imaged by optical microscope (Kyowa Tokyo, Japan, with a Moticam 2300 camera connected to the PC) and Scanning electron microscope (SEM). For SEM, samples were coated with approximately 5nm of gold layer, and placed on a stud before analysis.

3.6. MEASUREMENT OF FLUID PROPERTIES

Different standard techniques were employed to measure different fluid properties such as interfacial tension and viscosity.

3.5.1. Interfacial tension measurement

The Pendant drop and Du-Nouy Ring techniques were used to measure the interfacial tension values. The pendant drop method was also used to measure dynamic interfacial tension.

3.5.2. Viscosity measurement

The viscosity values of different aqueous sodium alginate solutions were measured using a double couette flow setup, which provided a high sensitivity measurement.

Chapter 4 Buoyancy-driven Drop Generation via Microchannel Revisited*

4.1. ABSTRACT

Droplets formed under the buoyancy force in a quiescent continuous phase provides a facile yet interesting system for fundamental studies on drop-rupture mechanism, which was a field of vast research interests prior to the arrival of the microfluidic techniques. The formation of macro-drops via a microchannel in buoyancy driven system is revisited for three low viscosity hydrocarbon oils using a wide range of surfactant concentrations. The dripping-to-jetting transition was found to occur at Bond number of ~ 0.85, reflecting the significance of buoyancy force even in the jetting regime. The pinch-off time and the satellite drops were found to have negligible impact on the final drop volume throughout the dripping regime. A modified force-balance model is presented which includes the dynamic interfacial tension based on surface-average age of the drop. The model clearly predicts a region where the drop size increases initially with dispersed phase flow rate (Q) due to increasing dynamic interfacial tension, followed by a region of constant drop size with Q, where the increase in interfacial force is compensated by an equal increase in the kinetic force. Polydispersity in the drops formed under the jetting regime was found to vary in accordance with the polydispersity in the break-up length of the drops. Interestingly, highly monodisperse drops were not limited to dripping regime and formed under the jetting regime at a higher frequency too but under certain flow rate and interfacial tension conditions.

* Chaurasia, A.S., Josephides, D.N. and Sajjadi, S., **2015**. Buoyancy-driven drop generation via microchannel revisited. *Microfluidics and Nanofluidics,* 18(5-6), pp. 943-953

4.2. INTRODUCTION

Uniform drops are widely desired in industry for specific applications such as standards, templates for creating uniform structured particles, self-assembly, and more importantly for biomedical or pharmaceutical applications such as radiology [65] or drug delivery [66]. Many general applications of drops also demand a high monodispersity with tuneable size, because drop uniformity can significantly affect the properties and responsive behaviour of the end product.

Uniform droplets are usually produced via techniques such as microfluidics [25,39,67] and membrane emulsification [68,69]. However, most recent studies on formation of uniform drops use flow systems such as microfluidic co-flow or flow-focus techniques [43,44,57,70,71,72,73]. In contrast, most studies on drop formation in a quiescent continuous phase under the influence of buoyancy [20,21,23,51,74,75,76,77,78,79] were carried out in 1960s-1990s. With the rapid advent of droplet-based confined microfluidic techniques for the formation of monodisperse emulsions, the focus of research seems to have shifted away from buoyancy driven and non-confined systems, which has been traditionally used as a means to generate uniform drops and measure interfacial tension [80,81]. Buoyancy driven drop formation is an apt system for fundamental studies [82] because it involves fewer dominant forces and variables controlling the drop rupture as compared to microfluidic techniques and also offers certain unique advantages that may not be easily achieved by the confined microfluidic approaches. One example is the formation of millimetre-sized droplets, which is well suited to a wide range of encapsulation applications [1,83].

The literature on buoyancy-driven systems points to a few controversial issues regarding the droplet formation such as the relevance of the pinch-off mechanism and the

correlation between flow rate and droplet polydispersity. Harkins and Brown [18] predicted the size of drops formed in a similar system, at a negligibly small flow rate, by equating interfacial tension force with buoyancy and also included a correction factor to accommodate the liquid which remained attached to the needle after detachment. Hayworth and Treybal [19] added the effect of velocity and drag to the Harkins and Brown equation. Later, Rao et al. [20] proposed a two-stage model in which the first stage dealt with the drop volume using Harkins and Brown equation, and the second stage took into account the fluid entering the drop during the pinch-off time until the complete detachment occurred. They developed a model for the pinch off time for two separate systems, one with low viscosity (low viscosity dispersed and continuous phase) and another with high viscosity continuous phase. This two-stage model was also applied to a two-aqueous phase system [21] to estimate the final drop volume. The pinch-off time appears to be less significant for low-viscosity dispersed phase and where the flow rate is low. However, to date there has been no actual experimental data reported for the pinch-off time for low viscosity conditions in buoyancy driven system.

An essential aspect of emulsification is the polydispersity of the drops generated. Surprisingly, there is no report that shows clearly how the polydispersity of drops varies with the dispersed phase flow rate in buoyancy-driven systems. In contrast, the variations in polydispersity of drops with flow rates for co-flow or flow-focusing microfluidic approaches have been discussed in the literature. Nie et al. [84] explored a flow-focusing microfluidic device for a large range of viscosities of dispersed phase. They concluded that a highly viscous dispersed phase produces droplets with a low polydispersity. However, no extensive effect of dispersed or continuous phase flow rates on polydispersity was presented. Cramer et al. [71] studied the polydispersity in droplet trains formed in dripping mode using a co-flow approach. Cordero et al. [85] investigated

the co-flow approach for drop formation and found that the polydispersity decreased with increasing dispersed phase flow rate in the jetting regime. Cramer [70] and Cramer et al. [71] also discussed the initial increase in polydispersity of droplets with increasing dispersed phase flow rate in jetting regime and the subsequent production of nearly monodisperse droplets at higher flow rates for a co-flow system. Chen et al. [57] explored drop formation mechanism in the same co-flow system using computation fluid dynamics simulations and concluded that dripping, as opposed to jetting, is a better way to obtain uniform drops.

Another important parameter which affects the drop formation is the time variations in the interfacial tension. As the drop grows, the continuous generation of new interfaces and diffusion-controlled surfactant transfer from the continuous phase onto the interface lead to a time-variant, dynamic, interfacial tension. Initial works mainly dealt with the effect of dynamic interfacial tension on a jetting liquid. Bohr [86] was first to consider the effect of fresh surface generation for a liquid jet formed in a gas and related it to the perturbations on the jet. Addison and Elliott [87], and Garner and Mina [88] developed a technique to measure surface tension which depends upon the surface age for liquid-liquid jets. Later, Van der Graaf et al. [69] demonstrated the importance of dynamic interfacial tension for drops formed under shear via membrane emulsification based on surface ageing. In confined microfluidics, which is usually operated at high drop formation frequency, the dynamic interfacial tension takes on a value close to that of pure oil-water interface [50]. However, the effect of dynamic interfacial tension on drop formation in a buoyancy driven system, especially at low flow rates, has remained unexplored.

In this chapter, we revisit drop formation in a buoyancy driven system and investigate in particular these three important issues; the relevance of pinch-off time and satellite drops

on final drop volume, the effect of dispersed phase flow rate on drop polydispersity, and the dynamic interfacial tension effects. We also characterise flow regimes and highlight the importance of buoyancy force in the jetting regime. A broad set of data using three hydrocarbon oils within a wide range of flow rates is presented. A fundamental analytical force-balance model is used, which is first validated against pure oil-water systems, and then modified for systems containing surfactant to include the effect of dynamic interfacial tension on drop size.

4.3. THEORY

Buoyancy-driven drop formation is defined as the condition under which buoyancy, among all other forces acting on the drop, remains as the dominant force for detaching the drop from the microchannel. We restrict our analytical analysis to dripping mode, which is characterized by the detachment of a drop close to the microchannel tip.

There are primarily four forces involved in a tug-of-war during the drop formation. [51] Two of these forces (buoyancy and kinetic) try to break the drop from the microchannel; and the other two (drag and interfacial tension) hold the drop back and keep it attached to the tip (Figure 4.1b). The interplay of these forces determines the amount of time the drop remains attached to the tip. The longer a drop stays attached, bigger the size of the drop will become, for a given size of microchannel, flow rate, and fluid properties. As long as the drop is held attached, the forces are deemed balanced, meaning that the disruptive forces are kept under check by the counter forces. With increasing buoyancy force as the drop grows, eventually a point is reached when the balance of the forces cannot be maintained anymore, leading to the detachment of drop. The detachment of the drop, in the dripping mode, begins with necking at a close distance from the tip.

Kinetic force, owing to the flow rate and density of the dispersed fluid, can be written as,

$$F_k = \rho_d \, Q_d \, u_d \tag{4.1}$$

where ρ_d, and u_d are the density and velocity of the dispersed phase, respectively. The subscript d denotes dispersed fluid for a two-phase system. Since the outer phase is stagnant, we use Q, instead of Q_d, throughout this report. This force is essentially driven by the mass flow rate of the fluid through the microchannel.

The buoyancy force, which is largely responsible for drop rupture, can be expressed as,

$$F_b = \Delta\rho \, g \, V_{drop} \tag{4.2}$$

Here $\Delta\rho$ is the density difference between dispersed and continuous phase and V_{drop} is the volume of the drop.

The main cohesive force acting on drop is the interfacial tension force, which is dependent on the properties of the two phases and the absence or presence of surfactant. The interfacial tension force is expressed as,

$$F_s = 2\pi r_w \, \sigma \, sin\theta \tag{4.3}$$

r_w is the wetting radius and may range from inner radius (r_{in}) to the outer radius (r_{out}) of the microchannel at the tip, σ is the interfacial tension, and θ is the contact angle as shown in Figure 4.1b. When the necking begins, θ takes a value of 90 degrees (i.e. $F_s = 2\pi r_w \, \sigma$).

Due to the quiescent continuous phase, the drag experienced by the drop (F_d) acts as a cohesive force, which can be estimated by the Stoke's law as follows.

$$F_d = 6\pi\eta_c r_{drop} v \tag{4.4}$$

where η_c is the viscosity of the continuous phase, r_{drop} is the drop radius (assuming it to be spherical), and v is the relative velocity between the drop and the stagnant continuous phase (drop growth velocity). The exact magnitude of drag is difficult to determine

accurately, especially when the drop is still attached to the microchannel and its surface is deformed. However, Equation 4.4 can still provide an acceptable estimation of drag, which is expected to be extremely low in the case under study. Equating all the forces at onset of rupture,

$$F_b + F_k = F_s + F_d \tag{4.5}$$

We show later that for the system under study, unlike several other methods of drop formation where drag dominates the drop formation process, [44] the drag is extremely low and can be ignored. An additional volume of fluid, $Q.t_p$, also enters the drop during the pinch-off time t_p. After neglecting drag and rearranging the terms, we obtain the following expression for the drop size in the dripping regime.

$$d_{drop} = 2\sqrt[3]{\frac{3}{4\pi}\left(\frac{F_s+F_d-F_k}{\Delta\rho\, g} + Q t_p\right)} \tag{4.6}$$

4.4. EXPERIMENTAL

The setup for the experiment is shown in Figure 4.1a. A hollow microchannel (ID: 230 µm OD: 410 µm) is submerged in a cuvette containing the continuous phase. The tip of the microchannel is orientated vertically. A syringe pump (Harvard pump 11 Elite) was used to pump the dispersed oil phase through the microchannel at given rates. Videos were captured, using a high speed camera (Photron Ultima APX Monochrome), for the entire duration of drop formation.

Three hydrocarbon oils, Octane (C8), Dodecane (C10) and Hexadecane (C16) were used (Sigma-Aldrich, purity 99%). To alter the interfacial tension, sodium dodecyl sulphate (SDS; Sigma-Aldrich, purity 99%) was added to the continuous phase (deionised water). Different surfactant concentrations (in wt %: 0, 0.10, 0.25, 0.50) in the continuous phase

were explored. The Critical Micellar Concentration (CMC) for SDS in deionised water was found to be 0.25 wt %. Chemicals were used as received.

Table 4.1 Physical properties of hydrocarbons at 21°C:

	C_8	C_{12}	C_{16}
Density (kg/m^3) †	702	749	773
Viscosity (mPa s) ‡	0.52	1.35	3.08
*Interfacial tension (mN/m)**			
0.00 wt% SDS	49.6	50.4	52.0
0.10 wt% SDS	20.5	20.9	21.5
0.25 wt% SDS	7.4	9.0	9.5
0.50 wt% SDS	7.1	8.7	9.3

† Sigma Aldrich's material safety data sheet
‡ C_8 (Hazardous Substances Data Bank - fact sheet); C_{12} (Chevalier et al. [89]); C_{16} (Awwad et al. [90])
* Measured by pendant drop method

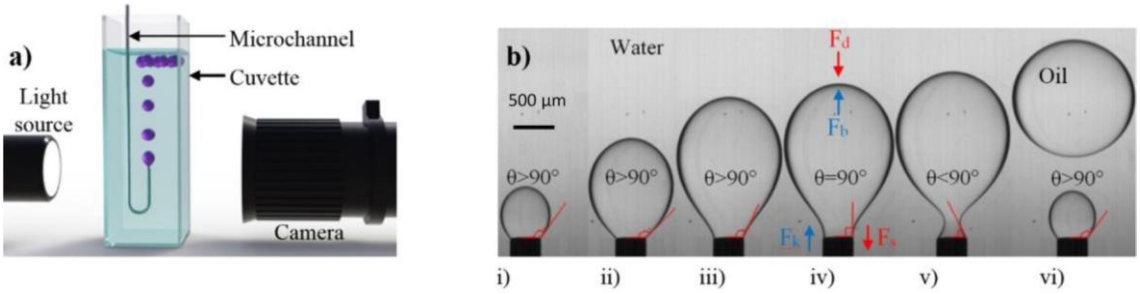

Figure 4.1 a) Schematic diagram of the experimental setup for the buoyancy-driven drop formation. b) Time evolution of contact angle for a typical drop (forces acting on the drop are also shown). The cohesive (in red) and the disruptive forces (in blue) are balanced at the rupture point when θ becomes 90°, as shown in the instance (iv).

Table 4.1 shows the physical properties of the oils used. The equilibrium interfacial tension values shown are against deionised water with appropriate concentrations of surfactant measured at 21°C with the pendant drop technique (First Ten Angstrom 200). All the experiments were performed at room temperature (21 ± 2˚C).

For drop size measurements, the large deformed drops, after detachment, were followed downstream until they attained circular shape, where their size was measured. The coefficient of variation was calculated by $\% \ C_v = 100 \ \frac{\sigma'}{\mu'}$, where σ' is the standard deviation of the drop sizes, and μ' is their mean.

4.5. RESULTS AND DISCUSSION

4.5.1. Drop size v/s oil type, flow rate, and surfactant concentration

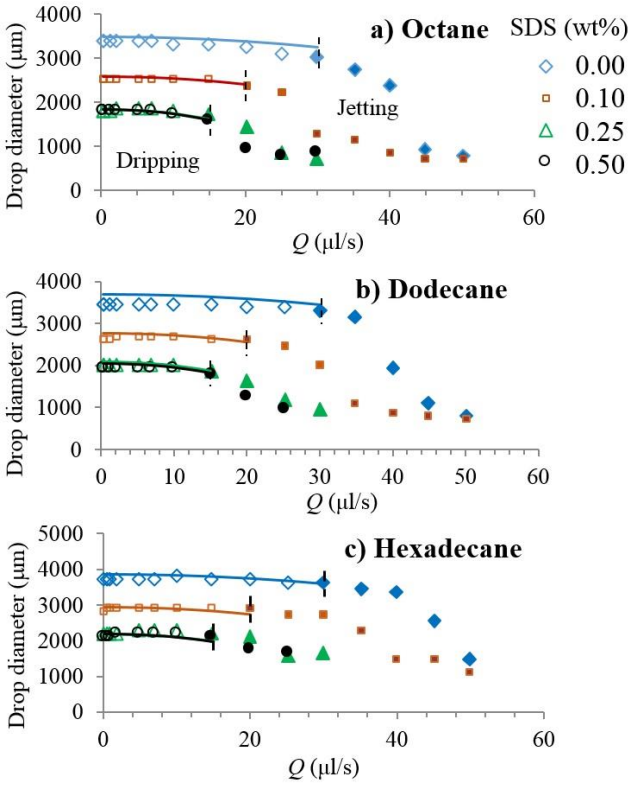

Figure 4.2 Effect of flow rate and surfactant concentration on the drop size for three oils. Solid lines represent model predictions (Equation 4.6, neglecting additional volume Q.tp). Empty (◇) and filled symbols (◆) stand for dripping and jetting regimes, respectively.

Figure 4.2 shows variation of drop size with Q for different hydrocarbons and surfactant concentrations. The drop size was found to increase slightly at extremely low values of Q in the presence of surfactant, while it remained relatively flat when no surfactant was

added. With further increase in Q, the drop size decreased. At the highest Q for all conditions, the drop size decreased to a size similar to the microchannel size (~500 μm).

As a general statement, higher chain length oils produced larger droplets. The density and interfacial tension (against pure water) of the oils increased with carbon chain length, as can be observed in Table 4.1. A higher density difference results in larger buoyancy force thus leading to smaller drops. Higher interfacial tension resulted in larger drops due to increased cohesive force.

4.5.2. Regimes of drop formation:

To eliminate any complexity related to dynamic interfacial tension, we first limit our analysis to pure (surfactant-free) systems, which do not show a significant change in interfacial tension with time. The data presented in Figure 4.2 point to different regimes for drop formation in the absence of surfactant. Here, we identify such regimes (and sub-regimes) by considering the forces acting on the drops as explained in theory section.

Dimensionless numbers are usually used to represent the effect of various forces acting on the drop during formation process. The Reynolds number ($Re = \rho_d u_d d_i / \mu_d$) was always less than 200 (laminar flow condition) in the dripping regime, while Re was 200 – 400 (transitional flow condition) for the drops formed in the jetting regime within the range of Q studied. The Weber number (We) shows the strength of kinetic force, the Bond number (Bo) represents the buoyancy force, and the Capillary number (Ca) accounts for the drag force, all against the interfacial tension force. Therefore, Equation 4.5 can be rewritten as:

$$We + Bo - Ca = 1.0 \tag{4.7}$$

where the Weber, Bond and Capillary numbers are strictly defined based on Equation 4.5, as follows.

$$We = \frac{\rho_d Q_d u_d}{2\pi r_w \sigma} \tag{4.8}$$

$$Bo = \frac{\Delta\rho\, g\, V_{drop}}{2\pi r_w \sigma} \tag{4.9}$$

$$Ca = \frac{F_d}{2\pi r_w \sigma} \tag{4.10}$$

Note that the above definitions are slightly different from what are usually used in the literature. However, they are more meaningful as they are defined based on the actual magnitudes of forces acting on drops.

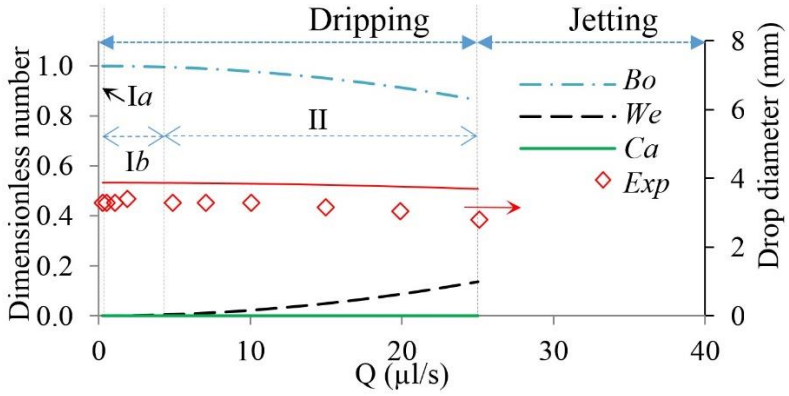

Figure 4.3 Flow regimes based on changes in forces with increasing Q for hexadecane drops formed in DI water. Region Ia refers to the condition where the equilibrium interfacial tension is reached before the drop detaches (similar to the Drop Weight Method (Tate [])), while the dynamic interfacial tension affects the drop formation in region Ib. In region II, buoyancy (Bo) remains the controlling force, though drops are detached with the help of kinetic force (We), leading to reduction in drop sizes. The red line is the drop size predictions (secondary axis) by Equation 4.6.

Figure 4.3 shows the variations in the Weber, Bond and Capillary numbers with *Q* for a surfactant-free system. At low *Q*, drops are primarily dominated by *Bo* (region I). Drops are detached close to the tip, also known as dripping regime, until *Q* ~ 30 µl/s. At the onset of jetting regime, which is characterized by detachment of drops much further away from the tip, the Bond number is roughly four times larger than the Weber number. This suggests buoyancy force is still the main driving force when jetting begins. In the

buoyancy-driven system with a stagnant outer phase, the outer capillary number *Ca* is close to zero (around three orders of magnitude smaller than other dominating forces), due to extremely low drag, as seen in Figure 4.3, so Equation 4.7 can be written as:

$$We + Bo \approx 1.0 \tag{4.11}$$

So far we have discussed about surfactant-free systems. With the introduction of surfactant, the map is slightly altered (not shown). For examples, the reduction of interfacial tension causes the transition from dripping to jetting to occur at a lower flow rate, and a region of slight rise in drop size appears at extremely low *Q* (region Ib). However, the *Ca* number still remains trivial.

With these changes in mind and in a broader context, we divide the dripping regime into two sub-regimes: Buoyancy *dominated* and *controlled* regime.

4.5.2.1. Buoyancy-dominated regime (I)

This regime is indicated by 'I' in Figure 4.3. For a surfactant-free system, the drop size remains constant throughout region I. However, a subdivision to Ia and Ib is useful when treating systems containing surfactant. In the narrow region Ia, the flow rate is so low (typical drop formation time ~ 2 min) that the equilibrium interfacial tension is reached well before the drop detaches, even in the presence of surfactant, leading to a constant drop size. Within this region (Ia), the kinetic force is insignificant, therefore Fb = Fs. Neglecting the additional volume Q.tp, Equation 4.6 can be reduced to what is known as Tate's Law [91].

$$\Delta\rho \; g \; V_{drop} = 2\pi r_w \, \sigma \, , \quad \rightarrow \quad d_{drop} = 2 \sqrt[3]{\left(\frac{3\sigma \, r_w}{2g \, \Delta\rho}\right)} \tag{4.12}$$

Equation 4.12 gives the maximum size of a pendant drop hanging at the tip at extremely low flow rates. It is also the basis for the Drop weight method for measuring interfacial tension [22]. As the kinetic force is nil, the drop size does not depend on *Q*.

In contrast, the drop size was found to increase with *Q* in region Ib, which is much wider than region Ia, in the presence of surfactant. We found that the force balance model fails to predict this rise in drop size, if dynamic interfacial tension is not considered. In this region, the kinetic force is still insignificant.

4.5.2.2. Buoyancy-controlled regime (II)

The difference between buoyancy-dominated and buoyancy-controlled region is the degree by which kinetic force contributes to drop detachment. In Region II, the drop size is significantly affected by the increased kinetic force due to high *Q*. Unlike in region Ib, the high kinetic force overcomes the drop size rise due to dynamic interfacial force, resulting in a decrease in the drop size with *Q*.

The jetting regime is differentiated from dripping regime by a sudden increase in the drop break-up length *L* [85], which is the distance from the point of detachment to the microchannel tip. We observed that, at the onset of jetting, *L* increases suddenly and approaches ~ 3 times the channel diameter. The transition from dripping to jetting was found to occur at We = 0.15 (see Figure 4.3). This transition was associated with a moderate decrease in drop size. In a conventional confined microfluidics, the driving force for jetting is usually the drag force, exerted by the continuous phase, which acts as a disruptive force, while buoyancy force is negligible. In contrast, the transition to jetting in buoyancy-driven systems occurs when buoyancy is still the largest disruptive force acting on the drop, while the drag that acts as a cohesive force is negligible.

4.5.3. Pinch-off time and satellite drop formation

We first discuss the relevance of pinch-off time for a low viscosity system. It has been reported that the drop size should be corrected to take into account the additional fluid that enters the drop during the pinch-off time [20,21]. Pinch-off time (t_p) is the time between when the contact angle reaches 90° and until the drop detaches (Figure 4.4a).

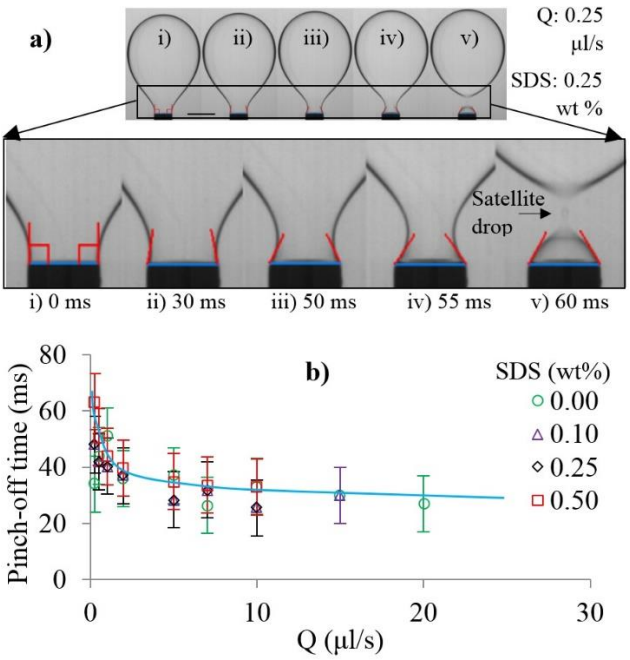

Figure 4.4 a) Micrographs showing the pinching-off of a dodecane drop in water containing 0.25 wt% SDS, for Q = 0.25 µl/s. Inset image shows a zoomed-in view of the pinch-off mechanism and the formation of a satellite droplet. Scale bar: 500 µm. b) Measured pinch-off time versus Q for dodecane at different SDS concentrations.

We measured the pinch-off time using a high-speed video camera with the typical time-scale resolution of ~1-5 ms. Figure 4.4b shows the pinch-off time for dodecane at the different surfactant concentrations and flow rates, as an example. Similar values were obtained for other two oils as well. The measurements show that the pinch-off times at different interfacial tensions and flow rates were in the range of 30-70 ms.

The volume of dispersed phase entering the drop during the measured pinch-off time ($Q.t_p$) was found to be less than 2% of the drop volume. Thus, this additional volume was

considered to be negligible and was safely ignored for all the calculations presented in this report. It is likely that this effect becomes more important if the dispersed phase viscosity is increased significantly.

The satellite droplets were observed in the dripping regime for all oils. In the absence of surfactant, the satellite drops were observed only at low flow rates (region I) but not in region II. A high interfacial tension avoids satellite drop formation by promoting a rapid pinching off of the liquid thread at the neck. The presence of surfactant, however, leads to the thinning and eventual pinch-off of the liquid thread at its two ends, resulting in the concomitant formation of a satellite drop [92,93]. However, adding the satellite drop volume to the experimental primary drop volume altered the final drop volume at most by ~1% for all the conditions explored, which is negligible. Similar observations have been made by Zhang [94]. It is worth pointing out that drop size underestimation due to neglecting the pinch-off volume nullified its overestimation due to neglecting the satellite drops, given their similar magnitudes.

4.5.4. Dimensionless analysis of drop formation

4.5.4.1. Pure oil-water systems

We analyse the results obtained for pure oil-in-water systems based on dimensionless numbers introduced earlier. Dimensionless numbers are frequently used in microfluidics in order to characterise the onset of drop ruptures [50] and transition from dripping to jetting [44]. Note that the dimensionless parameters here have strictly been defined based on force balance equations presented in Equation 4.8-4.10.

Figure 4.5a shows the Weber number versus Bond number curve obtained from the experimental size data. The straight line represents Equation 4.11. To calculate these dimensionless parameters, interfacial tension for the pure system was used.

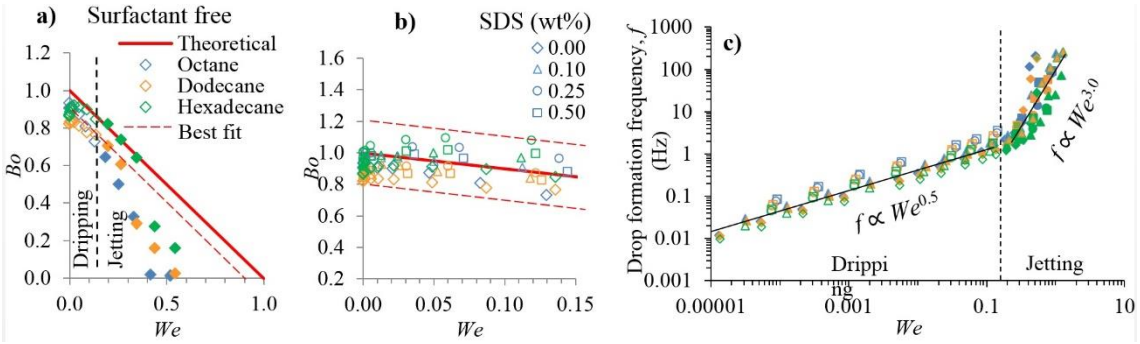

Figure 4.5 Weber number (We) versus Bond number (Bo) for a) surfactant-free systems and for b) all systems using surfactant explored in this work. Empty (◇) and filled symbols (◆) stand for drops formed in dripping and jetting regimes, respectively. c) Frequency of drop formation (f) versus We number for the three alkanes.

Figure 4.5a and Figure 4.5b show clearly that all the data points for the dripping and even the initial part of the jetting regime lie in the region of high Bond number and low Weber number, confirming the system is buoyancy driven for a majority of the range of Q explored. The transition from dripping to jetting was found to occur at the Weber number ~0.15, for all three oils, after which the data deviates away from the model prediction as the force balance model is not valid in jetting regime. We observe that for dripping regime in the surfactant-free systems, the data points fall on the line,

$$We + Bo \approx 0.90 \pm 0.1 \qquad (4.13)$$

This deviation from the force balance model has come to light only because surfactant-free systems are being dealt with. We do not know the reasons for this deviation. Factors not included in this analysis such as drag force and hydrostatic pressure [51] are extremely small and cannot affect the results significantly. The reproducibility of experiments was verified to be good. One source of possible experimental error is varying wetted microchannel tip area from the inner to the outer diameter. Care was taken to ensure that the dispersed phase fully wetted the outer microchannel tip periphery throughout the experiments. We can infer from Figure 4.5a and Figure 4.2 that Equation 4.6

overestimates the drop size for all oils examined. The deviation of ~10% in the *We* v/s *Bo* is translated to an error of ~20% % in terms of drop volume, and a smaller error, ~7%, in the drop diameter prediction. This error is therefore much greater than that can be accounted for by ignoring pinch-off time and formation of satellite drops.

Figure 4.5c shows the drop formation frequency (f) versus Weber number (We) for the three oils at different surfactant concentrations. The maximum frequency attainable within the dripping regime, f_{max} ~ 3 Hz, was two orders of magnitude smaller than that in the higher end of the jetting regime (~ 300 Hz). Interestingly, the increase in f with We is much faster in the jetting regime ($f \propto We^{3.0}$), as compared to that in the dripping regime ($f \propto We^{0.5}$). This suggests that a small increase in We (i.e. via altering Q or σ) can produce substantially more droplets in the jetting regime than in the dripping regime. This difference originates from the size of resulting drops being more sensitive to We number or Q in the jetting regime (see Figure 4.2). The above analysis reveals that a sudden variation in the rate of drop formation frequency with Weber number can be interpreted as a simple reliable criterion for predicting the transition from the dripping to jetting regime.

4.5.4.2. Oil-water-surfactant systems

The previous treatment avoided the presence of surfactants. While the equilibrium interfacial tension of water containing surfactant can be easily measured, their dynamic values are more difficult to obtain. The dynamics of interfacial tension is caused by gradual adsorption of surfactants onto the surface of drops. For now, we assume that the interfacial tensions are governed by their steady-state values. Dimensionless numbers presented in Figure 4.5b, which shows the plot of Weber number v/s Bond number for all oils used at different SDS concentrations, are based on this assumption.

The force balance equation now fits the experimental data within $We + Bo \approx 1.00 \pm 0.20$. One may conclude from a rather perfect fit of the data with the model predictions that Equation 4.11 holds for every system. However, we know from the analysis shown earlier that the surfactant-free size data do not completely fit the model. We understand that the improvement of drop size predictions in the presence of surfactant is mainly because equilibrium interfacial tensions were used (which are smaller than actual values), thus leading to overestimation of $We + Bo$.

4.5.5. A modified model with dynamic interfacial tension

A closer look at the data in Figure 4.2 would show an initial rise in drop size with Q. A zoomed-in view for the drop size data for the three oils dispersed in water having 0.1 wt % SDS is presented in Figure 4.6a. Rao et al. [20] also reported a similar rise in drop size at low values of Q in the presence of surfactant. They also explored low viscosity systems where drops formed under buoyancy force. However, it was hypothesized that the drop size increased as a result of increasing Q, without any subsequent effect on drop detachment time. However, we found that this rise could be better explained with the help of dynamic interfacial tension, as given below.

Before a surfactant can be adsorbed on the interface, it has to diffuse through the continuous phase and towards the interface. This indicates interfacial tension is a function of time. Dynamic interfacial tension was not included in the simple model explained in the previous section to avoid the complexity. An extended model is presented below which takes into account the change in interfacial tension with time during the formation of drops. The interfacial tension variation with time for octane-water system with 0.1 wt% (below CMC) and 0.25 wt% (at CMC) SDS, using Pendant drop method, are shown Figure 4.6b. The interfacial tension reduced with time until reaching its equilibrium value.

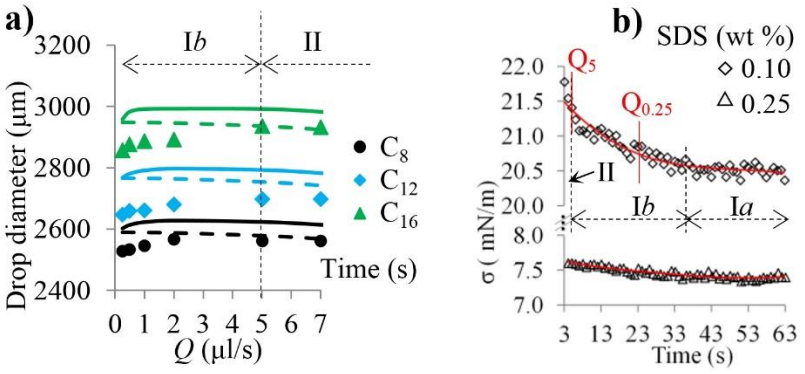

Figure 4.6 a) Prediction of the initial rise with Q in buoyancy dominated region I*b* by the modified model taking into account the dynamic interfacial tension (——) for octane, dodecane and hexadecane dispersed in water containing 0.1 wt% SDS. The predictions using equilibrium interfacial tension (- - -) fail to show the initial rise. b) Dynamics of interfacial tension at octane-water interface for two different concentrations of SDS in the water phase. The time taken in forming the pendant drop was ~3 s, during which interfacial tension could not be measured. The surface tension curve was fitted with best fit line $\sigma(t) = 10^{-7}\, t^4 - 4 \times 10^{-5}\, t^3 + 2.3 \times 10^{-3}\, t^2 - 7.18 \times 10^{-2}\, t + 21.534$ for 0.1 wt% SDS case.

In a typical interfacial tension measurement, the adsorption of surfactant on a steady surface is recorded. In a typical drop formation process, however, interface generation and surfactant diffusion/adsorption occur simultaneously. This means that at the instance of drop rupture, the interface formed early is exposed to the continuous phase for the longer period of time than the interface that formed later. As the interfacial area changes with time, a question to answer is what time should be considered as the characteristic time for surfactant adsorption onto the interface. We considered the surface-average age of the drop (t_{av}) as the real or characteristic time; $t_{av} = t$. Based on the time for drop formation of a spherical drop, the surface-average age of the drop can be related to the time of drop formation t_f as (see Appendix A for derivation),

$$t_{av} = 0.6 t_f \tag{4.14}$$

To introduce the surface-average age of the drop in the force-balance model, we considered the interfacial tension force [$F_s = 2\pi r_w \sigma(t)$] to be a function of the

characteristic time t_{av} (Equation 4.14). The time-dependent interfacial tension data from Figure 4.6b was solved simultaneously with Equation 4.1-4.3 to give the final drop size, using $\sigma(t) = \sigma(0.6t_f)$ with incremental time-steps until the disruptive forces equalled the cohesive forces. We also assumed a homogenous distribution of surfactant throughout the interface. The resulting drop size predictions are shown in Figure 4.6a (solid lines), where it can be observed that the initial rise in drop size (region I*b*) with *Q* can only be predicted if the dynamic interfacial tension is included.

We have briefly mentioned the reason for the rise in drop size in region Ib. Here we aim to quantify this. We consider a system, octane in the water containing 0.1 wt% SDS, with its drop size data shown in Figure 4.6a, and corresponding dynamic interfacial tension data given in Figure 4.6b. The domains of buoyancy-dominated (I*b*) and buoyancy-controlled (II) regimes of dripping are also shown on this figure. At the lowest *Q* explored (0.25 µl/s), the surface-average time of ~21s (calculated using the drop formation time of t_f = 35 s in Equation 4.14) is obtained that corresponds to interfacial tensions of ~ 20.8 mN/m (Figure 4.6b, $Q_{0.25}$). An increase in *Q* above 0.25 µl/s, within the region I*b*, raises the dynamic interfacial tension, thus leading to the rise in drop size. By increasing *Q* to 5 µl/s, wi wanted here the kinetic force starts to become effective (region II), initially the gain in kinetic force compensates the rise in interfacial force, resulting in a constant (maximum achievable) drop size. However, with further increase in *Q* in the region II, the drop size starts to decrease with *Q* as the kinetic force takes over.

The importance of dynamic interfacial tension at high flow rates, which is associated with a high rate of surface generation, is already known. The analysis presented here establishes its relevance even at low *Q*.

4.5.6. Polydispersity

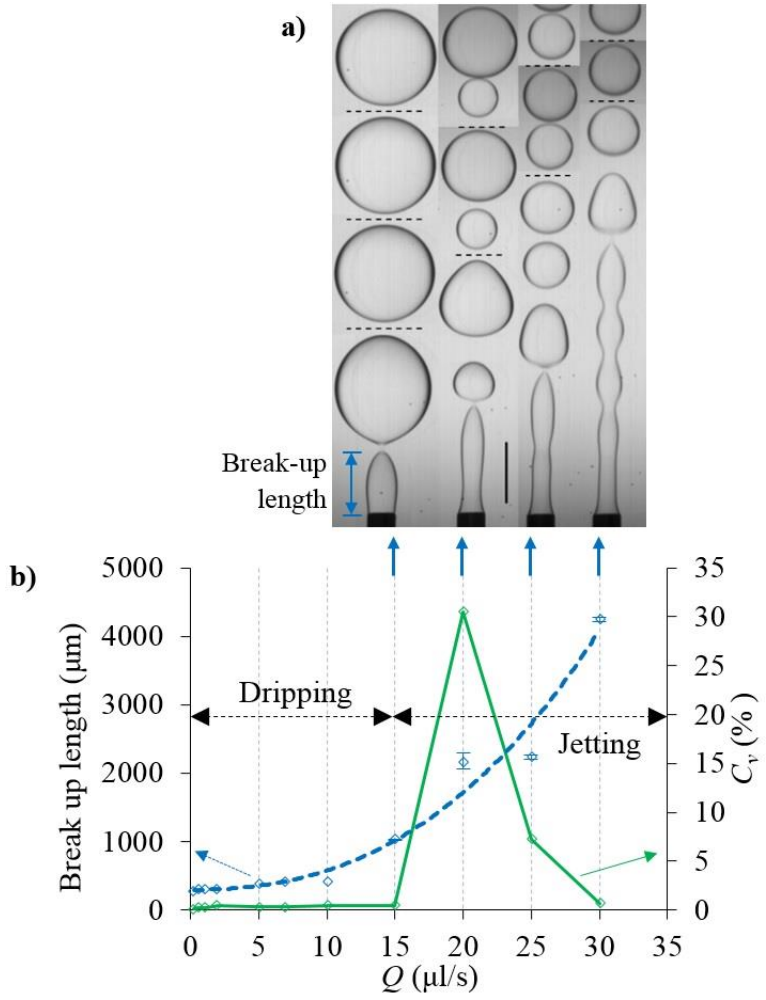

Figure 4.7 a) Micrographs of drops formed at different flow rates in jetting regime (scale bar: 1 mm), b) variations in breakup length L (.....) and coefficient of variation C_v (—) with flow rate Q for octane dispersed in water containing 0.5 wt% SDS.

The polydispersity of the drops produced at different flow rates, represented by the coefficient of variation C_v, was found to have strong relationships with the variation in break-up lengths, as previously reported [70,71,85]. Polydispersity in the break-up length (L) always resulted in polydispersity in the drop size. A typical case is shown in Figure 4.7a. The error bars, showing the statistical errors, indicate the polydispersity in L.

We found that a high drop formation frequency in the jetting regime can produce a similar degree of drop uniformity as that in dripping regime, under appropriate conditions.

Formation of monodisperse drops in jetting regime of a co-flow device was also observed by Cordero et al. [85]. They divided the jetting regime into two sub-regimes. The first jetting regime, which was achieved just after the transition from dripping, resulted in a high polydispersity. In the 2nd jetting regime, the polydispersity reduced with increasing dispersed phase flow rate. This difference was attributed to the poorly defined position of pinch-off in the first jetting regime, which gradually improved in the 2nd regime. The data obtained here supports this jetting behaviour and the correlation between the variations in pinch-off position and the polydispersity in the drops.

We found from micrographs that two populations of drops, primary and secondary drops, are usually formed during successive detachments (Figure 4.7a), which was the main reason for the increased polydispersity. However, above a critical flow rate, the size of the primary drop decreased while that of the secondary drop increased with Q, until both levelled off to an equal size, producing monodispersed drops. This is in contrast to a general notion that jetting is usually associated with a high degree of polydispersity [44,57,84].

Figure 4.8 shows a complete set of data for the L and C_v for the three oils at different surfactant concentrations, which show similar trends as observed in Figure 4.7. However, for surfactant-free systems, the polydispersity continues to increase with Q (in the range of Q explored here) after the onset of jetting, without any sign of retreat. This conclusion defines a new, and smaller, domain for the general notion mentioned above and suggests that uniform oil drops in surfactant-free systems can only be produced in dripping regime.

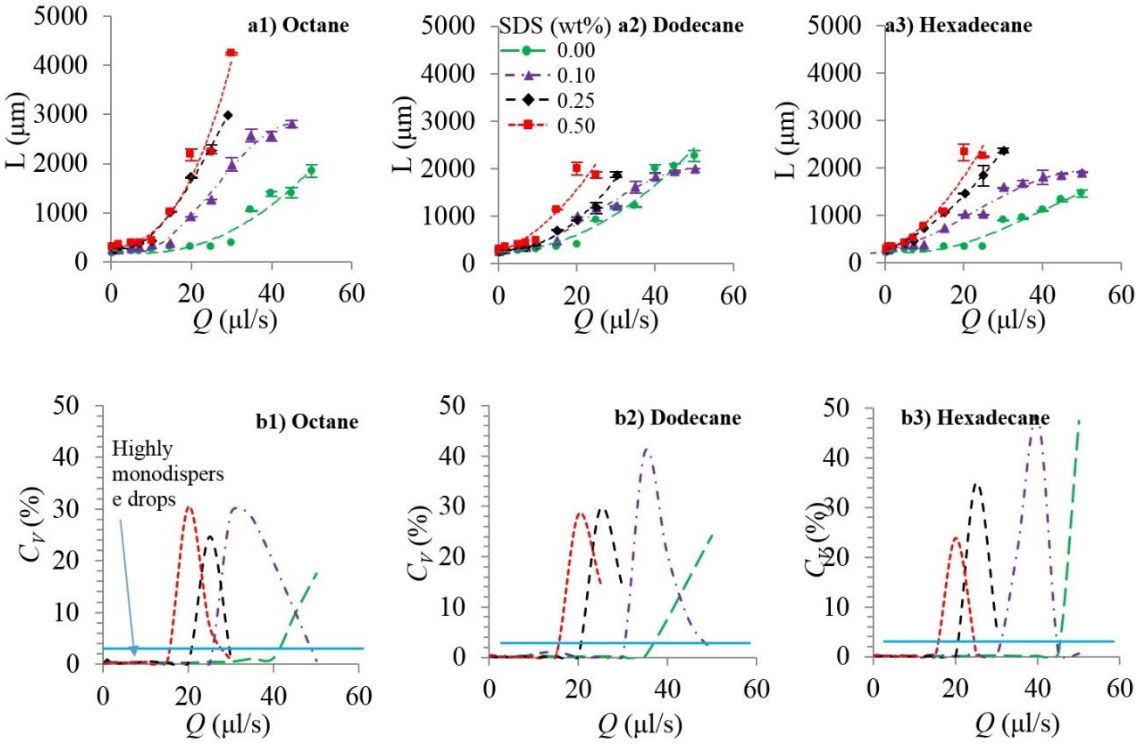

Figure 4.8 a) Measured break-up length (L) and b) corresponding coefficient of variation (% CV) in drop diameter plotted against the dispersed phase flow rate for three oils. The common legend for all graphs is shown in (a2).

We have earlier observed that jetting advances with decreasing interfacial tension (Figure 4.2). Interestingly, we also note in Figure 4.8 that the rise in polydispersity, which is associated with the onset of jetting, occurs at an even lower Q for the above CMC case (SDS, 0.5 wt %) than at the CMC (SDS, 0.25 wt %), even though the equilibrium interfacial is the same for both cases. This re-emphasises the importance of the dynamic interfacial tension in buoyancy assisted drop formation regimes.

4.6. CONCLUSION

Buoyancy-driven drop formation in a quiescent continuous phase offers a sound platform for mechanistic study of drop rupture in microchannels. Due to its simplicity, as compared to typical microfluidic systems (often involving complex flow conditions where viscous forces dominate), few forces dominate the drop formation. Yet, we see that the well-developed fundamental theories, which forms the basis for microfluidic droplet theory, still requires refinement.

We revisited the simple buoyancy driven system for three alkanes and addressed some controversial phenomena which are, the impact of pinch-off time on the final drop volume in low viscosity systems, dynamic interfacial tension effect at low flow conditions and variations in polydispersity in jetting regime.

Pinch-off time was found to be negligible for low viscosity systems explored. Even at the onset of jetting, the buoyancy force was noted to be much larger than the kinetic force. The drop formation theory was extended by including the dynamic interfacial tension effect based on surface-average age of the drop, which established the relevance of dynamic interfacial tension at low Q, where it caused an increase in the drop size. Even though the modified model improved the size prediction, it should be stressed that for a surfactant-free system, where the interfacial tension does not vary with time, a perfect prediction of droplet size could not be reached. Polydispersity in the drops formed under the jetting regime was found to be strongly dependent on the variation in the break-up lengths. It was observed that monodispersity improved with increasing flow rate after initial onset of jetting. This suggests that monodispersity can be tuned in the jetting regime under appropriate conditions to a level encountered only during dripping conditions, thereby increasing productivity.

Chapter 5 Millimetric Core-Shell Drops via Buoyancy-assisted Non-Confined Microfluidics[†]

5.1. ABSTRACT

Core-shell structures having millimetric dimensions have attracted a wide range of applications. Such structures cannot be achieved in typical microfluidic devices due to buoyancy-driven phase separation difficulties at low flow rates. A buoyancy assisted approach based on two-phase flow (core and shell phase) with the outer phase as quiescent and non-confined, is presented for producing large core-shell droplets. Buoyancy was found to be the dominant force for drop formation in the surfactant-free system, but considerably less effective in the presence of surfactants. The drop formation was mostly limited to the dripping regime when the surfactant concentrations were low. A simple force-balance model is developed for the prediction of the main drop and the core sizes, which are validated against the data obtained in a surfactant-free system. The suggested method gives highly monodisperse (coefficient of variation smaller than 3%) core-shell drops (radius R~800-3000 μm) with a wide range of absolute (t ~ 30-1000 μm) and relative (t/R ~0.03-0.80) shell thickness.

[†] Chaurasia, A.S. and Sajjadi, S., **2015**. Millimetric core-shell drops via buoyancy assisted non-confined microfluidics. *Chemical Engineering Science*, 129, pp. 260-270.

5.2. INTRODUCTION

Uniform core-shell drops made by micro-capillary based techniques [56,25] have found numerous applications within biomedical and pharmaceutical fields such as micro-reactors, [95] delivery vehicles in the form of liposomes [96] or microcapsules, [97] and controlled content release [30] using structures having ultra-thin shells. [60] The size of the drops decides its viability for any application. For certain purposes such as cell manipulation [1] and encapsulation, [83,98,99] large core-shell drops are required. Typical confined microfluidic approaches for the formation of core-shell drops via co-flow [56,100] or flow-focused [95,50,101] technique produce rather small-sized drops. In such approaches, the drop size becomes less dependent of the inner and middle phase flow rates and is mainly controlled by the outer phase flow, [56] due to a high drag. To produce large drops, a small outer phase flow rate is usually required. In both co-flow and flow-focusing approaches, application of low outer phase flow rates becomes non-feasible due to the problems associated with drop accumulation in the dead zones resulting mainly from gravity effects. To avoid this drawback, capillaries should be set up vertically to allow for continuous generation and buoyancy-driven transportation of resulting large drops.

Vertically orientated co-axial capillary setups have previously been employed to produce core-shell structures. Berkland et al [102,103] used a coaxial setup in which the inner and middle phases were jetted to create a coaxial jet stream in a carrier phase, which was then acoustically disturbed to create core-shell droplets. This technique was reported to give high control over drop size and shell thickness, but produced small droplets. Manukian and Toreki [104] also used a concentric nozzle setup, oriented vertically, to produce a core-shell compound jet in the outer phase, which then ruptured without external

disturbance to form core-shell drops. This process was used to commercially produce large core-shell structures, known as Hydrocapsules, ranging from 200 μm to 10 mm in diameter. However, drop formation from a jetting stream of liquid is usually associated with a low degree of droplet uniformity. [57] A vertically orientated co-flow microfluidic device with outer phase flow has also been employed to produce millimetre-scaled core-shell structures. [105] The presence of high outer phase flow, however, limited the drop size to a considerable degree. In all the cases discussed above, either the effect of buoyancy was suppressed (due to either the external disturbances or the drag force caused by the outer phase flow), or the monodispersity was compromised because the drops were formed due to the uncontrolled rupture of a compound jet.

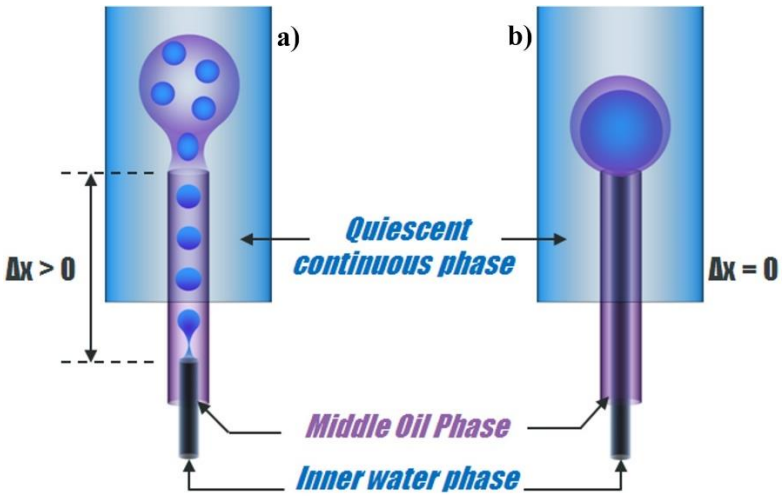

Figure 5.1 The schematic illustration of the difference in the mechanism of core shell formation under the influence of gravity when a) the inner capillary tip is placed far behind the outer capillary tip, and when b) both are kept at the same level.

Gaitzsch et al. [106] explored the formation of pendant water-in-oil-in-water droplet under the effect of buoyancy. However, the focus of this study was on the mechanism of expulsion of the water core from the pendant double emulsion due to partial coalescence in a surfactant-free system. A similar vertical setup has also been used to form multiple emulsions for studying their behaviour via electrophoretic manipulation, [82] which is an

easy and efficient method of transporting an oil phase through an oil environment. Recently, Schmit et al. [107] reported the formation of millimetre-sized double emulsions via a pendant drop method. This method, where the core was first formed at the tip of the inner nozzle, allowed a good control over the number of core droplets [56]. The core droplets then entered a pendant drop, which later detached from the outer tip (kept far ahead of the inner nozzle tip) under the influence of gravity, as shown in Figure 5.1a.

However, using such a two-step device prevents the formation of drops with large core and ultra-thin shelled drops, especially on the millimetre scale. [105] Furthermore, keeping the inner capillary tip far behind the outer tip usually leads to a lower uniformity of the core droplets due to the difficulties involved in the frequency matching of the core and the main drop formation. [105]

In this chapter, we report the use of a vertically oriented non-confined microfluidic device where buoyancy effect is significant. Generally the term "microfluidic" applies to devices that have at least one or more components (drop size, capillary tip size, etc.) below a millimetre scale. [108] This justifies the use of the term "non-confined microfluidics" for our system that employs two sub-mm dimensions (glass capillaries) and a third dimension (cuvette) that can vary between the diameter of drops and infinity. We kept the inner and the outer capillary tips at the same level to facilitate the formation of millimetric water-in-oil-in-water core-shell drops (Figure 5.1b) with better control over shell thickness. The capability of accommodating multiple capillaries in a non-confined environment that eliminates the difficulties associated with micro-capillary alignment in a restricted space as experienced in common microfluidic devices, [56,101,105] the elimination of the third pumping mechanism required for the outer phase due to a non-confined environment, and

the simplicity of buoyancy assisted transport of drops and their facile collections makes this design easy and economical for scale up.

In the proposed system, drag acts as a cohesive force, albeit its magnitude has been found to be negligible as compared to the dominant interfacial and buoyancy forces (Chapter 4). This extends the flow conditions (thus increases the productivity) under which uniform droplet formation via dripping occur, which is associated with high uniformity of droplets. It is also shown that the main drop and the core sizes can be predicted by a force-balance model, which is validated against a surfactant-free system. We demonstrate the production of core-shell drops having large sizes, between 1.6-6.0 mm in diameter.

5.3. EXPERIMENTAL

5.3.1. Materials

Octane (Sigma-Aldrich, 98%, density: 702 kg/m^3, viscosity: 0.52 mPa s) was used as received as the middle oil phase. Sodium dodecyl sulphate (SDS; 98.5%, Sigma-Aldrich) and Span85 (Sigma-Aldrich) were used as surfactants in the outer water and middle oil phase, respectively. De-ionised water (density: 998 kg/m^3, viscosity: 1 mPa s) was used as the inner water phase.

5.3.2. Device

The schematic of the non-confined microfluidic device is shown in Figure 2a. Two glass capillaries, circular (ID: 0.55 mm, OD: 1 mm) and square (IL: 1 mm, OL: 1.5 mm), were pulled using a pipette puller (P-1000, Sutter Instrument, Novato, USA). The tapered tips were cut to the desired sizes. The cross-sectional shape of the outer square capillary tip turned circular (ID: 290 µm, OD: 335 µm) after being pulled, while the inner capillary tip retained its circular cross-section (ID: 46 µm, OD: 70 µm).

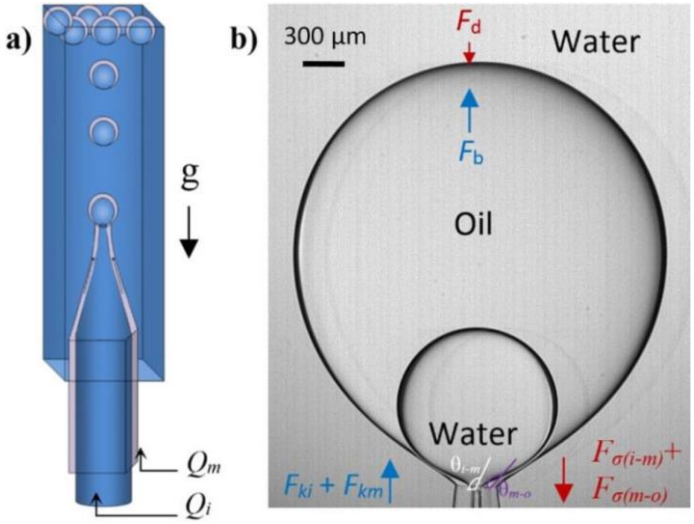

Figure 5.2 a) The schematic shows a non-confined microfluidic device for the formation of double emulsions. The inner water phase was introduced through the inner capillary at a volumetric flow rate Q_i, while the middle oil phase was pumped through the annular space between the inner and the outer capillary, at a volumetric rate of Q_m. b) Forces acting on the main drop are shown. F_σ: Interfacial tension force, F_k: Kinetic force, F_d: Drag force, F_b: Buoyancy force. The subscripts *i* and *m* refer to the inner and middle phase respectively.

The outer capillary's inner surface was made hydrophobic by treating it with n-Octadecyltrimethoxysilane, while its outer surface was kept hydrophilic by plasma cleaning (Femto Plasma cleaner, Diener). The inner capillary was treated to be hydrophobic throughout.The inner capillary was introduced in the outer capillary and was axially aligned with both the tips placed at same level (Figure 5.2b). Placing the two tips at the same level leads to a higher uniformity of the droplets as it circumvents the difficulties involved in the matching of core formation frequency and the main drop generation rate. [105] The axial alignment offset between the two tips was kept within ± 5.0 µm, which left plenty of clearance for the middle phase to asymmetrically engulf the inner phase. The coupled and aligned capillary-set was introduced inside an open cuvette (4.5 cm × 1 cm × 1 cm), which acted as the non-confined container for the quiescent outer water phase. The device was oriented vertically with the tip facing upward, as shown in the schematic (Figure 5.2a). The surface treatments and the device orientation discussed

here are favoured to produce water-in-oil-water emulsions. The oil phase was pumped (Harvard pump 11 Elite) through the gap between the outer and the inner capillary while the inner water phase was introduced through the inner capillary. Non-confinement provided by the open cuvette facilitated unobstructed drop growth until it detached from the tip. This was ascertained by choosing a cuvette wide enough, such that the drop was always smaller than the cuvette width throughout its formation under all conditions. The formed drops were collected at the top of cuvette.

The drop formation was recorded using a high-speed video camera (Photron Ultima APX Monochrome), while the frame rate at which the images were captured using the camera was varied between 100-1000 fps. The drops size measurements were carried out downstream where drops attained a spherical shape. A minimum of 10 drops were measured to calculate the coefficient of variation (% $C_v = 100\,\sigma'/\mu'$) where, σ' is the standard deviation of the drop sizes while μ' is their mean.

A surfactant-free system and a system including a small amount of surfactant in the middle and the outer phase were explored. A wide range of flow rates for the inner and the middle phase was explored for the drop formation.

5.4. THEORETICAL MODEL

The force-balance model for single drop formation under the buoyancy effect [18,19,20,21,51,76,77,78] is extended here to core-shell drop formation. Figure 5.2b shows different forces acting on the main drop during its formation. The detaching forces acting on the main drop are buoyancy force (F_b) and sum of kinetic forces due to the flow of inner and middle phases ($F_{ki} + F_{km}$), [51] which can be expressed as

$$F_b = \Delta\rho\, g\, V_m \tag{5.1}$$

$$F_{ki} = \rho_i Q_i u_i \; ; F_{km} = \rho_m Q_m u_m \tag{5.2}$$

Here $\Delta\rho$ is the density difference between the middle and the outer phase, whereas V_m is the volume of middle oil phase. Q is the volumetric flow rate and u is phase velocity at the tip cross section. The subscripts *i, m* and *o* stand for *inner, middle* and *outer* phase respectively, throughout this chapter.

For a simple drop, there is a single interface via which the interfacial force is exerted. In the case of double or higher order drops, which are associated with multiple interfaces, the overall interfacial tension force would depend on the number of interfaces present. [25,97] The total interfacial tension force, which holds the drop to the tip, can be expressed as,

$$F_\sigma = F_{\sigma(i\text{-}m)} + F_{\sigma(m\text{-}o)} = \pi d_{w\text{-}i}\, \sigma_{(i\text{-}m)} \sin\theta_{(i\text{-}m)} + \pi d_{w\text{-}o}\, \sigma_{(m\text{-}o)} \sin\theta_{(m\text{-}o)} \tag{5.3}$$

Here $d_{w\text{-}i}$ and $d_{w\text{-}o}$ are the wetting diameters at the inner and the outer capillary tips, respectively. The inner/middle interfacial tension and middle/outer interfacial tension are expressed as $\sigma_{(i\text{-}m)}$ and $\sigma_{(m\text{-}o)}$, respectively. Contact angle θ is the angle the interface makes with the tip surface.

The drag force (F_d) experienced by the growing core-shell drop by the stagnant outer phase also acts as a cohesive force. This force can be approximated using Stokes' law for the drag experienced by a sphere of radius R moving at a relative velocity v in an outer fluid having viscosity η, as $F_{do} = 6\pi R\eta v$. For conventional confined microfluidic devices with moving continuous phase, drag usually acts as a disruptive force. In the system under study, however, the drag acts as cohesive force because the outer phase is quiescent. The drag on the main drop, however, was calculated to be very small (~three orders of magnitude smaller) as compared to other forces under all conditions, hence was ignored.

From the force balance we have,

$$F_b + F_{ki} + F_{km} = F_\sigma \tag{5.4}$$

For simplicity sake, we assume that the contact angle θ becomes 90 degrees [51] when the disruptive forces exceed the cohesive ones, after which the pinch-off process begins. So,

$$\Delta\rho g V_m + \rho_i Q_i u_i + \rho_m Q_m u_m = 2\pi r_{w\text{-}i}\, \sigma_{(i\text{-}m)} + 2\pi r_{w\text{-}o}\, \sigma_{(m\text{-}o)} \tag{5.5}$$

This equation is rearranged to estimate the oil volume V_m (shell volume) as,

$$V_m = \frac{F_\sigma - (F_{ki} + F_{km})}{\Delta\rho\, g} \tag{5.6}$$

The inner drop volume (core volume) is then calculated as,

$$V_i = \frac{Q_i}{Q_m} V_m, \tag{5.7}$$

The main drop radius (R) and its corresponding core radius (r) can be obtained as,

$$R = \sqrt[3]{\frac{3(V_m + V_i)}{4\pi}} \tag{5.8}$$

$$r = \sqrt[3]{\frac{3V_i}{4\pi}} \tag{5.9}$$

5.5. RESULTS AND DISCUSSION

Two scenarios, one being the surfactant-free system, and the other with small amounts of surfactants in the outer water phase (0.1 wt% SDS) and the middle oil phase (0.1 wt% Span85), were explored for core-shell drop formation.

5.5.1. Surfactant-free system

In order to avoid complexities involved in the formation of core-shell drops in the presence of surfactants, we initially explored a surfactant-free system.

5.5.1.1.Phase map

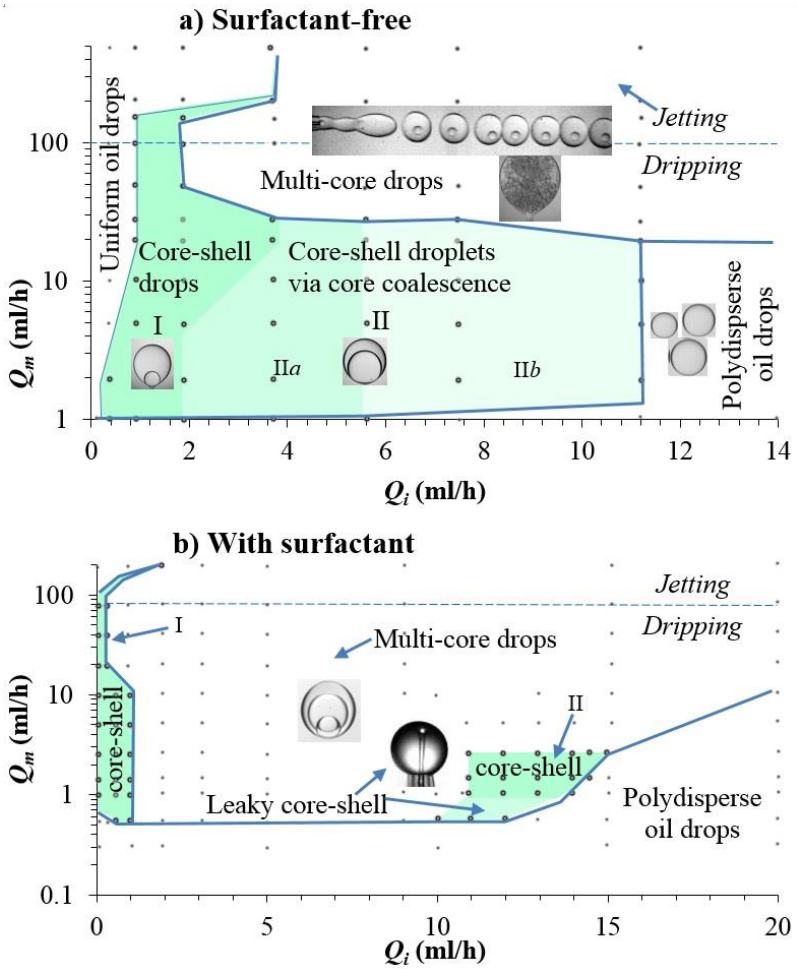

Figure 5.3 Phase maps for core-shell drop formation shown as middle v/s inner phase flow rate for a) surfactant-free and b) surfactant-added system where SDS and Span85 (both at 0.1wt%) were added to the outer and the middle phase, respectively. The jetting and dripping regimes shown only apply to the main drop (shell phase). Region II in surfactant-free system indicates the flow conditions under which initially multiple cores were formed via dripping (II*a*) and then via jetting (II*b*) of the inner phase, which later coalesced to produce drops with a single core. The inset image in (a) shows drops formed in the jetting regime. The inset images in (b) show a multi-core drop and the initial core-leakage which occurs in the *leaky core-shell* region. The large black empty circles indicate the experimental data points where core-shell drops were obtained, while the small black dots represent the conditions examined.

Figure 5.3a shows two different flow conditions [regions I and II (*a*,*b*)], under which core-shell drops were obtained in the surfactant-free system. The phase map for drop formation in the presence of surfactants (Figure 5.3b) will be discussed later.

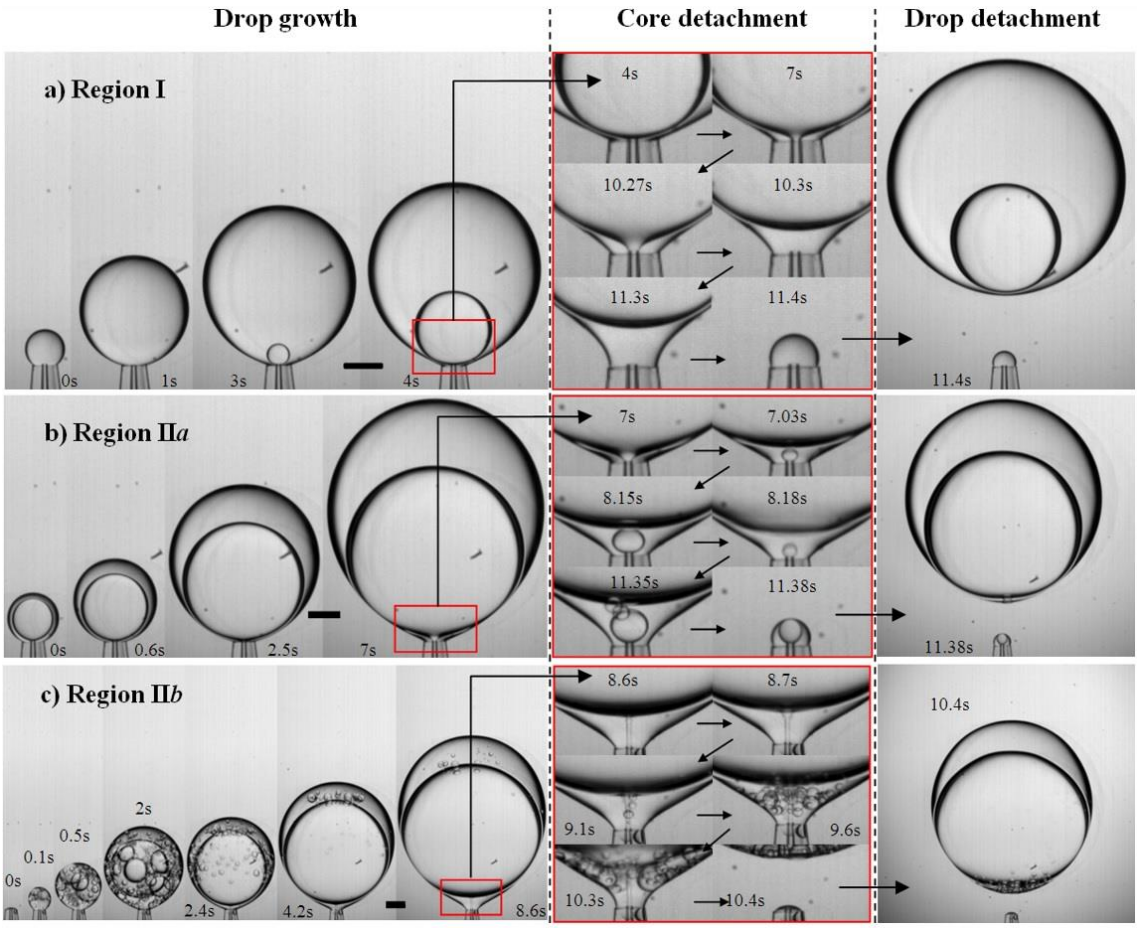

Figure 5.4 The time evolution of the drops formed in different regions of the surfactant-free system a) Region I where simple core-shell drops formed (Q_m: 5ml/h, Q_i: 0.5ml/h), b) Region II where core-shell drops formed in the dripping mode via coalescence of cores (region II*a* inset, Q_m: 5ml/h, Q_i: 4ml/h) and c) Region IIb where core-shell drops formed via coalescence of inner drops in the jetting mode (region II*b*, Q_m: 5ml/h, Q_i: 12ml/h) where a small inset image shows the water jet inside the oil drop broken into several inner drops. All scale bars: 500μm.

At higher Q_i, the increased kinetic force makes the inner drop detach much sooner than In region I, and at low Q_i, the core developed slowly, while attached to the inner channel tip, and detached only few moments before the main drop separated from the tip, thus producing typical single-core drop. It is observed that once a critical oil (shell) volume is reached, the core is detached (Figure 5.4a, vii), triggering the detachment of the main drop. In the absence of the inner interface, the outer interface is no longer able to pull together the drop via its interfacial force ($F_{\sigma(i\text{-}m)}$), leading to a quick detachment of the

main drop thereafter (Figure 5.4a, ix). Region I only extends little above the dripping–jetting (Q_m) threshold for the shell phase, where only drops with a very small core formed, due to the large drag exerted by the high Q_m.

the main drop. This leads to the formation of multiple inner drops. Depending on Q_m, the multiple drops have different fates. In the lower range of Q_m, indicated as region II, as the shell drop continues to grow at the tip, the multiple core drops coalesce to form a single large core drop by the time the shell drop is detached, similar to the observations made by Shao et al. [105]. The multiple cores in region II are formed in two ways, via dripping at intermediate Q_i (region II*a* Figure 5.4b) or jetting at high Q_i (region II*b* Figure 5.4c). At high values of Q_m, above region II, the internal core droplets did not coalesce together during the shell formation and also during the time, contained in the shell, they were travelling upward in the cuvette. This area is shown as the region of "multicore drops" on the phase maps. At higher Q_i beyond region II*b*, the inner phase jet simply broke through the middle phase and mixed with the outer phase. Also, no core-shell drops were formed when either Q_i or Q_m, or both were too low.

5.5.1.2.Drop size

Figure 5.4a and Figure 5.4d show the micrographs indicating variations in the core and shell (main) drop sizes with Q_i and Q_m. A complete range of size data obtained is presented in Figure 5.4b-c. In a typical confined microfluidics [56], the drop size is not affected significantly by Q_i because the drop rupture mechanism is dominated by the drag exerted by the outer flow, which forces the drop to detach once it reaches a definite size. Whereas in our system, with a quiescent outer phase, such a force is negligible and as a result, the size of drops is dictated by Q_i, as well as Q_m.

Generally, the shell drop size is small at a low Q_i but increases steadily with a rate depending on Q_m; the lower the Q_m the steeper the size increase. The reason that the drop size does not increase considerably with Q_i at high Q_m is because the shell volume takes less time to reach a critical volume (V_m) required to trigger the drop detachment, which leaves less time for the core to grow. The core size as well as the main drop size decreases with increasing Q_m, as shown in Figure 5.4d-e. Note that in a confined microfluidic approach, where drag controls the drop size, Q_m does not affect the drop size substantially [56]. We understand that in the system discussed here, a critical shell volume V_m should be reached before drops can be detached. This volume is reached quickly at a high Q_m thus reducing the core size.

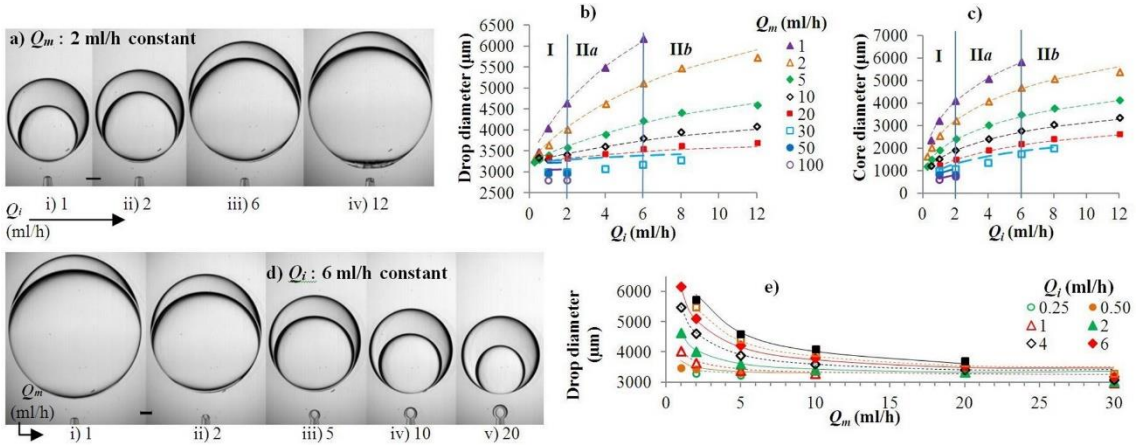

Figure 5.5 a) Micrographs of the variations in the drop size with increasing inner phase flow rate Q_i: i) 1ml/h, ii) 2ml/h, iii) 6ml/h and iv) 12ml/h at Q_m = 2ml/h. b) main drop and c) core size data (symbols) for the pure system with different oil flow rates. The dashed lines show model predictions. The legends shown in (b) also apply to (c). The sizes of drops produced in the jetting regime are not shown here. d) Reduction in the core size with increasing middle phase flow rate Q_m: i) 1ml/h, ii) 2ml/h, iii) 5ml/h, iv) 10ml/h and v) 20ml/h at Q_i = 6ml/h. Scale bars: 500μm. e) Main drop size versus Q_m with different Q_i for the pure system is presented.

In order to elaborate on the underlying mechanisms of drop formation, the evolution of drop size and morphology prior to detachment was studied. A typical time-evolution of drop formation is presented in Figure 5.4, which clearly shows that both core and shell

drop detach almost simultaneously, indicating that both interfaces contribute to cohesive forces. In fact in region I, the core detaches first (Figure 5.4a, 10.3s), while the main drop detaches just a few milliseconds later (Figure 5.4a, 11.4s). While in region II, the two interfaces are present throughout the drop formation until the instance of main drop detachment. It can thus be assumed that the core and the shell drop detach together in all the three regions. The shell drop always detached close to the tip for all the conditions explored, even when the inner phase was jetting, which is consistent with underlying mechanism of drop formation considered. The interfacial tension between pure water and octane was measured to be 49.6 mN/m using pendant drop method (FTA Instruments). This means, $\sigma_{(i\text{-}m)} = \sigma_{(e\text{-}m)} = 49.6$ mN/m. Using these values of interfacial tension in Equation 5.6-5.9, the drop sizes were predicted and presented in Figure 5.4b-c.

The size predictions fit rather well with the experimental data, thus validate the purely physical model (with no adjustable parameter) developed. Note that the interfacial force applied by the inner-middle interface is ~15% of the total interfacial force for the tip geometry used in this work, which significantly affects the predicted size. This confirms that the interfacial tension force due to the inner interface should be included in the force balance of a detaching core-shell drop, as suggested by other investigators [101,105]. The sizes of drops produced in the extremely limited jetting regime, for which the model is not valid, ranged between 600-2000 µm (inset image in Figure 5.3a), where the drop size decreased with increased jetting.

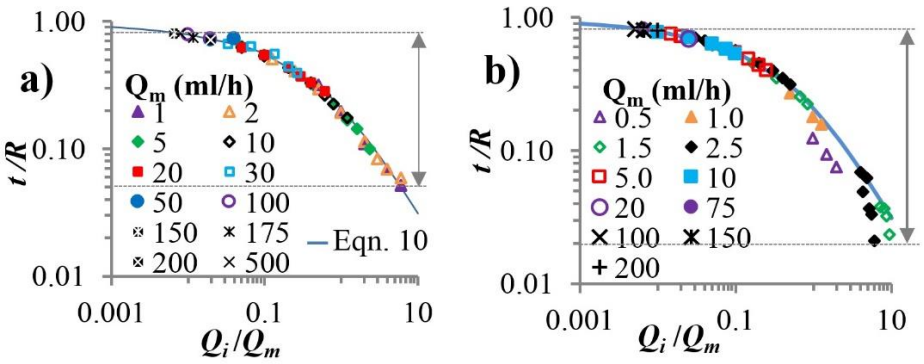

Figure 5.6 Variations in the relative shell thickness with Q_i/Q_m for a) surfactant-free and b) surfactant-added system. The lines represent Equation 5.10. The ranges of t/R are highlighted by the double-arrows.

The shell thickness t was found to decrease with increasing Q_i at a given Q_m. For comparison and understanding purposes, we analyse a normalized or relative shell-thickness (t/R; R: main drop radius) with respect to the flow rate ratio, which is correlated as [60,105],

$$\frac{t}{R} = 1 - \left(\frac{Q_i/Q_m}{Q_i/Q_m + 1} \right)^{1/3} \tag{5.10}$$

where shell thickness (t) is defined as $t = R - r$.

The theoretical t/R (Equation 5.10), based on the mass conservation (solid line in Figure 5.6), was used to verify the experimentally obtained relative shell thickness. Both mass balance equation and experimental data showed that the relative shell thickness (t/R) reduced exponentially with increasing ratio of inner to middle phase flow rate (Q_i/Q_m) with a close agreement.

For a surfactant-free system, the t/R varied with increasing Q_i/Q_m over a wide range (0.05-0.80 approximately), as shown in Figure 5.6a. However, it did not fall below 0.06 as the middle phase failed to form a thin shell around the core due to the high interfacial tension at both interfaces in the absence of surfactants, which led to the rupture of the shell before

the drop detached. Also, the drops formed in the absence of surfactants were quite unstable and coalesced instantly upon collision. All the drops formed under dripping had a coefficient of variation (% C_v) less than 3%.

5.5.2. Surfactant-added system

In the previous section, the force balance model was validated against the drop size data obtained in the absence of surfactants. We now explore the effect of surfactant on the drop formation mechanism, drop size and the minimum achievable shell thickness. Small amounts (0.1 wt % of the phases they are placed in) of Span85 and SDS are added to the middle oil and the outer water phase, respectively.

5.5.1.3.Phase map

The phase map for the formation of core-shell drops in the presence of surfactants has been shown earlier in Figure 5.3b. It marks two feasible regions, regions I and II, shown in green, where core-shell drops were obtained.

Drop formation in region I was the same as that in the surfactant-free system. Unlike the phase map for the surfactant-free case, there is a disconnecting space between the feasible regions, indicating that core-shell drops could only be achieved at low and relatively high Q_i. Within the intermediate range of Q_i, more than one core drop began to form within a single shell drop (inset image in Figure 5.3b), as noticed before (Figure 5.4b). However, because of the presence of surfactant in the middle phase, the core droplets were stable, and unlike the surfactant-free case they did not undergo coalescence to form core-shell drops. Drops formed in the presence of surfactants and under dripping condition had a coefficient of variation (% C_v) less than 3%.

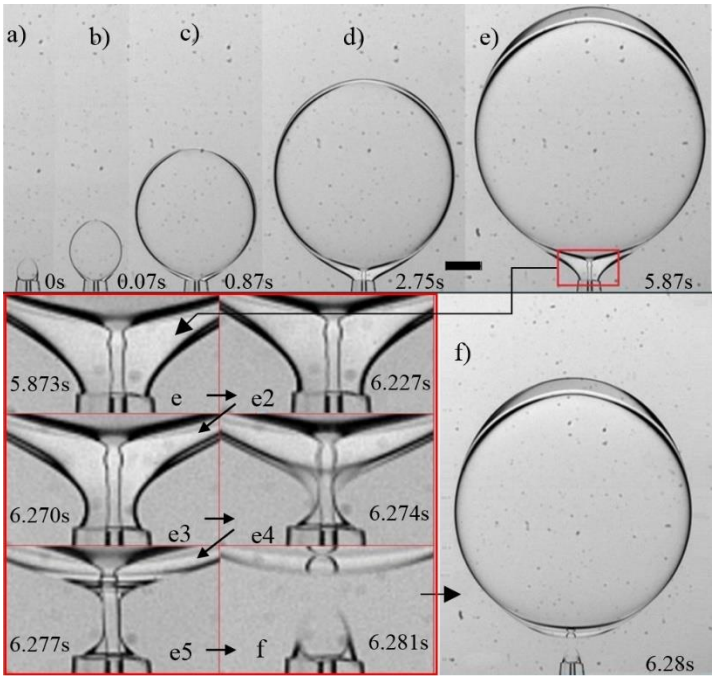

Figure 5.7 The time evolution of a core-shell drop formed with a jetting inner phase, in the presence of surfactants, corresponding to region II (Q_m: 1.5ml/h, Q_i: 12ml/h). The numbers indicate time in terms of seconds. Series of inset images (showing the sequence of events for e until f) show that the inner jet never detaches from the inner tip until the detachment of the main drop happens. Scale bar: 500μm.

In region II, which is comparable to region II*b* in the surfactant-free system, the core (inner) phase jetted inside the shell (middle) phase. However, unlike the breaking of the jet into several drops as encountered in the pure system (Figure 5.4c3) inset), here the inner jet did not rupture and fed the growing core until the main drop detached from the tip (Figure 5.7). The stability of the jet is most likely increased due to the lowered interfacial tension (because of the surfactant in the middle phase), which reduces the tendency of the jet to rupture [109,110].

The light green region below region II in the phase map (Figure 5.3b: leaky core-shell region) represents the regime of drop formation where the inner water phase initially escapes into the outer water phase (inset image in Figure 5.3b), while the shell (oil) drop continues to grow. This phenomenon occurs only at sufficiently low middle phase flow

rates that create a very small oil drop at the tip, which is easily penetrable by the high-velocity inner-water phase. The inner phase keeps escaping while the oil drop grows at the tip and around the escaping jet. As soon as the growing oil drop reaches a certain size, a distance of ~7-9 times the tip diameter above the tip the jet is destabilized and breaks off inside the oil drop to form water-in-oil drops. This phenomenon, which is undesirable since the inner phase leaks into the outer phase, is resolved at a sufficiently high Q_m, where the critical oil shell size for the jet break off is reached.

5.5.1.4. Drop size

The drops and their core sizes obtained for the system containing surfactants are presented in Figure 5.8. Similar to the surfactant-free system, the drop size increased with Q_i for a given Q_m in region I. However, the drop size decreased with increase in Q_i (Figure 5.8a) in region II (corresponding to region II*b* in the pure system), which is in contrast to what was observed in the pure system. The drop size decreased in region II because the kinetic force dominated over interfacial force at high Q_i due to the lowered interfacial tension achieved in the presence of surfactants (Figure 5.8b2). The drop size decreases with increasing Q_m, which is consistent with the observations made for the pure system.

The relative shell thickness (t/R) in the presence of surfactants (Figure 5.6b) was found to vary over a larger range of values as compared to the surfactant-free system (Figure 5.6a). The data points in Figure 5.6b that have larger deviation from Equation **5.**10 correspond to the leaky core-shell formation. Figure 5.6 shows that the minimum t/R obtained in the presence of surfactants was quite low (~0.02) and much smaller than that for the surfactant-free system (~0.05), suggesting that drops with thinner shells could be achieved at higher surfactant concentrations, as investigated in detail in Chapter 6.

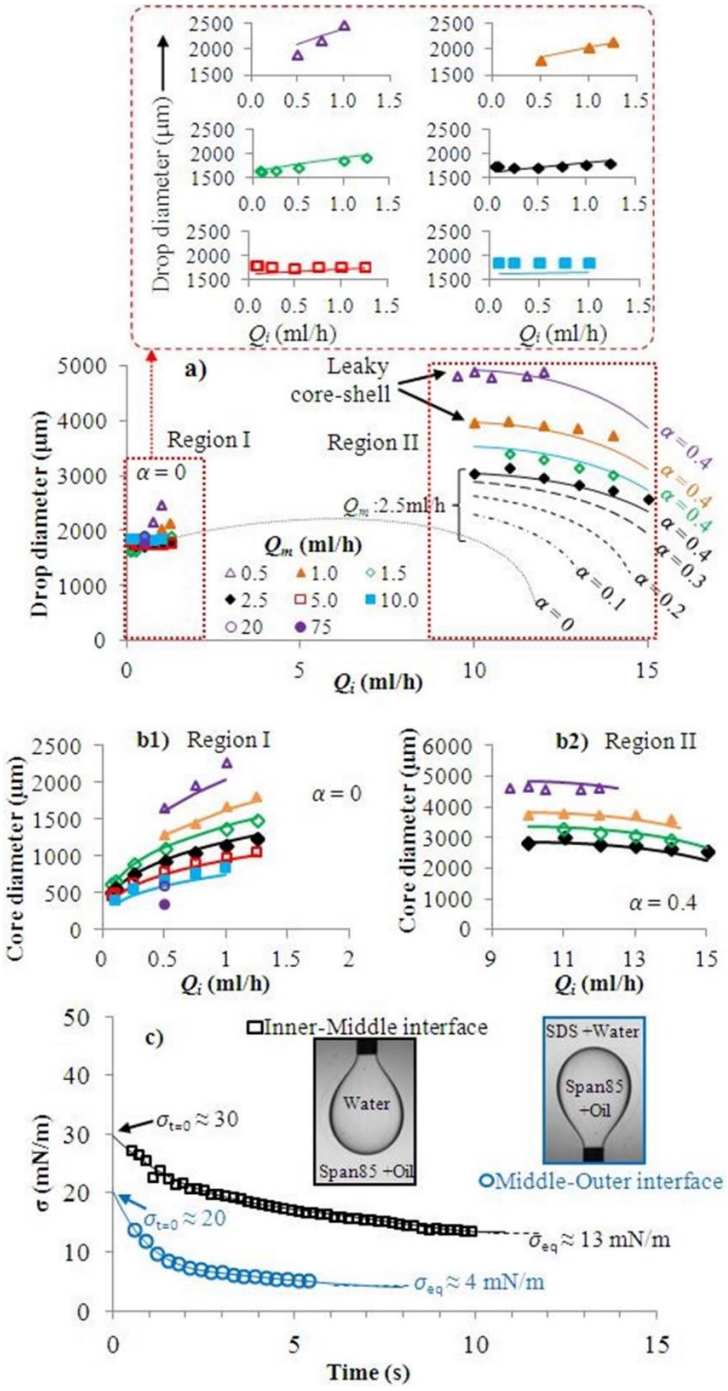

Figure 5.8 a) Drop diameter and b) Core diameter versus Q_i for different Q_m. Regions I and II correspond to those in Figure 5.4b. The sizes of drops produced in the jetting regime at $Q_m \geq 75$ ml/h are not shown here. The lines are the drop size predictions using the force balance model. The large inset in red box shows the zoomed-in view of drop size predictions in Region I. The correction factor α signifies the scaling up of the interfacial tension above the equilibrium values. c) Dynamic interfacial tensions at inner-middle and middle-outer interfaces measured separately using pendant drop technique. The inset images of the pendant drops are only for representations.

For region I, the shell (Figure 5.8a, large inset) and core size predictions (Figure 5.8b1) are calculated using the equilibrium interfacial tension of the interfaces. The equilibrium inner-middle and middle-outer interfacial tensions in the presence of surfactants, measured using pendant drop method, were $\sigma_{(i\text{-}m)} \approx 13$ mN/m and $\sigma_{(m\text{-}o)} \approx 4$ mN/m, respectively (Figure 5.8c). This difference is mainly because the outer interface has a lower equilibrium interfacial tension than the inner, as surfactants with different hydrophilicity-hydrophobicity balance are present on either side of the interface. These values suggest that for the concerned tip geometries, the interfacial force applied by the inner interface is ~35% of the total cohesive force ($F= \pi d_{w\text{-}o}\, \sigma_{(m\text{-}o)} + \pi d_{w\text{-}i}\, \sigma_{(i\text{-}m)}$, which is even more significant than that in the surfactant-free system.

We observe from Figure 5.8a (inset) that the predicted main drop and core sizes using the equilibrium interfacial tension values fit satisfactorily with the experimental data in region I. Given the low flow rates in this region, the rate of surface generation is rather slow and the assumption of both the interfacial tensions approaching the equilibrium values before the drop detachment appears to be sensible. In region II, however, the predictions using the equilibrium interfacial tension values were much smaller than the data (Figure 5.8a *region II*, for Q_m: 2.5ml/h, $\alpha = 0$).

The dynamic interfacial tensions measured separately for both the inner-middle and the middle-outer interfaces, as presented in Figure 5.8c, might suggest that the droplet formation time in region II is long enough to allow the equilibrium interfacial tension to be achieved. However, the model not only fails to predict the drop sizes in region II using the equilibrium values, but also, and even more importantly, fails to predict the trend of drop size variation with Q_i. The treatment of dynamic interfacial tension has been given in the literature in detail [111]. In Chapter 4 (4.5.5), we combined the dynamics of

interfacial tension with the characteristic drop formation time to arrive at a semi-empirical method to predict the drop size under the conditions similar to this work. For the current system, however, the adsorption dynamics of the surfactants are too complex to allow us to tackle it similarly. These complexities are; the presence of two types of surfactant (ionic and non-ionic) on each side of the outer oil-water interface with different lengths of diffusion path, rapid interface generation on the inner side of the interface and slow interface generation on the outer phase, and so on. One should also note that the σ-t curves shown in Figure 5.8c have been obtained separately for each interface (inset images in Figure 5.8c), which may not be an accurate representation of what happens during the drop formation when the two interfaces coexist. For these reasons, we adopted an empirical approach in the research.

In the lack of appropriate data, and based on the understanding explained above, we assumed that the dynamic interfacial tension (σ) can take a value between interfacial tension at time zero ($\sigma_{t=0}$) and that at equilibrium (σ_{eq}). The $\sigma_{t=0}$ for both interfaces were estimated by extending the line of best fit for interfacial tension v/s time curve to zero, as indicated in Figure 5.8c. We introduced a correction factor 'α' which would relate the dynamic interfacial tension (σ) to the $\sigma_{t=0}$ and the σ_{eq} as per the following expression.

$$\sigma = \alpha\, \sigma_{t=0} + (1-\alpha)\, \sigma_{eq} \qquad (5.11)$$

Here, 'α' ranges between 0-1 and represents the percentage increase in interfacial tension above σ_{eq}, with respect to the range of interfacial tension ($\sigma_{t=0}$ - σ_{eq}). For α = 0, the interfacial tension is settled down at the minimum (σ_{eq}), while for α = 1 it rises to the maximum ($\sigma_{t=0}$). For the sake of simplicity, both interfaces were scaled together equally.

It was found that for $\alpha=0.4$ (40% increase in interfacial tensions from equilibrium values), the drop size predictions adequately matched the experimental data for all the range of

Q_m data rather well, but more importantly, the trend of the predictions also improved to match that of the data (Figure 5.8, $\alpha=0.4$).

Interestingly, the model predictions also fit the experimental data in the 'leaky core-shell' region. This is not surprising as we measured the average leakage time was relatively short (~10% of the total time of drop formation).This reflects a ~3.5% error in the drop diameter, which is close to the experimental errors (~2.5%). The simple analysis presented here is just to indicate the importance of dynamic interfacial tension in elucidation of drop formation in microfluidics.

5.5.3. Dimensionless analysis and shell volume

To analyse the contribution of kinetic and buoyancy forces towards the detachment of the core-shell drop in the absence and presence of surfactants, we present a simple dimensionless analysis, which is similar to the analysis shown for the single drop formation study in a quiescent continuous phase, as discussed in Chapter 4 (4.5.4) . Two dimensionless parameters, Bond number (*Bo*) and Weber number (*We*), which represent the strength of kinetic and buoyancy force, respectively, are defined strictly based on Equation 5.4, as shown below.

$$We + Bo = 1.0 \tag{5.12}$$

Weber and Bond numbers are defined as follows.

$$\mathrm{We} = \frac{F_{ki}+F_{km}}{F_\sigma} \tag{5.13}$$

$$\mathrm{Bo} = \frac{\Delta\rho\ g\ Vm}{F_\sigma} \tag{5.14}$$

Given the negligible magnitude of drag force due to the quiescent continuous phase, the Capillary number, which represents the strength of drag force ($Ca = F_d / F_\sigma$), is not considered in this analysis.

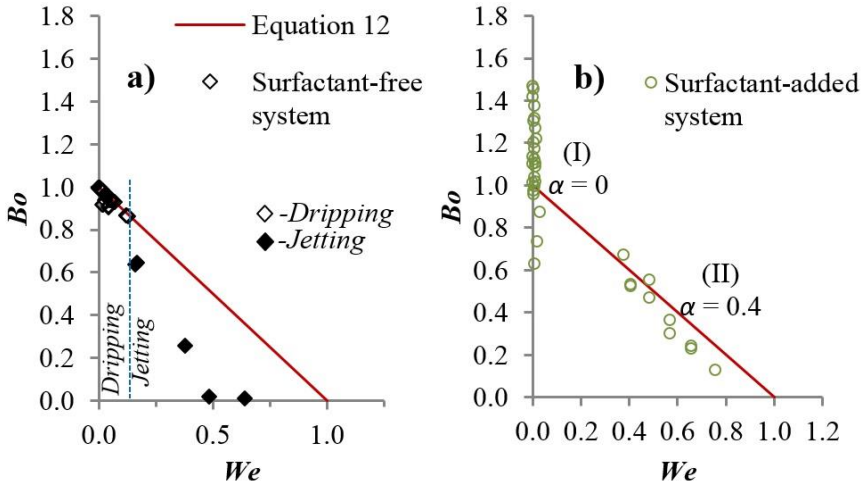

Figure 5.9 Bond number (*Bo*) versus Weber Number (*We*) for a) surfactant-free and for b) surfactant-added system explored for core-shell drop formation in a quiescent outer phase. The empty and filled symbols stand for drops formed in dripping and jetting regimes of the main drop, respectively. For the surfactant-added system, the points for leaky core-shell drops have been excluded. The drops formed in jetting regime in the presence of surfactants were also ignored due an extremely limited feasible regime, as shown in Figure 5.3b.

Figure 5.9a shows the Weber Number versus Bond Number for the experimental drop size data in the surfactant-free system. We observe that for the dripping regime in the surfactant-free system, the data points fall strictly on the line described by Equation 5.12, which validates the model. It can also be seen that the deviation from the line begins at $We \sim 0.15$, which marks the onset of jetting, where Equation 5.12 is not valid anymore. This is very similar to the observations made earlier for single drop formation in a buoyancy-driven system in Chapter 4 (4.5.4). These observations suggest that the deviation from $We + Bo = 1.0$ can be used as a reliable method to predict the onset of jetting in buoyancy-driven systems for single and core-shell drops.

Figure 5.9b shows the *We* v/s *Bo* line for the surfactant-added system. The drops formed in the leaky-core shell regions have been excluded. The data points for the dripping mode are split into two clusters. The first cluster (with $\alpha = 0$) is in the region of high Bond Number (~1.0 ± 0.4) and low Weber Number (~ 0.01), corresponding to the drops formed

at low Q_i (region I, Figure 5.3b). This indicates that the drops formed in this region are buoyancy-driven. A value greater than 1.0 obtained for the Bond number data points in the presence of surfactants, as shown in Figure 5.9b, indicates that the assumption of achieving the equilibrium interfacial tension (i.e., $\alpha = 0$) is not strictly correct even for a slow dynamic system such as those in region I. The second cluster (predicted with dynamic interfacial effect $\alpha = 0.4$), which corresponds to the drops formed at high Q_i (region II, Figure 5.3b), can be represented by $We + Bo \approx 1.0 \pm 0.1$. A high Weber Number (~0.4-0.8) in the dripping region suggests that the drop formation at high Q_i in the presence of surfactant is dominated by the kinetic force of the inner phase and only assisted by the buoyancy. At high interfacial tension (surfactant-free case), where the attaching forces are large, the kinetic forces are too small to balance Equation 5.4. As a result the balance can only be met by the time that shell drops have grown significantly (increased buoyance force). However, at low interfacial tension (the static $\sigma_{i\text{-}m}$ falls by 4 times, from 49.6 mN/m to 13 mN/m, and $\sigma_{m\text{-}o}$ by 10 times, from 49.6 mN/m to 4 mN/m in the presence of surfactants), the attaching forces are so small that can be overcome by the kinetic forces, while only assisted by the buoyancy force. Thus, the buoyancy completely dominates the drop detachment (in dripping regime) in surfactant-free system, while it remains considerably less significant in the presence of surfactants, especially at high Q_i. This is significantly different from what was earlier observed for a single drop formation in a similar system, where the buoyancy force dominated the drop rupture during the dripping mode regardless of surfactants [Chapter 4 (4.5.2)].

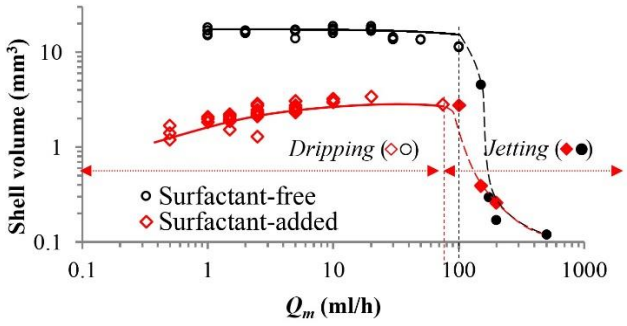

Figure 5.10 Shell volume (V_m) variation with middle phase flow rate (Q_m) for surfactant-free and surfactant-added system. The solid line shows the prediction of shell volume for surfactant-free system using Equation **5.6**. The solid lines represent the lines of best fit within dripping regime. The vertical lines represent the transition to jetting regime. The open (◇ ○) and closed symbols (◆ ●) represent the *dripping* and *jetting* of the overall drop respectively.

The magnitude of the buoyancy force acting on drops can be correlated with the shell (oil) volume of drops. Figure 5.10 shows that the shell volume (V_m) remains constant with Q_m in the absence of surfactants and in the dripping regime, where the buoyancy force is dominant. The shell volume reduces with increasing Q_m in the jetting regime, because of the sharp reduction in drop size, and becomes increasing independent of the surfactant concentrations at high Q_m. These observations are in agreement with our previous study on simple oil drop formation in a buoyancy-driven system [Chapter 4 (4.5.1)].

In the presence of surfactants, however, the shell volume increased with Q_m because of increasing effective interfacial tension (Figure 5.10). We think this is the reason for the predicted drop sizes in region I, calculated based on the equilibrium interfacial tensions and shown in Figure 5.8a (inset), not to be strictly accurate. We observed the same phenomenon in buoyancy driven formation of simple drops, even though the increase in drop size with Q was minor for the reasons explained in Chapter 4 (4.5.5).

Microfluidic systems are favoured for their capability to form and solidify drops one at a time and on the move, therefore shelf stability of such drops should not be of main

concern. However, drops formed with large cores in the absence of surfactants showed extreme instability, manifested by an instant exit of the internal core. All other drops showed sufficient stability for on-the-fly or post-processing, reaching around 5 min in the presence of low amount of surfactants as reported in this work, to several hours when ultrathin core-shell drops are formed using a larger quantity of surfactants, as shown later in Chapter 6.

5.6. CONCLUSION

A non-confined microfluidic approach for producing millimetric core-shell drops with only inner and middle phase flows was introduced. The drop formation was studied in the absence and presence of surfactants in the middle and outer phases. Millimetre-sized core-shell drops were produced under the influence of gravity, with a wide range of shell thickness (t ~ 30-1000 μm), which are difficult to obtain via conventional confined microfluidic devices.

The force-balance model developed for the prediction of single drop sizes [] was extended to the core-shell drops. The model was validated against a surfactant-free system, which avoided the uncertainties associated with the values of actual interfacial tension. For systems containing surfactants, a correction factor was introduced to the model to account for the deviation of the interfacial tension values from their equilibrium values.

While the use of surfactants is essential to render stability to the drops, they restricted the flow conditions under which core-shell drops could be formed. In the surfactant-free system, the onset of jetting for a core-shell drop formation occurred at Bo ~ 0.85 (as compared to We ~ 0.15) indicating a significant contribution of buoyancy force even at the beginning of jetting. This was similar to the observations made for a single drop formation in a similar buoyancy-driven system. In the presence of surfactants, drop formation under dripping condition was extended to We ~ 0.8. This led to the reduction of the oil-shell thickness or shell volume significantly, thereby decreasing the significance of buoyancy force at high Q_i, where kinetic force took over. This understanding is exploited to produce drops with ultra-thin shelled drops in a quiescent continuous phase, which is presented in Chapter 6.

Chapter 6 Large Ultrathin Shelled Drops Produced via Non-Confined Microfluidics[‡]

6.1. ABSTRACT

We present a facile approach for producing large and monodisperse core-shell drops with ultra-thin shells using a single-step process. A biphasic compound jet is introduced into a quiescent third (outer) phase that ruptures to form core-shell drops. Ultra-thin shelled drops could only be produced within a certain range of surfactant concentrations and flow rates, highlighting the effect of interfacial tension in engulfing the core in a thin shell. An increase in surfactant concentrations initially resulted in drops with thinner shells. However, the drops with thinnest shells were obtained at an optimum surfactant concentration, and a further increase in the surfactant concentrations increased the shell thickness. Highly monodisperse (coefficient of variation smaller than 3%) core-shell drops with diameter of ~200 μm - 2 mm with shell thickness as small as ~2 μm were produced. The resulting drops were stable enough to undergo polymerisation and produce ultra-thin shelled capsules.

[‡] Chaurasia, A.S., Josephides, D.N. and Sajjadi, S., 2015. Large Ultrathin Shelled Drops Produced via Non-Confined Microfluidics. Chemphyschem, 16(2), pp. 403-411.

6.2. INTRODUCTION

Core-shell droplets with ultra-thin shells can be used for producing particles with tailored features for encapsulation of biomaterials such as living cells [112,113], and the controlled release of its core content [30]. Ultra-thin shelled millimetre-sized core-shell drops are particularly useful in biotechnological fields for cell manipulation [1] and encapsulation [98,99], such as that of living cells [83]. On the other hand, capsules with ultra-thin shells mimic various naturally occurring thin-walled structures, such as viral capsids [114,115,116] and red blood cells [117], and could be used as a model system for fundamental study of their mechanical properties such as elasticity, thermal/osmotic collapse and indentation effect on the shells [118]. Ultra-thin shelled drops can also be used for preparation of capsules, via polymerization reactions, for direct measurement of osmotic strength [119]. In drug delivery systems utilising core-shell encapsulates where the drug is within the core, thin shells are preferable over thick shells as it can impart greater stability to the core-shell structure [60], and could also be useful to facilitate a high release rate [30]. In such cases shell permeability could be altered via appropriate material selections to tune release profiles rather than shell thickness [29]. Inverse ultra-thin drops have also been found as an innovative way to manipulate and transport oil drops, engulfed in a thin layer of water, in an oil continuous phase [82].

Conventional two-step emulsification methods to produce core-shell drops lack precision. A microfluidic approach to produce such structures provides high accuracy and precision as emulsions are formed on a drop-by-drop basis, giving high control over size, shell thickness [25,101] and morphology [120]. Reports on the formation of core-shell drops with ultra-thin shells are scarce. However, Kim et al. [60] demonstrated the formation of such structures (both O/W/O and W/O/W) using a 3D glass capillary-based microfluidic

device. The two drop formation mechanisms, *dripping* and *jetting*, were explained in terms of the flow rates. It was shown that a biphasic flow could be created inside the outer capillary, by taking advantage of surface affinities of the assembled micro-capillaries, which were ruptured to drops at the tip. A two-step co-flow approach in a 2D PDMS device, where the core initially formed at the first junction later acquires a shell at the second junction, has also been reported by Saeki et al. for formation of drops with ultra-thin shells [100,121]. In a similar PDMS based device, Abate et al. [122] explored 'one dripping instability' and 'two dripping instabilities' of multiple emulsion formation. The 'one instability' mechanism means that the core and the overall drop detached simultaneously at the end of the compound biphasic jet, while in the 'two instabilities', the core formed prior to the detachment of the overall drop. It was claimed that the drop formation via the 'one instability' approach helped in achieving drops with thinner shells. However, in all these studies the drop sizes were restricted much below the millimetre scale due to the high drag exerted by the outer phase flow. Recently, Shao et al [105] demonstrated the preparation of millimetre-sized drops with ultra-thin shells via vertically-oriented coaxial nozzle arrangements, but again using the outer flow as the driving force for drop rupture.

Making ultra-thin shelled structures under the effect of buoyancy rather than drag, to increase the drop sizes to the millimetre scale, has not been explored so far. Also, surfactant concentrations as a means to control the shell thickness have not been investigated in the literature yet.

In this chapter, we present a facile single-step bi-phasic flow approach for the formation of highly monodisperse large ultra-thin shelled drops in the absence of drag via two different modes, dripping and jetting, with drop radii (R) of ~100 μm to 1 mm and the

shell thickness (t) ranging between 2-30 μm, using a non-confined microfluidic set-up. We show that tuning of the shell thickness by varying the surfactant concentrations is possible. For the sake of discussion in this report, we define the shell thickness of a drop as '*ultra-thin*' when the relative shell thickness (t/R) is less than ~ 0.03. We explore the conditions, in terms of surfactant concentrations and flow rates, under which drops with this minimum relative shell thickness can be achieved.

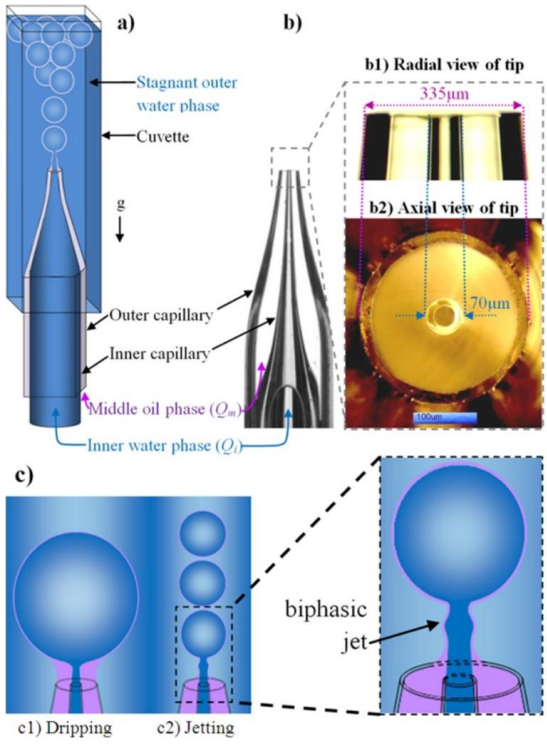

Figure 6.1 a) Setup schematic for formation of ultra-thin shelled drops in a non-confined microfluidic device with a quiescent outer phase consisting of a square and a circular capillary tube coupled together axisymmetrically. The inner and middle phases were introduced at volumetric flow rates of Q_i and Q_m, respectively. b) Image of a coupled-microcapillary set. The radial (b1) and axial (b2) views of the aligned capillary tips are shown. The outer square capillary can be seen to have turned circular after being pulled. c) Schematic representations of ultra-thin shelled drop formation in dripping (c1) and jetting (c2) regime.

Figure 6.1a-b show the schematic of the device and images of a typical coupled microcapillary set-up, while Figure 6.1c shows the schematic of an ultra-thin shelled drop formed via two dripping and jetting modes.

6.3. EXPERIMENTAL

6.3.1. Materials

Octane (98%, Sigma-Aldrich) was used as received as the middle oil phase. Sodium dodecyl sulfate (SDS) (98.5%, Sigma-Aldrich) and Span85 (Sigma-Aldrich) were used as surfactants in the outer water and middle oil phase, respectively. De-ionised water was used as the inner and outer water phase.

6.3.2. Device

The schematic of the device and images of a typical coupled microcapillary set-up has been shown in Figure 6.1a and Figure 6.1b, respectively. Two glass capillaries, circular (ID: 0.56 mm, OD: 1 mm) and square (IL: 1 mm, OL: 1.5 mm), were pulled using a pipette puller (P-1000, Sutter Instrument, Novato, USA). The tapered tips were cut to the desired sizes, coupled together and aligned axisymmetrically (Figure 6.1b). The cross-sectional shape of the outer square capillary turned circular at its tip (ID: 290 µm, OD: 335 µm) after being pulled, as shown in Figure 6.1b2, while the inner capillary tip (ID: 46 µm, OD: 70 µm) retained its circular cross-sectional shape. The concentric alignment offset between the two tips was kept below ±5 µm, which left plenty of clearances for the inner phase to remain axisymmetrically engulfed by the middle phase. The outer capillary's surfaces were selectively treated. Its inner surface was made hydrophobic by treatment with n-Octadecyltrimethoxysilane while its outer surface was made hydrophilic by plasma treatment of the surface (Femto Plasma cleaner, Diener). The tips of concentrically aligned capillaries were placed at the same level. The coupled and aligned capillaries (Figure 6.1b) were then introduced inside an open cuvette, which acted as the non-confined container for the outer water phase. The middle oil phase was pumped (Harvard pump 11 Elite) through the annular space between the outer and the inner capillary while the inner water phase was introduced through the inner capillary. The

outer water phase was kept quiescent throughout. Drop formation was recorded using a high-speed video camera (Photron FastCam Ultima APX - monochrome).

The two capillary orifices were chosen to be at the same level (Figure 6.1b1) to aid in the creation of single cored drops. We found that if the inner capillary tip is kept far behind the outer tip, it leads to the formation of drops with multiple cores [56]. In order to achieve ultra-thin shells, a biphasic flow should be created within the outer capillary [60], however, the stability of the biphasic jet could be affected by the geometry of the outer capillary. A failure to obtain a stable biphasic jet would lead to discontinuous core-shell drop formation. Placing the two tips at the same level eliminates the need to have a biphasic flow within the capillary and also leads to a higher uniformity of the droplets as the difficulties involved in matching the frequencies of the core and the overall droplet generation are avoided [105].

Two different regimes of drop formation, *dripping* and *jetting*, were observed, which has been discussed in detail in the results section. For monodisperse drops formed in the dripping regime, a minimum of 10 drops were measured to calculate the coefficient of variation (% $C_v = 100\ \sigma'/\mu'$) where, σ' is the standard deviation of the drop sizes while μ' is their mean. A minimum of 50 droplets were measured if they are formed in the jetting regime given the higher drop polydispersity observed under certain conditions.

6.4. RESULTS AND DISCUSSION

Five scenarios of surfactant concentrations in the outer (water) and middle (oil) phases were used to explore the formation of drops with ultra-thin shells, as listed in Table 6.1. In the first (surfactant-free, [S] = 0) and the second ([S] << CMC) scenario, drops with shell thickness of several hundred micrometres were obtained, which were found to be extremely unstable. Highly stable ultra-thin shelled drops were only achieved for three

scenarios using moderate to high concentrations of surfactants with extremely low values of interfacial tensions for the external interface, details of which are also listed in Table 6.1.

Figure 6.2a-c shows the flow-rate conditions (green on the map) under which core-shell drops with ultra-thin shells were formed at the three different surfactant concentrations ([S]), as described in Table 6.1 (c-e). These drops were only formed in the intermediate range of the inner-phase (Q_i) and middle-phase flow rate (Q_m) for various [S] scenarios. At low inner phase and high middle phase flow rates, drops with multiple cores formed as the inner drops detached at a higher frequency than the overall drop. Whereas at a high inner phase flow rate, the resulting inner water-phase jet simply broke through the middle phase and escaped to join the outer water phase. There was always a limited range of inner and middle phase flow rates that led to the formation of monodisperse drops with ultra-thin shells.

The range of Q_i for the formation of ultra-thin shelled drops varied for the three scenarios with little overlap. We observe from Figure 6.2a-c that the lower end of Q_i in the feasible regions becomes smaller with increasing surfactant concentrations, most likely due to the associated decrease in the dynamic interfacial tensions, even at [S] > CMC, but the range of Q_m is not affected as much. Figure 6.2d shows the domain of maximum Q_i/Q_m, which is required to achieve the minimum shell thickness.

Table 6.1 Five scenarios of surfactant concentrations ([S]) explored for core-shell drop formation are presented with equilibrium interfacial tension values at internal (σ_i) and external (σ_e) interfaces. Ultra-thin shelled drops were obtained for the last three scenarios only. Span85 and SDS were added to the middle and outer phase, respectively. The inner water phase was kept pure throughout. The CMC (Critical Micellar Concentration) values for SDS in water and Span 85 in octane were found to be 0.25 wt % and 0.8 wt %, respectively. Pendant drop method (First Ten Angstrom 200 Instrument) was used to measure interfacial tensions for first two scenarios, while for the last three scenarios (c-e) Du Nouy ring method (First Ten Angstrom 200 Instrument) was used. The σ_e values were found to be extremely low for scenarios (c-e), and could not be measured, hence are assumed to be less than the resolution of the device (~ 0.1 mN/m). SDS and Span85 were always placed in the outer water and middle oil phase, respectively.

Scenario	Surfactant concentrations	σ_i (mN/m)	σ_e (mN/m)
a) Surfactant-Free ([S] = 0)	0.00 wt% SDS 0.00 wt% Span85	49.6	49.6
b) Low surf. conc. ([S] << CMC)	0.10 wt% SDS 0.10 wt% Span85	13.0	4.0
c) Below CMC ([S] < CMC)	0.20 wt% SDS 0.40 wt% Span85	2.9	< 0.1
d) At CMC ([S] = CMC)	0.25 wt% SDS 0.80 wt% Span85	1.9	< 0.1
e) Above CMC ([S] > CMC)	0.50 wt% SDS 1.60 wt% Span85	1.8	< 0.1

6.4.1. Phase maps

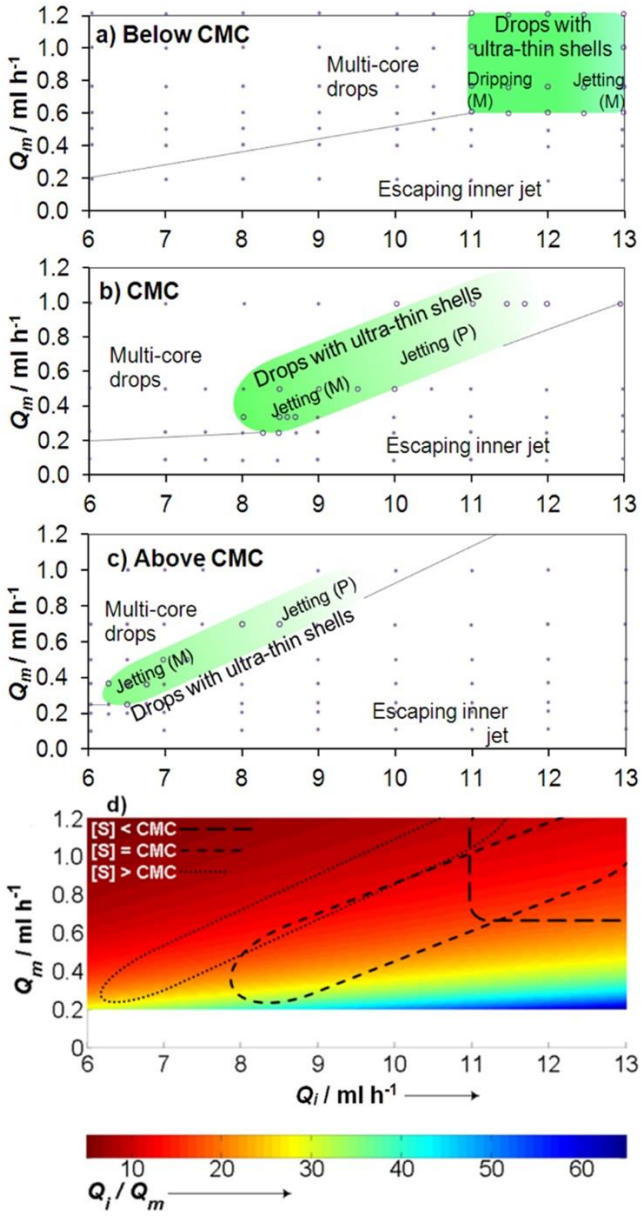

Figure 6.2 Phase maps for obtaining core-shell drops having ultra-thin shells at different surfactant scenarios a) below CMC; [S]<CMC , b) at CMC; [S]=CMC, and c) above CMC; [S]>CMC. (M: Monodisperse, P: Polydisperse drop formation region). The green regions (in a-c only) represent conditions where highly monodisperse drops were obtained, while the lighter green regions reflect the increase in polydispersity. The empty circles indicate the experimental data points where ultra-thin shelled drops were obtained, while the dots indicate the conditions which did not result in such droplets. d) Superimposed phase maps (a,b,c) highlighted with the intensity of Q_i/Q_m indicating that the highest inner-to-middle phase flow rate ratio (Q_i/Q_m) was feasible at [S] = CMC.

Increasing the surfactant concentrations transformed the rather broad feasible region for [S] < CMC, where the drops could be created by altering just one variable, to a narrow region for [S] > CMC. This implies that it would be relatively easy to produce a wide range of shell sizes at [S] < CMC by varying only one flow rate while keeping the other one fixed, whereas drop size alteration at higher surfactant concentrations could only be carried out by varying Q_i and Q_m simultaneously.

6.4.2. Regimes of drop formation

Core-shell drops with ultra-thin shells were formed under two regimes, *dripping* and *jetting*. The schematics for these mechanisms have been shown earlier in Figure 6.1c, while the time evolutions of one such drop formed via these two modes are shown in Figure 6.3a. Figure 6.3a1 illustrates the formation of a drop in the dripping mode at [S] < CMC. It is clearly seen that the drop grows at the tip (images i-v) while the neck undergoes elongation (vi) just before detachment (vii). The dripping regime is restricted to the case where the surfactant concentrations are below CMC so that the effective interfacial tension is sufficiently high to allow drops to adhere to the tip more strongly.

Ultra-thin shelled drops under the jetting regime could be produced in all three cases ([S] < CMC, = CMC and > CMC). Figure 6.3a2 shows the formation of a drop where both water and oil phases are jetting throughout drop formation. The inner phase jets due to its high kinetic force. A compound biphasic jet is created when the middle phase is entrained by the inner phase. This jet widens only slightly as it moves away from the tip. The jet interface ruptures, due to reduction in the jet velocity downstream, which causes the eventual detachment of the drop at a fixed distance from the tip.

Jetting during core-shell drop formation in a microfluidic device is often induced by increasing the outer phase flow rate. However, in the system under study, as the outer

phase is kept quiescent and the low velocity of the middle phase to obtain ultra-thin shells, the transition from dripping to jetting regime is caused by the increase in the inner phase velocity. Given the low velocity of the middle phase, which is essential to obtain ultra-thin shells in the current set up, the dripping-to-jetting transition could only be induced by increasing the inner phase flow rate, as shown in Figure 6.3b.

6.4.3. Drop size

For the sake of simplicity, only results for regions of monodisperse drop formation (C_v < 3%) for the three surfactant concentrations scenarios shown in Figure 6.2 are presented and discussed below.

The drop size decreased with increasing inner phase flow rate due to a high kinetic force, as shown in Figure 6.3b for a typical experiment. As discussed earlier, a considerable range of drop sizes was not possible to achieve in the jetting regime by varying only the inner phase flow rate. In order to achieve a wider range of drop sizes, both inner and middle flow rates were varied simultaneously, as shown in Figure 6.3c for [S] = CMC.

The nomenclature and equations to characterise core-shell drops are defined in Figure 6.4a. Assuming a concentric core-shell morphology, the shell thickness (t) was calculated as the difference between the radius of the drop (R) and the core (r), as shown in Figure 6.4a. Figure 6.4b shows drop size data obtained under the dripping and jetting regimes at different [S]. An increase in the middle phase flow rate decreased the drop size because it increased the drag on the inner drop and buoyancy on the overall drop. There is a sudden fall in drop size at a given value of Q_i for all Q_m values examined for [S] < CMC. A closer look at the video clips suggests that this is the region where transformation from dripping to jetting occurs (Figure 6.3b).

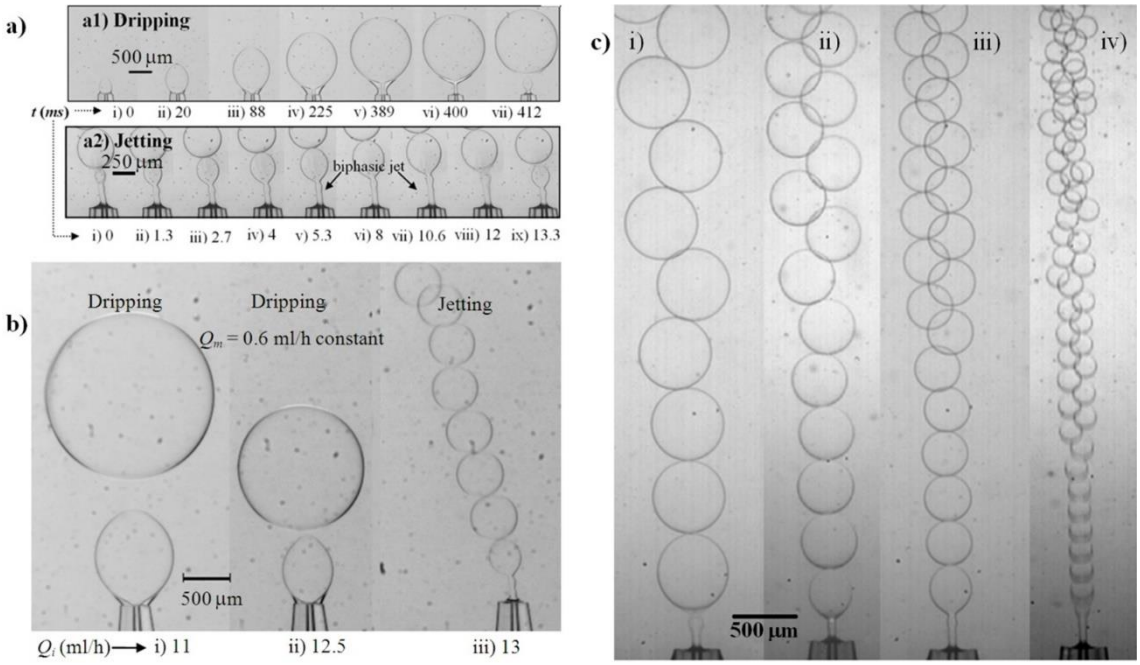

Figure 6.3 a) Time-evolution of formation of core-shell drops with ultra-thin shell in the dripping (a1: Q_m = 0.6 ml/h, Q_i = 12.25 ml/h) and jetting mode (a2: Q_m = 0.6 ml/h, Q_i = 13 ml/h) obtained at [S] < CMC. b) The transition from the dripping to jetting regime with increasing Q_i: i) 11, ii) 12.5, and iii) 13 ml/h at Q_m =0.6 ml/h ([S] < CMC). c) Reduction in drop sizes with simultaneous increase in the middle (oil) and inner (water) flow rates (all in ml/h). i) Q_m:0.25, Q_i :8.25; ii) Q_m:0.35, Q_i :8.6; iii) Q_m:0.5, Q_i :9; and iv) Q_m:1, Q_i :11.75 ml/h ([S] = CMC).

Such a sudden fall in the drop size immediately after the transition from dripping to jetting was also reported by Cramer et al. [71] for the single drops formed in a co-flow system. In that study, however, the transition to jetting regime occured due to the increased continuous phase flow, and the sudden drop size reduction was attributed to the high drag exerted by the more viscous continuous phase. Utada et al. [43,44] also discussed the importance of fluid properties for the dripping-jetting transition in a co-flowing system.

In our case, however, the outer phase is quiescent and has low viscosity (~ 1 mPa·s) which is the same as that of the dispersed phase. It should also be stressed that our observation is specific to the case of low outer interfacial tension and relatively higher inner interfacial tension. A more relevant comparison, therefore, could be against a study dealing with the

drop formation in a similar low viscosity, buoyancy-driven system where the continuous phase is stagnant, such as the system discussed in Chapter 4. In that report, we showed that, the size of the single drop decreased smoothly with the dispersed phase flow rate at the transition from the dripping to jetting regime. In fact, the sharpest increase in the drop formation frequency right after the transition point, was by a factor of ~1-2. In our current study, however, the drop formation frequency increased immediately after transiting to the jetting regime by a factor of ~10-20. The reason for such an unusually sudden fall in drop size at the transiton point could be due to the differing size of the two capillary orifices. The size of an ultra-thin shelled drop in the dripping regime depends on the outer capillary tip diameter (Figure 6.1c1, Figure 6.3a1), however, the drop size in the jetting regime, under the conditions used here (low Q_m and interfacial tension), depends on the width of the biphasic jet (Figure 6.1c2, Figure 6.3a2), which is controlled by the inner capillary tip. As the transition to the jetting regime occurs, the tip size determining the drop size falls suddenly (outer capillary ~ 4 × inner capillary). As a result, the drop size decreases correspondingly in the dripping regime. It is anticipated the drop size would fall even more sharply during the transition with decreasing inner-to-outer tip ratio.

Figure 6.4b suggests that in the jetting regime, the surfactant concentrations do not influence the achievable range of drop size significantly; however, it does affect the Q_i at which drops were formed. It can also be seen from Figure 6.4b that ultra-thin shelled drops could only be produced by lowering Q_i with increasing surfactant concentrations.

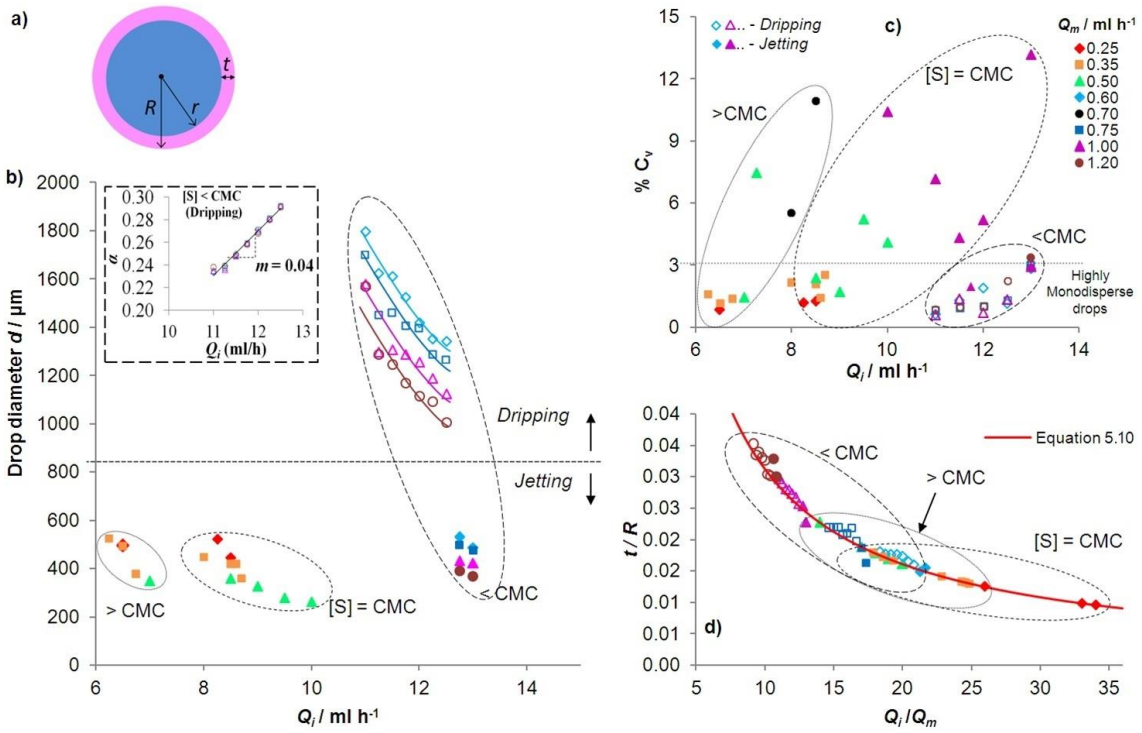

Figure 6.4 a) Schematic of a concentric core-shell structure. The shell thickness t is defined as the difference between the overall drop radius (R) and the core radius (r). b) Change in drop sizes with surfactant concentrations, Q_i and Q_m in dripping and jetting regimes. The empty symbols (◇ □...) show droplets formed under the dripping regime, while the filled symbols (◆■...) represent those formed under the jetting regime. The inset shows linear dependence of the interfacial tension scaling factor (α) on Q_i, as compared to almost no dependence on Q_m. The scaled values of σ_i and σ_e at Q_i: 11 ml/h were 13.6 and 2.8 *mN/m*, which increased to 16.4 and 3.6 *mN/m*, respectively, at Q_i = 12.5 ml/h. c) Coefficient of variation (% C_v) for drop sizes obtained at different surfactant concentrations. d) Variation in relative shell thickness (t/R) with inner-to-middle phase flow rate ratio (Q_i/Q_m). The solid line represents t/R by mass balance (Equation 5.10). The common legends are shown in (c).

It is known that the equilibrium interfacial tension reaches a constant value at [S] ≥ CMC. If the equilibrium interfacial tension is attained at [S] ≥ CMC during the time scales associated with drop rupture, lowering Q_i should result in an increase in drop size due to the reduced kinetic force, an effect which is observed in Figure 6.4b for any set of data at a given Q_m. However, we see from the same figure that the range of drop sizes obtained at the lower Q_i for [S] > CMC remains fairly similar to those obtained at higher Q_i for [S]

= CMC. We think this happens because the effective (dynamic) interfacial tension at [S] > CMC (which is twice the concentration of CMC) is lower than that at CMC. Therefore, for [S] > CMC, the lower kinetic force caused by decreasing Q_i is compensated by the decrease in the interfacial force (i.e. lower dynamic interfacial tension), leaving the size of drops almost unaffected.

The primary reason for the difference in effective interfacial tension during droplet rupture is probably due to the high rate of new interfaces being formed compared to the rate of diffusion of surfactants to the interfaces. An increase of surfactant concentrations would therefore result in higher diffusion rates to the interface therefore reducing the dynamic interfacial tension effect. This is a familiar phenomenon in microfluidic devices where the deviation from equilibrium interfacial tension becomes predominant at high flow rates, even above CMC concentrations [50,54]. This is also the reason that core-shell drops for [S] > CMC scenario were formed at lower Q_i than those at [S] = CMC. To further explore the effect of inner and middle phase velocities on the dynamic interfacial tension, the drop size data was fed into a force balance model and validated for drops formed in dripping regime.

For each drop size in the dripping regime (for 'below CMC case' only), a scaling factor α was used to scale both inner and outer interfacial tensions together linearly (for simplicity sake), using the relationship $\sigma = \alpha\ \sigma_{t=0} + (1-\alpha)\ \sigma_{eq}$. The α varied between its limits ($\sigma_{eq} - \sigma_{t=0}$), where σ_{eq} is the equilibrium interfacial tension and $\sigma_{t=0}$ is the interfacial tension when no surfactant belonging to the middle phase is present at the interface. The inner interfacial tension was assumed to vary between its equilibrium value (2.9 mN/m) and the value for a surfactant-free interface (49.6 mN/m). The range for the outer interfacial tension was kept between its equilibrium value (0.1 mN/m) and an upper limit

of 12 mN/m, where the latter corresponds to the equilibrium interfacial tension of SDS surfactant in the stagnant outer phase (we assume that SDS adsorption is fast compared to the time of drop formation). $\alpha = 0$ indicates that the interfacial tension is settled down at the minimum (σ_{eq}), while $\alpha = 1$ indicates it has risen to the maximum ($\sigma_{t=0}$). Calculations clearly indicate that the equilibrium interfacial tensions ($\alpha = 0$) fail to predict the size data by a large margin. By varying the scaling factor α (between 0-1), the inner and middle interfacial tension values were scaled to a value which satisfied the force balance model for the known drop size data. The variation in α with respect to Q_i and Q_m for drops formed in the dripping mode are shown in the inset of Figure 6.4b, which clearly confirms that the dynamic interfacial tension was dictated by the (high) inner phase flow rate, but was independent of the (low) middle phase flow rate.

For drop formation in a non-confined buoyancy driven system, the significance of buoyancy force in the jetting regime has been shown earlier [Chapter 4 (4.5.2)], where the Bond number (*Bo* = Buoyancy force/Interfacial tension force) was found to be as high as 85% of the total disruptive force (Bond plus Weber number) at the onset of jetting. This means that the buoyancy force was still the largest disruptive force contributing to the jet formation. For an ultra-thin shelled drop formed in a similar non-confined system, however, the buoyancy force becomes negligible (*Bo* < 10% of the total disruptive forces for all cases) due to the presence of very small amount of oil and a high velocity of the inner phase. This suggests that the vertical orientation of the device is not a pre-requisite for the formation of large ultra-thin shelled drops, but facilitates drops collection and transportation in the absence of an outer phase flow.

6.4.4. Drop uniformity

Another important finding is that the uniformity of resulting ultra-thin shelled drops is maximum at the lowest flow rates used within the feasible regions (**Figure 6.2**, dark green), and gradually deteriorates with increasing flow rates (light green). The dripping and jetting modes of drop formation have been observed in confined microfluidic approaches for making core-shell drops [60], though not explored in terms of drop uniformity. Here we attempt to elaborate on the reason for uniformity of the drops that can be achieved by the current set up. In a two-phase co-flow system, when the dispersed phase velocity is much higher than the continuous phase velocity at the capillary tip, the jet widens [123]. Similar widening jets for core-shell drops were also observed by Utada et al. [25]. However, in that case the jet widens due to the expansion of the tapered outer capillary (where the jet forms), thus reducing the jet velocity. It was hypothesized that the instabilities induced on the jet, due to its widening, fixed the location of drop rupture and thereby increasing drop monodispersity [25]. In our case, the reduction in velocity is even sharper as the outer phase is completely stagnant. We think this helps further in fixing the location of rupture of the biphasic jet, thus leading to the formation of highly monodisperse drops.

Figure 6.4c shows the percentage coefficient of variation (C_v) in the drops obtained at different Q_i and Q_m for different scenarios. To be able to differentiate between monodisperse and polydisperse droplets, we assumed that the droplets with $C_v < 3.0\%$ in this study could be considered as highly monodispersed droplets. We find from this figure that for [S] < CMC, the C_v increased slightly but steadily as the regime of drop formation transitioned from the dripping to jetting, while always remained smaller than 3.0%,. This agrees with the literature on single drops that dripping produces more monodisperse drops

than jetting [57]. For [S] ≥ CMC, where drop formation occurred only via jetting, the C_v increased with increase in both Q_i and Q_m.

6.4.5. Shell thickness

Figure 6.4d shows the domain of relative shell thickness (t/R) variations with Q_i/Q_m for the three scenarios explored. Here, it can be seen that increasing surfactant concentrations (i.e. lowering dynamic interfacial tension) does not necessarily lead to minimum t/R. The equation for t/R (Equation 5.10) suggests that the minimum relative shell thickness should be achieved at the lowest possible inner-to-middle phase flow rate ratio (Q_i/Q_m) [60,105]. The colours on the maps, shown in Figure 6.2d, indicate the magnitude of Q_i/Q_m.

The phase map reveals that the highest Q_i/Q_m was not achieved at the highest [S], but rather at an optimum concentration; [S] = CMC. This happens because operating conditions (the phase map) under which such drops can be created change (towards smaller Q_i) with increasing [S].

Due to the ultra-thin shells produced in all three scenarios, as presented in Table 6.1, and difficulties involved in detection of the boundaries of the shells, their direct measurement was not possible. Therefore, the shell thickness was calculated using Equation 5.10 for any drop with a given radius of R. However, this procedure for shell thickness calculation was also validated by two other methods. In one method, we measured the radius of an ultra-thin shelled drop before (R_b) and after its rupture to form an oil drop (R_a), as shown in Figure 6.5a, and calculated the shell thickness (t) using the relationship[60],

$$t = R_b - (R_b^3 - R_a^3)^{1/3} \tag{6.1}$$

As an example, for the ultra-thin shelled drop highlighted in Figure 6.5a, the shell thickness estimation using Equation 6.1 gave t = 4.06 µm, which is very close to that obtained using Equation 5.10, where t = 3.98 µm.

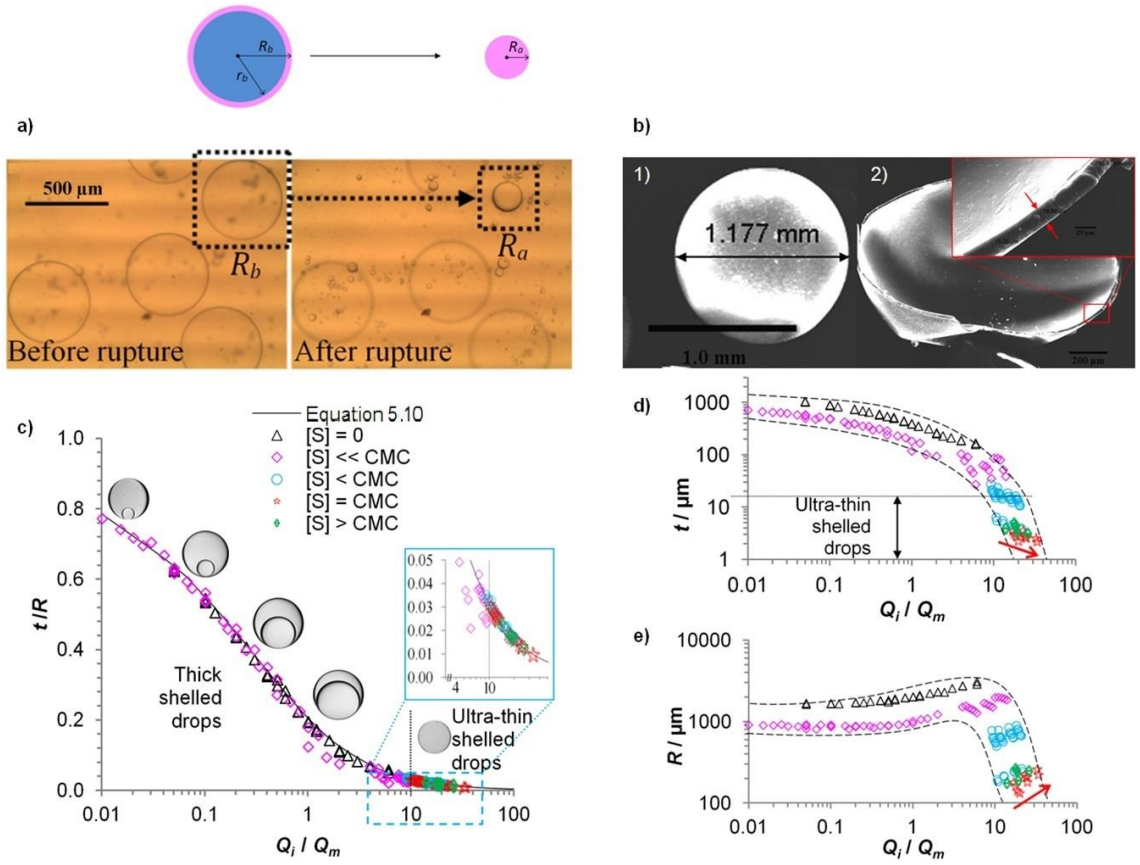

Figure 6.5 a) A schematic depicting the geometry of a core-shell drop before and after its rupture. The optical microscopic image shows an ultra-thin shelled drop before and after its rupture, which can be used to estimate the shell thickness according to Equation 6.1. b) Scanning Electron Microscopic image showing a millimetre-sized ultra-thin shelled capsule while it is intact (b1), and after it is broken (b2), with the inset showing the shell thickness after its polymerization. c) The t/R versus Q_i/Q_m curve for the thick-shelled and ultra-thin shelled drops together, showing its variation with all five surfactant concentrations scenarios explored (see Table 6.1 for the definitions of scenarios). The solid black line represents Equation 5.10. d) The absolute shell thickness t versus Q_i/Q_m. The dashed lines represent the fitted boundary lines. e) The drop radius R versus Q_i/Q_m. The common legends for (c), (d) and (e) are shown in (c).

Another indirect way of measuring the shell thickness is transforming the shell, via polymerisation, to a solid material that can be assessed by scanning electron microscopy (SEM). Furthermore, ultra-thin shelled capsules, as described in the introduction, are one of the main applications of ultra-thin shelled drops. In order to demonstrate that, we produced droplets with the shell phase consisting of Butyl methacrylate monomer (Sigma

Aldrich), 10 wt% Ethylene glycol dimethacrylate (Sigma Aldrich) as cross linker, 4 wt% Irgacure 907 (BASF) as photo initiator, 5 wt% Span80 (Sigma Aldrich) as surfactant, and 5 wt% Poly(ethylene glycol)-block-poly(propylene glycol)-block-poly(ethylene glycol) with average M_w ~ 2800 (Sigma Aldrich) as thickener. The outer water phase contained 1 wt% PVA (M_w = 85000-124000, degree of hydrolysis = 87% - 89%, Sigma Aldrich) as a stabiliser, while the inner water phase was kept pure. The shells of the droplets thus produced were polymerised by exposing them to a UV source (Honle, bluepoint 2 easycure) for ten minutes, while being stirred.

Figure 6.5b1 shows a SEM image of one such capsule obtained after the polymerisation, while Figure 6.5b2 shows the capsule cut into half, and the inset image reveals its shell thickness. The calculated shell thickness of the original drop was 17.42 µm, which is close to the solid shell thickness of 16.39 µm measured by SEM. The difference between the shell thicknesses obtained by the two methods is small, but can be attributed to the shell shrinkage during polymerisation. The polymerisation experiment also indicates that the resulting ultra-thin shelled drops are stable enough to undergo polymerisation reactions.

Using the calculated shell thickness t, and the mass conservation of the inner and middle phases, the relative shell thickness (t/R) can be correlated with the core-to-shell volume ratio (Q_i/Q_m), as given by Equation 5.10, which is represented as the solid line in Figure 6.4d. The theoretical t/R curve agrees with the experimentally obtained relative shell thickness values using the drop formation time data from video recordings.

6.4.6. Minimum shell thickness and drop size

To present in the broader context, the variations in t/R, t, and R with Q_i/Q_m for a wide range of surfactant concentrations are shown in Figure 6.5c, 6.5d and 6.5e, respectively.

As a general statement, core-shell drops with rather thick shells (t ~ 30 μm - 1 mm) were formed at low Q_i/Q_m (0.01-10) and surfactant concentrations ([S] = 0 or << CMC). The size of drops increased with decreasing surfactant concentrations. At moderate to high concentrations of surfactants, which allowed low effective interfacial tensions to be achieved, core-shell drops with relative shell thickness of t/R < 0.03 and absolute thickness of t ~ 2-30 μm were obtained at Q_i/Q_m ~ 10-35 (Figure 6.5c inset). The minimum relative (t/R), absolute (t) shell thickness, and drop size (R) was obtained at an optimum surfactant concentration (Figure 6.5c-e), which was [S] = CMC. Within this optimum scenario, however, there exists a trade-off between achieving either a minimum shell thickness or drop size. This is because drops with the minimum shell thickness were obtained at the lowest Q_m and the corresponding highest Q_i. A high Q_i reduces the drop size due to the high kinetic force, but a low Q_m counterbalances that effect by increasing the drop size due to a lower buoyancy force, resulting in an increase in drop size with Q_i/Q_m, as shown by the arrows in Figure 6.5d and 5e.

All materials used in this work have low viscosity (~1 mPa·s). However, several applications may demand the usage of high viscosity phases or more complex fluids, such as visco-elastic fluids [124], which could significantly alter the drop formation. Future works should be directed to exploring the effect of viscosity to provide a more comprehensive understanding of this method of ultra-thin shelled droplet production.

6.5. CONCLUSION

A facile single-step bi-phasic flow approach for formation of highly monodisperse core-shell drops having ultra-thin shells is presented. Phase maps were developed that allowed finding the conditions under which ultra-thin shelled drops can be produced. With small amounts of surfactants present in the system, giant core-shell drops having a large range

of shell thickness can be achieved. The required operating conditions, in terms of flow rates, to achieve ultra-thin shelled drops significantly changed with alteration in [S]. The shell thickness could significantly be reduced by lowering the interfacial tension of the outer interface. However, the phase map revealed that the drops with minimum drop size (R), absolute (t) and relative shell thickness (t/R) were achieved at an optimum surfactant concentration. Finally, the shell-thickness curves (Figure 6.5c-e) suggest that drops with ultra-thin shells can be obtained when the inner phase flow rate becomes at least approximately ten times the middle phase flow rate.

Chapter 7 Properties and Characterisation of Oil-Encapsulated Alginate Microfibres[§]

7.1. ABSTRACT

A unified microfluidic approach is presented for flexible fabrication of oil-encapsulated calcium alginate microfibers, where the oil phase was directly formed and encapsulated into the gelling alginate fiber. This allowed the adjustable tuning of the encapsulate geometry ranging from spherical to prolate ellipsoid, plug-like and tubular shapes. The segmented oil entities could also be selectively grouped by controlling the surface affinity of the oil-injecting inner capillary. A force-balance model was also introduced to predict the size of spherical encapsulates, which was validated against a non-gelling system. The fibers were also characterized for their spillage ratio, surface roughness and mechanical strength to provide a wide variety of information about these compound fibers. Tubular fibers had the highest oil volume, but were also most prone to accidental oil-core loss. A 2D mathematical reconstruction of the fiber's surface revealed that fibers having spherical and ellipsoid encapsulates enjoyed the highest surface roughness, indicating good fiber-interlocking properties. Tubular fibers endured maximum tensile force before failure, compared to fibers with other encapsulate geometries at fixed alginate phase ratio (ϕ_{alg}). Fibers with increased ϕ_{alg} withstood a higher tensile force. However, the strength of fibers reduced if the increase in ϕ_{alg} altered the encapsulate geometry from tubular to discrete oil segments. Tubular fibers also underwent maximum elastic and plastic deformation prior to failure.

[§] Submitted to *ACS Applied Materials & Interfaces* journal for publication.

7.2. INTRODUCTION

Sodium alginate is a naturally-occurring and biocompatible water-soluble material which form hydrogels when cross-linked with calcium ions. Calcium alginates are widely used for various biomedical and pharmaceutical applications. In particular, calcium alginate in the form of microfibers has found increasing biomedical applications such as in wound healing [125,126,127], cell encapsulation and tissue engineering [128,129]. These fibers are usually produced via wet spinning technique [130], in which an aqueous sodium alginate solution is injected into an aqueous calcium chloride bath, where the jet of alginate solution is gelled by the Ca^{2+} ions from the bath solution to convert it into a fibrous structure.

The properties of alginate microfibers can be further enhanced by embedding different inorganic additives in the hydrogel matrix of the fiber, such as silver compounds [131,132,133]. Alternatively, different aqueous as well as non-aqueous solutions can also be encapsulated within the fiber to increase its functionalities. For example, an aqueous medium containing proteins and cell dispersions can be loaded within alginate fibers in a tubular fashion, which is useful for tissue engineering applications, such as mimicking and reconstruction of fibre-shaped functional tissues [62]. On the other hand, alginate fibers encapsulating non-aqueous phases have also shown a variety of applications [33,36,64,134], such as improved water collection ability [63], which was attributed to multiple factors including the increase in Laplace force due to curvature gradient around the encapsulated-oil nodes. In general, both encapsulation geometries, tubular and segmented, have unique advantages and applications.

However, with the current encapsulation techniques, the encapsulation geometry is severely limited by the nature of the dispersed phase used. For example, a non-aqueous

dispersed phase can only be loaded in discrete segments, while an aqueous dispersed phase is restricted to its tubular encapsulation. Furthermore, the impact of encapsulation geometry on the surface morphology, encapsulation volume, and mechanical strength of the resulting fibers have not been studied yet, all of which could strongly influence the selection criteria for a particular application.

In this chapter, we introduce a unified and flexible microfluidic technique for oil encapsulation within alginate fibers, in which the encapsulation geometry can be precisely tuned from continuous tubular to equally spaced segments, and eventually to grouped segments. This is also the first report in the literature on fabrication of the whole range of possible encapsulate geometries for oil-loaded fibers including controlled grouping. We think the detailed information presented in this work about different properties and characterization of compound oil-loaded alginate microfibers could provide useful guidelines for identifying the optimum fiber geometry for a specific application.

7.3. EXPERIMENTAL

7.3.1. Materials

Sodium alginate and calcium chloride (Sigma Aldrich) were used as received. The middle phase constituted of sodium alginate (1.0 and 4.0 wt%) in the aqueous phase, which was introduced into an aqueous bath containing 4.0 wt% calcium chloride. Octane (99%, Sigma Aldrich) was used as received as the model inner-oil encapsulated phase.

7.3.2. Device

Figure 7.1a shows a schematic of the microfluidic device used to encapsulate oil phase within the alginate fiber. Two glass capillaries, circular (ID: 0.56 mm, OD: 1 mm) and square (IL: 1 mm, OL: 1.5 mm), were pulled using a pipette puller (P-1000, Sutter

Instrument, Novato, USA).The tapered tips were cut to the desired sizes, with the inner tip (ID: 40 µm, OD: 60 µm) aligned symmetrically with the outer tip (ID: 150 µm, OD: 175 µm). Both capillaries were plasma treated (Femto Plasma Cleaner, Diener) to be hydrophilic. The oil phase was pumped (Harvard Apparatus) through the inner capillary, while the alginate phase was introduced through the interstitial spaces between the two capillaries. The outer aqueous phase containing calcium chloride was kept quiescent, in which the coaxially aligned capillary setup was introduced vertically as shown in Figure 7.1a1. The formed fibers, an example of which is shown in Figure 7.1a2, were collected at the top of the cuvette, facilitated by the buoyancy force exerted by the encapsulated oil. A high-speed video recording camera (Photron FastCam SA-5 (monochrome)) was used to record fiber formation.

7.4. RESULTS AND DISCUSSION

7.4.1. From segmented to tubular oil encapsulation

The nature of oil encapsulates within an alginate microfiber can be symmetric or asymmetric with respect to its axial direction, depending on its location within the microfiber. We first discuss fabrication of fibers with axisymmetrically loaded oil entities (Figure 7.1a2), encompassing their different possible formats. In such a case, two encapsulation configurations exist; segmented and tubular. An aqueous inner phase can be encapsulated in a tubular configuration due to extremely low interfacial tension [33]. However, a hydrophobic inner phase is usually encapsulated in discrete segments [33,36], due to the high interfacial tension at oil-water interface acting to rupture the inner phase. We present an enhanced microfluidic approach that allows the segmented and tubular oil encapsulation to develop, using a single device in which the tip of capillary carrying the

oil phase is kept at the same level as that of the outer capillary, unlike the conventional approach [33,36].

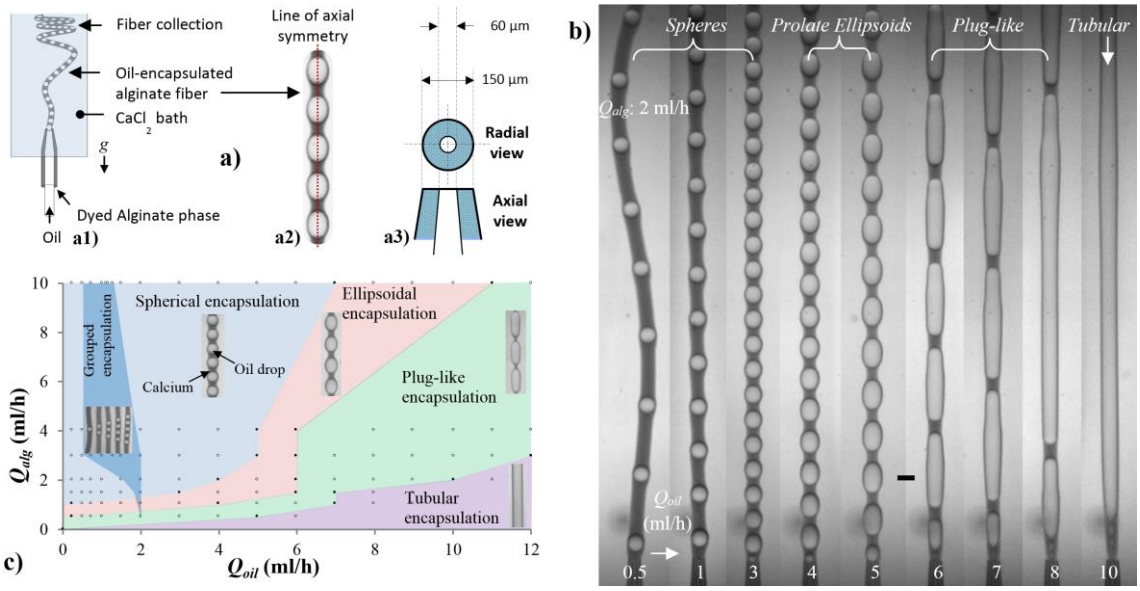

Figure 7.1 a1) A schematic of the microfluidic device used to produce oil-encapsulated alginate fiber. **a2)** An optical micrograph of an oil-embedded alginate microfiber, produced using an symmetrically aligned coaxial capillary setup **(a3)**. **b)** Variation in the shape of the oil segments encapsulated within the alginate fibers is shown. The figure shows that the nature of encapsulation can be switched between a segmented encapsulation (having spherical, ellipsoidal or plug-like shapes) and a continuous (tubular) encapsulation. The shape of discrete entities change from spherical to ellipsoidal to plug-like with increasing inner oil phase flow rate (Q_{oil}) at a given middle alginate phase flow rate (Q_{alg}: 2 ml/h), until further increase in Q_{oil} eventually leads to a tubular encapsulation of the inner phase. Scale bar: 200 µm. **c)** Phase map showing different regions of the middle-alginate phase (Q_{alg}) and inner-oil phase (Q_{oil}) flow conditions that led to diverse shapes of the encapsulated oil phase within the alginate fibers. All the circular symbols indicate the experimental data points explored, while the filled symbols indicate the data points lying at the transition boundaries between the different shapes obtained. This phase map was drawn for the middle phase with 1 wt% alginate concentration, and the outer phase having 4 wt% $CaCl_2$ concentration.

Figure 7.1b shows the evolution of fiber morphology from fibers encapsulating discrete oil segments as spheres, prolate ellipsoids (referred to as *ellipsoid* for simplicity) and plug-like to eventually a single straight tube filled up with oil, all obtained via increasing

the inner oil phase flow rate (Q_{oil}) at a constant middle alginate phase flow rate (Q_{alg}). Figure 7.1c shows the phase map for the types of oil-entity shapes encapsulated within the alginate fibers, obtained by a two-dimensional Q_{alg} versus Q_{oil} scan. At rather low Q_{oil} and high Q_{alg}, indicated by the light blue zone in the phase map, the encapsulated oil takes spherical shape because the droplet size remains small, relative to the fiber thickness. Within this region and at a fixed Q_{alg}, the droplet volume (v_{oil}) increases with $Q_{oil,}$ while maintains its spherical shape. The dark blue region, which relates to grouped oil encapsulation, is discussed later.

The volume of oil segments increases with Q_{oil}, which is characteristic of typical microfluidic drop formation mechanisms [71]. However, here the increase in oil segment volume alters its shape because of geometrical constraints imposed by the gelling shell, as seen in Figure 7.1b. At high Q_{oil}, the oil encapsulate becomes too big to be accommodated within the fiber as a spherical droplet, as a result it expands axially within the fiber (in the direction of fiber length) to form an ellipsoidal entity. Further increase in Q_{oil} only elongates the ellipsoidal segment axially within the fiber, thus leading to the formation of plug-like oil segments. When Q_{oil} is sufficiently increased, the inner phase ceases to rupture into discrete entities, thereby forming a stable tubular jet of the oil phase inside the fiber.

The sequence of morphological evolution with Q_{oil} remained the same (sphere, ellipsoid, plug-like and tubular) for all flow conditions studied. The only exception is at low Q_{alg} where it was possible to bypass the spherical and elliptical morphologies and move directly to plug-like and tubular due to low drag. Note that the tubular structures can be achieved for Q_{alg} > 4.0 ml/h too, but at a much higher Q_{oil} than explored in the map.

7.4.2. Grouping of encapsulated droplets

We discovered that the affinity of the inner glass capillary, which carries the oil phase, can affect the regular formation of oil droplets within the fiber, in a narrow range of flow conditions. This observation was exploited to activate or deactivate the grouping of oil encapsulates within the fiber in a controllable manner. A hydrophilic inner capillary facilitates the grouping of oil encapsulates having the same morphology within a narrow range of flow conditions, which is shown as a dark blue region in Figure 7.1c. The number of entities in such a group can be precisely controlled via fine alterations in the flow conditions, as shown in Figure 7.2c1. Such controlled grouping of encapsulated oil entities could be useful for local tuning of the fiber structure. It also provides defect-free bending points along the fiber, which could minimise the risk of accidental shell rupture and the associated oil-release while bending the fiber. The mechanism of grouping behaviour was found to be a result of the temporary blockage of hydrophilic inner capillary tip with the alginate phase, which was only observed at low oil phase flow rates. Once an oil droplet is formed, the capillary pressure at the tip reduces to a minimum value. At this reduced pressure, the aqueous alginate phase is able to force the oil phase to temporarily recede inside the inner capillary, to wet its inner hydrophilic surface, which is clearly seen in dye-free fibers (Figure 7.2c2).

The pressure build-up with time inside the capillary would eventually push the intruded alginate phase out of the inner capillary along with the oil phase. This expulsion of the alginate phase suddenly releases the built pressure, which results in a rapid outpour of a large volume of the oil phase, which ruptures into uniform multiple oil encapsulates under the influence of the drag force exerted by the middle phase. The upper limit of the built-up pressure increases with Q_{oil}, which increases the volume of oil being pumped out at

the instance of pressure release. This increases the number of oil entities in a group with Q_{oil}, as shown in Figure 7.2c1. At a high Q_{oil}, the alginate phase fails to push the oil in, hence it leads to a regular formation of oil encapsulates. This cycle of the build-up and release of pressure at the tip of a hydrophilic inner capillary leads to the grouped formation of the oil encapsulates.

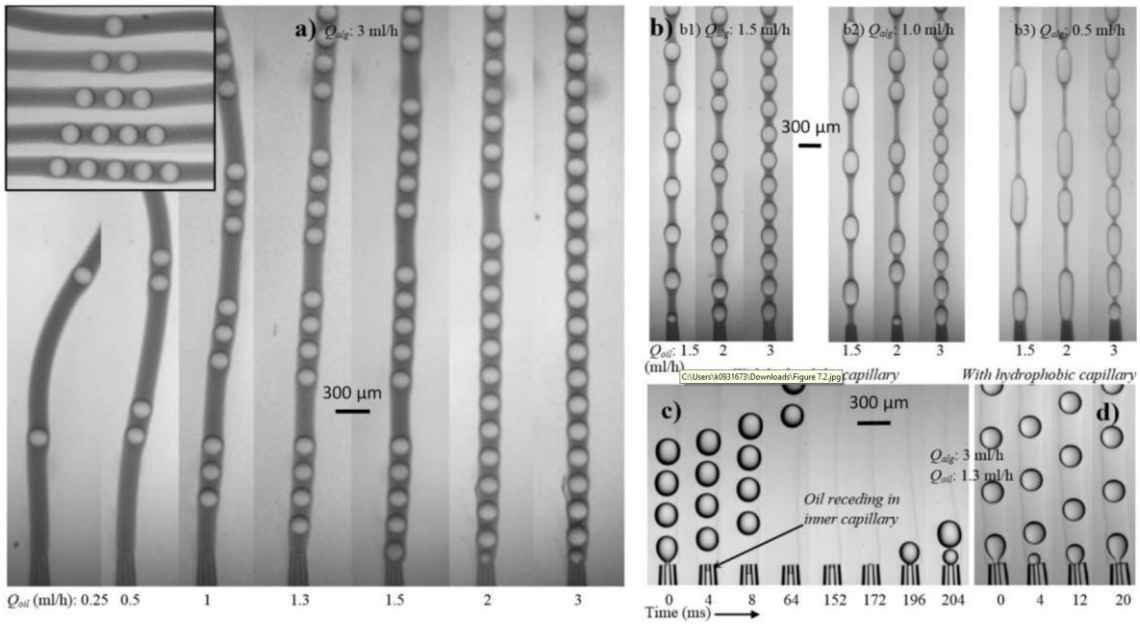

Figure 7.2 a) Precise grouping of the spherical oil droplets in the microfibers with varying Q_{oil} by employing a hydrophilic inner capillary. This grouping phenomenon can also be achieved for plug-like and ellipsoids, as shown in **(b)**. The mechanism of grouping behaviour is analysed with time-evolution images of dye-free fibers shown in **c)**, while the grouping behaviour can be muted by using a hydrophobic inner capillary (**d)**.

In order to demonstrate that this grouping phenomenon can be deactivated on demand, a new device with a hydrophobic inner capillary (having identical dimensions) was used to produce fibers under identical conditions. The grouping phenomena ceased to exist for this device, as the alginate phase did not like to wet the capillary. This prevented the receding of oil phase inside capillary, and hence eliminated the grouped formation of the oil entities. Figure 7.2d3 shows that the microfibers obtained under identical flow conditions from the device having a hydrophobic inner capillary display no grouping

behaviour. The oil entities for both grouped and ungrouped fibers were quite stable and remained inside the fibers in the hydrated state and after dehydration for several months.

7.4.3. Fine-tuning of segment shapes by varying alginate and calcium chloride concentration

In addition to flow rates, the concentrations of calcium chloride and sodium alginate, in the outer and middle phase respectively, can also regulate the shape of encapsulated entities. Figure 7.3a shows that the drops formed under the same flow rate conditions exhibit larger aspect ratio at higher $CaCl_2$ and alginate concentration.

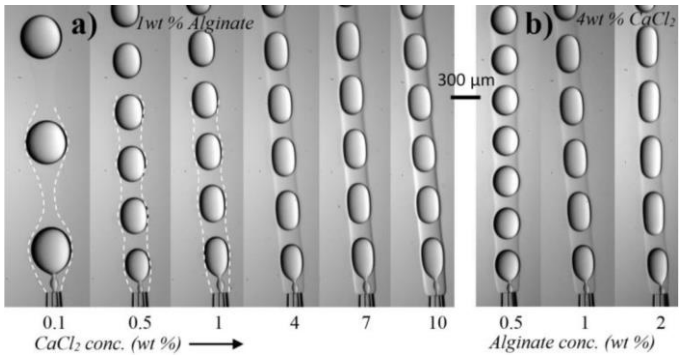

Figure 7.3 Shape variation of the encapsulated oil segments in alginate fibers by varying the concentrations of **(a)** $CaCl_2$ and **(b)** alginate in the outer and middle phase, respectively. The flow condition is fixed at Q_{alg} = 3 ml/h and Q_{oil} = 5 ml/h.

A low concentration of $CaCl_2$ leads to a weak and nearly invisible gelled interface, marked with white dashed lines in Figure 7.3a for 0.1-1.0 wt% $CaCl_2$ cases, which is prone to deformation caused by the inner oil segments which try to retain their spherical identity. On the other hand, the gelled interface at high $CaCl_2$ concentration is very prominent and visible as a result of faster gelation due to the abundance of Ca^+ ions (Figure 7.3a). A high sodium alginate and calcium chloride concentration resulted in the formation of a fast gelling non-deformable interface (Figure 7.3b), which was able to resist the radial drop expansion effectively and limit the oil segment's radial diameter to $d \approx t$ while allowing the droplet to expand axially ($D > d$).

7.4.4. Fibre morphologies and dimensions

The nomenclatures for a fiber and its encapsulated entity are shown in Figure 4a. Figure 7.4b-d show the size data for the minimum fiber thickness (t), the minor axis of oil segments d (referred to as *radial diameter*) and the fiber length between consecutive segments (z). Figure 7.4e reveals the external fiber morphology (t/T), where T is the maximum fiber thickness around the oil segment. Similarly, the geometry of encapsulated oil segments is presented in terms of d/D in Figure 7.4f. Figure 7.4g-4h convey information about the *frequency*, in terms of number of oil segments per unit length and *amplitude* of the fibers, respectively.

The minimum fiber diameter t varied only slightly with Q_{oil}, but increased considerably with Q_{alg} (Figure 7.4b), which is consistent with previous observations [33]. The segment's radial (d) and axial (D) diameters, which determine the volume of oil entities, remained constant at low Q_{oil} (Figure 7.4c and Figure 7.4f) where the segments were separated by long alginate fibers (z) in between (Figure 7.4d). At low Q_{oil}, a high Q_{alg} kept the entity small and therefore spherical (Figure 7.4f, $d/D \approx 1$) due to high drag exerted by the middle phase. The size of these spherical oil segments can be predicted by a simple force-balance model, which is explained later. A small increase in Q_{oil} in such conditions did not increase the segment volume, but increased its frequency, thereby reducing the fiber length z.

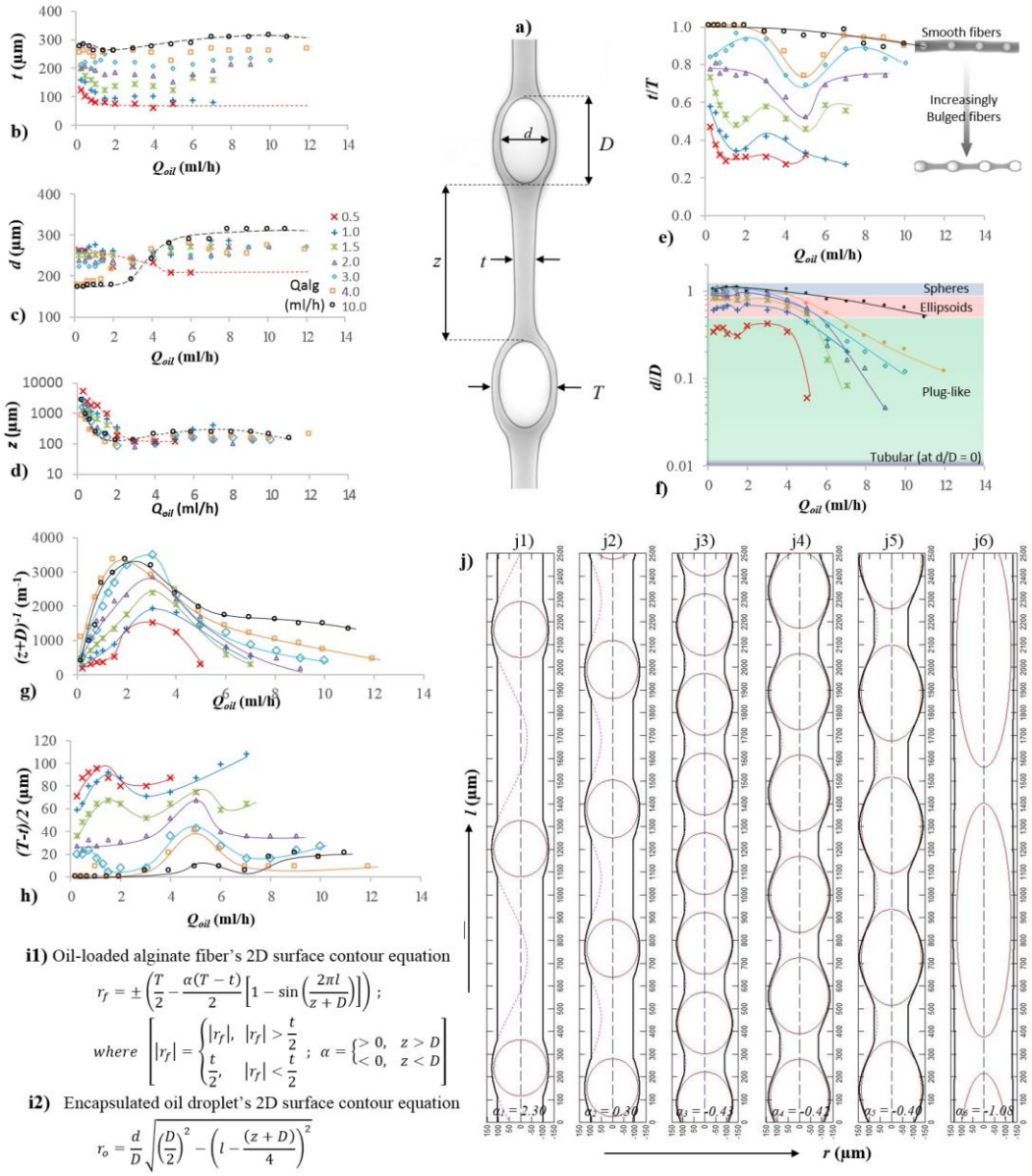

i1) Oil-loaded alginate fiber's 2D surface contour equation

$$r_f = \pm\left(\frac{T}{2} - \frac{\alpha(T-t)}{2}\left[1-\sin\left(\frac{2\pi l}{z+D}\right)\right]\right);$$

$$where \quad \left[|r_f| = \begin{cases} |r_f|, & |r_f| > \frac{t}{2} \\ \frac{t}{2}, & |r_f| < \frac{t}{2} \end{cases};\ \alpha = \begin{cases} > 0, & z > D \\ < 0, & z < D \end{cases}\right]$$

i2) Encapsulated oil droplet's 2D surface contour equation

$$r_o = \frac{d}{D}\sqrt{\left(\frac{D}{2}\right)^2 - \left(l - \frac{(z+D)}{4}\right)^2}$$

Figure 7.4 The assigned nomenclatures to various dimensions of an oil-encapsulated fiber are shown in **(a)**. Variations in the minimum fiber thickness (*t*), the radial diameter of oil segments (*d*) and the axial length of fiber segment (*z*) versus Q_{oil} are shown in **(b)**, **(c)** and **(d)** respectively. The dimensionless variations (*t*/*T* and *d*/*D*) are presented in **(e)** and **(f)** respectively, all plotted against Q_{oil} at different Q_{alg}. The red and black dashed trend lines in (b), (c) and (d) indicate the minimum and the maximum Q_{alg} respectively. The period of occurrence of oil segments in terms of distance (*z*+*D*) and their corresponding amplitudes ((*T*-*t*)/2) are shown in **(g)** and **(h)** respectively. The common legends for figures (b-h) are shown in (c). **(i)** The sinusoidal function r_f (i1), with constraints, and the elliptical function r_o (i2) are shown, which were fitted to the two-dimensional surface profiles of the fiber and the encapsulated oil segments respectively. j) Two-dimensional mathematical reconstruction (*l* versus *r*) of the surface contours of fibers shown in Figure 7.1b (Q_{oil}: 0.5ml/h - 6 ml/h), along with their oil encapsulates.

However, the volume of encapsulated entity increased with further increase in Q_{oil}, because of increased cohesive drag force on the forming droplet due to the velocity difference, which is proportional to $|Q_{oil}-Q_{alg}|$. In fact, the inner phase velocity was always higher than the middle phase velocity for all conditions explored. The segment's increased volume could not significantly bulge the gelled interface radially, as indicated by the nearly flat t/T curves for a fixed Q_{alg} (Figure 7.4e), therefore expanded itself in axial direction considerably, which increased D sharply (Figure 7.4f). The increase in D reduced z to a minimum as the oil segments were tightly packed against each other (Figure 7.4d). This increase in D also evolved their shape from spherical to ellipsoids and plug-like, until a tubular oil entity was eventually reached (Figure 7.1b and Figure 7.4f). As the shape of oil segments evolved with Q_{oil}, the fiber surface morphology changed correspondingly. Smooth fibers were obtained at high Q_{alg} due to large t (Figure 7.4e, $t/T \approx 1$), irrespective of the encapsulated segment shape. The local minima in the curves correspond to conditions where shape transition of the oil segments occurred.

The 2D surface profile of the wavy oil-loaded fibers can be conformed to a sinusoidal function, as shown in Figure 7.4i1. The encapsulated oil entities, which are the main reason for waviness of the fibers, can be expressed as an independent elliptical function for simplicity (Figure 7.4i2). Figure 7.4j illustrates the mathematical reconstruction of fiber surface profile for the oil-loaded fibers shown in Figure 7.1b (Q_{oil}: 0.5ml/h - 6 ml/h) (plotting code is given in Appendix B. The fiber frequency, $(z+D)^{-1}$, represents the number of oil segments per unit length, while the amplitude $((T-t)/2)$ stands for the maximum fiber thickness with respect to the minimum fiber thickness $t/2$. We later show how this structural model can simplify our discussion on the properties of the fibers.

7.4.5. Size estimation and analysis

A theoretical force-balance model is presented for predicting the volume of oil segments encapsulated in the alginate fiber. While the model can theoretically be extended to all types of segments, we limit our discussion to spherical oil segments (Figure 7.5a) due to the simplicity in drag force estimation. Four different forces act on an oil droplet during its formation: kinetic force (F_k), drag force (F_d), buoyancy force (F_b) and interfacial force (F_σ). Of these forces, only the interfacial force acts cohesively, which tends to keep the drop attached to the capillary tip. The expressions for these forces are presented below.

$$F_k = \underline{\rho_{oil}} \times Q_{oil} \times u_{oil} \tag{7.1}$$

$$F_\sigma = 2\pi \times r_w \times \sigma \tag{7.2}$$

$$F_b = \Delta\rho \times g \times \pi\,(d_{oil})^3 / 6 \tag{7.3}$$

$$F_d = 6\pi \times \eta_{alg} \times d_{oil}/2 \times \Delta v \tag{7.4}$$

where $\Delta v = v_m - v_d$ with v_m being as the average middle alginate phase velocity at tip cross section, and v_d as the velocity of the expanding drop. The v_d is calculated as the instantaneous velocity of the leading droplet interface at the instance of drop detachment, which can be expressed as $\frac{d(d_{oil})}{dt}$.

The resulting force balance equation can be expressed as,

$$F_\sigma = F_k + F_b + F_d \tag{7.5}$$

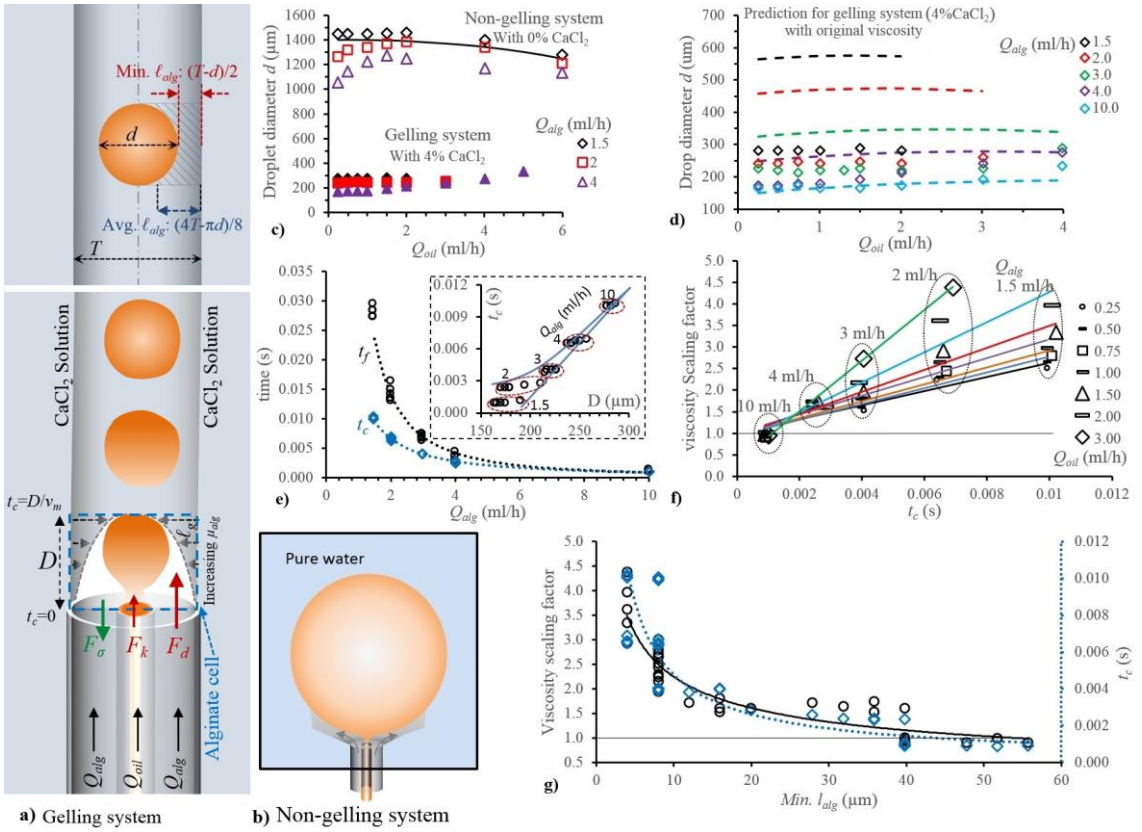

Figure 7.5 **a)** A schematic showing the force balance applied to the forming oil drop inside a gelling alginate fiber. The minimum ($diff_{min}$) and the average ($diff_{avg}$) diffusion distances are also illustrated. **b)** A schematic showing the formation of large oil drops in the absence of $CaCl_2$ in the outer aqueous phase. **c)** The graph shows the effect of gelation of alginate phase on the oil drop size, where the droplets formed at 0% $CaCl_2$ (Non-gelling system) and 4.0 % $CaCl_2$ (gelling system) are compared. The solid black line shows the drop size predictions for a non-gelling system when the drag exerted by the middle phase flow was completely neglected. **d)** Drop size predictions for a gelling system using original viscosity value. **e)** The comparison of characteristic time (t_c) and the drop formation time (t_f) plotted against the middle alginate phase flow rate (Q_{alg},). **f)** The reverse-calculated viscosity scaling factors using the model illustrated in (a) are plotted against the characteristic time (t_c) for different Q_{oil} and Q_{alg}. **g)** The viscosity scaling factor (primary axis) and the characteristic time (secondary axis) show a similar correlation when plotted against the minimum alginate shell thickness (l_{min}).

Equation 5 was solved iteratively for d_{oil}. We have previously used a similar model to predict the droplet size in a buoyancy assisted co-flow systems, as presented in Chapter 5. However, the significance of the current system is that the viscosity of alginate phase

varies with time, which is hard to predict. In order to validate the model, we conducted a number of runs in the absence of $CaCl_2$ in the outer phase (i.e., non-gelling system). Figure 7.5a-5b show the schematics for drop formation in gelling and non-gelling systems. The impact of gelation on the size of oil segments is illustrated in Figure 7.5b, which compares the droplet sizes obtained for the gelling system (with 4.0 wt% $CaCl_2$) against those for a non-gelling system (with 0 wt% $CaCl_2$). There was a significant difference between the scales of drag forces acting on drops in these two cases. In the absence of gelation, the middle alginate phase expanded around the forming oil droplet and mixed into the outer aqueous phase, thereby minimizing the drag exerted on the droplet and thus increasing its size. Not only the droplet size in the non-gelling case was much larger than that in the gelling case, but was even larger than the size of the outer tip, which sets the size of the jet. In the case of reacting gels, the gelling interface provided a confinement, which acted as a virtual extension of the outer capillary for the growing oil droplet. This allowed the middle alginate phase to flow through the virtual pipe and exert roughly the same magnitude of drag on the oil droplet as it would if the inner tip was placed behind the outer tip.

We first applied the model to non-gelling systems, where the viscosity of alginate phase remained constant (14.33mPas), to avoid the complexity associated with variations in the alginate viscosity due to continuous gelation. The model accurately predicted the drop sizes for the lowest alginate phase flow rates studied in this work for spherical droplets (Q_{alg}), as shown in Figure 7.5c, when the drag force was ignored from Equation 5. This clearly points to the absence of drag force due to the supressed velocity of the middle phase. For higher Q_{alg} values of 2 and 4 ml/h, a partial effect of the drag due to the increased middle phase velocity was observed.

The physical model was then applied to the gelling system where the viscosity experienced by oil drops was a function of diffusion rate of calcium ions into the alginate phase, flow rates and the concentration of two reactants. One can expect that for very high alginate phase flow rate, where the convective rate of transport of alginate phase is much greater than the diffusion rate of calcium ions, there will be little change in the viscosity of alginate phase during drop formation. Figure 7.5d compares the calculated results using the original viscosity of the alginate phase (14.33mPas) versus experimental data. The predictions for Q_{alg} = 10 ml/h fit very well with the experimental data, indicating that the model is directly applicable for the runs with $Q_{alg} \geq 10$ ml/h using the original viscosity data under the conditions of this study.

The importance of dynamic viscosity for $Q_{alg} < 10$ ml/h, cannot be further overemphasized than by the difference between the predicted results, using the original viscosity of the alginate phase (14.33mPas), and experimental data, as shown in Figure 7.5d. While the model was still able to predict the trend with Q_{oil} and Q_{alg}, it failed to predict the drop size by a great margin.

Before oil droplets start to experience the change in the viscosity of the media they are dispersed in, calcium ions have to diffuse from the outer calcium chloride solution to the droplets. The diffusion of calcium ions into the moving alginate phase, which is also associated with concomitant gelation, causes a progressing gel front to form, which changes the viscosity of the alginate phase. We define a characteristic time for the progression of gel front during drop formation. At the instance of drop detachment, when the force balance defined by Eqs. 1-5 is valid, the alginate phase has travelled a characteristic distance of D at the velocity of v_m, as shown in Figure 7.5a. This means that the alginate cell, engulfing a detaching droplet, can be defined by a characteristic "cell

contact time" of $t_c = D/v_m$ at the leading surface, and $t_c = 0$ at the lagging surface at tip level. The contact time indicates the time during which the alginate phase (cell) has been exposed to calcium ions, and as a result the gel front has progressed from the calcium chloride-sodium alginate boundary towards the centre of alginate fibers in the cell. It follows that the gel front, defined by ℓ_g, is maximum at the top surface and minimum at the bottom surface of the cell, with a decreasing trajectory in between depending on the kinetics of gelation. We now define ℓ_{alg} as the thickness of alginate phase around an encapsulate so that $(T\text{-}d)/2 < \ell_{alg} < T/2$. For a spherical droplet, ℓ_{alg} is minimum at the centreline of the droplet, but is maximum at the top and bottom of the cell enclosing the droplet (Figure 7.5a). The average value of ℓ_{alg} can be calculated as $(4T\text{-}\pi d)/8$. The relationship between D and t_c is shown in Figure 7.5e inset. The relationship becomes linear at high Q_{alg}.

There is also a characteristic time for droplets to form; droplet formation time t_f which is defined by v_{oil}/Q_{oil}. This is the time during which an oil droplet is still attached to the micro capillary tip and exposed to the passing alginate stream. Larger oil droplets obtained at low Q_{alg} have a longer formation and cell contact time, and are more likely to be affected by the progressing gel front. In contrast, for small droplets obtained at high Q_{alg}, the contact time t_c may become redundant by becoming equal to the drop formation time t_f (Figure 7.5e). This graph clearly shows that at low Q_{alg}, the actual contact time of an emerging droplet with its cell, before its detachment, is much shorter than its formation time. Therefore, the properties of the media cell engulfing the drop at the onset of detachment is only set at a fraction of t_f. However, the difference decreased exponentially with increasing Q_{alg} (Figure 7.5e), due to a decrease in drop size, until both characteristic

times converged, indicating that the drag is so dominant at high Q_{alg} that the droplet and its cell moved uniformly and simultaneously.

Having already ensured the validity of the model for cases with no significant change in the viscosity of the alginate phase, we reverse-calculated the required effective viscosity of the alginate phase to reproduce the size data. Figure 7.5f shows the variations in the viscosity scaling factor (S_η), normalised effective viscosity relative to the viscosity of alginate phase, with contact time for different Q_{alg} and Q_{oil}. A scaling factor of up to 4.5 was found to be sufficient to address the viscosity increase during gelation. The viscosity scaling factor scaled linearly with the characteristic cell contact time, with the slope depending on the oil phase flow rate (Figure 7.5a). Furthermore, Figure 7.5f also shows that a low Q_{alg} is associated with a high effective viscosity. This is because with an increase in the drop size, and as a result in the cell contact time, the alginate shell thickness (ℓ_{alg}) reduced while the gel front progressed further. This implies a shorter distance between the droplet surface and the gel front, $\ell_{alg} - \ell_g$, and a higher effective viscosity. By relating ℓ_{alg} with droplet size, one can conclude that the effective viscosity increased with Q_{oil} while decreased with Q_{alg}.

Figure 7.5g shows variations in S_η and t_c with ℓ_{alg}. It is interesting to note that ℓ_{alg} correlates with t_c as $\ell_{alg} \alpha t_c^{1/2}$, in a similar way that ℓ_g has been reported to correlate with time at $CaCl_2$ concentrations similar to the one used in this work; $\ell_g \alpha t_c^{1/2}$ [135]. The real distance between droplet surface and the gel front is $\ell_{alg} - \ell_g$, with the latter being unknown. Furthermore, even knowing ℓ_g would not solve the problem as it is not easy to estimate the effective viscosity of a heterogeneous media composed of a gel front and aqueous solution of alginate phase. However, we were able to show that the effective viscosity scales with ℓ_{alg}, which can be expressed as $S_\eta \alpha \ell_{alg}^{-1/2}$.

7.4.6. Encapsulation volume and associated morphological properties

The volume of oil loaded within a fiber can be increased with the oil phase flow rate, as seen in Figure 7.1a. This is usually associated with a change in segment morphology too. Therefore, a trade-off exists between preserving the desired oil entity's shape and maximising the encapsulation volume. However, there is a narrow range of flow conditions within which the desired segment morphology can be preserved at given range of flow conditions. These regions for particular segment morphology are depicted in Figure 7.6b, which shows a plot between the % oil volume encapsulated in a fiber, $\phi_{oil} = \left(\frac{Q_{oil}}{Q_{oil}+Q_{alg}} \times 100\right)$ and Q_{oil}, for different alginate phase flow rates. Within every specified region, the encapsulation volume can be fine-tuned by Q_{oil} without affecting the fiber shape, for which examples are shown in Figure 7.6a. Figure 7.6b reveals that the maximum ϕ_{oil} achievable for different fiber morphologies are in the ascending order of ~70% for spherical, ~80% for ellipsoidal, ~90% for plug-like, and >90% for tubular. The yellow region was found to be non-feasible due to the low alginate phase flow rates, under which the gelled alginate phase blocked the capillary tip, and stopped the fiber formation. Figure 7.6b also shows that for a fiber with given encapsulation ratio, there exists a number of possible morphologies. However, the optimum morphologies should be chosen based on the intended use of the fibers and specific properties sought.

The oil-loaded fibers can be characterised by morphological properties such as *spillage ratio* and *degree of waviness*, as well as mechanical properties such as tensile strength. The *spillage ratio*, which indicates the relative mass loss of encapsulated materials because of accidental damage, can be defined as the volume of each segment over total volume of the encapsulated oil in a unit length or volume of the fiber. A high frequency fiber has a small spillage ratio, but a fiber with a large amplitude has a high spillage ratio.

Fibers with lowest frequency and lowest amplitude, ideally the straight fibers, have an extremely high spillage ratio when D>>z, but show extremely low spillage ratio when z>>D. While Figure 7.6b shows that the tubular encapsulation may provide a higher encapsulation volume than any other configurations, it suffers from severe loss of encapsulated materials (high spillage ratio) in the case of accidental rupture of the alginate shell, at any location along the fiber. The spillage ratio also indicates ease of splitting the fibers. The medium continuity of tubular fibers would also prevent their efficient splitting as the core material would escape out from the point of rupture, which can pose a significant practical hindrance in fiber handling.

Fibers with a higher *degree of waviness* are more useful for making nonwoven fabrics and pads, as they provide better interlocking among the fibers. The frequency and amplitude of fibers can be used as an appropriate measure for the degree of waviness of a fiber, as shown in Figure 7.4i1. Fibers with higher frequency and amplitude demonstrate a higher waviness. Figure 7.4g shows that the frequency of oil segments, in terms of per unit length, and Figure 7.4h shows the amplitude. The frequency $[(z+D)^{-1}]$ increased with Q_{alg} as the reduction in droplet size with increasing drag reduced the D. The highest frequency was observed at an intermediate $Q_{oil} \approx$ 3ml/h for all sets, which was largely marked by the change in droplet geometry from spherical to prolate ellipsoids (Figure 7.4j3) and the associated increase in the axial length (D). The amplitude $[(T-t)/2]$ decreased with Q_{alg} (Figure 7.4h) as the reduction in droplet size with increasing drag reduced the d, which in turn increased t (Figure 7.4b). The amplitude showed two peaks when Q_{oil} was varied. The first peak, which occurred at a relatively low Q_{oil} (~ 1.5 ml/h), was more prominent at low Q_{alg}. The second peak was observed around Q_{oil} = 5ml/h,

beyond which the amplitude decreased as the fiber's surface flattened because the shape of the oil entities transformed from prolate ellipsoidal into plug-like shapes (Figure 7.1b).

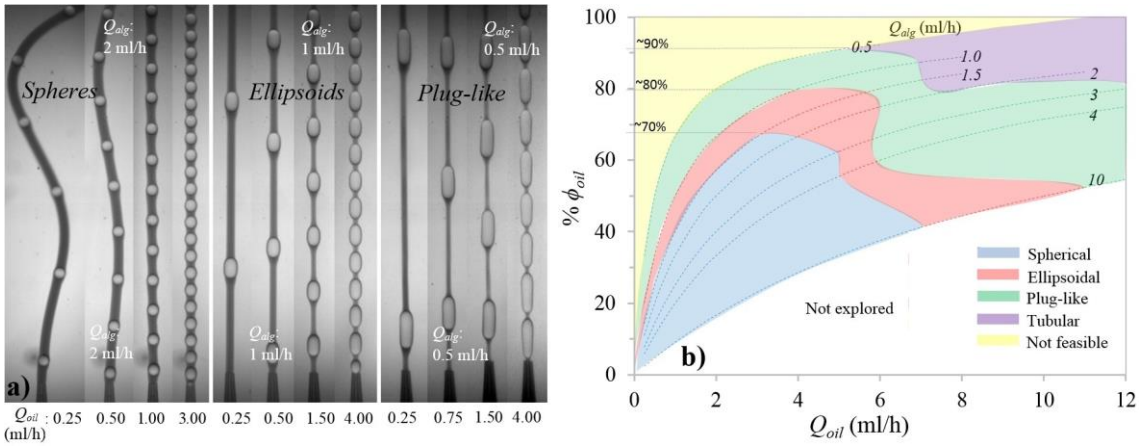

Figure 7.6 **a)** The inter-droplet distance is shown to be varied without altering the size of the encapsulated droplets having spherical as well as non-spherical shapes. The inter-droplet distance decreases by increasing the oil phase flow rate for all the drop shapes. **b)** Plot showing a % oil volume encapsulation achieved for different encapsulate shapes. Solid lines indicate the fixed Q_{alg} conditions.

These variations in frequency and amplitude with oil phase flow rate point to a criterion that the highest frequency occurs when the oil segments transform from spheres into prolate ellipsoids, while the maximum amplitude occurs at the transition between the ellipsoidal and plug-like segment shapes.

7.4.7. Mechanical properties

Alginate fibers are commonly used for making complex fibrous networks, such as 3D scaffolds used in tissue engineering [31,136,137,138]. These structures require fibers with high mechanical strength. However, the encapsulation of a liquid phase in a fiber, which is done to enhance the fiber's functional capabilities such controlled water collection [63], reduces the fiber strength, since a part of the solid polymer is replaced by the encapsulated liquid phase. Therefore, it would be useful to know what encapsulate configurations provide the fiber with best mechanical properties. These properties are most commonly

measured in terms of tensile strength via uniaxial tensile pull. The mechanical properties of synthetic fibers [139], and also simple and composite hydrogel fibers [140,141,142], have been reported in the literature. Here we report the uniaxial tensile testing of individual oil-encapsulated hydrogel microfibers for the first time.

The tensile testing of the fibers was conducted with the help of an extremely sensitive force-sensing device (DCA-100, First Ten Angstroms), a schematic of which is shown in Figure 7.7a, which is controlled via its computer software. The device has an immobile jaw holding a metal hanger on its top section, which is coupled with a built-in force sensing mechanism. The bottom stage, which is integrated with a stepper motor, can be moved upwards or downwards in the vertical direction at a desired velocity.

All the fibers were cut to a fixed length of 3 cm for mounting, with one end glued to the metal hanger on the top, while the other end glued to the bottom stage (Figure 7.7a). The glue (Devcon 5-minute epoxy) was left overnight to harden completely. To perform the uniaxial tensile testing, the bottom stage was moved down at a fixed velocity (0.2 mm/s), which pulled the fiber uniaxially until the fiber broke off.

The raw data was obtained in terms of the force experienced by the metal hanger attached to a fiber at a given strain. This data could give the maximum force (F_{max}) a fiber can withstand when axially pulled. The force-stress data were then processed to calculate the tensile stress on the fiber. A typical stress v/s strain curve is shown in Figure 7.7b, which defines the standard features associated with the tensile testing. The two main parameters characterising fibers are the Young's Modulus (E) and the Ultimate Tensile Strength (UTS). The E is the measure of the resistance of a material to change its shape within recoverable (*elastic*) deformation limits under tensile loading, while the UTS gives the maximum tensile stress a fiber can take before failure.

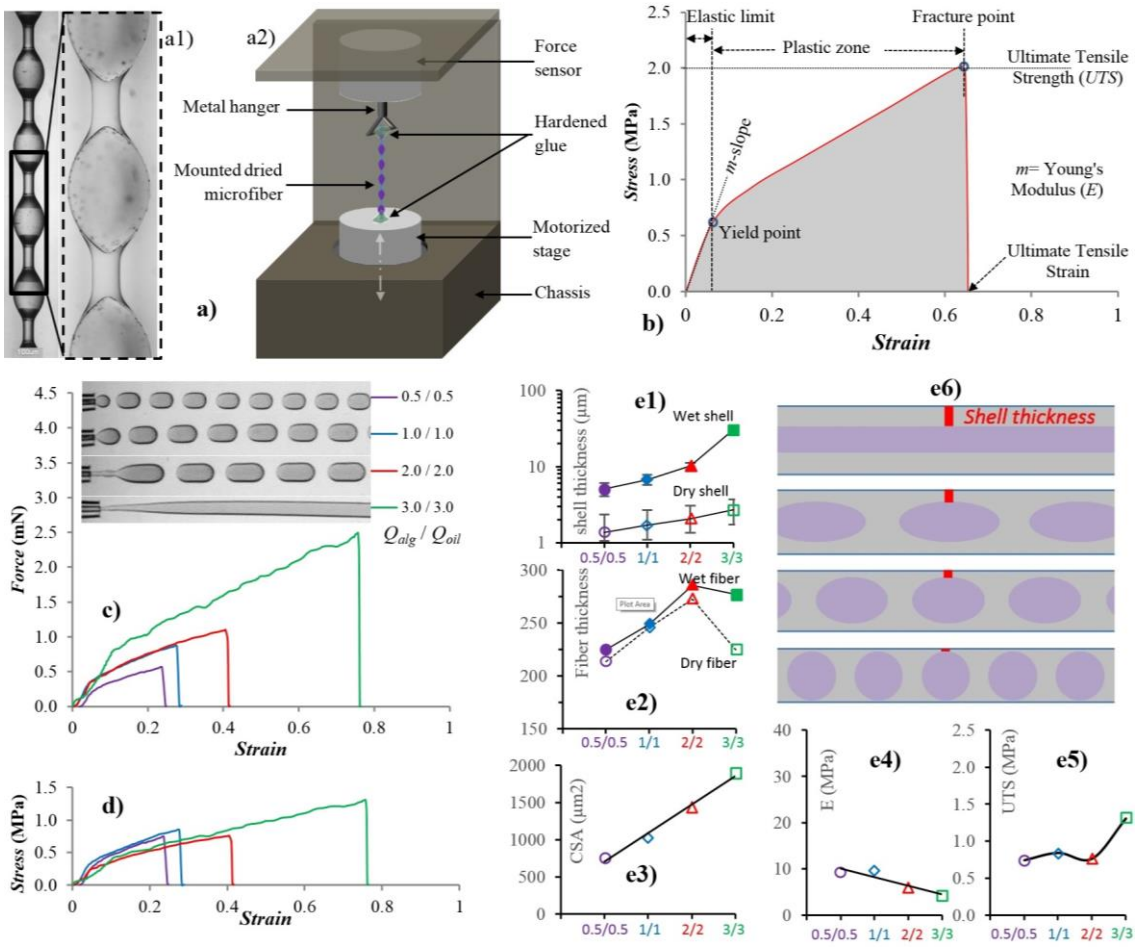

Figure 7.7 **a)** Micrograph in (a1) shows a dried alginate microfiber with oil encapsulates. The zoomed-in image, taken after immersing the fiber in an oil phase, shows the variation in the dried shell thickness around an oil encapsulate. (a2) shows the schematic of the setup used for uniaxial tensile testing of fibers. **b)** The graph shows a typical stress-strain curve obtained after a fiber's uniaxial tensile testing. The tensile testing results obtained in terms of 'force versus strain' and 'stress versus strain' for four fibers containing different encapsulate geometries at a fixed ϕ_{alg} are shown in **(c)** and **(d)** respectively. The shell thickness, fiber thickness and the cross-sectional area (*CSA*) of corresponding fibers are shown in (e1)-(e3). The calculated Young's modulus (*E*) and the measured ultimate tensile stress (*UTS*) are presented in (e4) and (e5) respectively. (e6) shows the reduction in the minimum shell thickness was the encapsulate morphology changes from tubular to plug-like, ellipsoidal and spherical.

To calculate the stress, the shell thickness at the thinnest points [*(T-d)/2*] where rupture occurred, as seen in Figure 7.4a, were measured to obtain the cross section area (*CSA*) for dry and wet states. Since the tensile testing was performed on dehydrated fibers (Figure

7.7a1), which are commonly used for scaffold fabrication, the shell thickness in dried state was used for stress calculations. It should be noted that fibers always broke off at their weakest points, which was around the thinnest shells at the centre of the oil segments for the fibers with discrete oil entities. However, the tubular fibers did not have a weakest point as the shell thickness was uniform across the fiber.

To understand the impact of the encapsulated droplet morphology on the fiber's mechanical properties, we compared four fibers having a fixed composition ratio (Figure 7.7c, ϕ_{alg}: 50%) but with different encapsulate geometries. It is important to note that these fibers were produced using pure oil, in order to eliminate the side effects associated with the presence of dye, and also a device having slightly different geometry with the one used for mapping, so the flow conditions shown for the encapsulate morphologies may not exactly match with the phase map shown in Figure 7.1b, but the mechanism to alter the encapsulate morphology from spherical to tubular remains the same.

Figure 7.7c shows the force-strain curves for fibers with different morphologies at fixed ϕ_{alg}. Among these fibers, the fiber with tubular configuration had the highest mechanical strength in terms of the failure load (F_{max}) and ultimate tensile strength (UTS) (Figure 7.7d and Figure 7.7e5). This is because the tubular geometry provides the largest shell thickness and shell cross-sectional area for a fixed ϕ_{alg}, as compared to other fibers having segmented oil encapsulates. The tubular fibers enjoy the largest shell thickness because they do not have pure alginate thread as encountered in other morphologies (z = 0) due to the oil forming a continuous phase in the middle of the fiber. However, the (minimum) shell thickness is quite small for discrete encapsulates, as the nodal spaces between adjacent droplets are filled by the alginate phase, which leaves less alginate volume around the oil segments in the fiber's periphery. Within discrete encapsulates, the

minimum shell thickness reduces as the segment shape changes from tubular to plug, ellipsoidal and spherical (Figure 7.7e6). The fiber with tubular oil entity underwent the highest deformation (strain) before failure, and also had the smallest Young's Modulus (E) (Figure 7.7e4), which suggests that these fibers are easy to deform within their elastic limits.

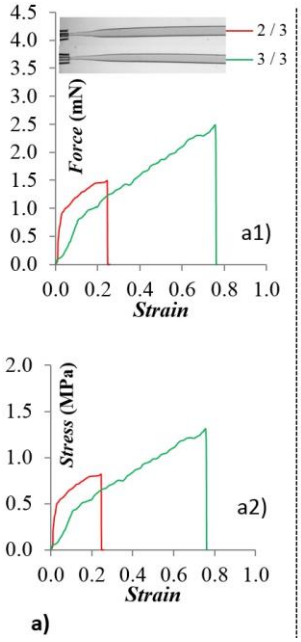

Fiber properties	Tubular		Spherical	
	2 / 3	3 / 3	2 / 1	3 / 1
Wet shell thickness (µm)	13.52	30.42	10.12	15.21
dry shell thickness (µm)	2.04	2.72	1.70	2.01
Wet fiber diameter (µm)	260.26	277.16	253.50	245.05
Dry fiber diameter (µm)	253.32	224.77	193.00	191.08
CSA (µm²)	1834.73	1897.45	891.58	1045.92
E (MPa)	22.30	4.22	17.86	12.30
UTS (MPa)	0.82	1.31	1.74	2.02
Dried fiber cross-section area (*CSA*) schematics				
Comparison of dried fiber diameter and *CSA*	$CSA_{2/3} = CSA_{3/3}$ $T_{2/3} > T_{3/3}$		$CSA_{2/1} < CSA_{3/1}$ $T_{2/1} = T_{3/1}$	

c) c1) c2)

Figure 7.8 The tensile testing data for fibers with **a)** tubular and **b)** spherical encapsulate geometry are compared at different ϕ_{alg}. **c)** The table lists the values of different specifications of the fibers used in (a) and (b).

We studied the effect of varying ϕ_{alg} on the mechanical properties of the fibers for two extreme geometries, spherical and tubular (Figure 7.8). For both cases, when the ϕ_{alg} was increased by increasing Q_{alg}, the fiber with the higher ϕ_{alg} showed improved mechanical strength in terms of the failure load (F_{max}) and ultimate tensile strength (UTS) (Figure 7.8a-8b). This is plausible as one can expect the minimum shell thickness and cross-sectional area of the fibers to increase with ϕ_{alg}, as observed for fibers with spherical oil droplets (Figure 7.8c2). The mechanical strength also improved with increasing ϕ_{alg} in the case of tubular fibers, however, this was achieved despite the two tubular fibers having

similar cross-sectional area (Figure 7.8c1). This occurred because the increase in ϕ_{alg} resulted in the formation of a thinner fiber but with a thicker shell. We therefore can conclude that for tubular fibers with similar *CSA* but different dimensions, the fiber with smaller diameter is stronger because of having a thicker shell. For elastic and plastic deformability, we found that for both configurations, the fiber with higher ϕ_{alg} showed a poorer resistance to elastic deformation (low *E*), and also underwent more plastic deformation.

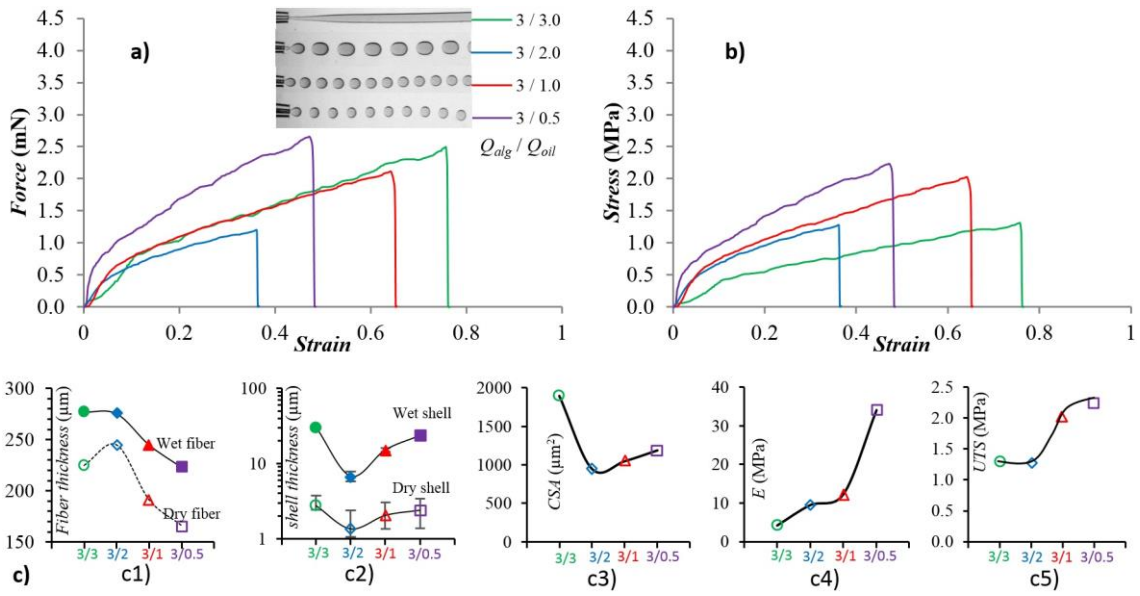

Figure 7.9 The force and stress variations against the measured strain for fibers with varying geometry and ϕ_{alg} are compared in **(a)** and **(b)** respectively, whose fiber and shell thickness and different properties (*CSA*, *E*, *UTS*) are compared in **(c)**.

We now analyse the impact of varying the ϕ_{alg} and encapsulate geometry on the fiber properties simultaneously (Figure 7.9). To do so, the ϕ_{alg} was increased by decreasing Q_{oil} in such a way that the tubular oil-encapsulate disintegrated into discrete entities due to increased drag (Figure 7.9a). In this case, the tubular and spherical configuration had the lowest and highest ϕ_{alg}, respectively. However, the tubular fiber was still able to withstand almost the largest tensile load (F_{max}) (Figure 7.9a), in spite of having the minimum ϕ_{alg}.

This is because the tubular fiber still had the largest cross-sectional area among all fiber types. However, its large *CSA* minimized its *UTS* considerably (Figure 7.9b and Figure 7.9c5).

Regarding fiber's deformation, the tubular fibers, which had the lowest ϕ_{alg}, underwent maximum plastic and elastic deformation, as indicated by a minimum *E* (Figure 7.9c4). This was a net result of combining the two counter effects on *E*, arising due to the tubular geometry and the low ϕ_{alg}. As observed earlier, the tubular geometry showed the smallest *E* among all geometries at a given ϕ_{alg} (Figure 7.7). For all geometries, *E* increased with deceasing ϕ_{alg} (Figure 7.8). Thus, a large deformation of the tubular fiber at low ϕ_{alg} indicates that the impact of encapsulate geometry on *E* outweighed the effect of ϕ_{alg}, which highlights the significance of encapsulate morphology on its mechanical properties.

7.5. CONCLUSION

A facile microfluidic approach was introduced for flexible oil encapsulation in alginate microfibers, which was based on the simultaneous formation and encapsulation of the oil phase. Using this method, one is able to tune the encapsulate shape across a wide spectrum of geometries (spherical, ellipsoidal, plug-like and tubular). Additionally, the shape of oil encapsulates could also be altered by making a more deformation-resistant calcium alginate shell at high alginate and calcium chloride concentration.

A fundamental physical force-balance model was also introduced to predict the size of spherical encapsulates. The proposed model accurately predicted the size of droplets formed in a non-gelling system, which ensured the validity of the model, as this system avoided the complexity associated with variations in the alginate viscosity due to continuous gelation. In case of a gelling system, the model correctly predicted the size of

droplets formed at high alginate phase flow rates (Q_{alg}), for which the viscosity did not change appreciably due to the high velocity of alginate phase. The significance of dynamic viscosity at low Q_{alg} was studied by comparing the droplet formation time (t_f) against the cell contact time (t_c), during which the alginate gel front progressed towards the droplet inside the fiber. At low Q_{alg} large spherical droplets with maximum t_c and minimum alginate thickness (ℓ_{alg}) were formed. This resulted in an approximately five-fold increase in the alginate phase viscosity, compared to its original viscosity.

The encapsulated oil entities were also selectively grouped by varying the surface affinity of the oil-injecting capillary. A hydrophilic inner capillary activated the grouping mechanism, while the number of droplets per group could be adjusted by the oil phase flow rate (Q_{oil}). The grouping phenomenon could also be switched off by treating the inner capillary to be hydrophobic. The oil entities for both grouped and ungrouped fibers were quite stable in the hydrated and dehydrated states for several months.

For a fixed fiber composition, indicated by the alginate phase ratio ϕ_{alg}, fibers with different surface morphologies and encapsulate geometries could be produced, implying that the selection of fiber for a particular application should be based on other properties of the fiber including *spillage ratio*, *degree of waviness* and *uniaxial tensile response*.

Fibers with spherical encapsulates were limited to a low encapsulation volume, but were most resistant to spillage after fiber split. On the other hand, fibers with tubular encapsulates were found to have the highest encapsulation volume, but also suffered from the highest spillage ratio, meaning they are prone to a colossal core-loss in case of an accidental fracture of the fiber.

To assess the degree of waviness, a 2D mathematical reconstruction of the fiber's surface profile was presented. In this reconstruction, a sinusoidal wave was fitted to a fiber's measured surface morphology, where a high frequency and amplitude of the fitted wave function indicated a high degree of waviness. The maximum frequency was noted in the fibers closely packed with spherical encapsulates, while the maximum amplitude was observed in the fibers fully packed with ellipsoidal encapsulates.

In terms of tensile properties, tubular fibers were able to endure the maximum tensile force (F_{max}) before failure at given alginate phase ratio (ϕ_{alg}), compared to fibers with other encapsulate geometries. Fibers with high ϕ_{alg}, for all encapsulate geometries, withstood a higher tensile force. However, the strength of fibers reduced at high ϕ_{alg} if the increase in ϕ_{alg} altered the encapsulate geometry from tubular to discrete oil segments. Regarding fiber deformation, tubular fibers underwent maximum elastic and plastic deformation prior to failure.

Chapter 8 Asymmetric Alginate Microfibres with configurable oil-encapsulates[**]

8.1. ABSTRACT

A new class of smart alginate microfibres with asymmetric oil encapsulates is introduced. These fibres were produced by injecting an aqueous alginate solution, asymmetrically loaded with oil entities through an eccentrically aligned inner capillary, into the outer aqueous calcium chloride solution to form alginate fibres. The fibre morphology could be tuned via altering the size, location and frequency of the oil encapsulates. These asymmetric fibres revealed significant potential for applications where conventional symmetric fibres failed to perform. We show how asymmetric encapsulated fibres can become dehydrated-sensitive, and trigger the release of encapsulates if their hydration level drops below a critical value. We also demonstrate the capability of asymmetric fibres to carry and release multiple cargos in parallel. Additionally, we show how the triggered-response could be switched-off on demand by stabilizing the oil encapsulates. Such passive asymmetric fibres are featured by simultaneous release of two-core compartments at the fracture site, which suggests the possibility of producing fibres with self-repairing properties.

[**] Submitted to *Small* journal for publication.

8.2. INTRODUCTION

Biocompatible calcium-alginate microfibres are widely used in a variety of formats such as non-woven fibre pads and scaffolds, in pharmaceutical and biomedical applications like wound healing [125,126,127] and tissue engineering [128,129,143]. The range of applications of alginate microfibres has been extended by encapsulating various aqueous [62,144] as well as non-aqueous core [36,63] materials in the fibre's shell matrix. To further enhance the fibre's multi-functional capabilities, encapsulation of multiple phases has also been reported [64].

Geometrically, encapsulation within fibres can be obtained in broadly two ways, symmetric and asymmetric, with respect to the fibre's central axis. The latter configuration can result in fibres with a variety of surface morphologies, particularly in dried state. However, there is no information available in the literature regarding asymmetric fibres except for multi-tubular fibres produced via asymmetric injection of multiple aqueous phases in parallel in a gelling alginate phase [34,35]. While symmetric fibres enjoy from uniformity in structure and morphology, which is ideal for many applications, they suffer from lack of versatility in dealing with novel applications where encapsulations interaction or rupture is sought, or fibres with variant morphology are desired.

The conventional *two-step* encapsulation strategy [33,134], where the oil droplets are formed prior to their encapsulation, can only produce fully concentric or symmetric encapsulation of the oil droplets, even if the droplets are produced asymmetrically, as shown in Figure 8.1a1. This is because the oil droplets initially formed upstream in asymmetric positions, tend to move to the central axial location, before being encapsulated at a considerable distance downstream. This has been observed even in the

case of simultaneous asymmetric injection of two parallel oil streams [36], a schematic of which is shown in Figure 8.1a2. The resulting symmetric fibres (Figure 8.1b), when dehydrated, resulted into symmetric dried fibres with trapped oil encapsulates (Figure 8.1c-d).

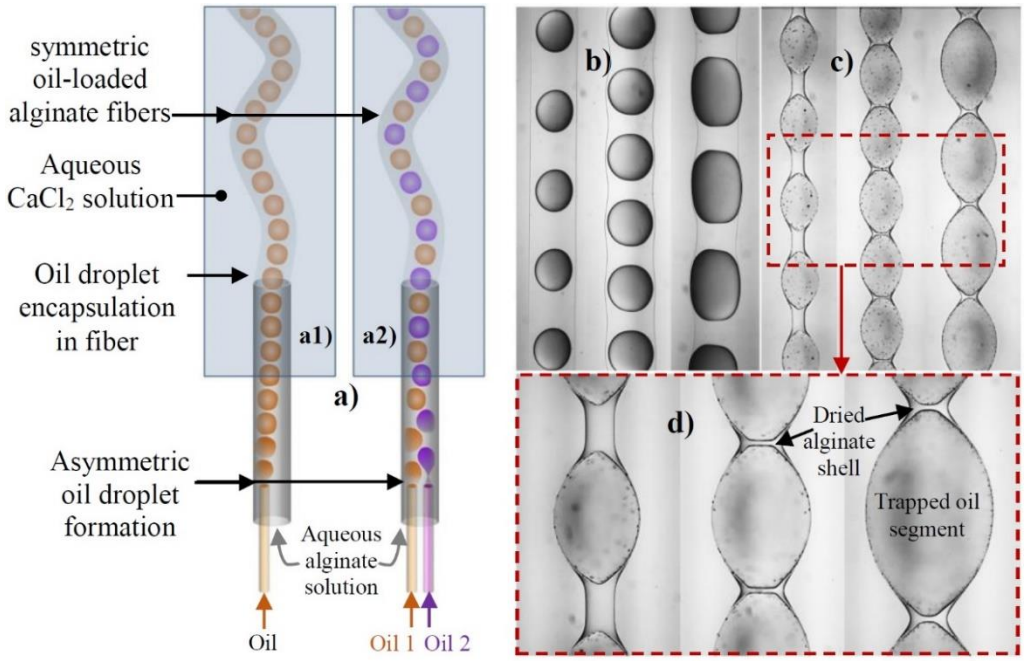

Figure 8.1 a) Schematics of two conventional microfluidic device-configurations used to produce symmetric oil-encapsulated alginate fibres with different one or more types of linearly arranged oil droplets. The micrographs of hydrated (b) and dehydrated (c) symmetric fibres are shown, while (d) shows a zoomed-in micrograph of the fibres.

We introduce a facile microfluidic approach for tunable asymmetric encapsulation of oil in alginate microfibres, which is based on the simultaneous (*one-step*) formation and encapsulation approach, where the droplets are directly trapped within the gelling fibre in desired locations. We also present a number of potential applications of asymmetric fibres which cannot be met by symmetric fibres. In one example, we show that the oil cores can be efficiently released upon dehydration of the microfibre having asymmetric encapsulates, whilst completely preserving the fibre structure. We further demonstrate the capability of such fibres to carry and release multiple cargos in parallel, and also how

these fibres can be made responsive to mechanical failure via a possibility for displaying a self-repairing feature.

8.3. EXPERIMENTAL

8.3.1. Materials

The middle phase constituted an aqueous solution of 1 wt% sodium alginate, while the outer aqueous bath contained 4 wt% calcium chloride. Octane (99%, Sigma Aldrich) was used as received as the model inner-oil encapsulated phase. Sodium alginate and calcium chloride (Sigma Aldrich) were used as received. Sudan Red and Sudan Black (FastColours UK) were used as the oil-soluble dyes. Sodium dodecyl sulfate (SDS) and Tween 20 were used as water-soluble surfactants (Sigma Aldrich).

8.3.2. Device

Figure 8.2a shows two schematics of the different microfluidic device configurations used to encapsulate oil within the alginate fibre. The device fabricated as per the configuration shown in Figure 8.2a1 used two glass capillaries, circular (ID: 0.56 mm, OD: 1 mm) and square (IL: 1 mm, OL: 1.5 mm). The inner capillary were pulled using a pipette puller (P-1000, Sutter Instrument, Novato, USA). The tapered tips were cut to the desired sizes, after which the inner capillary tip (ID: 40 µm, OD: 60 µm) was aligned non-axisymmetrically towards the left edge of the outer capillary tip, with the outer tip (ID: 150 µm, OD: 175 µm). Both capillaries were plasma treated (Femto Plasma Cleaner, Diener) to be hydrophilic. The oil phase was pumped (Harvard Apparatus pumps) through the inner capillary, while the alginate phase was introduced through the interstitial spaces between the two capillaries. The coupled capillary setup was introduced vertically in a cuvette, which housed the quiescent outer aqueous phase containing calcium chloride as shown in Figure 8.2a1.

The device fabrication for the second configuration (Figure 8.2a2) was done using a completely different approach, since the tips of two tapered capillaries could not be inserted together inside the outer tapered capillary. The straight forward use of parallel straight capillaries was also not feasible, as the thin and long capillary (with OD: 80μm) was very flexible, and its tip could not be fixed at a particular location. To circumvent this problem, multiple straight capillaries were assembled to make compound inner capillaries for two inner oil phases, as shown in Figure 8.2b1. Two such assembled capillaries were inserted in a tapered supporting capillary (Figure 8.2b2), with the two tips protruding ~2 mm outside the tapered tip of the supporting capillary. The two tips were aligned at a same level and at a fixed distance from each other (~40 μm), and immobilized by the glue applied on both ends of the supporting capillary. This compound assembly was introduced inside a tapered outer capillary, and the coupled inner tips were aligned at the same level as that of the outer capillary, as shown in Figure 8.2d.

The resulting fibres were collected at the top of the cuvette, facilitated by the buoyancy force exerted by the encapsulated oil. A high-speed camera (Photron FastCam SA-5 (monochrome)) was used to record the fibre formation.

The drying behaviour of the fibre was monitored by measuring the variation in the weight of a given fibre at room temperature. Precautions were taken to ensure the excess volume of water adhering on fibre external surface was removed, by placing the sample on a piece of water absorbing paper, prior to weighing. The saturation swelling ratio of fibres (S_{sat}), expressed as $S_{sat} = \left(\frac{w_{wet} - w_{dry}}{w_{dry}}\right)$, was calculated by measuring the weight of a fully hydrated (w_{wet}) and fully dried (w_{dry}) simple alginate fibre. Fibre drying occurred in an oven to a constant weight at 70℃. The saturation swelling ratio for the alginate fibre was found to be ~10.1. The swelling ratio at which the shell rupture occurs is given by $s_{rup} =$

$\frac{w_r \times 100}{S_{swell}}$, where w_r is the weight of water remaining in the gel at the instance of shell rupture, which was calculated via $w_r = w_{wet} - w_{oil} - w_{dry}$. Typical values of w_{wet}, w_{dry}, and w_{oil} for a given length of the fibre chosen for presentation in Figure 8.6d were 8.1, 3.2, and ~0.3 mg, respectively.

8.4. RESULTS AND DISCUSSION

8.4.1. Asymmetric oil encapsulation via one-step encapsulation strategy

To produce asymmetric fibres, we merged the two distinct steps, drop formation and encapsulation, usually used for the fabrication of encapsulated fibres, into a *single-step* process (Figure 8.2a1) where the droplets were formed directly into the gelling fibre. This approach instantly locked the droplets inside the gelled fibre at the locations they were formed, thus preventing their movements. This single-step strategy also allowed for the droplets to be loaded asymmetrically, as shown in Figure 8.2a1. A typical resulting asymmetric fibre is shown in Figure 8.2c1.

The composition and functionality of the asymmetric fibres can be further enhanced by encapsulating more than one type of hydrophobic materials in a single fibre. The realization of such a hybrid fibre architecture has previously been demonstrated by Yu et al [36]. with the use of an intricate *two-step* approach coupled with digitally controlled valves and additional compensatory flows of the alginate phase. However, this approach also produced symmetric fibres with linearly arranged compound droplet sequences. To fabricate asymmetric fibres with two kinds of hydrophobic encapsulates, we extended our *one-step* encapsulation strategy by using two parallel inner glass capillaries to form two independent sequences of droplets, directly fed into a gelling alginate fibre (Figure 8.2a2). The tip cross-section of the device is shown in Figure 8.2d, while a typical hybrid asymmetric fibre encapsulating two droplet sequences is shown in Figure 8.2c2.

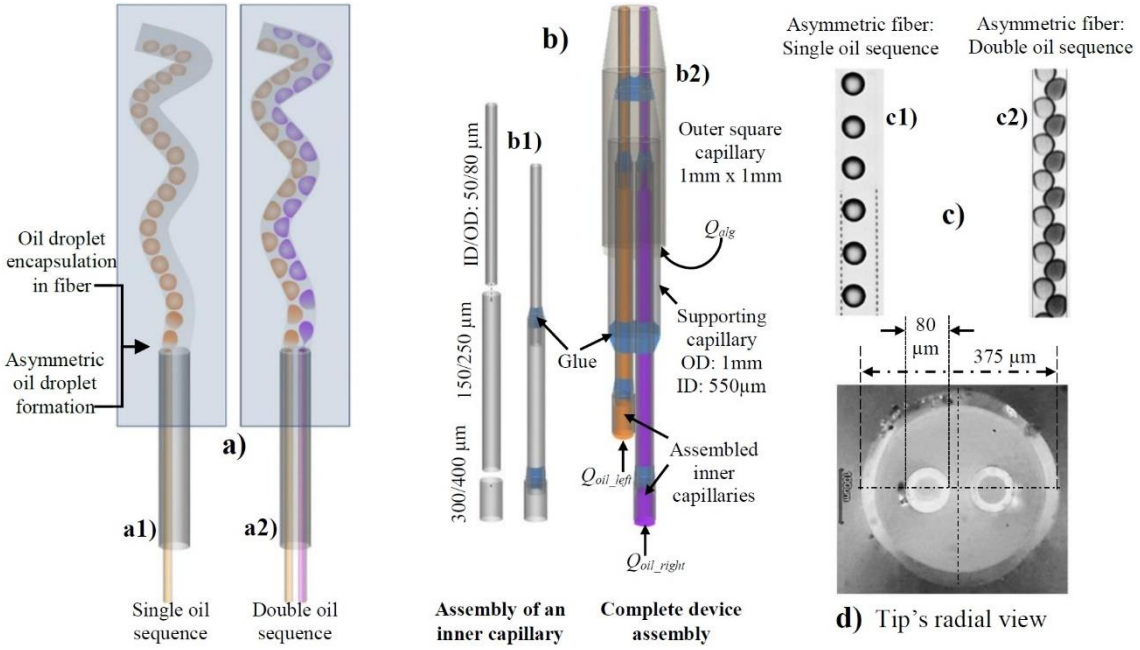

Figure 8.2 a) Schematics of two microfluidic device configurations, based on simultaneous droplet formation and encapsulation, used to produce oil-encapsulated alginate fibres with one-component non-asymmetric (a1), and two-component non-asymmetric (a2) oil encapsulates. b) The schematic shows a glass micro-capillary assembly (b1), and the overall assembly of the microfluidic device (b2) for asymmetric oil encapsulation. c) Optical micrographs of a typical one-component asymmetric (c1) and two-component asymmetric (c2) fibre are shown, which were produced using the configurations shown in a1 and a2, respectively. d) The tip cross-section of the assembled device.

The droplet size, frequency and location in each stream can be individually manipulated to tune the surface morphology of asymmetric fibres. The droplet size of each stream can be independently adjusted with the corresponding oil phase flow rate, without affecting the size of its neighboring droplet sequence. However, this may affect the asymmetry of the encapsulated droplets with respect to the fibre's axis. This is illustrated in Figure 8.3a, where only the flow rate of the left stream (light-coloured) increased to: 0.125, 0.25, 0.50, 1.0, 2.0, 4.0, and 6.0 mlh^{-1}, while the flow rate of the right stream (dark-coloured) was fixed at 1.0 mlh^{-1}. The maximum asymmetry was observed when the droplets in both sequences were of similar sizes and at an inclination of ~45º (Figure 8.3a3-a4).

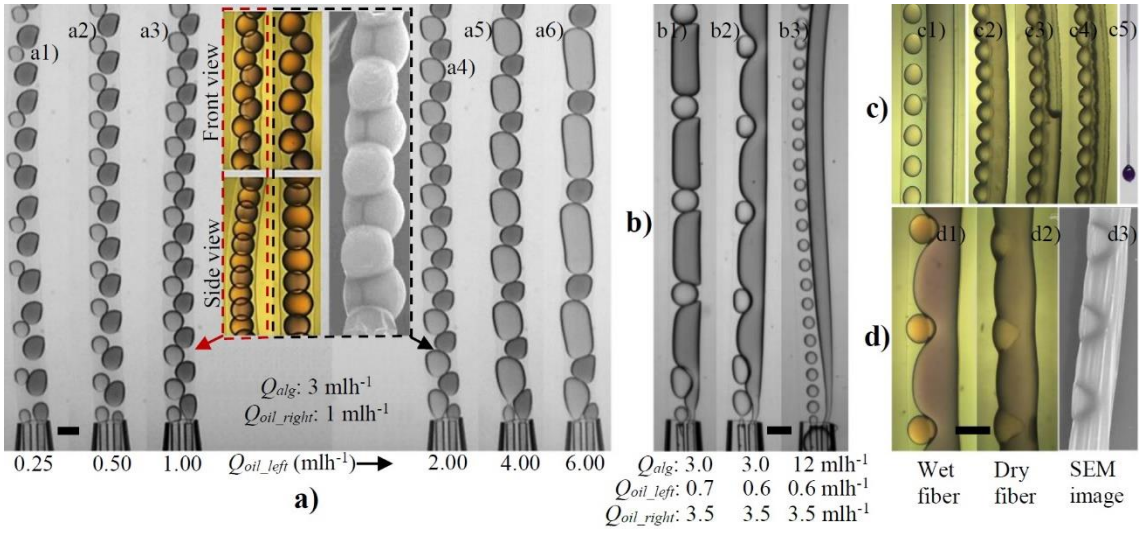

Figure 8.3 a) The formation of alginate fibres with two-component asymmetric oil encapsulation and the evolution of encapsulate asymmetry with the oil phase flow rate are shown. The left-sided oil droplets are dyed with Sudan Red (FastColours UK), while the right ones are dyed with Sudan Black (FastColours UK). The two sets of inset images in the centre (a7) show the front view (top) and the side view (bottom) of two such fibres (shown in a3 and a4) in the hydrated state. The SEM image of a dried asymmetric fibre (a4) is also shown in a7. b) The micrographs show that a symmetric fibre can be turned into asymmetric fibre by altering droplet size on the left stream (b2), whose wet and dry state images are also shown in (d). A more defined encapsulation of tubular and spherical droplets can be easily achieved by decreasing the droplet size and tubular width via increasing Q_{alg} (b3). The fibre having tubular and spherical encapsulates in wet and dry states are shown in (c1) and (c2) respectively. If such a fibre is split, the oil from tubular encapsulate escapes while the segmented encapsulates remain trapped (c3-c5). All scale bars are 200µm.

The asymmetric surface morphology of these fibres can be clearly seen from the SEM images shown in Figure 8.3a4 (inset). As the droplet size in one sequence increased, the arrangement of the resulting droplets became less asymmetric due to increased interaction between the two oil phases, until eventually the formation of asymmetric encapsulates became impossible as the droplets tended to arrange linearly and symmetrically (Figure 8.3a6).

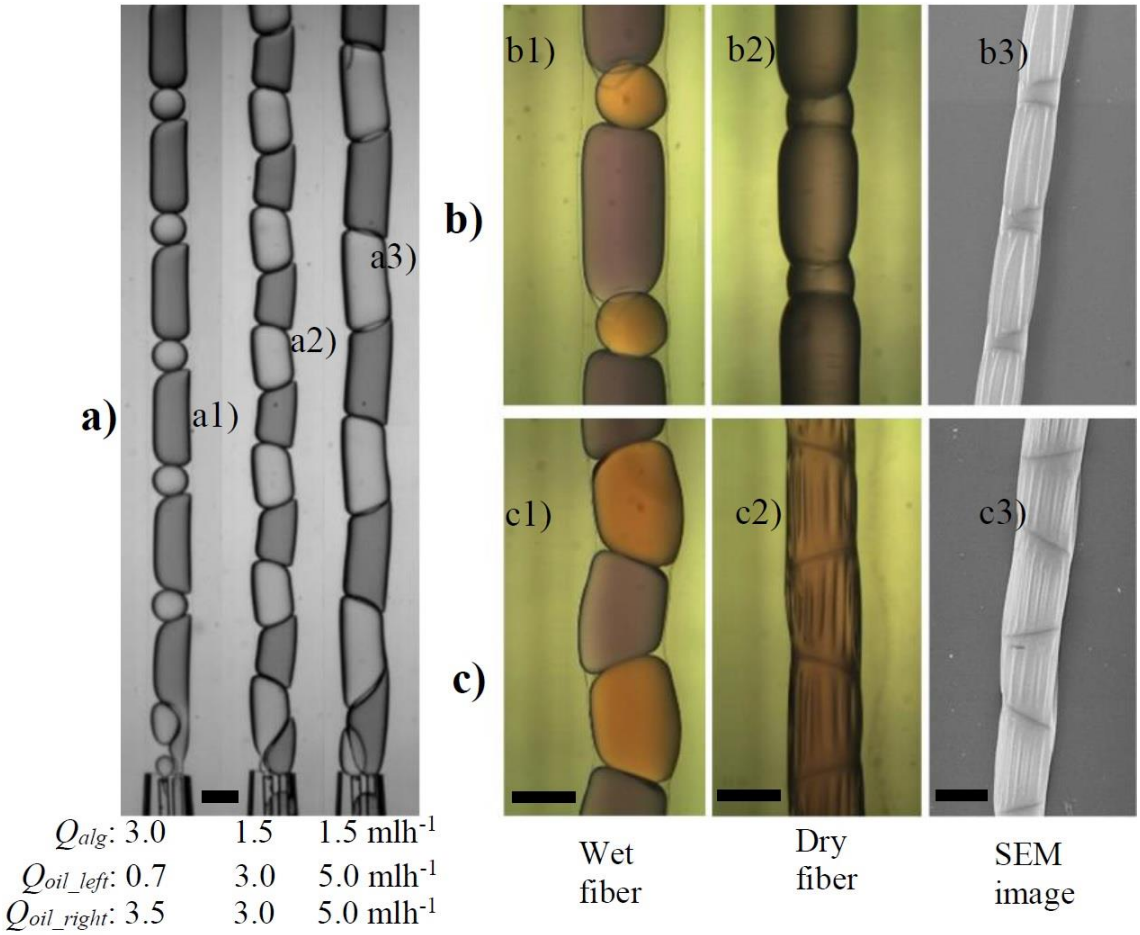

Figure 8.4 a) Compound oil-loaded alginate fibres with symmetric morphology obtained at increased size of both encapsulates are presented. The morphology of fibres shown in (a1) and (a2) under hydrated and dehydrated states are also shown in (b) and (c) respectively. All scale bars are 200µm.

This loss of fibre asymmetry can be revived by minimizing the interaction between the two oil streams, for example by the inclusion of the tubular and segmented oil encapsulates in the fibres. This was achieved by reducing the spherical droplet size, via increasing the alginate phase flow rate, which minimized its interactions with the adjacent oil phase and allowed it to evolve as a tubular jet (Figure 8.3b2). The phase interaction was fully suppressed at a higher alginate phase flow rate resulting in the formation of fibres containing a smooth tubular oil phase in parallel with oil droplets (Figure 8.3b3). These fibres, as shown in Figure 8.3c1, benefit from having both encapsulation

geometries, where tubular geometry provides a high encapsulation volume, while segmented geometry provides robustness against complete oil loss in the event of fibre split (a low spillage ratio). The fibre takes an asymmetric surface profile upon dehydration, with a smooth surface around the tubular oil section and a wavy profile around the segmented oil droplets (Figure 8.3c2).

Increasing the volumetric flow rates of both oil streams to a great extent intensified the interaction between them, which further compromised the fibre's asymmetry, and led to the formation of fibres with large linearly-arranged alternating oil plugs (Figure 8.4a). An important property of these fibres is that all appeared to be flat upon dehydration (Figure 8.4b3 and 8.4c3), a feature not observed for the symmetric fibres made by conventional methods, examples of which are shown in Figure 8.1.

8.4.2. Strategies for hybrid assembly of asymmetric microfibres

By careful adjustment of the size and frequency of the asymmetric oil encapsulates, dehydrated fibres with a variety of surface morphologies can be produced. Fibres with customized morphologies could be used as building blocks for fabricating hybrid fibre films or pads for usage in biomedical applications such as wound healing. For such applications, the accurate handling and precise arrangement of individual fibres, to prevent unwanted fibre twisting and fractures, are some of the major practical challenges to be resolved. However, recent developments in fibre manipulation techniques, such as magnetic manipulation of fibres via encapsulation of magnetic mineral oil solutions [134], could provide a controlled methodology for desired fibre manipulation of individual fibres.

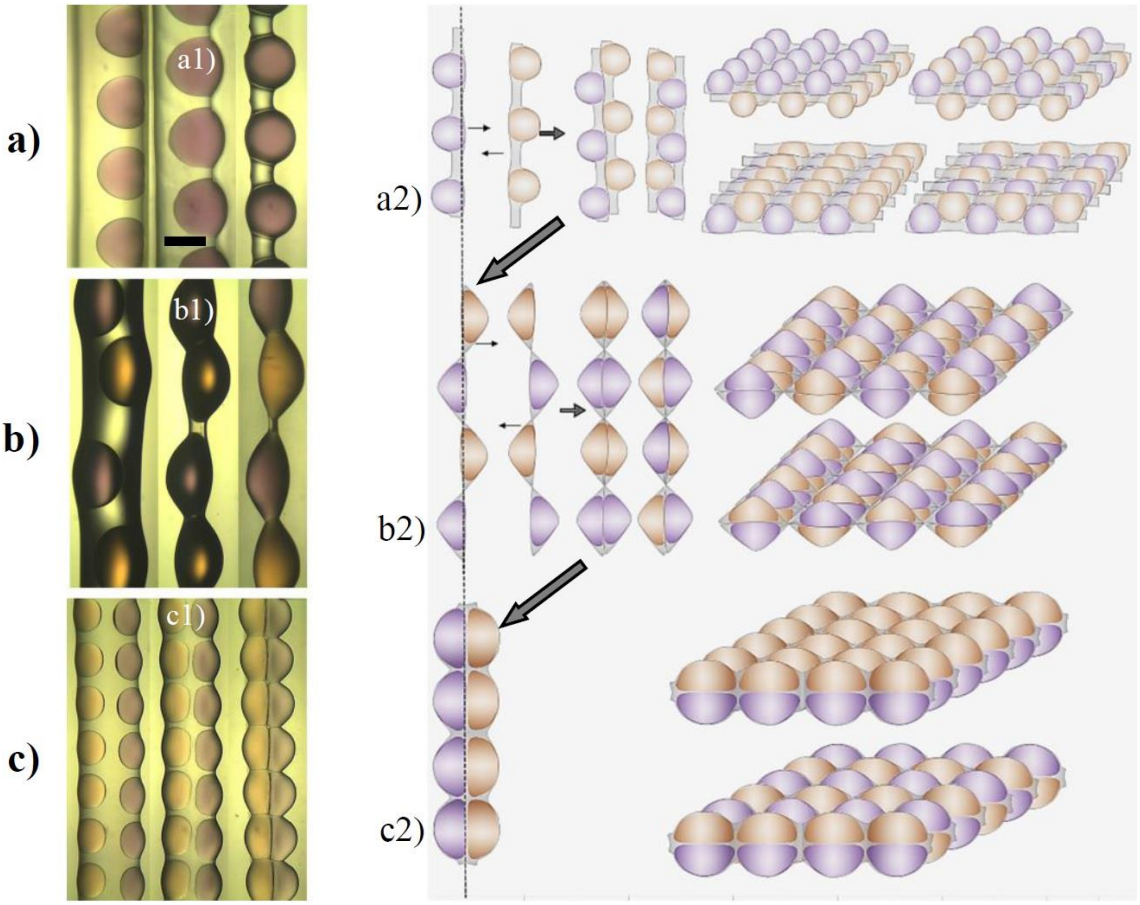

Figure 8.5 Micrographs of three different asymmetric oil-loaded alginate fibres a) simple asymmetric, b) alternating asymmetric, and c) Yanus-like, along with schematics of their arrangements into various fibre pads. The common scale bar shown in (a) is 200µm.

The simplest type of asymmetric dried fibre, which consists of a single sequence of asymmetric oil-encapsulates, has a flat surface on one side and a wavy morphology on the other (Figure 8.5a1). Two such fibres could be intertwined in two geometrically different ways, the alternating asymmetric arrangement and the interlocking 'clicked-fibre' arrangement (Figure 8.5a2), to produce thin alginate sheets. These two configurations can be further arranged to prepare four different fibre pads.

A more complex fibre structure consisting of two sequences of asymmetric encapsulates can be directly produced by synchronizing the droplets frequency. To make fibres with alternating asymmetric morphology, large droplets at a low frequency were produced

(Figure 8.5b1). A pair of these fibres can be combined to produce a fibrous building block having symmetric wavy morphology with configurable oil compositions, as shown in Figure 8.5b2. These fibres can be intertwined to create two varieties of fibre pads.

If oil droplets from the two streams can be generated simultaneously while their size being controlled to be smaller than the half of the alginate fibre, then it would be possible to produce Janus-like structures as shown in Figure 8.5c1. These fibres can be arranged to produce two additional varieties of fibre pads.

Overall, the proposed *one-step* oil-encapsulation strategy is capable of fabricating asymmetric as well as symmetric hybrid alginate microfibres with a wide variety of morphologies.

8.4.3. Potential applications

We demonstrate two examples of the potential applications of asymmetric oil-loaded fibres to highlight their significance.

8.4.3.1. Fabricating dehydration-responsive microfibres for core-release applications

We introduce a benign and simple core-release mechanism for asymmetric fibres. Currently, only one report exists in the literature that demonstrates a core-release mechanism from alginate fibres via dissolution (or uncrosslinking) of its shell in sodium citrate [64]. A more benign approach for releasing the core from the fibre, where the alginate shell is preserved, could be useful, as a destructive release mechanism may not be suitable, as well as practical, for many delicate applications. Before moving on to demonstrate the release mechanism, we first discuss how the conventionally oil-loaded alginate fibres respond upon dehydration. The dehydrated symmetric fibres, shown in

Figure 8.1c-1d, were stable and maintained their encapsulated entities with time irrespective to the segment shape, which is consistent with previous observation [36].

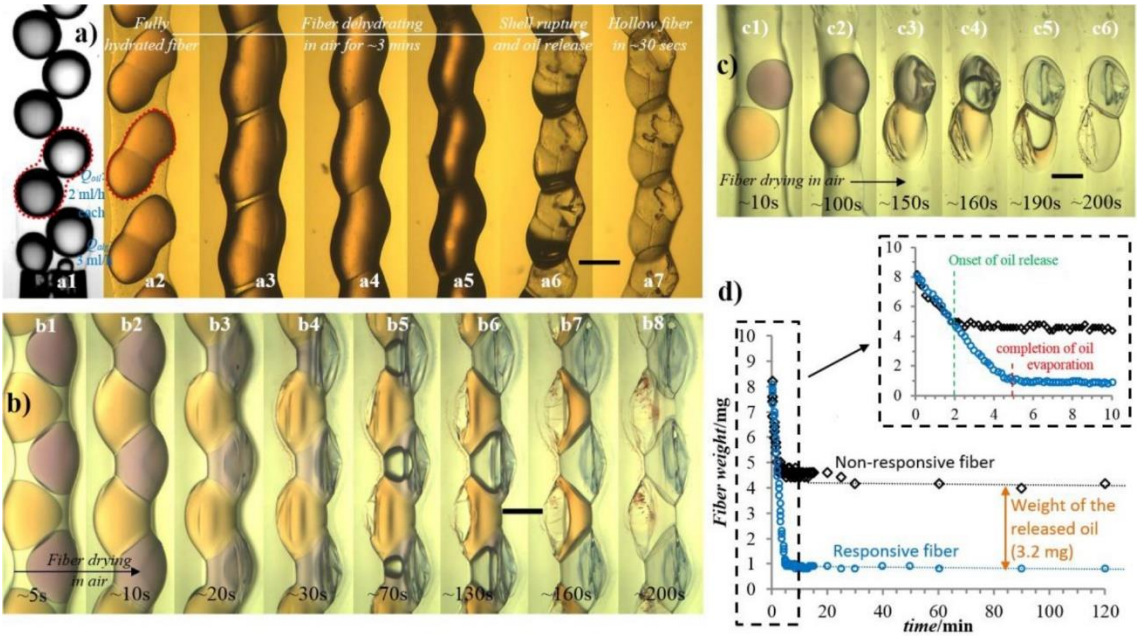

Figure 8.6 a) Fibre containing two asymmetric oil droplet sequences in the absence of surfactant, and their eventual paired arrested coalescence (a2) are shown. The release of oil from this dumbbell-shaped one-component oil segment is triggered by drying this microfibre (a3-a6), which eventually leaves behind a hollow microfibre, as shown in a7. b) The optical micrographs show the time evolution of a dehydrating microfibre containing two sequences of oil droplets added non-axisymmetrically, which are eventually released. The alginate phase contained an extremely small amount of surfactant (0.01 wt% Tween 20). c) The time evolution of the core-release from a poorly loaded fibre with adjacent alternating droplets is shown. d) Time variation in the fibre weight for the fibre hydration-responsive fibre shown in (a). The inset graph shows a zoomed-in view of the dynamics of the dehydration (drying) at room temperature in the initial ten minutes. All scale bars are 200µm.

To produce dehydration-responsive fibres, fibres with a single stream of asymmetrically encapsulated oil segments were used (Figure 8.2a1). This modification was intended to apply asymmetric stresses on the shell by transferring the high pressure within the droplets, built up due to the shell dehydration/contraction, towards the thinner edge of the

shell, which may crack under the increasing pressure and release the core content. However, the shell did not rupture upon dehydration (Figure 8.5a1).

We found that an inclined dumbbell-shaped oil-encapsulate, which touches the fibre edges on both sides, has a great potential for dehydration-induced shell rupture. Such entities could not be made by using a single stream of oil droplets. We used two off-centred streams of oil droplets, as shown in Figure 8.2a2, to produce inclined oil entities via inducing arrested coalescence of adjacent droplets formed in the absence of surfactants. However, a large clearance between the alternating droplets did not allow coalescence to occur. Consequently, the resulting fibres failed to build sufficient stress for shell rupture upon dehydration despite their non-symmetric features (Figure 8.5b1). When both droplet sequences were synchronised to form simultaneously (Figure 8.5c1), an interesting Janus-like symmetric fibre resulted, but did not rupture upon drying either.

When the oil droplets from both sequences were alternatively produced and closely packed in the fibre (Figure 8.6a1), every pair of oil droplets in the fibres underwent arrested coalescence. This resulted in a series of inclined dumbbell-shaped oil segments (Figure 8.6a2) that ruptured the shell upon drying, as shown in Figure 8.6a7. We found that the size-proportion of the two alternating oil droplets determines whether the core would be released upon fibre dehydration. If the volume of one droplet became too large in comparison to the other (Figure 8.3a6), the fibre lost its asymmetry, thus did not release the core upon dehydration. These surfactant-free fibres were quite resilient in hydrated state and contained the oil droplets for a minimum of seven months without undergoing any undesirable release via leakage. The fibres were also found to be robust against storage in pure water for several months, as they did not lose their responsive function.

The release behaviour was analyzed by monitoring the time-evolution of the weight of a sample responsive fibre during its dehydration. This weight-evolution was compared against a similar curve for a non-responsive fibre, where the oil droplets were stabilized by the addition of surfactant (1.0 wt% Tween20) to the alginate phase. Both samples were prepared using identical flow conditions and formulation. Figure 8.6d shows the reduction in the fibre weight during the dehydration process for both responsive and non-responsive fibres. The weight of the responsive fibre settled down to a smaller value than that for the non-responsive fibre, as the oil released from the fibre evaporated. The instance of the shell rupture and the concomitant oil-release can be understood as the point of deflection between the two curves (Figure 8.6d inset). The difference between the weights of the two fibres after 2h of drying at room temperature (~3.20 mg) was found to be nearly equal to the weight of the oil encapsulated in the sample fibre (~3.26 mg). The inset graph reveals that the onset of shell rupture and also the time taken for the released oil to completely evaporate correlates well with the time-scale shown in Figure 8.6a. For this particular fibre, the swelling ratio at the instance of the shell rupture (S_{rup}) was found to be ~15% of the saturation swelling ratio (S_{sat}). This implies the fibres released oil when their water content fell below 15% of their maximum water intake.

The release feature of the dumbbells was independent of other droplet pairs (dumbbells). This means that the oil content (encapsulated volume) of these responsive fibres could be easily tailored by generating the droplets at a reduced frequency, as shown in Figure 8.6c1. This configuration also led to the shell rupture upon dehydration, as shown in Figure 8.6c6.

The responsive microfibres could only be formed within a narrow range of alginate concentration (1 ± ~0.25 wt%) under the conditions of this study. We explored that a too

low alginate concentration would allow a rapid coalescence of the adjacent oil droplets, thus preventing the formation of the inclined dumbbell-shaped oil segments, which was a pre-requisite to rupture the shell upon dehydration. On the other hand, a high alginate concentration was found to result in a strong alginate shell around the oil droplets, which resisted the shell rupture upon dehydration. Additionally, the spacing between the two inner tips, and their location relative to the outer capillary tip also play important roles in the formation of fibres. If the two inner capillaries were too close (< ~20µm), the parallel oil phases coalesced prior to droplet formation. On the other hand, if the two tips were far apart from each other, implying that they were too close to the outer capillary tip (< ~40µm), the droplets escaped out of the alginate phase before gelation could occur. In spite of this narrow range of formulation and flow conditions, there exists an operational window within which the onset of rupture, in terms of fibre hydration level, can be adjusted. Such tailored responsive fibres with a graded release threshold could open up opportunities for moisture monitoring in wound healing applications.

One can imagine that for applications which demand simultaneous release of two or more components, a bundle of mixed responsive fibres can be used, where the release of two components occur from different fibres. However, a smart design would involve the concomitant release of the two components from a single fibre. Here, we demonstrate that the proposed release mechanism can be extended further to include the triggered release of two components, which confers multi-functionality to such responsive fibres. We demonstrate this by loading two sequences of different oil droplets, similar to that shown in Figure 8.6a1. We can see from Figure 8.6b1 that all (non-coalescing) pairs of droplets take an inclined dumbbell-like morphology when they come to close contact, which is the requirement for dehydration-induced release. To maintain the droplets identity, the droplet coalescence should be avoided prior to release. This poses a formidable task,

because while the presence of surfactant can hinder coalescence, results show that it may also make the fibres non-responsive to dehydration because of improved stability of the inclusions. A wide range of surfactant concentrations in the middle alginate phase was investigated, and it was found that using an extremely small concentration of surfactant (0.01 wt% Tween 20) in the alginate phase was sufficient to prevent the coalescence (Figure 8.6b1), yet low enough to allow the shell to rupture upon dehydration (Figure 8.6b4-b8). The use of higher surfactant concentration failed to produce responsive microfibres. The oil droplets in the fibres were quite stable against coalescence or leakage in hydrated state for a minimum of several months.

8.4.3.2. Towards fabrication of self-repairing microfibres

Fibres are usually susceptible to accidental mechanical fractures and breakages during their handling and operation. This is particularly true for dehydrated alginate fibres which are quite brittle. A possible remedy for reparation of the fibre at the fractured locations is to apply binding materials. However, it is not easy to identify the locations where ruptures occur nor they are easily accessible, especially in 3D fibrous networks, which would require a hands-free repairing mechanism.

In this section, we demonstrate how the asymmetric encapsulation strategy can be adopted to produce self-repairing fibres that allow simultaneous release of oil-based adhesive encapsulates upon their mechanical rupture. Fibres with asymmetric encapsulates can be tailor made to withstand a deired level of mechanical force. Such fibres will release adhesive materials if the force applied on them surpasses the designed tolerance. These asymmetric fibres, which act as sensor, can then be interwound with simple alginate fibres with a simillar mechanical strength. This ensure that the asymmetric fibres release the

adhesives and bind the fibres around the locations where the force exceeded the maximum tolerance and ruture occured.

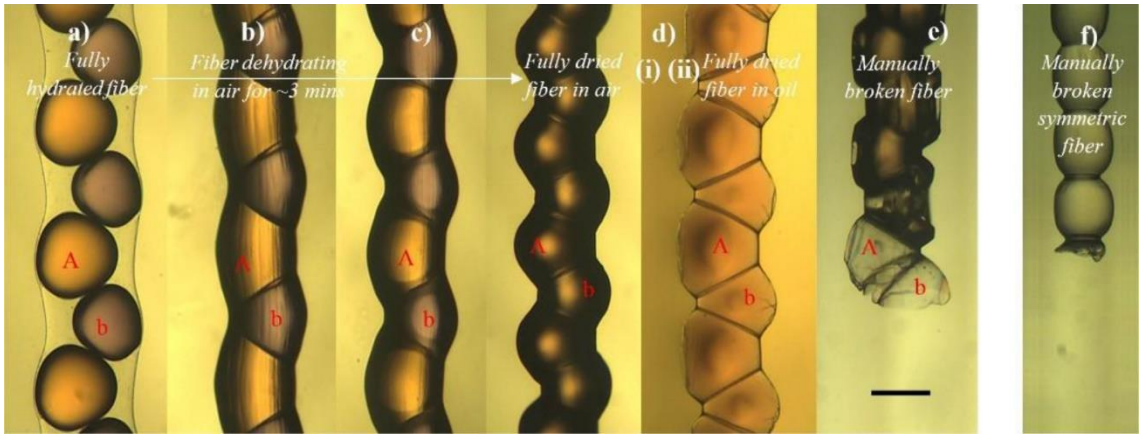

Figure 8.7 The micrographs show the formation of a multi-segmental fibre, obtained by dehydrating the fibre made with a high concentration of surfactant ((a) 1.0 wt% Tween 20; also shown in Figure 1d5). The alginate shell remains intact after dehydration, as visible in (d). When the dried fibre is broken by manual axial pull, the fibre splits in a way that releases core content from two neighboring and alternating segments, as shown in (e). The image in (d(i)) is dark due to high refractive index mismatch (air outside, oil inside), making the empty segments visible, as shown in (e). The image in (f) shows the rupture of one oil segment when a symmetric dried fibre is manually split. The scale bar is 200µm.

Broadly, two characteristics are required for the self-repairing fibres. First, the two reactive components should be independently encapsulated in a discrete fashion to avoid any premature reaction induced by coalescence. Second, the contents from alternating reactive parts should be released simultaneously at the same location to facilitate timely reaction in the event of the fibre split. The latter condition requires that both compartments share a large interface so that the rupture of one compartment automatically ruptures the second one.

All the compartmented microfibres with oil encapsulates reported in literature [33,36,63,64,134] have linear and discrete arrangement for the alternating compartments, which would fail to rupture simultaneously when the fibre is split. This limitation is

demonstrated Figure 8.7f, which shows that only a single compartment breaks when a fibre with linearly arranged encapsulated segments is split. This problem can be elegantly circumvented by encapsulating the alternating segments non-axisymmetrically, as shown in Figure 8.7a, using surfactant (1.0 wt% Tween20) in the alginate phase. The surfactant prevented both droplets coalescence and shell rupture prior to and after dehydration. The fibres, when dehydrated, gradually evolved into an array of close-packed compartments in a non-linear and a rather zigzag fashion (Figure 8.7d). The location of the droplet pairs is usually the weakest point along the fibre length, from where the fibre would usually begin to rupture when axially pulled or exposed to tensile stress. These fibres when split, released the contents from two adjacent compartments at the point of rupture (Figure 8.7e).

The separation distance between droplet pairs, and encapsulation volume, can be easily adjusted by altering the flow conditions, similar to that shown in Figure 8.6c. A simultaneous release of two reactive components, followed by a fast reaction, could reinforce not only the asymmetric fibre itself, bul also all neighboring fibres that suffered the breakage under the same load. Note that, similar to the structures designed for dehydration-responsive fibres, only compartments of almost equal size could be used. A too large volume for one component made the fibre symmetric with linearly arranged independent segments, (Figure 8.3a6), which released only one reactive component if ruptured due to an external stress. In this section, we demonstrated the proof of concept for the fabrication of such smart reactive microfibres using standard oils, but the practice can be easily extended to reactive oils.

8.5. CONCLUSION

A flexible one-step microfluidic approach was introduced for the fabrication of hybrid oil-encapsulated alginate microfibres with asymmetric encapsulates. Fibres with custom-designed internal architectures were produced by direct wet spinning and configuring the encapsulate location, size and frequency. Strategies for intertwining these fibrous building blocks to create complex fibre assemblies were demonstrated. An advantage of fibres with asymmetric encapsulates was exhibited by fabricating dehydration-responsive microfibres which displayed a core-release mechanism triggered by dehydration of the hydrogel shell. The compound shape of oil segments, achieved due to asymmetric encapsulation, promoted the shell rupture upon dehydration, which could be muted by adding surfactants to the alginate phase if required. Several factors, such as the formulation and device configuration, affected the fabrication of dehydration-responsive microfibres. The dehydration-induced release mechanism was also extended to fibres with double oil cargoes. As another potential application of the proposed asymmetric oil encapsulation, fibres with improved response to mechanical rupture were produced. These fibres showed simultaneous release of disimilar core materials around the fracture location, which could be exploited as reactive encapsulates for potential use in making self-repairing fibre pads.

Chapter 9 Gas-Filled Alginate Microfibres[††]

9.1. ABSTRACT

A facile buoyancy-assisted microfluidic technique for gas-encapsulation in alginate microfibres is presented, using a co-axial glass capillary setup. An aqueous sodium alginate solution was injected through the outer capillary into a quiescent bath of aqueous $CaCl_2$ solution, to form calcium alginate fibres. The air phase was introduced via the inner capillary through a pressure regulator, where the air pressure was varied between ~0.1-1.5 psi. The tubular and segmented air-encapsulate geometry was achieved via a one-step and two-step encapsulation method, respectively. A high calcium chloride concentration in the outer phase always produced fibres with smooth surface morphology, irrespective of the bubble size. To achieve fibres with wavy morphology, the alginate shell was made more deformable by slowing down the gelling dynamics via using a low $CaCl_2$ concentration. A slow gelation process also caused the partially gelled alginate fibres to stretch during formation, due to the buoyancy force exerted by the trapped air bubbles, a feature which was exploited to produce ultrathin alginate microfibres. The gas-filled microfibres were also morphed to produce other novel fibres structures, such as alginate fibres with segmented aqueous cores and beaded microfibres.

[††] Manuscript under preparation for journal publication.

9.2. INTRODUCTION

Gas-filled materials are characterised by their light-weight and low-density structures, which makes them an ideal candidate for energy-efficient transportation purposes. Several naturally-occurring structures also take advantage of their internal gas-filled cavities, such as aquatic plants use the large air-chambers in their leaves to stay afloat [145].

Gas-filled materials can also be artificially constructed, using advanced microfluidic techniques, to tune their shape and composition for a variety of applications. For example, Abbaspourrad et al. [146] demonstrated microfluidic formation of gas-filled micro-capsules with tuneable shell thickness, which were designed to withstand high-pressure environment. Similarly, Wan et al. [147] and Wang et al. [148] employed microfluidic techniques for forming gas-filled double emulsions, which were polymerised to fabricate hollow hydrogel microspheres and porous microparticles.

The encapsulation of a gaseous phase in bio-compatible materials, such as calcium alginate hydrogels, further increases the range of applications of void materials. For example, Huang et al. [149] fabricated calcium-alginate microbubbles on a millimetre scale by collecting uniform bubbled-alginate drops in calcium chloride solution. This technique was exploited by Yang et al. [150] to produce nanoparticles-alginate composite bubbles. More complex biocompatible void structures have also been reported. In one such case, Wang et al. [151] produced gas-filled micro-capsules with calcium alginate shell, and packed them together to obtain highly ordered 3D alginate scaffold, which were used for advanced tissue engineering applications.

While several investigations have been carried out to form a variety of gas-filled structures, there are very few reports on the formation of highly structured bubble-filled fibres using microfluidic techniques. Recently, Hou et al. [152] reported the generation of bubble-filled silica microfibres, which were used as filler materials to produce light-weight polydimethylsiloxane (PDMS) composites. Regarding the bubble encapsulation in biocompatible microfibres, only one report exists in the literature. In this study, Kang et al. [153] developed a complex microfluidic approach, integrated with multiple computer-controlled pneumatic valves, to encapsulate a variety of materials in alginate microfibres, including air bubbles.

In this chapter, we introduce a buoyancy-assisted microfluidic approach for facile formation of bubble-filled alginate microfibres with tuneable encapsulate geometry and fibre surface morphology. The proposed technique uses a vertically-oriented coaxial glass capillary setup, for gas-in-alginate flow formation, which is introduced in a non-confined quiescent aqueous solution of calcium chloride to form air-filled alginate microfibres. The resulting fibres move upwards due to the buoyancy force and are collected on the surface. The air-encapsulate geometry and size are altered with air and alginate phase flow conditions, while the fibre's surface morphology is tuned by varying the alginate and calcium chloride concentration. We take advantage of the slow gelation dynamics to produce ultrathin alginate microfibres via buoyancy-assisted stretching of the gelling fibres.

9.3. EXPERIMENTAL

9.3.1. Materials

Sodium alginate and calcium chloride (Sigma Aldrich) were used as received. The middle phase constituted of sodium alginate (1.0 and 4.0 wt%) in the aqueous phase, which was introduced into an aqueous bath containing a wide range of calcium chloride concentration. 1.0 wt% Tween 20(Sigma Aldrich) was used as a surfactant in the aqueous alginate phase. A regulated flow of filtered and compressed air was used as the inner gas-phase.

9.3.2. Device

Figure 9.1a shows the schematics of two microfluidic devices for *one-step* and *two-step* encapsulation of air within the alginate fibres. To fabricate the devices, a circular capillary (ID: 0.10 mm, OD: 0.17 mm) was inserted into a wider capillary (ID: 0.30 mm, OD: 0.40 mm). Both capillaries were used as received without surface treatments. To make the device for *one-step* encapsulation, the inner capillary tip was placed at the same level with the outer capillary tip, while the inner tip was kept behind the outer tip for a *two-step* encapsulation. The air phase was introduced via the inner capillary at a controlled pressure, using a digital pressure gauge (Omega) with a 0.1 psi resolution. The alginate phase was introduced through the interstitial spaces between the two capillaries. The outer aqueous phase containing calcium chloride was kept quiescent, in which the coaxially aligned capillary setup was introduced vertically as shown in Figure 9.1a. The formed fibres, examples of which are shown in Figure 9.1b, were collected at the top of the cuvette, facilitated by the buoyancy force exerted by the encapsulated air bubbles. A high-speed video recording camera (Photron FastCam SA-5 (monochrome)) was used to record fibre formation.

9.4. RESULTS AND DISCUSSION

Gas-filled alginate microfibres were produced using a *one-step* and *two-step* microfluidic device configurations, respectively (Figure 9.1a), and were obtained in two different formats, *tubular* and *segmented* encapsulation, as shown in Figure 9.1b.

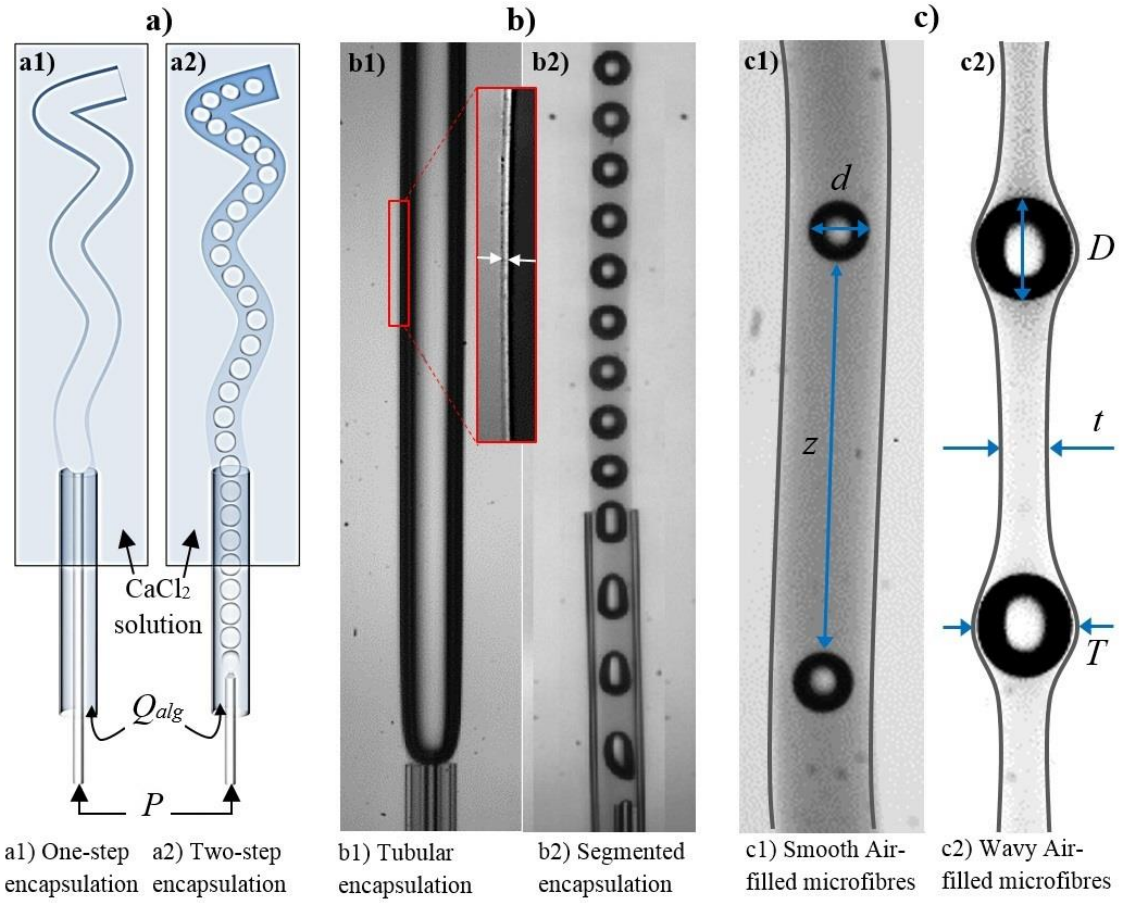

Figure 9.1 a) Schematics of the *one-step* and *two-step* air-in-alginate microfluidic encapsulation approach. **b)** Optical micrographs showing the formation of tubular (b1) and segmented (b2) air encapsulates. The arrows in the inset image shows the shell thickness of the tubular microfibre. **c)** Fibres with segmented encapsulates having smooth (c1) and wavy (c2) surface morphology. The assigned nomenclatures to different fibres dimensions are also illustrated.

9.4.1. Tubular air-encapsulation

Alginate microfibres with tubular air-encapsulates were formed via the *one-step* encapsulation approach, which is characterised by having the inner and outer capillary tips at the same level, as schematically depicted in Figure 9.1a1. This is the same encapsulation approach which was adopted to tune the oil droplet location within the fibre (Chapter 7). In case of air encapsulation, the tubular fibres were formed within a limited range of flow conditions, which required a sufficiently high alginate phase flow rate (Q_{alg}) and high air pressure (P). As an example, the tubular fibre shown in Figure 9.1b1 was obtained at Q_{alg} = 15 ml/h and at an air pressure of 0.8 psi. A low Q_{alg} formed a thin and weak hydrogel shell, which failed to contain the pressurised air encapsulates and resulted in punctured fibres, which allowed the air phase to escape. On the other hand, a low-pressure air flow could not reach the Laplace pressure needed to exit the flow through the inner capillary tip to produce simple alginate fibres. When air pressure was high enough to overcome the Laplace pressure, large air bubbles were formed, but they could not be engulfed by the alginate shell. As a result, punctured fibres were formed. Large bubbles were formed outside the outer capillary because the drag acting on the forming bubbles was minimised. The significant reduction in drag is one of the features of *one-step* encapsulation approach, which has been elaborated upon in Chapter 5 and Chapter 7 (Figure 7.5b).

A tubular microfiber could only be formed at high encapsulation volume (ϕ_{air}), which resulted in the formation of extremely thin shells, as highlighted in Figure 9.1b1 (inset), similar to the observation for tubular oil encapsulation (Figure 7.6). A high ϕ_{air} is required because a gaseous jet inside an aqueous phase should be forced to form by substantially increasing the inner phase flow rate, to overcome the high surface tension.

9.4.2. Segmented air-encapsulation

Within the limited range of flow conditions explored via the one-step approach, the segmented or discrete encapsulation of air microbubbles was not observed. However, it is theoretically expected that segmented air encapsulates could be achieved, via the one-step approach, at a significantly high alginate phase flow rate that usually prevents the formation of large bubbles, but such high Q_{alg} values were not explored during the investigation. An alternative *two-step* encapsulation approach was adopted (Figure 9.1a2), which broke down the air phase into a stream of tiny microbubbles inside the outer capillary at low Q_{alg} due to a sufficient drag exerted by the flowing alginate phase. The stream of air bubbles is carried by the alginate phase towards the exit orifice of the outer capillary, where the bubbles get trapped in the hydrogel fibre formed due to reaction between the alginate phase and calcium ions present in the outer phase.

The bubble size can be tuned by regulating the alginate phase flow rate and the air pressure. The volumetric flow rate of the inner gas phase increases with the air pressure. This reduces the shear stress on the forming gas bubble at the inner capillary tip, thereby increasing the bubble size (Figure 9.2a). An increase in the alginate phase flow rate, on the other hand, increases the shear stress on the bubble during its formation, thereby reducing its size, as shown in Figure 9.2b.

In addition to varying the alginate phase flow rate and air pressure, the bubble size can also be adjusted by the surfactant concentration in the middle alginate phase. An increase in the surfactant concentration reduced the surface tension between the gas phase and the aqueous alginate phase and thus decreased the bubble size (Figure 9.2c).

9.4.3. Surface roughness of air-filled microfibres

The surface morphology of a fibre is an important property, which can be classified as *smooth* and *wavy*, where the smooth fibre is characterised by a flat profile across the length of the fibre, while a wavy morphology is identified with a significant variations in the diameter along the fibre length, indicating high surface roughness (See Chapter 7). Wavy fibres, compared to smooth fibres, have higher surface roughness due to the non-uniform surface area across their length, which could be useful for several applications, such as enhanced water collection properties due to the bulged surfaces at regular intervals [63].The degree of waviness, introduced in Chapter 7, is a measure of the surface roughness of a fibre.

For gas-filled microfibres, tubular fibres had a smooth surface morphology in wet and dry state, whereas fibres with segmented bubbles always showed wavy morphology after dehydration. However, the surface morphology of fibres encapsulating segmented bubbles could be tuned to vary from smooth to wavy in the wet state.

9.4.1.1.Smooth fibres

The surface roughness of fibre is determined by the gelling dynamics of the alginate phase, which depends on the alginate and calcium chloride concentration. The fibre geometry for a typical smooth and a wavy fibre is shown in Figure 9.1c1 and Figure 9.1c2, respectively A high concentration of both reactants (both 4 wt%) always led to fibres with smooth surface due to rapid and strong gelation (Figure 9.2). In case of a low $CaCl_2$ concentration (1 wt%), smooth fibres, characterised by the bubble diameter being smaller than the fibre thickness, were only observed at high alginate phase flow rate (Q_{alg}).

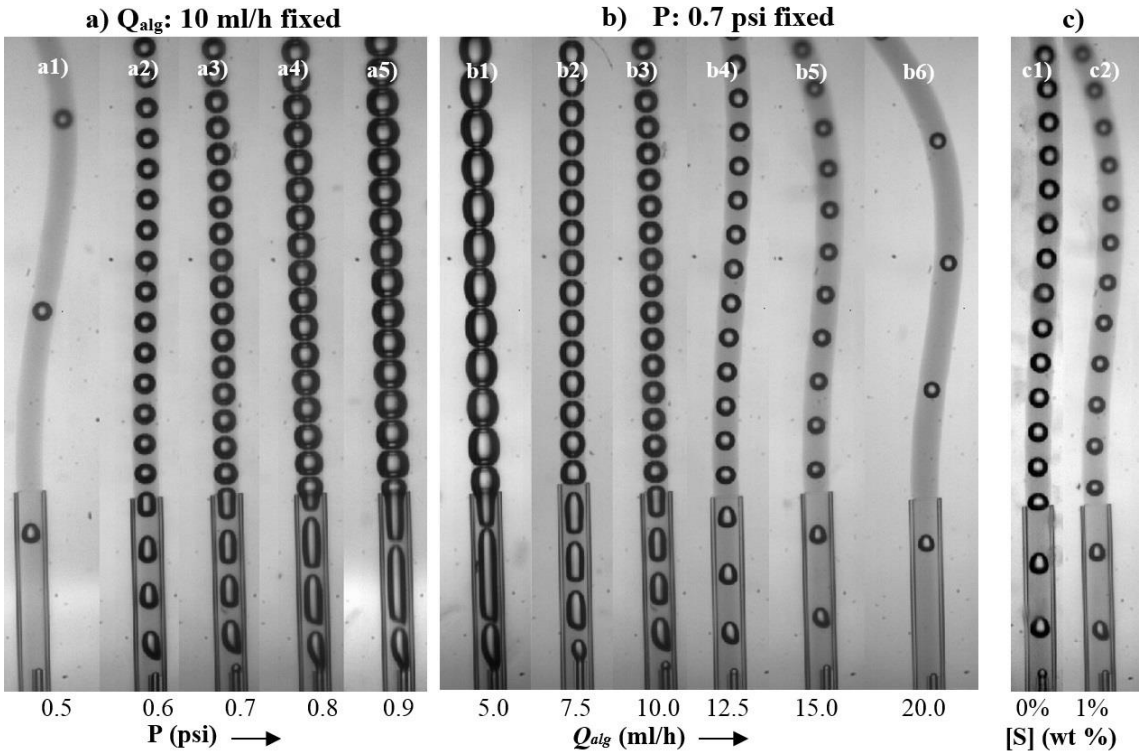

Figure 9.2 Effect of increasing **a)** air pressure and **b)** alginate phase flow rate on the formation of smooth gas-loaded alginate microfibres at 4wt% Alginate and 4wt% $CaCl_2$ concentration in the middle and outer aqueous phase, respectively. 1wt% Tween20 was added in the alginate phase to stabilize the bubbles. **c)** A reduction in the bubble size in the presence of surfactant.

The smooth morphology of the fibres formed at high alginate and $CaCl_2$ concentration was not affected by the increase in bubble size, as observed in Figure 9.2a5. Instead, the strongly gelled smooth hydrogel interface deformed the air bubbles to become ellipsoidal (Figure 9.2b1).

9.4.1.2. Wavy fibres

We observed in the previous section that the wavy fibres could not be formed at high alginate and $CaCl_2$ concentration. An alternative approach to produce wavy fibres could be to reduce the alginate fibre thickness between the consecutive encapsulates, by reducing Q_{alg} [33]. However, we also observed that the fibre formation suffered from a risk of outer tip blockage at low Q_{alg}. This failure occurred at high $CaCl_2$ concentration

due to a premature gelation of the alginate phase inside the outer capillary near its tip, due to a fast diffusion of Ca+ ions into the slow moving alginate phase.

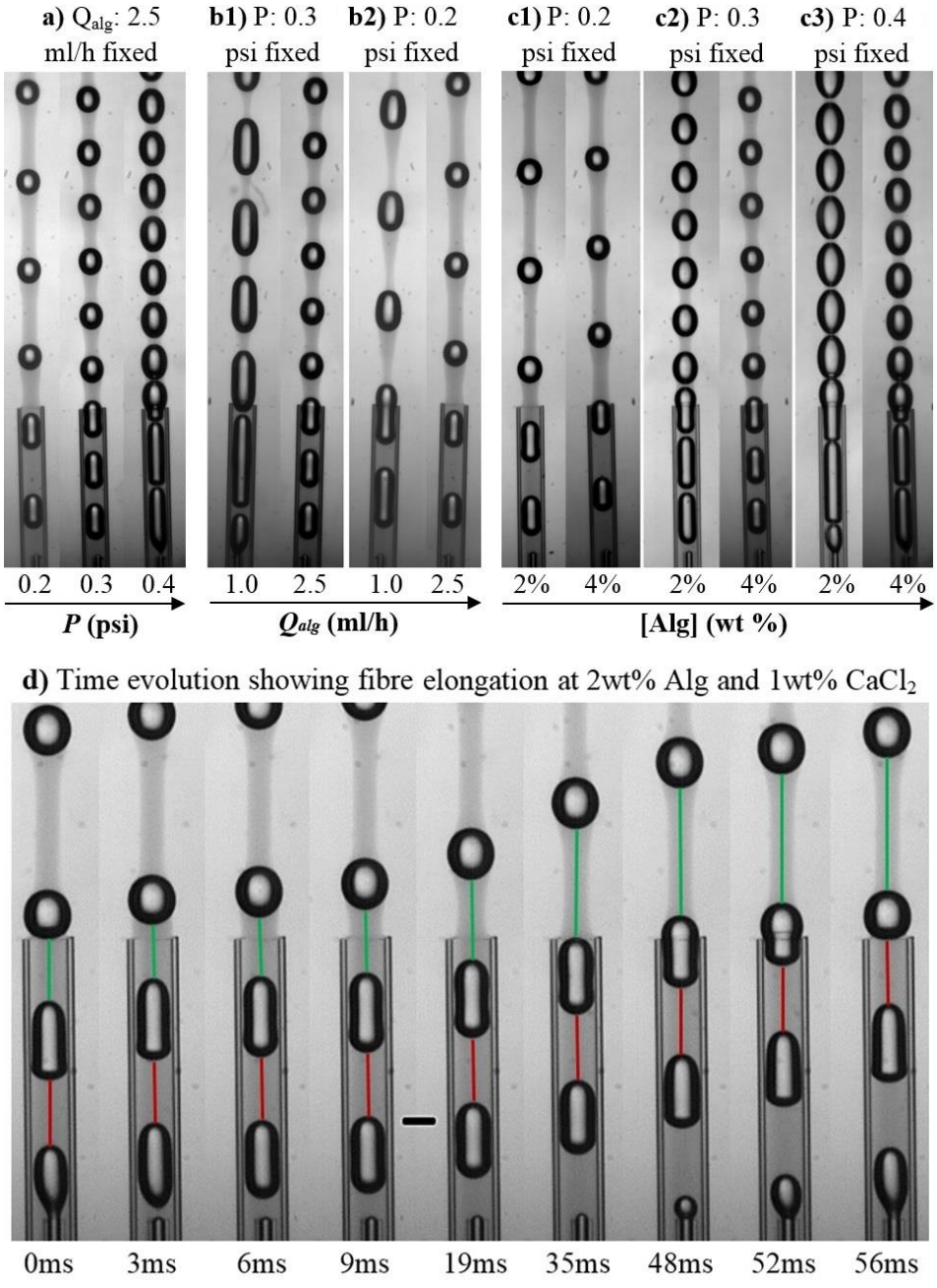

Figure 9.3 Formation of wavy air-encapsulated alginate microfibres at 4wt% Alginate and 1wt% $CaCl_2$ concentration is shown in wet state, where the wavy surface morphology can be tuned by varying the **a)** air pressure and **b)** Q_{alg}. **c)** Effect of alginate concentration on the fibre morphology studied at three different air pressures and a fixed Q_{alg}: 2.5 ml/h. **d)** Time-evolution of fibre formation at low alginate and CaCl2 conc. (2wt% and 1wt%, respectively), showing fibre elongation during its formation at 0.2psi air pressure.

To achieve fibres with wavy surface morphology, the gelling process should be slowed down by reducing the $CaCl_2$ and alginate concentration. The effects of reduced calcium chloride and alginate concentrations in the middle and outer phase, respectively, on surface morphology are shown in Figure 9.3a-b and Figure 9.3c, respectively. A weak gel formed around the encapsulated bubbles, due to either low $CaCl_2$ concentrations in the outer phase (Figure 9.3a-b), or the low volume of alginate present in the shell phase (Figure 9.3c), easily deformed in the radial direction when the bubble size was increased. This also helped in forming fibres at significantly low Q_{alg} (~ 1 ml/h, Figure 9.3b1) without blocking the inner capillary tip, which further assisted in forming fibres with increased surface roughness.

9.4.4. Ultra-thin microfibres via buoyancy-driven stretching:

The presence of air in the fibre provides another mechanism by which the morphology of fibres can be tailored. Additionally, the lean alginate phase was observed to elongate significantly during gelation, which reduced the alginate fibre diameter (t) even further. A time-evolution of the alginate phase elongation during gelation at low alginate concentration is shown in Figure 9.3d. It is clear that the distance between consecutive air drops inside tube remained almost constant, but increased as soon as air bubbles left the tube under the influence of buoyancy.

This buoyancy-driven thinning of fibres was utilised to produce ultra-thin alginate microfibres with extremely high surface roughness. This was achieved by using an extremely low concentration of $CaCl_2$ (upto 0.05 wt%) in the outer calcium chloride solution, as shown in Figure 9.4, which only allowed an extremely low rate of gelation.

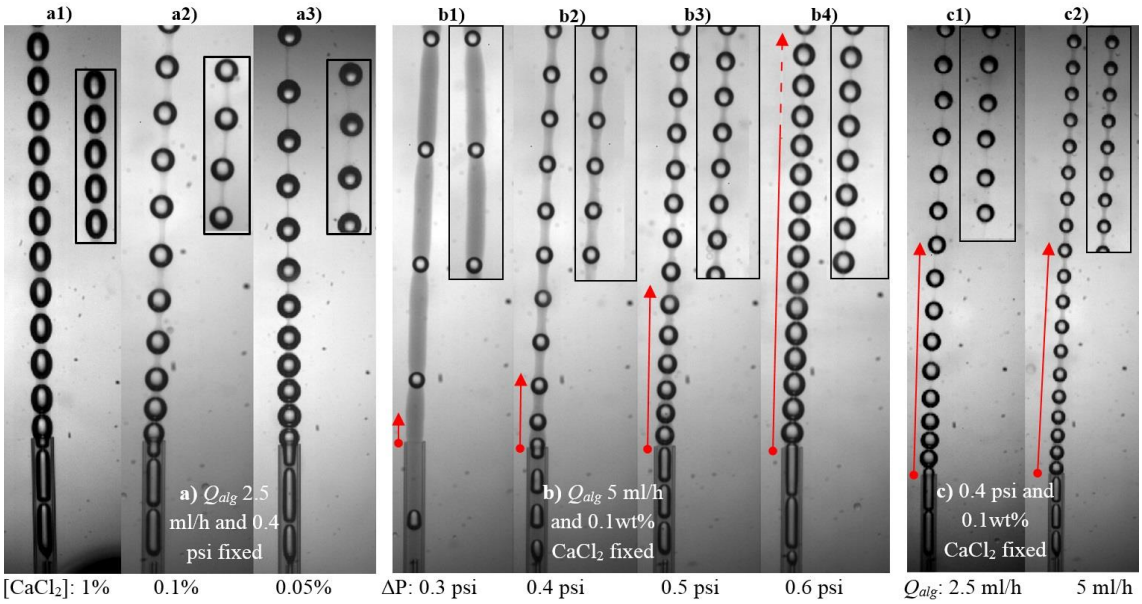

Figure 9.4 Effect of **a)** calcium chloride concentration, **b)** air pressure, and **c)** alginate phase flow rate (Q_{alg}) on the fibre elongation. The inset images show the corresponding steady-state fibre geometries captured downstream, after the elongation has completed. The red arrows indicate the distance from the outer capillary tip, at which the stretching of the fibres stopped. The middle phase contained 4wt% alginate and 1wt% Tween20 in all cases.

At such a low $CaCl_2$ concentration, the alginate phase could be elongated to a much greater length by the accelerating stream of air bubbles, before it completely gelled. Figure 9.4a3 clearly shows that the distance or the thread length between consecutive air bubbles (z) increased, accompanied by a continuous thinning of the thread as the fibre moved upward, until further stretching was stopped when the gelling fibre achieved sufficient strength with time to withstand the tensile force. This extreme stretching of the middle alginate phase resulted in the formation of ultrathin microfibres (~10µm diameter for fibre shown in Figure 9.4a3) in wet state, and also in extremely wavy alginate nanofibres with air encapsulates in dry state.

In addition to varying the calcium chloride and alginate concentrations, the stretching phenomenon could also be tuned by altering the air pressure and alginate phase flow rate, as shown in Figure 9.4b and Figure 9.4c, respectively. An increase in the air pressure

further reduced the fibre thickness (Figure 9.4b), due to the increase in bubble size and the associated buoyancy force, and also created more surface area to be covered, which reduced the alginate volume between consecutive bubbles. The thinning of fibre with increasing air pressure also increased the distance at which the stretching stopped (marked by red lines in Figure 9.4b), which was caused by the faster transportation of the alginate phase resulting from the increased rate of bubble formation.

On the other hand, while the alginate phase flow rate did not significantly affect the maximum stretched length for fibres, but increased the fibre thickness (Figure 9.4c). The increase in fibre thickness was also assisted by the reduction in bubble size.

9.4.5. Dehydration-induced morphological variations

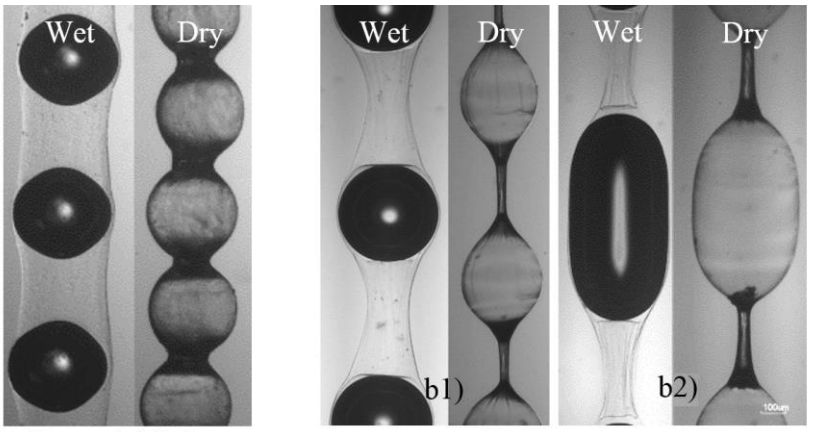

a) Wet and dried states of smooth fibres

b) Wet and dried states of wavy fibres with spherical and plug-like bubble encapsulates

Figure 9.5 Free-space drying of **a)** smooth and **b)** wavy fibres with discrete air encapsulates.

The alginate fibres are widely used in dried state in different formats, such as free-standing fibres and non-woven pads. Therefore, not only it is important to study the fibre morphology after they are dehydrated, but also the dehydration method can itself provide an alternative way of altering fibres morphology.

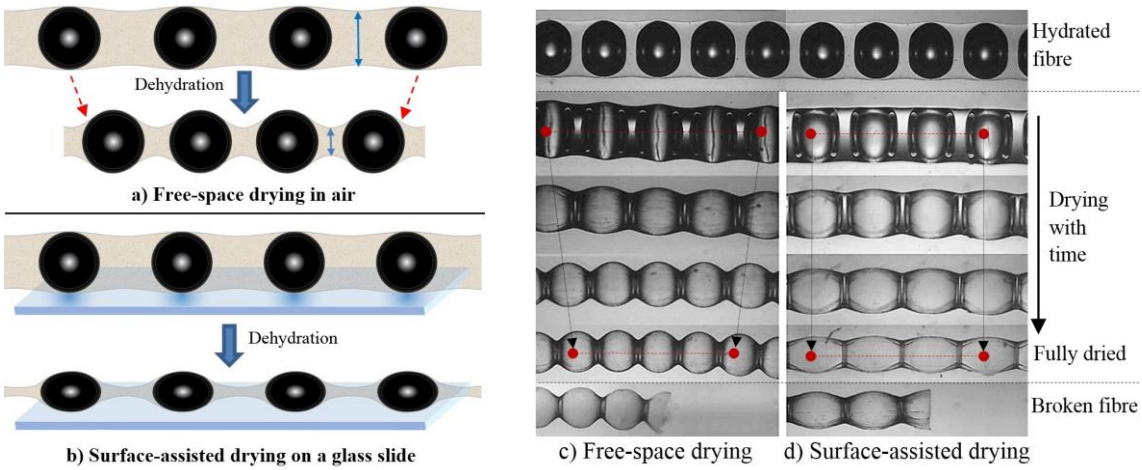

Figure 9.6 Comparison of the morphological variation of air-encapsulated alginate fibre by **a)** free-space drying and **b)** surface-assisted drying.

The images of smooth and wavy gas-filled microfibres after their dehydration are shown in Figure 9.5a and Figure 9.5b, respectively. A typical free-space dehydration of an alginate fibre, where the fibre surface is completely surrounded by air from all sides, causes considerable shrinkage across its two axis, namely length and diameter, as shown in Figure 9.6a, however, the length of resulting dried fibre reduces more significantly. An alternative surface-assisted drying mechanism is presented, which does not allow axial shrinkage in the fibres, and retains their full length even after dehydration, a schematic of which is shown in Figure 9.6a. In this process, the wet fibre is placed on a dry and flat (glass) surface for dehydration, instead of being held in the free-space air. Figure 9.6c-d shows a comparison between the two drying mechanisms of the same fibre. In case of surface-assisted drying, the bulged locations on the fibre's wet surface, formed because of the air bubbles within, stick to the hydrophilic glass surface due to capillary forces, thus securely pinning the fibre down on the surface (Figure 9.6d). The pinning of the fibre did not allow it to shrink axially upon its dehydration and thus maintained its original fibre length. To compensate for the lack of axial shrinkage, however, the fibre underwent more radial shrinkage, while deforming the shape of encapsulate without rupturing the

shell, and transformed the spherical encapsulate to an ellipsoidal one. This mechanism works well for smooth as well as wavy fibres, as the smooth fibres also turned wavy during their dehydration.

9.4.6. Potential applications

In addition to the formation of ultrathin alginate microfibres, achieved via buoyancy-assisted stretching, we present two potential applications of undertaking bubble encapsulation in microfibres. We demonstrate how a bubble-filled fibre can be appropriately morphed into different novel fibre morphologies, such as hydrogel microfibres with segmented aqueous encapsulates and beaded alginate microfibres.

9.4.6.1. Fabrication of alginate microfibres with segmented aqueous encapsulates

While tubular encapsulation may provide advantages such as high encapsulation volume (Figure 7.6), it suffers from a high *spillage ratio* (7.4.6), that is, fibres with tubular encapsulate geometry are highly susceptible to complete core-loss after an accidental rupture, especially during their handling. Fibres with segmented encapsulates, on the other hand, are highly robust against core-loss due to the discontinuous encapsulated phase. However, the encapsulation of an aqueous phase in alginate microfibres always results into its tubular encapsulation due to the low interfacial tension between the alginate phase and the inner water phase. In this section, we demonstrate how the air-encapsulated microfibres can be transformed into alginate fibres with segmented aqueous encapsulates.

To produce alginate fibres with segmented water cores, the air bubbles were allowed to dissolve out in water, during which the core-space was re-filled by water from the continuous phase. To promote the dissolution of the trapped air bubbles, the gelation of

the hydrogel shell was interrupted prematurely, before its complete gelation, by removing the fibre from the calcium chloride solution immediately after its formation, and immersing it in a bath of pure water (Figure 9.7a). The air bubbles slowly dissolved away into the pure water, in ~30 minutes for the figure shown in Figure 9.7a1, while the space thus created was replaced by water from the continuous phase. To confirm that the dissolution of air bubbles in water happened because of incomplete alginate gelation, the bubble-filled fibres were also observed in a calcium chloride solution for 2 hours after its formation, but did not show any sign of air-core dissolution.

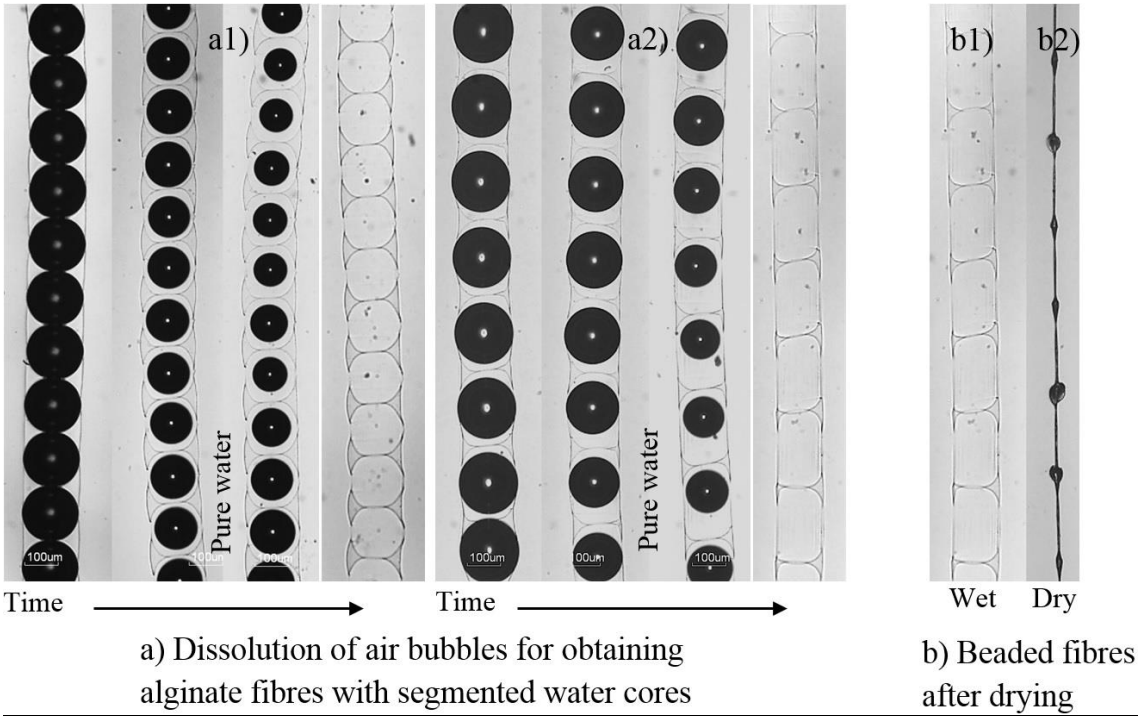

Figure 9.7 a) Dissolution of (a1) small and (a2) large discrete air-encapsulates from the fibres by immersing the fibres in pure water immediately after their formation in aqueous calcium chloride solution. **b)** A fibre with segmented water cores is dehydrated to obtain beaded alginate fibres.

This approach for fabrication of fibres with segmented aqueous cores also has its limitations. For example, large molecules with long polymer chains may not be able to pass through the alginate phase and be encapsulated. However, the range of application can be extended by creating a lightly crosslinked macro porous hydrogel matrix via

altering the alginate and calcium chloride concentrations, which can tune the pore size between a few nanometres to tens of micrometres, as discussed by Simpliciano et al. [154].

9.4.6.2. Fabrication of beaded alginate microfibres

Variation in the fibre's thickness at regular intervals may lead to the formation of fibres with bead-like structures. The presence of such bead-like structures can significantly alter the fibre's properties under certain conditions. For example, recent investigations have shown that the heterogeneous beaded-fibre structure enables a non-woven fibre mesh to achieve enhanced de-wetting properties due to the increased surface roughness [155,156]. In electrospinning techniques, the beads-on-string structure is obtained by tuning the fluid properties such as surface tension and viscosity [157,158], which affects the spacing between the beads. In wet spinning approaches, beads are formed by inducing interfacial instabilities [159]. However, these methodologies lack precision, accuracy, and flexibility to controllably tune the bead size and frequency.

We introduce a stepwise approach to fabricate beaded calcium alginate microfibres with uniform and tunable bead structures. Firstly, we formed alginate microfibres with uniformly spaced air bubbles and replaced the air-cores with water phase, as discussed in the previous section. These fibres with segmented water-cores were then dehydrated. After their complete dehydration, the fibres structure morphed into beaded alginate microfibres with uniformly spaced beads, as shown in Figure 9.7b. The advantage of this approach is that the frequency of the beads can be precisely and accurately tuned with the entrapped bubble frequency, while the bead size can be controllably varied with the alginate volume present between the consecutive bubbles. Furthermore, this approach can be extended to achieve more complex surface morphologies with exquisite precision,

such as alternating small and large bead structures by simultaneous encapsulation of two bubble streams.

9.5. CONCLUSION

A facile buoyancy-assisted microfluidic technique was introduced for a continuous fabrication of air-filled alginate microfibres with tuneable encapsulate and fibre morphology. An aqueous solution of sodium alginate was introduced through a vertically oriented glass capillary into the outer calcium chloride solution, which reacted with the calcium ions from the outer phase to form calcium-alginate hydrogel microfibres. The air phase, introduced into the alginate phase through an inner glass capillary, was trapped in the hydrogel network and formed air-filled fibres. The air-encapsulation was explored using *one-step* and *two-step* configurations. The one-step approach, where the inner capillary tip was kept at the same level with the outer tip, led to the formation of tubular air-filled fibres, while the two-step encapsulation, where there was a distance between the two tips, resulted in fibres with segmented air bubbles.

A wide range of segmented bubble size and geometry, including spherical, ellipsoidal and plugs, was obtained by altering the air and alginate phase flow conditions. The surface morphology of the fibres turned from smooth to wavy with decreasing calcium chloride concentration due to slowing down of the gelation process. The slow gelation dynamics, and the strong buoyancy force exerted by trapped bubbles, were exploited to produce ultrathin alginate microfibres (~10um diameter). The fibres were stretched further with increasing bubble size and decreasing alginate phase flow rate.

A new dehydration-based approach for altering fibre morphology was introduced. This technique, termed as *surface-assisted drying*, prevented the axial shrinkage of fibers

during dehydration by pinning them on a hydrophilic surface, thus allowing a substantial radial deformation of the encapsulates.

The bubble-filled alginate microfibres were also morphed to produce different types of fibre structures, such as alginate fibres with segmented aqueous cores and beaded microfibres. This was achieved via dissolution of the entrapped air bubbles in water through weakly gelled shells, as water replaced the air. The dehydration of fibres with segmented water cores transformed them into beaded alginate microfibres.

Chapter 10 Conclusions and Recommendations for Future Studies

10.1. CONCLUSIONS

A hybrid microfluidic emulsification technique, termed as 'buoyancy-assisted microfluidics', was introduced as an alternative emulsification tool to produce uniform structures. This approach combined the operational advantages of the microfluidic technology, such as high droplet uniformity, with the convenience and scalability of a buoyancy-assisted system due to a quiescent outer phase. The proposed system was employed to form a wide range of highly monodisperse simple and compound emulsions on a wide range of drop sizes, particularly on a millimetre scale, which is usually difficult to achieve using the conventional microfluidic techniques. The buoyancy-assisted microfluidic device was also employed to undertake buoyancy-favoured encapsulation applications, such as encapsulation of low density oil droplets and air bubbles in hydrogel microfibres. The investigations provided a unified approach for facile fabrication of a wide range of novel materials, including millimetre-sized ultrathin shelled capsules and dehydration-responsive microfibres. A summarised conclusion, highlighting the key findings from each case-study, is presented below.

Buoyancy-driven Drop Generation via Microchannel Revisited:

- The buoyancy-assisted system was revisited for a critical analysis of the drop formation mechanism using three different alkanes.
- Three controversial phenomena, namely the relevance of pinch-off time and satellite drop formation on the final drop size in low viscosity systems, the effect of dynamic interfacial tension at low phase velocity conditions, and the variations in drop uniformity in the jetting regime were investigated.
- The exclusion of fluid flow volume during pinch-off time, combined with the estranged satellite drop volume, was found to be negligible (less than 3% of the final drop volume) for low viscosity systems.
- The dynamic interfacial tension was found to be important at low flow rates (Q). Polydispersity of the drops in the jetting regime was found to be strongly related to the fluctuations in the break-up lengths, where the drop uniformity increased with Q after the onset of jetting.
- We also extended the existing force-balance model to include the effect of dynamic interfacial tension to address the discrepancy in drop size prediction at low Q. Additionally, a dimensionless analysis was performed which revealed that the buoyancy force dominates even at the onset of jetting in a buoyancy-driven system.

Millimetric Core-Shell Drops via Buoyancy-assisted Non-Confined Microfluidics:

- The buoyancy-assisted drop formation was extended to obtain core-shell drops on a millimetre scale using a coaxial capillary arrangement. A wide range of drop sizes (200μm-6mm) and shell thickness (2μm-1mm) were achieved.
- The surfactant concentration in the middle and the outer phase was the primary variable for tuning the shell thickness. While the use of small amount of surfactants helped minimize the shell thickness, it restricted the flow conditions under which stable and uniform drop could form.
- A fundamental physical model was developed for drop and core size prediction, which was validated for a surfactant-free system. The dimensionless analysis revealed that the buoyancy force dominated the core-shell drop formation at the onset of jetting regime, similar to the simple drop formation. However, the addition of surfactants, which promoted the formation of thin shelled drops, allowed the kinetic force to exceed the buoyancy effect at the onset of jetting.

Large Ultrathin Shelled Drops Produced via Non-Confined Microfluidics:

- Higher surfactant concentrations (below, at, and above CMC) were also explored to achieve ultrathin shelled drops.
- However, the minimum absolute and relative shell thickness, as well as the minimum drop size, was found at an intermediate surfactant concentration.
- The shell phase of these double emulsions were polymerised to fabricate ultrathin shelled capsules on a millimetre scale.

Properties and Characterisation of Oil-Encapsulated Alginate Microfibres:

- The buoyancy-assisted technique took advantage of buoyancy to produce fibres encapsulated with low density oil phases, which could be easily collected at the surface due to buoyancy effect.
- Compound fibres with a wide range of oil encapsulate geometry were produced, which ranged from segmented tubular to plug-like, ellipsoidal and spherical, and eventually to grouped discrete segments.
- A characterisation method for fibres was introduced, and the impact of encapsulate geometry on different fibre properties, such as the encapsulation volume, spillage ratio, surface roughness and mechanical strength, were investigated.
- Fibres with spherical and ellipsoidal encapsulates showed maximum surface roughness and minimum spillage ratio, respectively indicating excellent fibre interlocking properties and minimal core-loss in accidental fibre fracture, but allowed a low encapsulation volume.
- In contrast, tubular fibres provided maximum encapsulation volume, but suffered from a high spillage ratio and a smooth surface morphology.
- For a fixed oil-core to alginate-shell volume ratio, the fibre with tubular encapsulate underwent maximum elastic and plastic deformation under tensile loading, before withstanding a maximum tensile force until failure.
- Fibres with increased alginate shell volume ratio (ϕalg) withstood a higher tensile force. However, the strength of the fibres reduced at high ϕalg if the increase in ϕalg changed the encapsulate geometry from tubular to discrete oil segments.

Asymmetric Alginate Microfibres with configurable oil-encapsulates:

- The oil encapsulation in fibres was also extended to encapsulation of parallel oil streams to fabricate multi-compartmental fibres, where the droplets were encapsulated while being formed.
- This encapsulation technique allowed the fabrication of fibres with tuneable encapsulate location within the fibres, from symmetric to fully asymmetric position.
- The droplet size and frequency in asymmetric fibres were tuned to produce active fibres, which fracture their shells upon their dehydration. These active fibres could be useful for benign core-release applications, which do not require dissolution of the shell to release the core.
- The composition and morphology of asymmetric fibres were also tuned to demonstrate enhanced response to mechanical failure, where different core components, such as reactive ones, were released simultaneously. This could form the basis to obtain fibres which demonstrate self-repairing properties upon their mechanical fracture.

Gas-Filled Alginate Microfibres:

- In the last section, the buoyancy-assisted microfluidics was employed to encapsulate air micro-bubbles within the alginate fibres. Such fibres could be potentially used to build light-weight composites.
- Furthermore, the buoyancy force due to the trapped air bubbles was utilised to produce ultrathin microfibres by stretching the gelling alginate phase. To further enhance the buoyancy-assisted stretching, the gelling dynamics were slowed down by reducing the calcium chloride concentration in the outer phase.

- These bubble-encapsulated fibres were also manipulated to produce fibres with segmented aqueous encapsulates, which are generally difficult to achieve. Additionally, the air-filled fibres were also morphed to produce beaded microfibres with controllable bead size and frequency.

10.2. RECOMMENDATIONS FOR FUTURE STUDIES

As this thesis reports the first extensive investigation carried out on the buoyancy-assisted microfluidic emulsification approach, particularly on compound emulsification, several further studies need to be conducted to fully realise and utilise the unique set of advantages this hybrid mechanism offers. In this regard, few likely future extensions have been presented below, which are expected to provide further insights into the distinctive features of buoyancy-assisted microfluidics.

a) Millimetric drops are highly susceptible to destabilisation mechanisms, such as coalescence and creaming, due to the high contact area between drops, and increased body forces. The use of surfactants may help stabilise large drops for some time, but their long-term stability still remains a major concern. The buoyancy-driven system can be used to stabilise millimetric drops, without the need of surfactants, by precipitating a thin coating on the drop's surface via *coacervation*, before the drops come in contact at the surface. Such a surfactant-free stabilisation can be achieved because the slow motion of drops in a quiescent continuous phase allows sufficient time for the precipitation to occur.

b) The formation of large ultrathin shelled drops can be further extended to produce higher-order millimetric drops with compound multi-layered and multi-compartmental structures, such as onion-type triple emulsions and dumbbell-like ultrathin shelled doublets.

c) The release of the core-content from the ultrathin shelled capsules can also be regulated by making the shell porous. For such applications, the shell should be made of a high-internal phase emulsion (HIPE), which would lead to the formation of pores in the shell upon polymerisation, where the pore size would depend on the size of dispersed micro-droplets in the shell phase. The rate of release can be increased by enlarging the pore size, or decreased by reducing the size of pores.

d) The dehydration-responsive microfibres can be further tuned to fabricate fibres with more advanced core-release responses, such as fibers with controlled-release, in contrast with burst-release in this work, and fibers with selective-release, by producing a Janus-like fibre with responsive and non-responsive halves.

e) The oil and air encapsulation in a gelling alginate phase can be utilised to produce a wide range of simple alginate fibres with anisotropic surface morphologies. This can be achieved via enabling a (buoyancy-assisted) forced escape of the segmented oil/air encapsulates, which can alter the shape of the fibre surface during their exit in a controllable manner. The sharpness and magnitude of the regular deformations inflicted on the fibers can be tuned via altering the alginate and calcium chloride concentrations.

Appendix A

Derivation of surface-average age (t_{av}) of a growing spherical drop:

We assume the drop is always spherical while growing at the tip of the channel. *Q* is the constant volumetric flow rate feeding the drop; *A* is the surface area of the drop having radius *r* at any time *t*.

The interface created at the beginning of the drop formation has the longest age, which is equivalent to the time of drop formation t_f. Similarly, the surface generated at the point of drop detachment has the shortest (zero) surface age. Thus, the surface-average age of a drop, which is eventually ruptured at t_f with volume V_f, area A_f and radius r_f, can be expressed by,

$$t_{av} = \frac{1}{A_f}\int_0^{A_f} (t_f - t)\, dA$$

$$t_{av} = t_f - \frac{1}{QA_f}\int_0^{r_f} \frac{4\pi r^3}{3}\, 8\pi r dr$$

$$t_{av} = t_f - \frac{1}{QA_f}\left(\frac{2V_f A_f}{5}\right)$$

$$t_{av} = t_f - \frac{2}{5}t_f = 0.6t_f$$

Note that the surface-average age of the drop is independent of volumetric flow rate.

Appendix B

MATLAB code for 2D-reconstruction of symmetric oil-encapsulated microfibres

```
clear all
close all
clc
%% Time specifications:

Fs = 10; % samples per second
dt = 1/Fs; % seconds per sample
StopTime = 2500; % seconds
t = (0:dt:StopTime-dt)'; % seconds
%% Sine wave:
z1=715.905;
D1=246.5895;
d1=238.635;
T1=254.544;
t1=206.817;
Fc1 = 1/(z1+D1);                    % hertz
x1 = ((T1-t1)/2+2.3*(T1-t1)/2)*sin(2*pi*Fc1*t);% basic sine func
x1=x1-2.3*(T1-t1)/2;                  % scale down the original sine wave
x1(x1<0)=0;                      % cut off negative values
x1=x1+t1/2;                  % Scale up to tmin value
x1neg=-x1;
x1ori=((T1-t1)/2+2.3*(T1-t1)/2)*sin(2*pi*Fc1*t)-2.3*(T1-t1)/2+t1/2;
y0=zeros(1,StopTime*Fs,'uint32');
a1=D1/2;
b1=d1/2;
StopTimeelp1a = (z1+D1)/4+D1/2; % seconds
telp1a = ((z1+D1)/4-D1/2:1/1000:StopTimeelp1a); % seconds
xelp1a=b1/a1*((a1*a1-((telp1a-(z1+D1)/4).^2)).^(1/2));
xelp1nega=-xelp1a;
StopTimeelp1b = (z1+D1)/4+D1/2+(z1+D1); % seconds
telp1b = ((z1+D1)/4-D1/2+(z1+D1):1/1000:StopTimeelp1b); % seconds
xelp1b=b1/a1*((a1*a1-((telp1b-(z1+D1)/4-(z1+D1)).^2)).^(1/2));
xelp1negb=-xelp1b;
StopTimeelp1c = (z1+D1)/4+D1/2+2*(z1+D1); % seconds
telp1c = ((z1+D1)/4-D1/2+2*(z1+D1):1/1000:StopTimeelp1c); % seconds
xelp1c=b1/a1*((a1*a1-((telp1c-(z1+D1)/4-2*(z1+D1)).^2)).^(1/2));
xelp1negc=-xelp1c;

z2=357.9525;
D2=254.544;
d2=230.6805;
T2=246.5895;
t2=190.908;
Fc2 = 1/(z2+D2);                    % hertz
x2 = ((T2-t2)/2+0.3*(T2-t2)/2)*sin(2*pi*Fc2*t);% basic sine func
x2=x2-0.3*(T2-t2)/2;                  % scale down the original sine wave
x2(x2<0)=0;                      % cut off negative values
x2=x2+t2/2;                  % Scale up to tmin value
```

```
x2neg=-x2;
x2ori=((T2-t2)/2+0.3*(T2-t2)/2)*sin(2*pi*Fc2*t)-0.3*(T2-t2)/2+t2/2;
y0=zeros(1,StopTime*Fs,'uint32');
a2=D2/2;
b2=d2/2;
StopTimeelp2a = (z2+D2)/4+D2/2; % seconds
telp2a = ((z2+D2)/4-D2/2:1/1000:StopTimeelp2a); % seconds
xelp2a=b2/a2*((a2*a2-((telp2a-(z2+D2)/4).^2)).^(1/2));
xelp2nega=-xelp2a;
StopTimeelp2b = (z2+D2)/4+D2/2+(z2+D2); % seconds
telp2b = ((z2+D2)/4-D2/2+(z2+D2):1/1000:StopTimeelp2b); % seconds
xelp2b=b2/a2*((a2*a2-((telp2b-(z2+D2)/4-(z2+D2)).^2)).^(1/2));
xelp2negb=-xelp2b;
StopTimeelp2c = (z2+D2)/4+D2/2+2*(z2+D2); % seconds
telp2c = ((z2+D2)/4-D2/2+2*(z2+D2):1/1000:StopTimeelp2c); % seconds
xelp2c=b2/a2*((a2*a2-((telp2c-(z2+D2)/4-2*(z2+D2)).^2)).^(1/2));
xelp2negc=-xelp2c;
StopTimeelp2d = (z2+D2)/4+D2/2+3*(z2+D2); % seconds
telp2d = ((z2+D2)/4-D2/2+3*(z2+D2):1/1000:StopTimeelp2d); % seconds
xelp2d=b2/a2*((a2*a2-((telp2d-(z2+D2)/4-3*(z2+D2)).^2)).^(1/2));
xelp2negd=-xelp2d;
StopTimeelp2e = (z2+D2)/4+D2/2+4*(z2+D2); % seconds
telp2e = ((z2+D2)/4-D2/2+4*(z2+D2):1/1000:StopTimeelp2e); % seconds
xelp2e=b2/a2*((a2*a2-((telp2e-(z2+D2)/4-4*(z2+D2)).^2)).^(1/2));
xelp2nege=-xelp2e;

z3=79.545;
D3=270.453;
d3=246.5895;
T3=254.544;
t3=182.9535;
Fc3 = 1/(z3+D3);                    % hertz
x3 = ((T3-t3)/2-0.43*(T3-t3)/2)*sin(2*pi*Fc3*t);% basic sine func
x3=x3+0.43*(T3-t3)/2;                % scale down the original sine
wave
x3(x3<0)=0;                      % cut off negative values
x3=x3+t3/2;                 % Scale up to tmin value
x3neg=-x3;
x3ori=((T3-t3)/2-0.43*(T3-t3)/2)*sin(2*pi*Fc3*t)+0.43*(T3-t3)/2+t3/2;
y0=zeros(1,StopTime*Fs,'uint32');
a3=D3/2;
b3=d3/2;
StopTimeelp3a = (z3+D3)/4+D3/2; % seconds
telp3a = ((z3+D3)/4-D3/2:1/1000:StopTimeelp3a); % seconds
xelp3a=b3/a3*((a3*a3-((telp3a-(z3+D3)/4).^2)).^(1/2));
xelp3nega=-xelp3a;
StopTimeelp3b = (z3+D3)/4+D3/2+(z3+D3); % seconds
telp3b = ((z3+D3)/4-D3/2+(z3+D3):1/1000:StopTimeelp3b); % seconds
xelp3b=b3/a3*((a3*a3-((telp3b-(z3+D3)/4-(z3+D3)).^2)).^(1/2));
xelp3negb=-xelp3b;
StopTimeelp3c = (z3+D3)/4+D3/2+2*(z3+D3); % seconds
telp3c = ((z3+D3)/4-D3/2+2*(z3+D3):1/1000:StopTimeelp3c); % seconds
xelp3c=b3/a3*((a3*a3-((telp3c-(z3+D3)/4-2*(z3+D3)).^2)).^(1/2));
xelp3negc=-xelp3c;
StopTimeelp3d = (z3+D3)/4+D3/2+3*(z3+D3); % seconds
telp3d = ((z3+D3)/4-D3/2+3*(z3+D3):1/1000:StopTimeelp3d); % seconds
xelp3d=b3/a3*((a3*a3-((telp3d-(z3+D3)/4-3*(z3+D3)).^2)).^(1/2));
xelp3negd=-xelp3d;
StopTimeelp3e = (z3+D3)/4+D3/2+4*(z3+D3); % seconds
```

```
telp3e = ((z3+D3)/4-D3/2+4*(z3+D3):1/1000:StopTimeelp3e); % seconds
xelp3e=b3/a3*((a3*a3-((telp3e-(z3+D3)/4-4*(z3+D3)).^2)).^(1/2));
xelp3nege=-xelp3e;
StopTimeelp3f = (z3+D3)/4+D3/2+5*(z3+D3); % seconds
telp3f = ((z3+D3)/4-D3/2+5*(z3+D3):1/1000:StopTimeelp3f); % seconds
xelp3f=b3/a3*((a3*a3-((telp3f-(z3+D3)/4-5*(z3+D3)).^2)).^(1/2));
xelp3negf=-xelp3f;
StopTimeelp3g = (z3+D3)/4+D3/2+6*(z3+D3); % seconds
telp3g = ((z3+D3)/4-D3/2+6*(z3+D3):1/1000:StopTimeelp3g); % seconds
xelp3g=b3/a3*((a3*a3-((telp3g-(z3+D3)/4-6*(z3+D3)).^2)).^(1/2));
xelp3negg=-xelp3g;
StopTimeelp3h = (z3+D3)/4+D3/2+7*(z3+D3); % seconds
telp3h = ((z3+D3)/4-D3/2+7*(z3+D3):1/1000:StopTimeelp3h); % seconds
xelp3h=b3/a3*((a3*a3-((telp3h-(z3+D3)/4-7*(z3+D3)).^2)).^(1/2));
xelp3negh=-xelp3h;

z4=111.363;
D4=334.089;
d4=262.4985;
T4=278.4075;
t4=174.999;
Fc4 = 1/(z4+D4);                    % hertz
x4 = ((T4-t4)/2-0.42*(T4-t4)/2)*sin(2*pi*Fc4*t);% basic sine func
x4=x4+0.42*(T4-t4)/2;                % scale down the original sine
wave
x4(x4<0)=0;                      % cut off negative values
x4=x4+t4/2;                 % Scale up to tmin value
x4neg=-x4;
x4ori=((T4-t4)/2-0.42*(T4-t4)/2)*sin(2*pi*Fc4*t)+0.42*(T4-t4)/2+t4/2;
y0=zeros(1,StopTime*Fs,'uint32');
a4=D4/2;
b4=d4/2;
StopTimeelp4a = (z4+D4)/4+D4/2; % seconds
telp4a = ((z4+D4)/4-D4/2:1/1000:StopTimeelp4a); % seconds
xelp4a=b4/a4*((a4*a4-((telp4a-(z4+D4)/4).^2)).^(1/2));
xelp4nega=-xelp4a;
StopTimeelp4b = (z4+D4)/4+D4/2+(z4+D4); % seconds
telp4b = ((z4+D4)/4-D4/2+(z4+D4):1/1000:StopTimeelp4b); % seconds
xelp4b=b4/a4*((a4*a4-((telp4b-(z4+D4)/4-(z4+D4)).^2)).^(1/2));
xelp4negb=-xelp4b;
StopTimeelp4c = (z4+D4)/4+D4/2+2*(z4+D4); % seconds
telp4c = ((z4+D4)/4-D4/2+2*(z4+D4):1/1000:StopTimeelp4c); % seconds
xelp4c=b4/a4*((a4*a4-((telp4c-(z4+D4)/4-2*(z4+D4)).^2)).^(1/2));
xelp4negc=-xelp4c;
StopTimeelp4d = (z4+D4)/4+D4/2+3*(z4+D4); % seconds
telp4d = ((z4+D4)/4-D4/2+3*(z4+D4):1/1000:StopTimeelp4d); % seconds
xelp4d=b4/a4*((a4*a4-((telp4d-(z4+D4)/4-3*(z4+D4)).^2)).^(1/2));
xelp4negd=-xelp4d;
StopTimeelp4e = (z4+D4)/4+D4/2+4*(z4+D4); % seconds
telp4e = ((z4+D4)/4-D4/2+4*(z4+D4):1/1000:StopTimeelp4e); % seconds
xelp4e=b4/a4*((a4*a4-((telp4e-(z4+D4)/4-4*(z4+D4)).^2)).^(1/2));
xelp4nege=-xelp4e;
StopTimeelp4f = (z4+D4)/4+D4/2+5*(z4+D4); % seconds
telp4f = ((z4+D4)/4-D4/2+5*(z4+D4):1/1000:StopTimeelp4f); % seconds
xelp4f=b4/a4*((a4*a4-((telp4f-(z4+D4)/4-5*(z4+D4)).^2)).^(1/2));
xelp4negf=-xelp4f;

z5=159.09;
D5=421.5885;
d5=270.453;
```

```
T5=286.362;
t5=151.1355;
Fc5 = 1/(z5+D5);                    % hertz
x5 = ((T5-t5)/2-0.4*(T5-t5)/2)*sin(2*pi*Fc5*t);% basic sine func
x5=x5+0.4*(T5-t5)/2;                % scale down the original sine wave
x5(x5<0)=0;                    % cut off negative values
x5=x5+t5/2;                % Scale up to tmin value
x5neg=-x5;
x5ori=((T5-t5)/2-0.4*(T5-t5)/2)*sin(2*pi*Fc5*t)+0.4*(T5-t5)/2+t5/2;
y0=zeros(1,StopTime*Fs,'uint32');
a5=D5/2;
b5=d5/2;
StopTimeelp5a = (z5+D5)/4+D5/2; % seconds
telp5a = ((z5+D5)/4-D5/2:1/1000:StopTimeelp5a); % seconds
xelp5a=b5/a5*((a5*a5-((telp5a-(z5+D5)/4).^2)).^(1/2));
xelp5nega=-xelp5a;
StopTimeelp5b = (z5+D5)/4+D5/2+(z5+D5); % seconds
telp5b = ((z5+D5)/4-D5/2+(z5+D5):1/1000:StopTimeelp5b); % seconds
xelp5b=b5/a5*((a5*a5-((telp5b-(z5+D5)/4-(z5+D5)).^2)).^(1/2));
xelp5negb=-xelp5b;
StopTimeelp5c = (z5+D5)/4+D5/2+2*(z5+D5); % seconds
telp5c = ((z5+D5)/4-D5/2+2*(z5+D5):1/1000:StopTimeelp5c); % seconds
xelp5c=b5/a5*((a5*a5-((telp5c-(z5+D5)/4-2*(z5+D5)).^2)).^(1/2));
xelp5negc=-xelp5c;
StopTimeelp5d = (z5+D5)/4+D5/2+3*(z5+D5); % seconds
telp5d = ((z5+D5)/4-D5/2+3*(z5+D5):1/1000:StopTimeelp5d); % seconds
xelp5d=b5/a5*((a5*a5-((telp5d-(z5+D5)/4-3*(z5+D5)).^2)).^(1/2));
xelp5negd=-xelp5d;
StopTimeelp5e = (z5+D5)/4+D5/2+4*(z5+D5); % seconds
telp5e = ((z5+D5)/4-D5/2+4*(z5+D5):1/1000:StopTimeelp5e); % seconds
xelp5e=b5/a5*((a5*a5-((telp5e-(z5+D5)/4-4*(z5+D5)).^2)).^(1/2));
xelp5nege=-xelp5e;

z6=159.09;
D6=1026.1305;
d6=246.5895;
T6=262.4985;
t6=182.9535;
Fc6 = 1/(z6+D6);                    % hertz
x6 = ((T6-t6)/2-1.08*(T6-t6)/2)*sin(2*pi*Fc6*t);% basic sine func
x6=x6+1.08*(T6-t6)/2;                % scale down the original sine
wave
x6(x6<0)=0;                    % cut off negative values
x6=x6+t6/2;                % Scale up to tmin value
x6neg=-x6;
x6ori=((T6-t6)/2-1.08*(T6-t6)/2)*sin(2*pi*Fc6*t)+1.08*(T6-t6)/2+t6/2;
y0=zeros(1,StopTime*Fs,'uint32');
a6=D6/2;
b6=d6/2;
StopTimeelp6a = (z6+D6)/4-(z6+D6)/2-D6/2+D6; % seconds
telp6a = ((z6+D6)/4-(z6+D6)/2-D6/2:1/1000:StopTimeelp6a); % seconds
xelp6a=b6/a6*((a6*a6-((telp6a+(z6+D6)/4).^2)).^(1/2));
xelp6nega=-xelp6a;
StopTimeelp6b = (z6+D6)/4-(z6+D6)/2-D6/2+D6+(z6+D6); % seconds
telp6b = ((z6+D6)/4-(z6+D6)/2-D6/2+(z6+D6):1/1000:StopTimeelp6b); %
seconds
xelp6b=b6/a6*((a6*a6-((telp6b+(z6+D6)/4-(z6+D6)).^2)).^(1/2));
xelp6negb=-xelp6b;
StopTimeelp6c = (z6+D6)/4-(z6+D6)/2-D6/2+D6+2*(z6+D6); % seconds
```

```
telp6c = ((z6+D6)/4-(z6+D6)/2-D6/2+2*(z6+D6):1/1000:StopTimeelp6c); %
seconds
xelp6c=b6/a6*((a6*a6-((telp6c+(z6+D6)/4-2*(z6+D6)).^2)).^(1/2));
xelp6negc=-xelp6c;

title('Fiber Morphology');
subplot(6,1,1), plot(t,y0,'--
',telp1a,xelp1a,'red',telp1a,xelp1nega,'red',telp1b,xelp1b,'red',telp1
b,xelp1negb,'red',telp1c,xelp1c,'red',telp1c,xelp1negc,'red')
hold on
plot(t,x1ori,':m','LineWidth',0.1)
hold on
plot(t,x1,'black','LineWidth',2)
hold on
plot(t,x1neg,'black','LineWidth',2)
ylim([-150 150])
xlim([0 2500])
set(gca,'XTick',[0:100:2500]);
set(gca,'YTick',[-150:50:150]);

subplot(6,1,2), plot(t,y0,'--
',telp2a,xelp2a,'red',telp2a,xelp2nega,'red',telp2b,xelp2b,'red',telp2
b,xelp2negb,'red',telp2c,xelp2c,'red',telp2c,xelp2negc,'red',telp2d,xe
lp2d,'red',telp2d,xelp2negd,'red',telp2e,xelp2e,'red',telp2e,xelp2nege
,'red')
hold on
plot(t,x2ori,':m','LineWidth',0.1)
hold on
plot(t,x2,'black','LineWidth',2)
hold on
plot(t,x2neg,'black','LineWidth',2)
ylim([-150 150])
xlim([0 2500])
set(gca,'XTick',[0:100:2500]);
set(gca,'YTick',[-150:50:150]);

subplot(6,1,3), plot(t,y0,'--
',telp3a,xelp3a,'red',telp3a,xelp3nega,'red',telp3b,xelp3b,'red',telp3
b,xelp3negb,'red',telp3c,xelp3c,'red',telp3c,xelp3negc,'red',telp3d,xe
lp3d,'red',telp3d,xelp3negd,'red',telp3e,xelp3e,'red',telp3e,xelp3nege
,'red',telp3f,xelp3f,'red',telp3f,xelp3negf,'red',telp3g,xelp3g,'red',
telp3g,xelp3negg,'red',telp3h,xelp3h,'red',telp3h,xelp3negh,'red')
hold on
plot(t,x3ori,':m','LineWidth',0.1)
hold on
plot(t,x3,'black','LineWidth',2)
hold on
plot(t,x3neg,'black','LineWidth',2)
ylim([-150 150])
xlim([0 2500])
set(gca,'XTick',[0:100:2500]);
set(gca,'YTick',[-150:50:150]);

subplot(6,1,4), plot(t,y0,'--
',telp4a,xelp4a,'red',telp4a,xelp4nega,'red',telp4b,xelp4b,'red',telp4
b,xelp4negb,'red',telp4c,xelp4c,'red',telp4c,xelp4negc,'red',telp4d,xe
lp4d,'red',telp4d,xelp4negd,'red',telp4e,xelp4e,'red',telp4e,xelp4nege
,'red',telp4f,xelp4f,'red',telp4f,xelp4negf,'red')
hold on
```

```
plot(t,x4ori,':m','LineWidth',0.1)
hold on
plot(t,x4,'black','LineWidth',2)
hold on
plot(t,x4neg,'black','LineWidth',2)
ylim([-150 150])
xlim([0 2500])
set(gca,'XTick',[0:100:2500]);
set(gca,'YTick',[-150:50:150]);

subplot(6,1,5), plot(t,y0,'--
',telp5a,xelp5a,'red',telp5a,xelp5nega,'red',telp5b,xelp5b,'red',telp5
b,xelp5negb,'red',telp5c,xelp5c,'red',telp5c,xelp5negc,'red',telp5d,xe
lp5d,'red',telp5d,xelp5negd,'red',telp5e,xelp5e,'red',telp5e,xelp5nege
,'red')
hold on
plot(t,x5ori,':m','LineWidth',0.1)
hold on
plot(t,x5,'black','LineWidth',2)
hold on
plot(t,x5neg,'black','LineWidth',2)
ylim([-150 150])
xlim([0 2500])
set(gca,'XTick',[0:100:2500]);
set(gca,'YTick',[-150:50:150]);

subplot(6,1,6), plot(t,y0,'--
',telp6a,xelp6a,'red',telp6a,xelp6nega,'red',telp6b,xelp6b,'red',telp6
b,xelp6negb,'red',telp6c,xelp6c,'red',telp6c,xelp6negc,'red')
hold on
plot(t,x6ori,':m','LineWidth',0.1)
hold on
plot(t,x6,'black','LineWidth',2)
hold on
plot(t,x6neg,'black','LineWidth',2)
ylim([-150 150])
xlim([0 2500])
set(gca,'XTick',[0:100:2500]);
set(gca,'YTick',[-150:50:150]);

hold on
```

References

[1] Chang, T.M.S. 2004, "Artificial Cell Bioencapsulation in Macro, Micro, Nano, and Molecular Dimensions: Keynote Lecture", *Artificial Cells, Blood Substitutes, and Immobilization Biotechnology*, vol. 32, no. 1, pp. 1-23.

[2] Tadros, T.F. 2013, "Emulsion Formation, Stability, and Rheology" in *Emulsion Formation and Stability* Wiley-VCH Verlag GmbH & Co. KGaA, , pp. 1-75.

[3] Vladisavljevic, G.T. & Williams, R.A. 2005, "Recent developments in manufacturing emulsions and particulate products using membranes", *Advances in Colloid and Interface Science*, vol. 113, no. 1, pp. 1-20.

[4] Xu, S.Q., Nie, Z.H., Seo, M., Lewis, P., Kumacheva, E., Stone, H.A., Garstecki, P., Weibel, D.B., Gitlin, I. & Whitesides, G.M. 2005, "Generation of monodisperse particles by using microfluidics: Control over size, shape, and composition", *Angewandte Chemie-International Edition*, vol. 44, no. 5, pp. 724-728.

[5] Van Aken, G.A. & Zoet, F.D. 2000, "Coalescence in highly concentrated coarse emulsions", *Langmuir*, vol. 16, no. 18, pp. 7131-7138.

[6] Aben, S., Holtze, C., Tadros, T. & Schurtenberger, P. 2012, "Rheological investigations on the creaming of depletion-flocculated emulsions", *Langmuir*, vol. 28, no. 21, pp. 7967-7975.

[7] Dickinson, E. 2010, "Flocculation of protein-stabilized oil-in-water emulsions", *Colloids and Surfaces B: Biointerfaces*, vol. 81, no. 1, pp. 130-140.

[8] Voorhees, P.W. 1985, "The theory of Ostwald ripening", *Journal of Statistical Physics*, vol. 38, no. 1-2, pp. 231-252.

[9] Sander, J.S., Isa, L., Rühs, P.A., Fischer, P. & Studart, A.R. 2012, "Stabilization mechanism of double emulsions made by microfluidics", *Soft Matter*, vol. 8, no. 45, pp. 11471-11477.

[10] Sonneville-Aubrun, O., Bergeron, V., Gulik-Krzywicki, T., Jönsson, B., Wennerström, H., Lindner, P. & Cabane, B. 2000, "Surfactant films in biliquid foams", *Langmuir*, vol. 16, no. 4, pp. 1566-1579.

[11] Domínguez, A., Fernández, A., Gonzalez, N., Iglesias, E. & Montenegro, L. 1997, "Determination of critical micelle concentration of some surfactants by three techniques", *Journal of chemical education*, vol. 74, no. 10, pp. 1227-1231.

[12] Nusselder, J.J.H. & Engberts, J.B.F.N. 1992, "Toward a better understanding of the driving force for micelle formation and micellar growth", *Journal of colloid and interface science*, vol. 148, no. 2, pp. 353-361.

[13] Miller, R., Joos, P. & Fainerman, V.B. 1994, "Dynamic surface and interfacial tensions of surfactant and polymer solutions", *Advances in Colloid and Interface Science*, vol. 49, no. C, pp. 249-302.

[14] Savart, F. 1833, *Ann. Chim*. 53, 337, plates in vol. 54.

[15] Eggers, J. 2006, "A brief history of drop formation", *Nonsmooth Mechanics and Analysis*, Springer.

[16] Plateau, J. 1849, *Acad. Sci. Bruxelles Mem.* XXIII, 5.

[17] Rayleigh, L. 1879, Proc. London Math. Soc. 10, 4.

[18] Harkins, W.D. & Brown, F.E. 1919, "The determination of surface tension (free surface energy), and the weight of falling drops: The surface tension of water and benzene by the capillary height method", *The Journal of the American Chemical Society*, vol. 41, no. 4, pp. 499-524.

[19] Hayworth C.B., Treybal R.E. 1950, "**Drop formation in two-liquid-phase systems**", Industrial and Engineering Chemistry Research

[20] Rao, E.V.L., Kumar, R. & Kuloor, N.R. 1966, "Drop Formation Studies in Liquid-Liquid Systems", *Chemical Engineering Science*, vol. 21, no. 10, pp. 867-&.

[21] Barhate, R.S., Patil, G., Srinivas, N.D. & Raghavarao, K.S.M.S. 2004, "Drop formation in aqueous two-phase systems", *Journal of Chromatography A*, vol. 1023, no. 2, pp. 197-206.

[22] Yildirim, O.E., Xu, Q. & Basaran, O.A. 2005, "Analysis of the drop weight method", *Physics of Fluids*, vol. 17, no. 6, pp. 1-13.

[23] Richards, J.R., Lenhoff, A.M. & Beris, A.N. 1994, "Dynamic breakup of liquid-liquid jets", *Physics of Fluids*, vol. 6, no. 8, pp. 2640-2655.

[24] Gravesen, P., Branebjerg, J. & Jensen, O.S. 1993, "Microfluidics - a review", *Journal of Micromechanics and Microengineering*, vol. 3, no. 4, pp. 168-182.

[25] Utada, A.S., Lorenceau, E., Link, D.R., Kaplan, P.D., Stone, H.A. & Weitz, D.A. 2005, "Monodisperse double emulsions generated from a microcapillary device", *Science*, vol. 308, no. 5721, pp. 537-541.

[26] Jeong, W., Kim, J., Kim, S., Lee, S., Mensing, G. & Beebe, D.J. 2004, "Hydrodynamic microfabrication via "on the fly" photopolymerization of microscale fibers and tubes", *Lab on a Chip - Miniaturisation for Chemistry and Biology*, vol. 4, no. 6, pp. 576-580.

[27] Duncanson, W.J., Zieringer, M., Wagner, O., Wilking, J.N., Abbaspourrad, A., Haag, R. & Weitz, D.A. 2012, "Microfluidic synthesis of monodisperse porous microspheres with size-tunable pores", *Soft Matter*, vol. 8, no. 41, pp. 10636-10640.

[28] Xu, J.-., Chen, R., Wang, Y.-. & Luo, G.-. 2012, "Controllable gas/liquid/liquid double emulsions in a dual-coaxial microfluidic device", *Lab on a Chip - Miniaturisation for Chemistry and Biology*, vol. 12, no. 11, pp. 2029-2036.

[29] Ye, C., Chen, A., Colombo, P. & Martinez, C. 2010, "Ceramic microparticles and capsules via microfluidic processing of a preceramic polymer", *Journal of the Royal Society Interface*, vol. 7, no. SUPPL. 4, pp. S461-S473.

[30] Abbaspourrad, A., Carroll, N.J., Kim, S. & Weitz, D.A. 2013, "Polymer Microcapsules with Programmable Active Release", *Journal of the American Chemical Society*, vol. 135, no. 20, pp. 7744-7750.

[31] Luo, Y., Lode, A. & Gelinsky, M. 2013, "Direct plotting of three-dimensional hollow fiber scaffolds based on concentrated alginate pastes for tissue engineering", *Advanced Healthcare Materials*, vol. 2, no. 6, pp. 777-783.

[32] Kang, E., Choi, Y.Y., Chae, S.-., Moon, J.-., Chang, J.-. & Lee, S.-. 2012, "Microfluidic spinning of flat alginate fibers with grooves for cell-aligning scaffolds", *Advanced Materials*, vol. 24, no. 31, pp. 4271-4277.

[33] He, X.-., Wang, W., Deng, K., Xie, R., Ju, X.-., Liu, Z. & Chu, L.-. 2015, "Microfluidic fabrication of chitosan microfibers with controllable internals from tubular to peapod-like structures", *RSC Advances*, vol. 5, no. 2, pp. 928-936.

[34] Cheng, Y., Zheng, F., Lu, J., Shang, L., Xie, Z., Zhao, Y., Chen, Y. & Gu, Z. 2014, "Bioinspired multicompartmental microfibers from microfluidics", *Advanced Materials*, vol. 26, no. 30, pp. 5184-5190.

[35] Cheng, Y., Yu, Y., Fu, F., Wang, J., Shang, L., Gu, Z. & Zhao, Y. 2016, "Controlled Fabrication of Bioactive Microfibers for Creating Tissue Constructs Using Microfluidic Techniques", *ACS Applied Materials and Interfaces*, vol. 8, no. 2, pp. 1080-1086.

[36] Yu, Y., Wen, H., Ma, J., Lykkemark, S., Xu, H. & Qin, J. 2014, "Flexible fabrication of biomimetic bamboo-like hybrid microfibers", *Advanced Materials*, vol. 26, no. 16, pp. 2494-2499.

[37] Xu, J.H., Li, S.W., Tan, J., Wang, Y.J. & Luo, G.S. 2006, "Controllable preparation of monodisperse O/W and W/O emulsions in the same microfluidic device", *Langmuir*, vol. 22, no. 19, pp. 7943-7946.

[38] McDonald, J.C., Duffy, D.C., Anderson, J.R., Chiu, D.T., Wu, H., Schueller, O.J.A. & Whitesides, G.M. 2000, "Fabrication of microfluidic systems in poly(dimethylsiloxane)", *Electrophoresis*, vol. 21, no. 1, pp. 27-40.

[39] Shah, R.K., Shum, H.C., Rowat, A.C., Lee, D., Agresti, J.J., Utada, A.S., Chu, L.-., Kim, J.-., Fernandez-Nieves, A., Martinez, C.J. & Weitz, D.A. 2008, "Designer emulsions using microfluidics", *Materials Today*, vol. 11, no. 4, pp. 18-27.

[40] Brody, J.P., Yager, P., Goldstein, R.E. & Austin, R.H. 1996, "Biotechnology at low Reynolds numbers", *Biophysical journal*, vol. 71, no. 6, pp. 3430-3441.

[41] Burns, M.A., Mastrangelo, C.H., Sammarco, T.S., Man, F.P., Webster, J.R., Johnson, B.N., Foerster, B., Jones, D., Fields, Y., Kaiser, A.R. & Burke, D.T. 1996, "Microfabricated structures for integrated DNA analysis", *Proceedings of the National Academy of Sciences of the United States of America*, vol. 93, no. 11, pp. 5556-5561.

[42] Duffy, D.C., McDonald, J.C., Schueller, O.J.A. & Whitesides, G.M. 1998, "Rapid prototyping of microfluidic systems in poly(dimethylsiloxane)", *Analytical Chemistry*, vol. 70, no. 23, pp. 4974-4984.

[43] Utada, A.S., Fernandez-Nieves, A., Gordillo, J.M. & Weitz, D.A. 2008, "Absolute instability of a liquid jet in a coflowing stream", *Physical Review Letters*, vol. 100, no. 1.

[44] Utada, A.S., Fernandez-Nieves, A., Stone, H.A. & Weitz, D.A. 2007, "Dripping to jetting transitions in coflowing liquid streams", *Physical Review Letters*, vol. 99, no. 9.

[45] Thorsen, T., Roberts, R.W., Arnold, F.H. & Quake, S.R. 2001, "Dynamic pattern formation in a vesicle-generating microfluidic device", *Physical Review Letters*, vol. 86, no. 18, pp. 4163-4166.

[46] Gañán-Calvo, A.M. & Gordillo, J.M. 2001, "Perfectly monodisperse microbubbling by capillary flow focusing", *Physical Review Letters*, vol. 87, no. 27 I, pp. 2745011-2745014.

[47] Marín, A.G., Campo-Cortés, F. & Gordillo, J.M. 2009, "Generation of micron-sized drops and bubbles through viscous coflows", *Colloids and Surfaces A: Physicochemical and Engineering Aspects*, vol. 344, no. 1-3, pp. 2-7.

[48] Serra, C., Berton, N., Bouquey, M., Prat, L. & Hadziioannou, G. 2007, "A predictive approach of the influence of the operating parameters on the size of polymer particles synthesized in a simplified microfluidic system", *Langmuir*, vol. 23, no. 14, pp. 7745-7750.

[49] Umbanhowar, P.B., Prasad, V. & Weitz, D.A. 2000, "Monodisperse emulsion generation via drop break off in a coflowing stream", *Langmuir*, vol. 16, no. 2, pp. 347-351.

[50] Erb, R.M., Obrist, D., Chen, P.W., Studer, J. & Studart, A.R. 2011, "Predicting sizes of droplets made by microfluidic flow-induced dripping", *Soft Matter*, vol. 7, no. 19, pp. 8757-8761.

[51] Wang, W., Ngan, K.H., Gong, J. & Angeli, P. 2009, "Observations on single drop formation from a capillary tube at low flow rates", *Colloids and Surfaces A: Physicochemical and Engineering Aspects*, vol. 334, no. 1-3, pp. 197-202.

[52] Zhou, C., Yue, P. & Feng, J.J. 2006, "Formation of simple and compound drops in microfluidic devices", *Physics of Fluids*, vol. 18, no. 9.

[53] Hong, Y. & Wang, F. 2007, "Flow rate effect on droplet control in a co-flowing microfluidic device", *Microfluidics and Nanofluidics*, vol. 3, no. 3, pp. 341-346.

[54] Xu, J.H., Dong, P.F., Zhao, H., Tostado, C.P. & Luo, G.S. 2012, "The dynamic effects of surfactants on droplet formation in coaxial microfluidic devices", *Langmuir*, vol. 28, no. 25, pp. 9250-9258.

[55] Okushima, S., Nisisako, T., Torii, T. & Higuchi, T. 2004, "Controlled production of monodisperse double emulsions by two-step droplet breakup in microfluidic devices", *Langmuir*, vol. 20, no. 23, pp. 9905-9908.

[56] Chang, Z., Serra, C.A., Bouquey, M., Prat, L. & Hadziioannou, G. 2009, "Co-axial capillaries microfluidic device for synthesizing size- and morphology-controlled polymer core-polymer shell particles", *Lab on a Chip - Miniaturisation for Chemistry and Biology*, vol. 9, no. 20, pp. 3007-3011.

[57] Chen, Y., Wu, L. & Zhang, C. 2013, "Emulsion droplet formation in coflowing liquid streams", *Physical Review E - Statistical, Nonlinear, and Soft Matter Physics*, vol. 87, no. 1.

[58] Kim, S.-. & Weitz, D.A. 2011, "One-step emulsification of multiple concentric shells with capillary microfluidic devices", *Angewandte Chemie - International Edition*, vol. 50, no. 37, pp. 8731-8734.

[59] Abate, A.R. & Weitz, D.A. 2009, "High-order multiple emulsions formed in poly(dimethylsiloxane) microfluidics", *Small*, vol. 5, no. 18, pp. 2030-2032.

[60] Kim, S.-., Kim, J.W., Cho, J.-. & Weitz, D.A. 2011, "Double-emulsion drops with ultra-thin shells for capsule templates", *Lab on a Chip - Miniaturisation for Chemistry and Biology*, vol. 11, no. 18, pp. 3162-3166.

[61] Shin, S.-., Park, J.-., Lee, J.-., Park, H., Park, Y.-., Lee, K.-., Whang, C.-. & Lee, S.-. 2007, ""On the fly" continuous generation of alginate fibers using a microfluidic device", *Langmuir*, vol. 23, no. 17, pp. 9104-9108.

[62] Onoe, H., Okitsu, T., Itou, A., Kato-Negishi, M., Gojo, R., Kiriya, D., Sato, K., Miura, S., Iwanaga, S., Kuribayashi-Shigetomi, K., Matsunaga, Y.T., Shimoyama, Y. & Takeuchi, S. 2013, "Metre-long cell-laden microfibres exhibit tissue morphologies and functions", *Nature Materials*, vol. 12, no. 6, pp. 584-590.

[63] He, X.-., Wang, W., Liu, Y.-., Jiang, M.-., Wu, F., Deng, K., Liu, Z., Ju, X.-., Xie, R. & Chu, L.-. 2015, "Microfluidic Fabrication of Bio-Inspired Microfibers with Controllable Magnetic Spindle-Knots for 3D Assembly and Water Collection", *ACS Applied Materials and Interfaces*, vol. 7, no. 31, pp. 17471-17481.

[64] Um, E., Nunes, J.K., Pico, T. & Stone, H.A. 2014, "Multicompartment microfibers: Fabrication and selective dissolution of composite droplet-in-fiber structures", *Journal of Materials Chemistry B*, vol. 2, no. 45, pp. 7866-7871.

[65] Yang, X. 2007, "Nano- and microparticle-based imaging of cardiovascular interventions: Overview", *Radiology*, vol. 243, no. 2, pp. 340-347.

[66] Mitragotri, S. & Lahann, J. 2009, "Physical approaches to biomaterial design", *Nature Materials*, vol. 8, no. 1, pp. 15-23.

[67] Vladisavljevic, G.T., Shahmohamadi, H., Das, D.B., Ekanem, E.E., Tauanov, Z. & Sharma, L. 2014, "Glass capillary microfluidics for production of monodispersed poly

(dl-lactic acid) and polycaprolactone microparticles: Experiments and numerical simulations", *Journal of colloid and interface science*, vol. 418, pp. 163-170.

[68] Joscelyne, S.M. & Trägårdh, G. 2000, "Membrane emulsification - A literature review", *Journal of Membrane Science*, vol. 169, no. 1, pp. 107-117.

[69] Van Der Graaf, S., Schroën, C.G.P.H., Van Der Sman, R.G.M. & Boom, R.M. 2004, "Influence of dynamic interfacial tension on droplet formation during membrane emulsification", *Journal of colloid and interface science*, vol. 277, no. 2, pp. 456-463.

[70] Cramer, C. 2004, "Continuous drop formation at a capillary tip and drop deformation in a flow channel. Laboratory of Food Process Engineering", *Swiss Federal Institute of Technology (ETH) Zürich ISBN:3-905609-22-3*, .

[71] Cramer, C., Fischer, P. & Windhab, E.J. 2004, "Drop formation in a co-flowing ambient fluid", *Chemical Engineering Science*, vol. 59, no. 15, pp. 3045-3058.

[72] Sauret, A. & Shum, H.C. 2012, "Beating the jetting regime", *International Journal of Nonlinear Sciences and Numerical Simulation*, vol. 13, no. 5, pp. 351-362.

[73] Josephides, D.N. & Sajjadi, S. 2014, "Microfluidic Method for Creating Monodisperse Viscous Single Emulsions via Core-Shell Templating", *Microfluid.Nanofluid.*, , pp. 1-8.

[74] Clanet, C. & Lasheras, J.C. 1999, "Transition from dripping to jetting", *Journal of Fluid Mechanics*, vol. 383, pp. 307-326.

[75] De Chazal Lem & Ryan J.T. 1971, "Formation of organic drops in water", *AIChE Journal*, vol. 17, no. 5, pp. 1226-1229.

[76] Heertjes, P.M., de Nie, L.H. & de Vries, H.J. 1971, "Drop formation in liquid-liquid systems-I prediction of drop volumes at moderate speed of formation", *Chemical Engineering Science*, vol. 26, no. 3, pp. 441-449.

[77] Scheele, G.F. & Meister, B.J. 1968, "Drop formation at low velocities in liquid-liquid systems", *AIChE J.*, vol. 14, no. 1, pp. 9-15.

[78] Walters, T.W. & Marschall, E. 1988, "Drop formation in liquid-liquid systems", *Experiments in Fluids*, vol. 7, no. 3, pp. 210-213.

[79] Zhang, D.F. & Stone, H.A. 1997, "Drop formation in viscous flows at a vertical capillary tube", *Physics of Fluids*, vol. 9, no. 8, pp. 2234-2242.

[80] Del Río, O.I. & Neumann, A.W. 1997, "Axisymmetric drop shape analysis: Computational methods for the measurement of interfacial properties from the shape and dimensions of pendant and sessile drops", *Journal of colloid and interface science*, vol. 196, no. 2, pp. 136-147.

[81] Saad, S.M.I., Policova, Z. & Neumann, A.W. 2011, "Design and accuracy of pendant drop methods for surface tension measurement", *Colloids and Surfaces A: Physicochemical and Engineering Aspects*, vol. 384, no. 1-3, pp. 442-452.

[82] Schoeler, A.M., Josephides, D.N., Chaurasia, A.S., Sajjadi, S. & Mesquida, P. 2014, "Electrophoretic manipulation of multiple-emulsion droplets", *Applied Physics Letters*, vol. 104, no. 7.

[83] Bremond, N., Santanach-Carreras, E., Chu, L.-. & Bibette, J. 2010, "Formation of liquid-core capsules having a thin hydrogel membrane: Liquid pearls", *Soft Matter*, vol. 6, no. 11, pp. 2484-2488.

[84] Nie, Z., Seo, M., Xu, S., Lewis, P.C., Mok, M., Kumacheva, E., Whitesides, G.M., Garstecki, P. & Stone, H.A. 2008, "Emulsification in a microfluidic flow-focusing device: Effect of the viscosities of the liquids", *Microfluidics and Nanofluidics*, vol. 5, no. 5, pp. 585-594.

[85] Cordero, M.L., Gallaire, F. & Baroud, C.N. 2011, "Quantitative analysis of the dripping and jetting regimes in co-flowing capillary jets", *Physics of Fluids*, vol. 23, no. 9.

[86] Bohr, N. 1909, "Determination of the Surface-Tension of Water by the Method of Jet Vibration", *Philosophical Transactions of the Royal Society A: Mathematical, Physical and Engineering Sciences*, vol. 209.

[87] Addison, C.C. & Elliott, T.A. 1950, "The properties of freshly formed surfaces. Part XV. The application of the contracting liquid-jet technique to the measurement of tensions at liquid-liquid interfaces", *Journal of the Chemical Society (Resumed)*, , pp. 3090-3096.

[88] Garner, F.H. & Mina, P. 1959, "Surface ageing at liquid-liquid interfaces: Part 1. - Calibration of contracting jet method", *Transactions of the Faraday Society*, vol. 55, pp. 1607-1626.

[89] Chevalier, J.L.E., Petrino, P.J. & Gaston-Bonhomme, Y.H. 1990, "Viscosity and density of some aliphatic, cyclic, and aromatic hydrocarbons binary liquid mixtures", *Journal of Chemical and Engineering Data*, vol. 35, no. 2, pp. 206-212.

[90] Awwad, A.M., Al-Azzawi, S.F. & Salman, M.A. 1986, "Volumes and viscosities of benzene + n-alkane mixtures", *Fluid Phase Equilibria*, vol. 31, no. 2, pp. 171-182.

[91] Tate, T. 1864, "On the magnitude of a drop of liquid formed under different circumstances", *Philos.Mag.*, vol. 27, no. 181.

[92] Zhang, X. & Basaran, O.A. 1995, "An experimental study of dynamics of drop formation", *Physics of Fluids*, vol. 7, no. 6, pp. 1184-1203.

[93] Zhao, C.-., Miller, E., Cooper-White, J.J. & Middelberg, A.P.J. 2011, "Effects of fluid-fluid interfacial elasticity on droplet formation in microfluidic devices", *AIChE Journal*, vol. 57, no. 7, pp. 1669-1677.

[94] Zhang, X. 1999, "Dynamics of drop formation in viscous flows", *Chemical Engineering Science*, vol. 54, no. 12, pp. 1759-1774.

[95] Shum, H.C., Bandyopadhyay, A., Bose, S. & Weitz, D.A. 2009, "Double Emulsion Droplets as Microreactors for Synthesis of Mesoporous Hydroxyapatite", *Chemistry of Materials*, vol. 21, no. 22, pp. 5548-5555.

[96] Shum, H.C., Lee, D., Yoon, I., Kodger, T. & Weitz, D.A. 2008, "Double emulsion templated monodisperse phospholipid vesicles", *Langmuir*, vol. 24, no. 15, pp. 7651-7653.

[97] Chen, P.W., Erb, R.M. & Studart, A.R. 2012, "Designer polymer-based microcapsules made using microfluidics", *Langmuir*, vol. 28, no. 1, pp. 144-152.

[98] Lewinska, D., Bukowski, J., Kozuchowski, M., Kinasiewicz, A. & Werynski, A. 2008, "Electrostatic microencapsulation of living cells", *Biocybernetics and Biomedical Engineering*, vol. 28, no. 2, pp. 69-84.

[99] Uludag, H., De Vos, P. & Tresco, P.A. 2000, "Technology of mammalian cell encapsulation", *Advanced Drug Delivery Reviews*, vol. 42, no. 1-2, pp. 29-64.

[100] Saeki, D., Sugiura, S., Kanamori, T., Sato, S. & Ichikawa, S. 2010, "Microfluidic preparation of water-in-oil-in-water emulsions with an ultra-thin oil phase layer", *Lab on a Chip - Miniaturisation for Chemistry and Biology*, vol. 10, no. 3, pp. 357-362.

[101] Vladisavljevic, G.T., Shum, H.C. & Weitz, D.A. 2011, Control over the shell thickness of core/shell drops in three-phase glass capillary devices.

[102] Berkland, C., Pollauf, E., Pack, D.W. & Kim, K. 2004, "Uniform double-walled polymer microspheres of controllable shell thickness", *Journal of Controlled Release*, vol. 96, no. 1, pp. 101-111.

[103] Berkland, C., Pollauf, E., Varde, N., Pack, D.W. & Kim, K. 2007, "Monodisperse liquid-filled biodegradable microcapsules", *Pharmaceutical research*, vol. 24, no. 5, pp. 1007-1013.

[104] Manukian, A. & Toreki, W. 2008, "Inc.ARS, Gainsville FL Hydrocapsules®: a new method for aqueous drug delivery", *Drug Delivery Technol.Mag.*.

[105] Shao, T., Feng, X., Jin, Y. & Cheng, Y. 2013, "Controlled production of double emulsions in dual-coaxial capillaries device for millimeter-scale hollow polymer spheres", *Chemical Engineering Science*, vol. 104, pp. 55-63.

[106] Gaitzsch, F., Gäbler, A. & Kraume, M. 2011, "Analysis of droplet expulsion in stagnant single water-in-oil-in-water double emulsion globules", *Chemical Engineering Science*, vol. 66, no. 20, pp. 4663-4669.

[107] Schmit, A., Courbin, L., Marquis, M., Renard, D. & Panizza, P. 2014, "A pendant drop method for the production of calibrated double emulsions and emulsion gels", *RSC Advances*, vol. 4, no. 54, pp. 28504-28510.

[108] Nguyen, N.-. & Wereley, S.T. 2002, "Fundamentals and Applications of Microfluidics", Artech House, *Technology and Engineering*, ISBN:1-58053-343-4.

[109] Sauret, A., Spandagos, C. & Shum, H.C. 2012, "Fluctuation-induced dynamics of multiphase liquid jets with ultra-low interfacial tension", *Lab on a Chip - Miniaturisation for Chemistry and Biology*, vol. 12, no. 18, pp. 3380-3386.

[110] Josephides, D.N. & Sajjadi, S. 2015, "Increased drop formation frequency via reduction of surfactant interactions in flow-focusing microfluidic devices", *Langmuir*, vol. 31, no. 3, pp. 1218-1224.

[111] Li, X., Shaw, R., Evans, G.M. & Stevenson, P. 2010, "A simple numerical solution to the Ward-Tordai equation for the adsorption of non-ionic surfactants", *Computers and Chemical Engineering*, vol. 34, no. 2, pp. 146-153.

[112] Orive, G., Hernández, R.M., Gascón, A.R., Calafiore, R., Chang, T.M.S., De Vos, P., Hortelano, G., Hunkeler, D., Lacík, I., Shapiro, A.M.J. & Pedraz, J.L. 2003, "Cell encapsulation: Promise and progress", *Nature medicine*, vol. 9, no. 1, pp. 104-107.

[113] Seiffert, S. 2013, "Microgel capsules tailored by droplet-based microfluidics", *ChemPhysChem*, vol. 14, no. 2, pp. 295-304.

[114] Ivanovska, I.L., De Pablo, P.J., Ibarra, B., Sgalari, G., MacKintosh, F.C., Carrascosa, J.L., Schmidt, C.F. & Wuite, G.J.L. 2004, "Bacteriophage capsids: Tough nanoshells with complex elastic properties", *Proceedings of the National Academy of Sciences of the United States of America*, vol. 101, no. 20, pp. 7600-7605.

[115] Michel, J.P., Ivanovska, I.L., Gibbons, M.M., Klug, W.S., Knobler, C.M., Wuite, G.J.L. & Schmidt, C.F. 2006, "Nanoindentation studies of full and empty viral capsids and the effects of capsid protein mutations on elasticity and strength", *Proceedings of the National Academy of Sciences of the United States of America*, vol. 103, no. 16, pp. 6184-6189.

[116] Klug, W.S., Bruinsma, R.F., Michel, J.-., Knobler, C.M., Ivanovska, I.L., Schmidt, C.F. & Wuite, G.J.L. 2006, "Failure of viral shells", *Physical Review Letters*, vol. 97, no. 22.

[117] Park, Y., Best, C.A., Badizadegan, K., Dasari, R.R., Feld, M.S., Kuriabova, T., Henle, M.L., Levine, A.J. & Popescu, G. 2010, "Measurement of red blood cell mechanics during morphological changes", *Proceedings of the National Academy of Sciences of the United States of America*, vol. 107, no. 15, pp. 6731-6736.

[118] Paulose, J., Vliegenthart, G.A., Gompper, G. & Nelson, D.R. 2012, "Fluctuating shells under pressure", *Proceedings of the National Academy of Sciences of the United States of America*, vol. 109, no. 48, pp. 19551-19556.

[119] Kim, S.-., Lee, T.Y. & Lee, S.S. 2014, "Osmocapsules for direct measurement of osmotic strength", *Small*, vol. 10, no. 6, pp. 1155-1162.

[120] Choi, C.-., Kim, J., Nam, J.-., Kang, S.-., Jeong, S.-. & Lee, C.-. 2014, "Microfluidic design of complex emulsions", *ChemPhysChem*, vol. 15, no. 1, pp. 21-29.

[121] Saeki, D., Sugiura, S., Kanamori, T., Sato, S. & Ichikawa, S. 2010, "Formation of monodisperse calcium alginate microbeads by rupture of water-in-oil-in-water droplets with an ultra-thin oil phase layer", *Lab on a Chip - Miniaturisation for Chemistry and Biology*, vol. 10, no. 17, pp. 2292-2295.

[122] Abate, A.R., Thiele, J. & Weitz, D.A. 2011, "One-step formation of multiple emulsions in microfluidics", *Lab on a Chip - Miniaturisation for Chemistry and Biology*, vol. 11, no. 2, pp. 253-258.

[123] Hernández, E.C., Gundabala, V., Nieves, A.F. & Gordillo, J.M. 2009, "Scaling the drop size in coflow experiments", *New J.Phys.*, vol. 11, pp. 075021.

[124] Seiffert, S. & Weitz, D.A. 2010, "Controlled fabrication of polymer microgels by polymer-analogous gelation in droplet microfluidics", *Soft Matter*, vol. 6, no. 14, pp. 3184-3190.

[125] Mahsood, R. & Miraftab, M. 2014, "Novel materials for moist wound management: Alginate-psyllium hybrid fibres", *Journal of wound care*, vol. 23, no. 3, pp. 153-159.

[126] Sun, J. & Tan, H. 2013, "Alginate-based biomaterials for regenerative medicine applications", *Materials*, vol. 6, no. 4, pp. 1285-1309.

[127] Ahn, S.Y., Mun, C.H. & Lee, S.H. 2015, "Microfluidic spinning of fibrous alginate carrier having highly enhanced drug loading capability and delayed release profile", *RSC Advances*, vol. 5, no. 20, pp. 15172-15181.

[128] Onoe, H. & Takeuchi, S. 2015, "Cell-laden microfibers for bottom-up tissue engineering", *Drug discovery today*, vol. 20, no. 2, pp. 236-246.

[129] Daniele, M.A., Boyd, D.A., Adams, A.A. & Ligler, F.S. 2015, "Microfluidic strategies for design and assembly of microfibers and nanofibers with tissue engineering and regenerative medicine applications", *Advanced Healthcare Materials*, vol. 4, no. 1, pp. 11-28.

[130] Su, J., Zheng, Y. & Wu, H. 2009, "Generation of alginate microfibers with a roller-assisted microfluidic system", *Lab on a Chip - Miniaturisation for Chemistry and Biology*, vol. 9, no. 7, pp. 996-1001.

[131] Qin, Y. 2005, "Silver-containing alginate fibres and dressings", *International Wound Journal*, vol. 2, no. 2, pp. 172-176+139.

[132] Trial, C., Darbas, H., Lavigne, J.-., Sotto, A., Simoneau, G., Tillet, Y. & Téot, L. 2010, "Assessment of the antimicrobial effectiveness of a new silver alginate wound dressing: A RCT", *Journal of wound care*, vol. 19, no. 1, pp. 20-26.

[133] Neibert, K., Gopishetty, V., Grigoryev, A., Tokarev, I., Al-Hajaj, N., Vorstenbosch, J., Philip, A., Minko, S. & Maysinger, D. 2012, "Wound-healing with mechanically

robust and biodegradable hydrogel fibers loaded with silver nanoparticles", *Advanced Healthcare Materials*, vol. 1, no. 5, pp. 621-630.

[134] Sun, T., Hu, C., Nakajima, M., Takeuchi, M., Seki, M., Yue, T., Shi, Q., Fukuda, T. & Huang, Q. 2015, "On-chip fabrication and magnetic force estimation of peapod-like hybrid microfibers using a microfluidic device", *Microfluidics and Nanofluidics*, vol. 18, no. 5-6, pp. 1177-1187.

[135] Potter, K., Balcom, B.J., Carpenter, T.A. & Hall, L.D. 1994, "The gelation of sodium alginate with calcium ions studied by magnetic resonance imaging (MRI)", *Carbohydrate research*, vol. 257, no. 1, pp. 117-126.

[136] Mano, J.F., Silva, G.A., Azevedo, H.S., Malafaya, P.B., Sousa, R.A., Silva, S.S., Boesel, L.F., Oliveira, J.M., Santos, T.C., Marques, A.P., Neves, N.M. & Reis, R.L. 2007, "Natural origin biodegradable systems in tissue engineering and regenerative medicine: Present status and some moving trends", *Journal of the Royal Society Interface*, vol. 4, no. 17, pp. 999-1030.

[137] Izadifar, Z., Chen, X. & Kulyk, W. 2012, "Strategic design and fabrication of engineered scaffolds for articular cartilage repair.", *Journal of functional biomaterials*, vol. 3, no. 4, pp. 799-838.

[138] Colosi, C., Costantini, M., Latini, R., Ciccarelli, S., Stampella, A., Barbetta, A., Massimi, M., Devirgiliis, L.C. & Dentini, M. 2014, "Rapid prototyping of chitosan-coated alginate scaffolds through the use of a 3D fiber deposition technique", *Journal of Materials Chemistry B*, vol. 2, no. 39, pp. 6779-6791.

[139] Kwon, K., Shipley, R.J., Edirisinghe, M., Ezra, D.G., Rose, G.E., Rayment, A.W., Best, S.M. & Cameron, R.E. 2014, "Microstructure and mechanical properties of synthetic brow-suspension materials", *Materials Science & Engineering C-Materials for Biological Applications*, vol. 35, pp. 220-230.

[140] Mirabedini, A., Foroughi, J., Romeo, T. & Wallace, G.G. 2015, "Development and Characterization of Novel Hybrid Hydrogel Fibers", *Macromolecular Materials and Engineering*, vol. 300, no. 12, pp. 1217-1225.

[141] Dey, K., Khan, R.A. & Chowdhury, A.M.S. 2011, "Fabrication and Mechanical Characterization of Calcium Alginate Fiber-Reinforced Polyvinyl Alcohol Based Composites", *Polymer-Plastics Technology and Engineering*, vol. 50, no. 7, pp. 698-704.

[142] Liu, L., Jiang, L., Xu, G.K., Ma, C., Yang, X.G. & Yao, J.M. 2014, "Potential of alginate fibers incorporated with drug-loaded nanocapsules as drug delivery systems", *Journal of Materials Chemistry B*, vol. 2, no. 43, pp. 7596-7604.

[143] Lee, K.H., Shin, S.J., Park, Y. & Lee, S.-. 2009, "Synthesis of cell-laden alginate hollow fibers using microfluidic chips and microvascularized tissue-engineering applications", *Small*, vol. 5, no. 11, pp. 1264-1268.

[144] Chung, B.G., Lee, K.-., Khademhosseini, A. & Lee, S.-. 2012, "Microfluidic fabrication of microengineered hydrogels and their application in tissue engineering", *Lab on a Chip - Miniaturisation for Chemistry and Biology*, vol. 12, no. 1, pp. 45-59.

[145] Sifton, H.B. 1945, "Air-Space Tissue in Plants", *Botanical Review*, vol. 11, no. 2, pp. 108-143.

[146] Abbaspourrad, A., Duncanson, W.J., Lebedeva, N., Kim, S., Zhushma, A.P., Datta, S.S., Dayton, P.A., Sheiko, S.S., Rubinstein, M. & Weitz, D.A. 2013, "Microfluidic Fabrication of Stable Gas-Filled Microcapsules for Acoustic Contrast Enhancement", *Langmuir*, vol. 29, no. 40, pp. 12352-12357.

[147] Wan, J., Bick, A., Sullivan, M. & Stone, H.A. 2008, "Controllable microfluidic production of microbubbles in water-in-oil emulsions and the formation of porous microparticles", *Advanced Materials*, vol. 20, no. 17, pp. 3314-3318.

[148] Wang, W.-., Chen, R., Xu, J.-., Wang, Y.-. & Luo, G.-. 2014, "One-step microfluidic approach for controllable production of gas-in-water-in-oil (G/W/O) double emulsions and hollow hydrogel microspheres", *RSC Advances*, vol. 4, no. 32, pp. 16444-16448.

[149] Huang, K., Lin, Y., Chang, W., Wang, Y. & Yang, C. 2013, "A Facile Fabrication of Alginate Microbubbles Using a Gas Foaming Reaction", *Molecules*, vol. 18, no. 8, pp. 9594-9602.

[150] Yang, C., Wang, W., Grumezescu, A.M., Huang, K. & Lin, Y. 2014, "One-step synthesis of platinum nanoparticles loaded in alginate bubbles", *Nanoscale Research Letters*, vol. 9, pp. 277.

[151] Wang, C., Yang, K., Lin, K., Liu, H. & Lin, F. 2011, "A highly organized three-dimensional alginate scaffold for cartilage tissue engineering prepared by microfluidic technology", *Biomaterials*, vol. 32, no. 29, pp. 7118-7126.

[152] Hou, L., Jiang, H. & Lee, D. 2016, "Bubble-filled silica microfibers from multiphasic flows for lightweight composite fabrication", *Chemical Engineering Journal*, vol. 288, pp. 539-545.

[153] Kang, E., Jeong, G.S., Choi, Y.Y., Lee, K.H., Khademhosseini, A. & Lee, S.-. 2011, "Digitally tunable physicochemical coding of material composition and topography in continuous microfibres", *Nature Materials*, vol. 10, no. 11, pp. 877-883.

[154] Simpliciano, C., Clark, L., Asi, B., Chu, N., Mercado, M., Diaz S., Goedert, M., & Mobed-Miremadi, M. 2013 "Cross-Linked Alginate Film Pore Size Determination Using Atomic Force Microscopy and Validation Using Diffusivity Determinations," *Journal of Surface Engineered Materials and Advanced Technology*, Vol. 3 No. 4A, pp. 1-12.

[155] Yoon, Y.I., Moon, H.S., Lyoo, W.S., Lee, T.S. & Park, W.H. 2008, "Superhydrophobicity of PHBV fibrous surface with bead-on-string structure.", *Journal of colloid and interface science*, vol. 320, no. 1, pp. 91-5.

[156] Zhan, N., Li, Y., Zhang, C., Song, Y., Wang, H., Sun, L., Yang, Q. & Hong, X. 2010, "A novel multinozzle electrospinning process for preparing superhydrophobic PS films with controllable bead-on-string/microfiber morphology", *Journal of colloid and interface science*, vol. 345, no. 2, pp. 491-495.

[157] Fong, H., Chun, I. & Reneker, D.H. 1999, "Beaded nanofibers formed during electrospinning", *Polymer*, vol. 40, no. 16, pp. 4585-4592.

[158] Zander, N.E. 2013, "Hierarchically Structured Electrospun Fibers", *Polymers*, vol. 5, no. 1, pp. 19-44.

[159] Maeda, K., Onoe, H., Takinoue, M. & Takeuchi, S. 2015, "Observation and Manipulation of a Capillary Jet in a Centrifuge-Based Droplet Shooting Device", *Micromachines*, vol. 6, no. 10, pp. 1526-1533.